

UNIVERSITAT DE BARCELONA

Modeling the radial glia niche: Deciphering key mechanotransduction components

José Pablo Soriano Esqué

ADVERTIMENT. La consulta d'aquesta tesi queda condicionada a l'acceptació de les següents condicions d'ús: La difusió d'aquesta tesi per mitjà del servei TDX (**www.tdx.cat**) i a través del Dipòsit Digital de la UB (**diposit.ub.edu**) ha estat autoritzada pels titulars dels drets de propietat intel·lectual únicament per a usos privats emmarcats en activitats d'investigació i docència. No s'autoritza la seva reproducció amb finalitats de lucre ni la seva difusió i posada a disposició des d'un lloc aliè al servei TDX ni al Dipòsit Digital de la UB. No s'autoritza la presentació del seu contingut en una finestra o marc aliè a TDX o al Dipòsit Digital de la UB (framing). Aquesta reserva de drets afecta tant al resum de presentació de la tesi com als seus continguts. En la utilització o cita de parts de la tesi és obligat indicar el nom de la persona autora.

ADVERTENCIA. La consulta de esta tesis queda condicionada a la aceptación de las siguientes condiciones de uso: La difusión de esta tesis por medio del servicio TDR (**www.tdx.cat**) y a través del Repositorio Digital de la UB (**diposit.ub.edu**) ha sido autorizada por los titulares de los derechos de propiedad intelectual únicamente para usos privados enmarcados en actividades de investigación y docencia. No se autoriza su reproducción con finalidades de lucro ni su difusión y puesta a disposición desde un sitio ajeno al servicio TDR o al Repositorio Digital de la UB. No se autoriza la presentación de su contenido en una ventana o marco ajeno a TDR o al Repositorio Digital de la UB (framing). Esta reserva de derechos afecta tanto al resumen de presentación de la tesis como a sus contenidos. En la utilización o cita de partes de la tesis es obligado indicar el nombre de la persona autora.

WARNING. On having consulted this thesis you're accepting the following use conditions: Spreading this thesis by the TDX (**www.tdx.cat**) service and by the UB Digital Repository (**diposit.ub.edu**) has been authorized by the titular of the intellectual property rights only for private uses placed in investigation and teaching activities. Reproduction with lucrative aims is not authorized nor its spreading and availability from a site foreign to the TDX service or to the UB Digital Repository. Introducing its content in a window or frame foreign to the TDX service or to the UB Digital Repository is not authorized (framing). Those rights affect to the presentation summary of the thesis as well as to its contents. In the using or citation of parts of the thesis it's obliged to indicate the name of the author.



UNIVERSITAT DE BARCELONA

Modeling the radial glia niche: Deciphering key mechanotransduction components.

University of Barcelona PhD Biomedicine Program

PhD Student: José Pablo Soriano Esqué

PhD Thesis Supervisor: Dra. Soledad Alcántara Horrillo

Va per tu papa

AGRAÏMENTS

Com la glia radial d'aquesta tesi, l'entorn és primordial, estimula i frustra, determina i transforma, tranquil·litza i altera. Una tesi, que anàloga a un organisme, no es fa sola. Quin sentit té una cèl·lula sense les seves germanes, companyes, i d'altres que van i venen, apareixent al llarg de la seva vida? Una cèl·lula es defineix per les característiques intrínseques, i en ella resideix el poder del canvi, sobreviure o morir, però els factors externs, tenen igual o més poder per definir el camí que prendrà. Una sinergia, que esdevé dins d'un marc temporal, a vegades definit, a vegades sobrepassat. Jo -la cèl·lula-, una tesi -el resultat final-, i després de gairebé 6 anys, tota la gent que m'ha acompanyat i ha posat el seu gra de sorra per a que aquesta feina surti endavant. Així doncs, i sense més preàmbuls, i tot i que es llegeix la primera però s'escriu al final, procediré amb els agraïments pertinents, perquè com bé deia el meu pare sempre: "és de ben nascut, ser agraït" i crec, que no hi podria estar més en acord, aquesta és la màxima que cal dur sempre a la avantguarda. Així que, abans que res, GRÀCIES.

Intentaré ser breu, cosa que em costa i evidentment no em caracteritza, però vull agrair a totes les persones que també han permès que estigui on estic. I tot comença durant la carrera, on a l'hora d'escollir un article per a fer un treball, de totes les opcions que hi havia, hi va haver un que em va robar absolutament tota la atenció, que va ser el de la Marta Mattotti, publicat el 2012, i que jo vaig llegir aquell mateix any, i, justament, és l'article que serveix de fonament de tota la meva tesi. És un final de cicle, d'un jove amb el cap ple de pardals (encara en tinc, però potser no tants), que va tindré l'oportunitat de fer el TFG amb un grup que formava part d'aquell article, el liderat per la Dra. Elisabeth Engel, també va ser ella qui ens va fer escollir els articles, sense saber aleshores, que allò marcaria el meu camí fins aquí, gràcies. D'allà a Irlanda, d'Irlanda a Saragossa, on vaig descobrir el món de la modelització, de la mesura, de la caracterització, dels patrons, i que pràcticament tot, per molt complex que sigui, es pot aproximar. Saragossa és el segon punt d'inflexió de la meva vida, on conec al Jesús (en parlarem més tard) i al Manu, i gràcies a les eines que em van donar, se'm va ocórrer la possibilitat d'incloure aquests coneixements a quelcom creia que tenia potencial, que era aplicar-los d'alguna forma al sistema nerviós central, sense treure'm del cap l'article de 2012. I aquí, el primer email que ens vam creuar amb la Sole, un dilluns 1 de febrer de 2016, on concretem una cita per veure'ns el divendres. Les coses a foc lent, quelcom que també em caracteritza i a vegades desespera, però vaig tenir la sort que, igual que a la Sole, al Manu, líder del grup Multiscale in Mechanical and Biological Engineering, li va sembla genial la idea de poder fer un TFM combinat amb la Universitat de Barcelona. Sinergia feta. Un octubre de 2016 començo un TFM que acabaria defensant el desembre de

2017, i que seria el preludi d'una tesi que començaria l'octubre de 2018 i acabaria a principis de 2024. GRÀCIES.

Sole, simplemente gracias, i gracias de todo corazón. Apostaste por mí, me diste una oportunidad, y depositaste tu confianza en algo que no sabíamos si iba a resultar. Me brindaste mi primer contrato, sabiendo mi limitación para poder pedir becas, y, aun así, tiramos adelante. Creo que hay una cosa que te caracteriza y que es el motor de todo este proceso y es tu curiosidad, tu forma de pensar, y sobre todo, esa mentalidad disruptiva, la de romper con lo dogmático (obviamente con rigor, sentido, y lógica), e ir un poco más allá por raro que parezca. Nos hemos reído, alegrado y enfadado, pero eso es lo normal en un proceso de crecimiento. Me has enseñado a ser meticuloso, perfeccionista y a dudar hasta de mi sombra (eso casi en exceso), pero creo que es importante para ganar sentido crítico. Has tenido paciencia, caos y desorden me identifican como el Pax6 y la nestina a la glía radial. Por muchas cosas te doy las gracias, y muchas cosas me dejo, pero hay algo, que creo que está por encima de todo y es tu predisposición. Siempre disponible, y no hay nada que me haga más gracia que recordar una pregunta simple a las 19:00 de la tarde, independientemente del día, se puede convertir en una discusión científica de 2h. Simplemente gracias, Sole.

Ahora voy con Zaragoza (Zgz), un segundo hogar para mí. Desde el TFM a ahora, gracias, Manu, y, sobre todo, gracias, Carlos. Hahahaha, que paciencia has tenido conmigo, un ángel de la guarda del Matlab. Que fácil y que eficientemente haces todo, como muchas veces te he dicho, soy tu fan, y así se va a quedar. Muchas gracias por todo, y como te he dicho muchas veces, espero contar siempre contigo. Del grupo de Manu, gracias Mª Ángeles y gracias Mª José, por escucharme cada vez que vengo a visitaros, y aguantar mis chapas sobre lo que estábamos haciendo. Es un regalo como me siento cada vez que voy a veros, siempre tenéis un rato para mí y me transmitís el cariño que siento que me tenéis, que, por supuesto, es mutuo. GRACIAS.

Y por supuesto, gracias, Manu (Zgz), que, junto a Daniel (UB), gracias, Daniel, me habéis orientado y guiado durante todo este proceso, creo que no he podido tener más suerte que la de teneros como miembros de mi comisión de seguimiento. No solo me habéis ayudado en la tesis per se, sino con unas comisiones que han tenido un gran porcentaje de mentoring, escucha, y consejos, y siempre abiertos a discutir o comentar cualquier cosa. Que trato humano tan increíble que tenéis. GRACIAS.

No solo en lo laboral, sino en lo personal, Zgz es mi segundo hogar. Apareciste a mitad de mi tesis, una revelación, y te has convertido en una pieza fundamental de este trabajo y de mi desarrollo personal. Estadística, una de las 3 asignaturas que compensé durante

la carrera, nunca llegué a imaginar que la encontraría tan fascinante y emocionante y todo fue gracias a ti Jesús. Siempre alegre, predispuesto y entusiasta, rebosas ilusión y devoción por lo que haces y de la misma forma lo transmites. Haces que lo difícil parezca fácil, y no solo eso, sino que has conseguido que un tarugo como yo consiga entenderla, más o menos. Que extremadamente difícil es hacer esto que haces sin darte cuenta. Además, me has abierto las puertas de tu casa y de tu familia que estoy encantado de haber conocido, me has hecho sentir como uno más. Gracias por ser tan buena persona y tener siempre tiempo y dedicación, a cualquier hora y día de la semana, por preocuparte por mí en lo personal y lo profesional. También por ofrecerme tu despacho, que cuando llego instalo mis pantallas y cosas, e introducirme a todos y cada uno de los miembros del departamento de estadística y allegados. Ha sido genial poder conocer, a parte a todos los miembros, especialmente a Jorge y a Zeus, personas con un gran potencial y buen corazón. GRACIAS.

Ara ja toca el nostre grup, DN. Em poso a pensar, escric i esborro, i no se ni per on començar (encara que això ja és un començament i és redundant). Ja no entraré en detalls de la meravellosa impressió (òbviament ironia) que els hi vaig causar als que serien dos grans pilars del meu desenvolupament com a investigador, Aina i Rafa. Tan diferents i tant rellevants a parts iguals. Alba Aina, et va tocar ensenyar-m'ho tot. A mi, un maldestre intent d'investigació que amb prou feines sabia fer anar una pipeta i que disposava les coses a les llibretes que després ni jo entenia, i tu, amb el teu ordre i detall escrupolós, totalment inigualable. Tot i que d'entrada se que no et queia gaire bé, no vaig perdre l'esperança, i darrera d'aquella façana de persona seria, residia un cor enorme amb uns principis indestructibles: la família, la justícia, el feminisme i el català. No vull deixar-me el teu sentit de l'humor i permetre'm que no sigui un ignorant en quan als temes més importants com son els salseos internacionals que òbviament son informació bàsica i necessària per sobreviure avui en dia. Gracies per la paciència i per permetrem conèixer-te. Ara tu Rafa, tetexenko, res més que quin plaer més gran conèixer una persona com tu. Quin cap que tens i quina forma de veure la vida. Les grans xapes filosòfiques i la quantitat incommensurable de pitis i cafès parlant del cosmos, els rotomotores, i les coses més essencials de la vida. Em vas ensenyar a tractar als animals, a escoltar a les rates, a observar-les i humanitzar-les, en la mesura del que es necessari, tard o d'hora farem un brindis per Robespierre. Mai sabrem quina música li agradava més però segur que podríem fer-nos una idea. Gracies per tenir sempre un espai per intercedir en lo mes personal, d'una forma sincera i amb sentit. Gracies al dos, us porto sempre a dins. I ara, com no, no podia mencionar a ningú mes que a l'Alfonso, i ara ja ho escric en català que vas sobradíssim per entendre-ho. Vas

arribar i ho vas fer per quedar-t'hi, no en l'àmbit físic sinó en l'emocional. No m'oblidaré mai d'un consell que m'ha fet pensar molt en molts moments, i que de tant en tant recordo, i és que hi ha vida més enllà del laboratori, que he de gaudir tot el que faci, que per molt que ens apassioni el que fem, s'ha de tenir temps per gaudir de tota la resta. I quina raó que tens. I també, en la part professional, vas ser tu el que em vas fer obrir el meló, que quin meló, el d'estudiar les mitocòndries i si podria haver-hi canvis associats a l'estímul mecànic. Em vas donar anticossos per provar i em vas aconsellar en tot moment, i encara que ara fa temps que no et consulto, properament ho faré, perquè tenim feina en aquest camp. Gràcies Alfonso, creo que te debo el hacerte algún litrillo de parafo, que me ha salvado el culo más de una vez (hahaha aquí cal que et doni les gracies Cris per fer-lo i tenir-lo sempre a punt). I ja per últim, agrair als estudiants que he tingut la sort d'ensenyar i tutoritzar, començant per la Núria, a qui només vaig ensenyar les tècniques bàsiques de laboratori i va treballar amb mi amb tota la part del YAP/TAZ i la β-catenina inicialment. En segon lloc, tu Gemma, moltes gràcies per tot, la predisposició i les ganes d'aprendre i millorar, i d'entusiasmar-te tant amb el projecte com jo. Vas desenvolupar tota la part de les mitocòndries i junts vam tancar tot el bloc de Westerns, quina llauna els Westerns. Però del no res, vas acabar sent una crack i et sortien increïblement be. Tots els resultats estan en aquesta tesi, per tant, sense tu, no hagués pogut ser possible. I gràcies per la paciència d'aguantar-me, que vaja un jo, deu t'ho pagui. Vas entrar en un moment crític, anàvem amb mascareta, però quan ens la vam poder treure es va veure quelcom que et caracteritza i és el somriure i la alegria, que espero que no perdis i t'acompanyi sempre. I per últim tu Alex. Quina troballa!! He empezado escribiendo en catalán, pero no he podido continuar, me has ganado la batalla en eso, pero no por nada, sino porque no he podido cambiarlo. Que buen corazón tienes y que sinceridad. Humilde y trabajador y con una capacidad de adaptación y sentido de la justicia increíble. Me pillaste en una época de mucho estrés y tuviste que aguantar mis arreones. Me has permitido reflexionar muchas veces y hacer que me diera cuenta de que estaba haciendo las cosas mal, que por muy cabreado que este no lo puedo pagar con nadie más que conmigo mismo (suena catastrófico y por suerte no ocurrió muchas veces, pero con que ocurra una, es suficiente). Me has hecho ser mejor persona y esto te lo agradezco mucho. He disfrutado mucho verte crecer, desde tu TFG a tu TFM. Una evolución espectacular y digna del mejor Michael Jordan de la época, del mejor MC tanto del West como del Est. Trabajo, constancia y voluntad son las virtudes que profesas y creo que son la base para cualquier futuro posible. Que suerte he tenido. GRÀCIES.

Lab 5101, començant per vosaltres Ricardo, Vanessa i Celia. Us estaré sempre agraït per oferir-me el primer contracte de professor universitari. Encara que les circumstàncies ho van facilitar, vau confiar en mi i vau lluitar cada una de les vegades que s'acabava el contracte per a que pugues continuar amb vosaltres. M'heu obert les portes del vostre grup de vat a vat i m'he sentit un membre més. Rigor, dedicació y sobretot, ganes de fer-ho bé i transmetre als estudiants de primer la passió per la ciència. M'enduc una part de cada un de vosaltres, en el personal i el professional. I com reiteradament dic, gracies per la paciència d'aguantar-me i tenir sempre el despatx obert per a qualsevol tipus de consulta, des de més emocionals fins a les estrictament professionals. GRACIES.

Alain i Cris, quin gust més gran haver-vos conegut i compartit aquesta última etapa. Em vaig quedar orfe quan va marxar l'Aina i em vau adoptar i cuidar com un més. Alain, que conversas más buenas hemos tenido en sala de cultivos, en el pasillo, comiendo. Me las llevo todas y cada una y creo que han mejorado mucho mi forma de ver el mundo de la investigación. Cris, comandanta, presidenta de la comisión de festejos y no sé qué más ahora, em vaig quedar la missió de parlar amb tu en català i quin goig. Quina gran persona ets i quin bon cor que tens, responsable a més no poder que a l'hora t'ha fet patir de més, però tot i així, sempre, absolutament sempre, disposada a ajudar i a escoltar. Como nos gustan los chismes y que gran aliada has encontrado con Ana. He après molt, de la vida, de la cuina, i del feminisme. A favor de discutir amb tu, dona gust i sempre he après coses noves, ja siguin punts de vista o a comprendre més sobre el masclisme inherent d'aquesta societat. Anna amb tu he pogut posar en pràctica tots els meus coneixements adquirits durant els meus primers anys amb l'Aina, de segur que us haguéssiu entès, suposo que es el que hi ha, Swiftie se nace, no se hace. Jajajajaj. Cosa que també puc aplicar al madridisme, que s'hi neix. Que bé ens ho hem passat, Barça o Madrid, és igual, poques persones tant futboleres com tu he conegut. I per últim, Pere, arribes l'últim però agafes ràpidament posicions capdavanteres, gran professional, millor persona. M'has transmès pausa i serenor, i il·lusió per les petites coses, ets un bon exemple a seguir. Per últim, enumerar a tots els que heu format part d'aquest grup, des del Korrodi, David, Ananda, Pili, Marta, Adri, Mar, Dana, Piedad, i tots els tècnics i persones que han anat venint. GRÀCIES.

I l'últim gran bloc. Alberto, quina sort que has arribat quan has arribat, quina sort conèixer-te. Vas arribar en un dels moments més importants de la meva tesi i la teva energia ens ha contagiat a tots. Quina forma de treballar tant summament espectacular, i ho dic de tot cor. Passió, voluntat, meticulositat, professionalitat, i mil adjectius que podria utilitzar. Ràpidament m'has escoltat i m'has aconsellat tant amb la tesi com amb la vida, i m'has tractat sempre de tu a tu. La humilitat et caracteritza, però tant com la

Sole i el Jesús, tens una capacitat d'explicar les coses d'una forma tant senzilla, que això, com ja he dit, només ho fan els que en saben molt. La FENS de 2022, amb tu i la Zaida em va obrir els ulls, em vau transmetre la vostra visió del món científic i les ganes de fer més coses, i millor, amb un sentit crític i rigorós. Quina sort que he tingut. I gràcies a tu, he pogut compartir aquests últims anys amb la Gisele, i més recentment, la Marta.

Gisele y Marta, muchas gracias por vuestra paciencia y ganas de hacer las cosas bien. Sin vosotras probablemente hubiera colapsado. Desde compartir momentos de estabulario, poner orden y revisar todos los reactivos, a hacer los pedidos, que madre mía los pedidos, que pereza y que necesarios son hahahahah. Y también gracias por las risas y los buenos momentos tanto de lab o comiendo. GRACIAS.

Gracies Sandra, que junt amb l'Alberto i la Sole, heu creat una sinergia entre grups que no te res més que coses positives. Gràcies per la capacitat crítica i de mirar mes enllà, de fer-me sempre preguntes que em deixen pensant durant uns dies, inclús setmanes, i m'han permès comprendre el mètode científic d'una forma diferent a com el tenia entès. I com no, gracies Andrea, Laura i Isa per els bons moments i les rises, per les vostres recomanacions i intervencions quan presento, sempre bones i que generen més feina (ejem..), i deixar-vos molestar quan estic imprimint o vaig a omplir l'aigua i passo a saludar. GRACIES.

Ahora os toca a vosotros, Ros & friends. Quién diría que al final ha resultó todo lo que hemos hecho del calcio. Que, al 100%, esto no hubiera sido posible sin ti. Nadie sabe la de horas que le hemos echado para sacar esto adelante, salvo tú y yo. Lo que nos costó ponerlo a punto, la cantidad de pruebas previas que hicimos para al final, conseguir unos datos que merecían la pena. Compañeros clandestinos, lunes, martes y miércoles hasta las 00:00 de la noche, y hasta más tarde. GRACIAS. Y gracias a Alex y Anna, compañeros de pitis, y a Nuria, Galyna, y Ricardo (breve y bueno).

Per la 4ta planta també tinc especial agraïment al José Carlos, per les consultes sobre metabolisme, a la Petra, per ensenyar-me a fer els anàlisis de lactat i glucosa, a l'Andy, per escoltar-me i ser tant proper com ets, i ajudar-nos amb l'Àlex durant el seu TFM, al Fran, per escoltar les meves xapes sobre el calci i tenir sempre la porta oberta, i mostrar predisposició a ajudar-me en tot moment, i per últim, al grup de l'Eloi, al Victor i la Yara, que de tant en tant, quan pujàveu al criòstat us enganxava per banda i us tocava aguantar els meus rotllos. GRACIES.

Ara baixant a la 3ra planta, aquesta tesi no hagués estat possible sense les innumerables hores de confocal, dia i nit, laborables i festius. Benja, gracies per ensenyar-me el món de la microscòpia i compartir tantes hores com hem fet, parlant de

settings, del Barça i l'Espanyol, o de la vida. Gràcies Esther i Bea, per la vostra predisposició a ajudar-me sempre, a ensenyar-me utilitzar les PCR. GRACIES

Y por último en lo relativo a Bellvitge, gracias, Juan, por tu humor y aceptar mi evolución del café solo, al café con leche, al café con leche de avena (eso no es leche), al café descafeinado con leche de avena que eso ya no sabemos ni lo que es. Gràcies als de manteniment, al Gabi, per tenir sempre una estona per xerrar, i per ensenyar-me les entranyes de Bellvitge, ojo, que hi ha una gavina que esta com un llum, i al José, un còmplice, que sense ell, els experiments del calci no haguessin pogut ser possibles. I per acabar, a la Jessica, gràcies per cuidar dels ratolins i de la sala tant bé. Una extensió que m'ha facilitat molt les coses, sempre disposada a avançar-me la informació per evitar-me viatges innecessaris a l'estabulari.

També agrair la paciència a tots els meus amics, de Barcelona, de Masnou, de Saragossa, o de Madrid. M'heu donat l'espai necessari per evadir-me quan ho he necessitat i el recolzament en moments difícils. Heu esperat a que arribi, sempre tard, i inclús alguna vegada no he arribat. No us heu enfadat mai, tot i que aquest últim any la meva disponibilitat ha estat pràcticament nul·la. Us estimo a tots, moltíssimes gràcies! Quiero aprovechar para hacerte una mención especial Leo, te incluyo en este bloque porque creo que así tiene que ser. Desde el Máster hasta ahora, distintos caminos, pero al final hemos acabado haciendo cosas juntos. Gracias por tu tiempo en el análisis del single-cell y por toda tu contribución en algunos resultados de esta tesis. Muchísimas gracias.

I com ve tots sabeu i que per alguna raó es diu, que els últims seran els primers. Infinites gracies a la meva família, al meu pare, en pau descansi, quina il·lusió li feia que estigues fent el doctorat, quines preguntes més difícils em plantejava que avui en dia no sabria respondre, no se si ho aconseguiré mai això. A la meva mare, per fer de mare, per estimar-me i sempre tenir una estona per escoltar-me i deixar-me espai per a que el meu temperament huracanat flueixi i així sentir-me millor, i per ser tan sabia, i donar-me sempre bons consells. A la Irina, el Monxo i la Carla, els millors germans del mon, i ho sento per si els que ho llegiu en teniu, però es així. A la Beth, la petita gran esperança d'aquesta família. A la tieta, per ser la millor tieta del mon i preguntar-me casi cada 1 o 2 mesos com va la tesi, no has desesperat i ni un sol dia, toca passar revista. Al Pascual, por querernos como si fuéramos familia, que, de hecho, lo eres, porque todos te hemos escogido como tal, y gracias por ayudarme como solo tú sabes que lo has hecho. Us estimo molt, i gràcies per aguantar-me tot aquest temps que se de sobres que no us ho he posat fàcil.

I per últim, no tinc més que paraules d'amor, agraïment, i tendresa per com has portat aquests anys de tesi. Vam començar que encara no havia ni començat la tesi, i jo, que tinc un problema amb els tempos, et vaig dir que res, en 3 anys està..... JAJAJAJA quasi 6 anys després.... Santa paciència, a sobre m'has hagut d'aguantar i acceptar moltes coses que no tothom estaria disposat. Des d'arribar a les 11, 12, 1, 2 de la nit perquè m'he quedat treballant, a no poder fer coses els findes, a tenir que acompanyar-me a Bellvitge perquè he d'anar a l'estabulari o a canviar el medi un dissabte o diumenge abans de marxar amb la furgo, a no ser tant present com hagués volgut. Per moltes més coses que em deixo, gracies per estimar-me, i ser com ets, perquè en cap moment he sentit dubte, ni que no creguessis en el que estava fent. Gracies Laura, t'estimo inifint!

Perdoneu pel rotllo, soc així, i no ho puc evitar, no podia no dir tot el que sentia i com ho sentia, tot i que m'he reprimit per no excedir-me (encara que ja ho he fet).

GRACIES DE TOT COR A TOTHOM.

ABSTRACT

Radial glial (RG) are the principal neural stem cells of the embryonic brain, giving rise to intermediate progenitors and fate-committed neural cell types, and serving as a mechanical scaffold for neuron migration and correct cortical patterning. The lack of RG cells in the adult brain is considered a hallmark of the reduced endogenous brain regenerative capacity in some species. From the mechanobiology point of view, brain histogenesis encompasses a continuum of mechanical cues, metabolic shifts and transcriptional changes that orchestrate the construction of a healthy brain through a fine-tuned balance of mechanotransducive processes. The use of biomaterial-based strategies provides an excellent opportunity to model the architectural features of the embryonic brain. Ln2PMMA is an RG biomimetic substrate of poly methyl methacrylate with 2μm linear topography that reproduced the surface properties and mechanical anisotropy of the RG niche during embryonic brain development, with the capability to induce cultured astrocytes to dedifferentiate into functional RG cells. Although the mechanotransducive components underlying this process are largely unknown. In this Doctoral Thesis, we used mouse cortical glial cultures and ln2PMMA RG biomimetic material as a robust biomechanical tool for the in vitro analysis of mechanotransducive mechanisms involved in RG linage differentiation, allowing us to define some of the mechano-electrical -metabolic and -nuclear components of the astrocyte-RG lineage progression in response to substrate biomechanical cues. First, we developed a unified image segmentation analysis, based on MATLAB algorithms, for the extraction of morphology parameters from subcellular structures, linked to biochemically identified cells from microscopy images. Second, we developed a multivariate logistic regression model for fitting RG probability based in nuclear morphology parameters and cell density. The application of this model to our experimental data revealed the existence of intrinsic RG nuclear constraints, and that nuclear deformation and changes in nuclear lamins ratio precedes the expression of NSC/RG markers. Third, by using pharmacological inhibitors and Ca^{2+} imaging, together with RG molecular markers, we determined the implication of excitatory and inhibitory mechanosensitive ion channels, changes in CaMKII activity and in intracellular calcium dynamics, in the biomechanical induction of RG. Fourth, we identified a metabolic switch from astrocyte to RG, involving changes in mitochondrial dynamics and a bias towards increased aerobic glycolysis and anabolic metabolism. Finally, the application of the RGM model to image datasets from mouse and human neural cells allows us to identify the evolutionary conservation of RG nuclear constraints. Converting our RGM model, and their future improved versions, into an invaluable tool with unsuspected possibilities for the analysis of brain development.

TABLE OF CONTENTS

AGRAÏMENTS **5**

ABSTRACT **13**

TABLE OF CONTENTS **15**

Tables and Figures **19**

FIGURES 19

TABLES 22

SUPPLEMENTARY 22

ABBREVIATIONS **23**

1. INTRODUCTION **25**

1.1. What are radial glia cells? 27

1.1.1. RG in brain development 28

1.1.2. RG lineage progression and characterization 32

1.1.3. RG-astrocyte transformation and adult brain regenerative capacity 34

1.1.4. The role of Ca2+ during corticogenesis 36

1.1.5. RG metabolism during corticogenesis 39

1.1.6. Mitochondrial morphology and dynamics 42

1.2. Mechanotransduction components 45

1.2.1. The mechanical brain 46

1.2.3. Cellular cytoskeleton in glial cells 49

1.2.4. The nucleus as a mechanosensitive organelle 52

1.2.5. Mechanosensing transcriptional co-activators in RG lineage progression 56

1.2.6. Mechanoelectrical signals: Mechanosensitive ion channels 60

1.2.7. Calcium signaling toolkit in astrocyte lineage cells 64

1.3. Mechanical and Biomaterial-based strategies for brain regeneration 66

1.4. The arising of modeling and multiparametric models 68

2. GOALS **73**

3. MATERIALS AND METHODS **77**

3.1. Animals and cell cultures 79
Cortical primary cultures 79
Human induced pluripotent stem cells (iPSCs) 79
Human neural progenitor cells (hNPCs) 79
Brain Organoids 80
Fetal tissue samples and human radial glia cell (RGC) cultures 81
3.2. PMMA micropatterning, characterization and sterilization 82
3.3. Immunofluorescence 82
3.4. Western Blot 83
3.5. Lactate assays 87
3.6. Image processing 87
Mitochondrial morphology characterization 87
Cell nuclei segmentation 88
3.7. Logistic regression model construction 92
Image Variable definition 92
Type and definition of response 93
Type of model 94
Selected model 94
Describing the equation and model validation 97
Model Application 98
3.8. Publicly available single-cell transcriptomics data analysis 100
3.9. Pharmacological treatments 100
3.10. Calcium Imaging 101
3.11. Statistical analysis 104
4. RESULTS 105
4.1. Implication of MSCs and Ca^{2+} signaling in the biomechanical induction of RG. 107
4.1.1. Temporal sequence of In2PMMA biomechanical induction of phenotypic changes in glial cultures 107

4.1.2. Expression of mechanoelectrical transduction components during mouse RG linage progression. 108

4.1.3. Identification of MSCs potentially relevant in ln2PMMA biomechanical induction of RG. 110

4.1.4. Pharmacological validation of MSCs and Ca^{2+} signaling implication in the biomechanical induction of RG. 111

4.1.5. Evaluation of intracellular Ca^{2+} dynamics in glial cells grown on control and ln2PMMA substrates. 115

4.2. Effect of ln2PMMA biomechanical signals in the metabolic signature and mitochondrial dynamics of glial cells. 119

4.1.1. Characterization of the metabolic signature of glial cells grown on ln2PMMA and control substrates. 119

4.1.2. Analysis of mitochondrial dynamics in glial cells grown on ln2PMMA and control substrate. 122

4.3. Role of nuclear deformation in the biomechanical induction of RG. 125

4.3.1. Nuclear morphology analysis. 125

4.3.2. Development of a logistic regression model for fitting RG probability based in nuclear morphology parameters. 129

Model Selection 130

Interpretation and behavior of model variables 132

Model equation selection 134

RGM model application to the datasets used for fitting the model 135

The LogOdds ratio function F(0) identified intrinsic mechanical nuclear constrains in RG 138

Model Validation 141

Confounding effect of the cell cycle progression in RGM model predictions 143

4.3.3. Application development to easily apply RGM model 144

4.4. RGM model application to identify relationships between nuclear deformation and different mechanotransduction components 145

4.4.1. RGM model application to predict RG in glial cell cultures across time. 145

4.4.2. RGM model application to evaluate the relationship between lamins A-C/B1 ratio and nuclear deformation. 148

4.4.3. RGM model application to evaluate the relationship between mechanosensitive transcriptional cofactors and nuclear deformation. 151

4.4.4. RGM model application to evaluate the relationship between Ca^{2+} signaling and nuclear deformation. 154

4.4.5. RGM model application to evaluate the relationship between mitochondrial dynamics and nuclear deformation. 157

4.5. Conservation of RG nuclear morphology constraints across species 159

4.6. RGM model limitations for 3D and in vivo applications 164

5. DISCUSSION 167

Methodological considerations related to glial cell type identification 169

Methodological considerations related to image analysis tools 171

Methodological considerations related to the RGM model construction 172

Temporal sequence of glial response to ln2PMMA biomechanical signals 175

Mechanoelectrical transduction components of glial response to ln2PMMA biomechanical signals 178

Metabolic rewiring and mitochondrial network adaptation during glial response to ln2PMMA biomechanical signals 180

Evolutive conservation of RG nuclear allometry 183

Integrated hypothesis of the mechano-electrical -metabolic and -nuclear components during biomechanical dedifferentiation of astrocytes into RG 185

6. CONCLUSIONS 189

7. CONTRIBUTIONS 193

8. BIBLIOGRAPHY 197

9. SUPPLEMENTARY FIGURES 231

10. ANNEX 241

Tables and Figures

FIGURES

Figure I- 1 RG identification in the primate brain.. 28
Figure I- 2 Interkinetic nuclear migration (INM) is lost during cortical development.. ... 29
igure I- 3 Evolution of the RG scaffold. 31
Figure I- 4 Cell differentiation and cortex expansion during development in the gyrencephalic brain.. 32
Figure I- 5 Radial glia lineage differentiation in the developing and postnatal brain.. ... 33
Figure I- 6 Intrinsic and extrinsic cues that determine astrocytic development. 35
Figure I- 7 Summary of Intracellular calcium signaling regulation in the nervous system.. 38
Figure I- 8 Schematic representation of cortical vascularization during embryonic development.. 40
Figure I- 9 Glucose metabolism in aerobic and anaerobic conditions. 41
Figure I- 10 Mitochondrial fusion and fission mechanisms. 44
Figure I- 11 Scaled view of brain and cellular components. 47
Figure I- 12 Mechanotransduction in the developing brain. 48
Figure I- 13 Intermediate filament organization. 51
Figure I- 14 Nuclear mechanosensitive mechanisms.. 53
Figure I- 15 Molecular machinery governing nuclear mechanotransduction.. 54
Figure I- 16 Schematic overview of extrinsic modulators influencing transcription of mechanoresponsive genes.. 56
Figure I- 17 YAP/TAZ expression during brain development.. 57
Figure I- 18 Schematic overview of RG adherent junctions in the apical surface..... 59
Figure I- 19 YAP/TAZ and β-catenin destruction complex. 59
Figure I- 20 Two models of mechanosensitive ion channel gating. 61
Figure I- 21 Schematic representation of intracellular calcium regulation in astroglia. . 65
Figure I- 22 Ln2PMMA mimic the RG niche and induce astrocyte dedifferentiation into RG cells. 68
Figure I- 23 From the outside to the cell function. Schematic overview of mechanotransduction pipeline. 70
Figure M- 1 Nuclei segmentation results from maximum and average projections were similar..... 89
Figure M- 2 Nuclei counterstained with Hoechst is better for nuclei segmentation 90
Figure M- 3 Schematic of nuclear and perinuclear fluorescence intensity extraction. .. 91

Figure M- 4 Nuclei segmentation App pipeline. 92

Figure R-4.1- 1 Changes of MSCs and Ca^{2+} signaling-related genes during mouse cerebral cortex development in astrocyte-RG cell lineages.. 110
Figure R-4.1- 2 MSCs protein expression changes induced by ln2PMMA biomechanical signals. 111
Figure R-4.1- 3 Experimental approach to explore the role of Ca^{2+} signaling in ln2PMMA mechanical adaptation.. 112
Figure R-4.1- 4 Pharmacological validation of mechanosensitive cation channels and downstream Ca2+ signaling implication in the biomechanical induction of RG..... 113
Figure R-4.1- 5 Ln2PMMA substrate, KN93 and GsMTx4 treatments reduced lamins A-C/B1 ratio..... 114
Figure R-4.1- 6 Summary of MSCs candidates to mediate ln2PMMA bioelectrical signaling in glial cells. 116
Figure R-4.1- 7 Evaluation of intracellular Ca^{2+} concentration in glial cells grown on control and ln2PMMA substrates. 117
Figure R-4.1- 8 Ln2PMMA substrate modify spontaneous calcium activity in glial cells. 118

Figure R-4.2- 1 Ln2PMMA induced a shift in key metabolic enzymes in glial cells.. .. 120
Figure R-4.2- 2 Ln2PMMA increase PCK2 expression in glial cells..... 121
Figure R-4.2- 3 Ln2PMMA biomechanical adaptation induced a generalized mitochondrial network remodeling in glial cells..... 123
Figure R-4.2- 4 Ln2PMMA induce mitochondrial reshape and network rewiring in RG lineage cells. 124

Figure R-4.3- 1 Time-dependent changes in nuclear morphology and alignment in control and ln2PMMA glial cultures..... 126
Figure R-4.3- 2 Nuclear shape follows cell type-specific dynamics over time in control and ln2PMMA. 127
Figure R-4.3- 3 Cellular composition and multivariate kernel density estimation of nuclear morphology changes in glial cultures grown for 3DIV on control and ln2PMMA.. 129
Figure R-4.3- 4 The model delimitated a specific RG nuclear morphology.. 133
Figure R-4.3- 5 Application of control equation to data used for fitting.. 134
Figure R-4.3- 6 Application of ln2PMMA equation to data used for fitting.. 135

Figure R-4.3- 7 RGM model application to glial subpopulations expressing different lineage marker combinations.. 137
Figure R-4.3- 8 *LogOdds ratio* function defined a threshold for RG nuclear morphologies. 139
Figure R-4.3- 9 Fitting of potential RG nuclei on the RG region delimitated by F(0) surface. 141
Figure R-4.3- 10 Validation of RGM model. 142
Figure R-4.3- 11 Actively cycling cells present a specific non-RG nuclei morphology pattern. 143
Figure R-4.3- 12 RGM application workflow, interface, and visual outcomes. 144

Figure R-4.4- 1 Validation of RGM model. 146
Figure R-4.4- 2 Time-dependent changes in glial nuclei fitting in the RG region delimitated by F(0) surface. 147
Figure R-4.4- 3 Changes in lamin A-C/B1 ratio over time. 148
Figure R-4.4- 4 The increase of lamins A-C/B1 ratio negatively correlates with RG mechanical factor over time. 150
Figure R-4.4- 5 Ln2PMMA effect on β-catenin and YAP/TAZ expression and subcellular distribution. 152
Figure R-4.4- 6 β-catenin nucleo-cytoplasmic ratio does not corelated with specific nuclear morphologies. 153
Figure R-4.4- 7 RG defined by RGM model matched with intracellular Ca^{2+} concentration and activity patterns profiles defined by expression markers. 155
Figure R-4.4- 8 KN93 treatment induce cell-type specific changes in nuclear morphology. (A-D) Density plots with model fitted probabilities, control substrate in blue and ln2PMMA substrate in red.. 156
Figure R-4.4- 9 RG defined by RGM model matched with specific mitochondrial morphologies and network organization defined by the expression of RG markers... 157

Figure R-4.5- 1 RG nuclear morphology conservation across species.. 160
Figure R-4.5- 2 Human RG nuclear segmentation.. 162
Figure R-4.5- 3 Percentages of nuclei above F(0) form hRG and hNeuron nuclei. 162

Figure R-4.6- 1 hiPSc cultures exceeds cell density RGM model limits. 164
Figure R-4.6- 2 3D brain organoids confocal image and segmentation render. 165

Figure D- 1 Summary of the principal findings associated to ln2PMMA biomechanical induction of astrocyte to RG dedifferentiation. 186

TABLES

Table M- 1 Antibodies used to characterize neural populations. 82
Table M- 2 Antibodies used in section 4.1, 4.2 and 4.3. 83
Table M- 3 Antibodies used in section 4.1 and 4.2. 84
Table M- 4 Microscope conversions used to scale image segmentation parameters. .. 91
Table M- 5 Summary of cell-type markers used to define RG, Non-RG and confusing cells. 93
Table M- 6 Terms that define RG based on nuclear morphology parameters in control and ln2PMMA substrates.. 95
Table M- 7 Summary of AIC and AUC of the selected model. 96

Table R-4.3- 1 Summary of the different models developed.. 130
Table R-4.3-2 Relevant terms in the selected model grouped by its substrate dependence. Estimated coefficients, standard error of coefficients, z-value, and p-value (Pr(>|z|)) for every term of the model.. 131

SUPPLEMENTARY

Figure S1 KN93 and GsMTx4 inhibitors did not induce additional cell apoptosis. 233
Figure S2 Complete WB membranes presented in section 4.2.. 234
Figure S3 Nuclear area follows cell type-specific dynamics over time in control and ln2PMMA. 234
Figure S 4 TBR2 antibody is not suitable for ICC. 235
Figure S5 Descriptive of data used for fitting. 236
Figure S6 Model terms behavior in control and ln2PMMA substrates at different cell density scenarios. 237
Figure S7 Different dynamisms of Nuclei and Cytoplasm β-catenin but not YAP/TAZ ratio of astrocytes dedifferentiation over time.. 238
Figure S8 Multiple comparison results of AREA and ECCENTRICITY of nuclei treated with GsMTx4 and KN93 inhibitors. 238
Figure S 9 Advanced 3D segmentation procedure. 239

Table S1 Area and Eccentricity of glial cells in control and ln2PMMA.. 235

ABBREVIATIONS

RG: radial glia

NSC: neural stem cell

IPC: intermediate progenitor cells

BLBP: brain lipid-binding protein

Pax6: paired box protein

Sox2: sex determining region (SYR)-box 2

CNS: central nervous system

NE: neuroepithelial cell

INM: Interkinetic nuclear migration

oRG/bRG : outer or basal radial glia

VZ: ventricular zone

SVZ: subventricular zone

oSVZ: outer subventricular zone

aRG: apical radial glia

Tbr1: T-box brain 1

Tbr2: T-box brain 2

Gsx2: GS homeobox 2

GFAP: Glial fibrillary acidic protein

JAK: Janus kinase

STAT: signal transducer and activator of transcription

BMP: bone morphogenetic protein

SMAD: mothers against decapentaplegic (MAD) homolog proteins

ER: endoplasmic reticulum

OPC: oligodendrocyte progenitor cell

CaM: Calmodulin

CaMKII: Ca^{2+}/Calmodulin activated kinase II

CaN: Calcineurin

PCK2: phosphoenolpyruvate carboxykinase 2

PDH: pyruvate dehydrogenase

PFKFB3: 6-phosphofructo-2-kinase/fructose-2,6-biphosphatase 3

TCA: tricarboxylic acid

OXPHOS: oxidative phosphorylation

ROS: reactive oxygen species

MnSOD: manganese superoxide dismutase

GPX: glutathione peroxidase

IMM: inner mitochondrial membrane

OMM: outer mitochondrial membrane

OPA1: optic atrophy 1

Mfn2: mitofusin 2

DRP1: GTPase dynamin-related protein 1

$\Delta\Psi_m$: mitochondrial membrane potential

MSC: mechanosensitive ion channels

TRP: transient receptor potential

ASIC: acid sensing ion channels

ECM: extracellular matrix

MF: actin-based microfilaments

MT: tubulin-based microtubules

IF: intermediate filaments

INM: inner nuclear membrane

ONM: outer nuclear membrane

NPCs: nucleopore complexes

YAP: yes-associated protein

TAZ: Transcriptional co-activator with PDX-binding motif

PCP: planar cell polarity

K2P: two-pore-domain potassium channels

Kv7: Voltage-gated potassium channels

ENaC: epithelial sodium channels

Cx: connexins

SOCE: store operated calcium entry

TBI: traumatic brain injury

Ln2PMMA: poly methyl methacrylate 2µm linear topography

P0: postnatal day 0

DIV: days *in vitro*

iPSCs: induced pluripotent stem cells

hNPC: human neural progenitor cells

E: eccentricity

A: area

RGM: radial glia mimetic model

AIC: Akaike information criterion

AUC: area under the curve

GsMTx4: grammostola spatulate mechanotoxin 4

PH3: phosphohistone 3

1. INTRODUCTION

1.1. What are radial glia cells?

The term “Radial Glia” (RG) was established by Pasko Rakic in 1972 when electron microscopy and H_3-thymidine (2H-TdR) autoradiography technically surpass the silver staining from Golgi method (Rakic, 2003) (Figure I-1). Nonetheless, all previous investigations, with minor variations, have pointed out that RG cells were elongated cells with apical-basal polarity, and then diverge into specialized neuronal and glial precursors (Rakic, 2003, 2009). During brain development and depending on the stage, the RG, which is considered the principal embryonic neural stem cell (NSC), have neurogenic or gliogenic potential, and gives rise to all subset of neural cell types but microglia: neurons, astrocytes and intermediate progenitors (IPC), which give rise to neurons (nIPC and Tri-IPC), astrocytes (Tri-IPC) or oligodendrocytes (oIPC and Tri-IPC) (Malatesta et al., 2000a; Rakic, 2003).

The main RG features are listed below:

(1) Apical-basal polarity and long radial process (A. R. Kriegstein & Götz, 2003).

(2) Apically located centrosome (Hockfield, 1985).

(3) They express a specific pattern of intermediate filaments: glial fibrillar acidic protein (GFAP) expression, early in primates, in late corticogenesis in mice (Rakic, 2003), nestin (Hockfield, 1985), (Barry & McDermott, 2005), vimentin (Barry & McDermott, 2005).

(4) They express the brain lipid binding protein (BLbP) (Barry & McDermott, 2005).

(5) They express the transcription factor Pax6 and Sox2 (Wen et al., 2008).

(6) Its presence is transient in mammals CNS (Rakic, 2003).

(7) Support neuron migration (Rakic, 2003).

In some non-mammalian vertebrate species, RG cells persist throughout the adult lifespan and the presence of RG-like cells in the adult brain has been considered a hallmark of endogenous adult brain regeneration. Nonetheless, many efforts were made to unveil the presence of adult NSC in mammals, which are present in different brain regions and encompass a huge transcriptional heterogeneity (Obernier & Alvarez-Buylla, 2019).

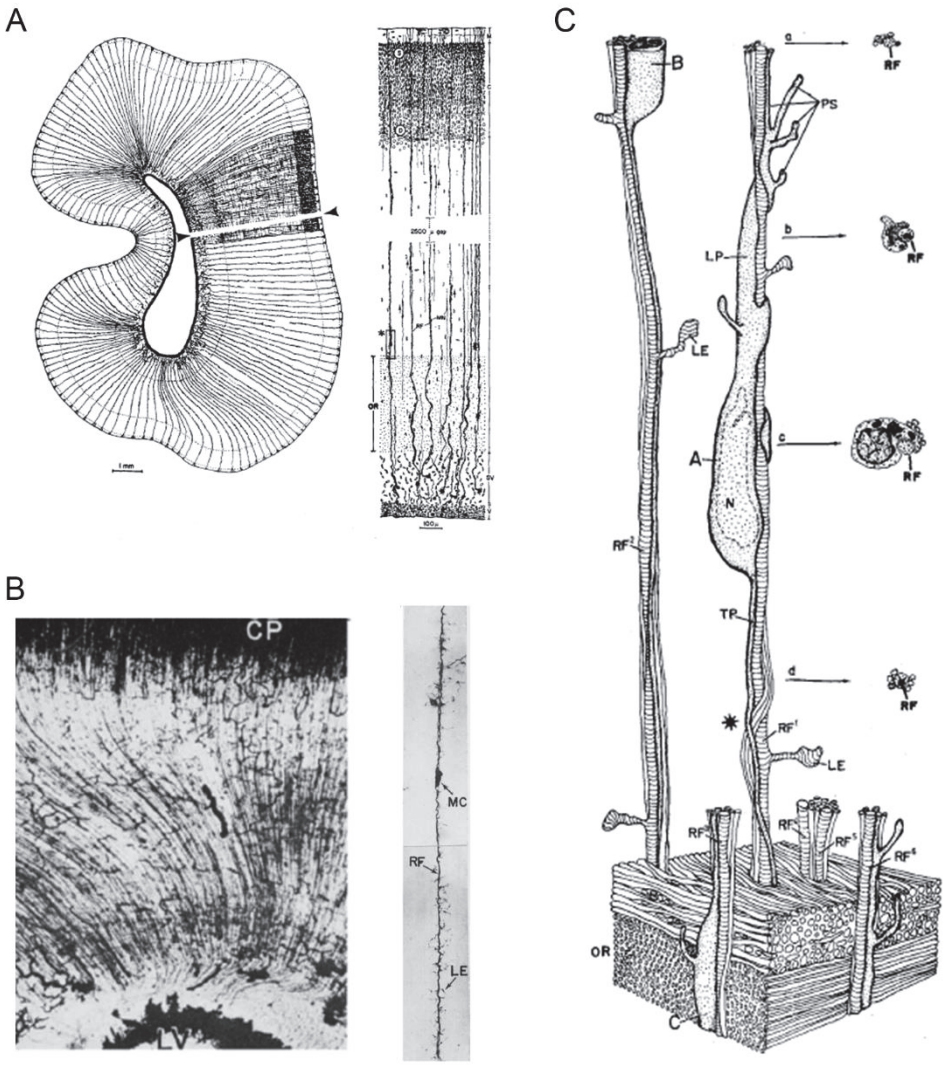


Figure I- 1 **RG identification in the primate brain.** (A) Camera lucida drawing of a Golgi-impregnated coronal section at the parieto-occipital level of brain of a 97-day monkey fetus. Adjacent drawings correspond to an inset of the whole coronal section pointed with black arrows. (B) Photomicrographs of the Golgi impregnated telencephalon of a 97-day monkey fetus. Inset is a magnification of one fiber. RF: radial fiber, MC: migrating cell; LE: lamellate expansions. (C) 3D semi-diagrammatic reconstruction of RG and migrating cells in the intermediate zone. A,B,C: migrating cells; N: Nucleus; LP and TP: leading and trailing processes. Adapted from (Rakic, 1972).

1.1.1. RG in brain development

After neural induction, a single layer of neuroepithelial cells (NE) form the neural plate that elongates posteriorly, bends to form the neural folds, and zips, creating a tubular structure called the neural tube. The neural tube is patterned into different domains, the anterior part of the neural tube will generate the brain and the posterior part the spinal cord. The central canal (lumen) of the neural tube precedes the brain ventricular system. The region close to the lumen is the ventricular (apical) zone, and the outer part of the neural tube is the pial (basal) surface (Stiles & Jernigan, 2010).

NE has the typical apical-basal epithelial polarity, by extending from apical to basal surfaces and proliferate undergoing symmetric divisions that expand the progenitor pool. The NE cell cycle is synchronized to the interkinetic nuclear migration (INM) process, consistent in nuclear displacement along cell axis to perform S phase (DNA replication) in the basal surface and the M phase (mitosis) in the apical surface (Paridaen & Huttner, 2014; Uzquiano et al., 2018). At the end of mitosis, NE lose their apical anchorage and the daughter cells re-established the basal contact by processes extension (Figure I-2A). The apical-basal polarity of NE together with progenitor pool expansion transform the initial single cell neuroepithelium into a pseudostratified neuroepithelium (Andrews et al., 2022). The rate of progenitor pool expansion determines the differences in cortical development between species.

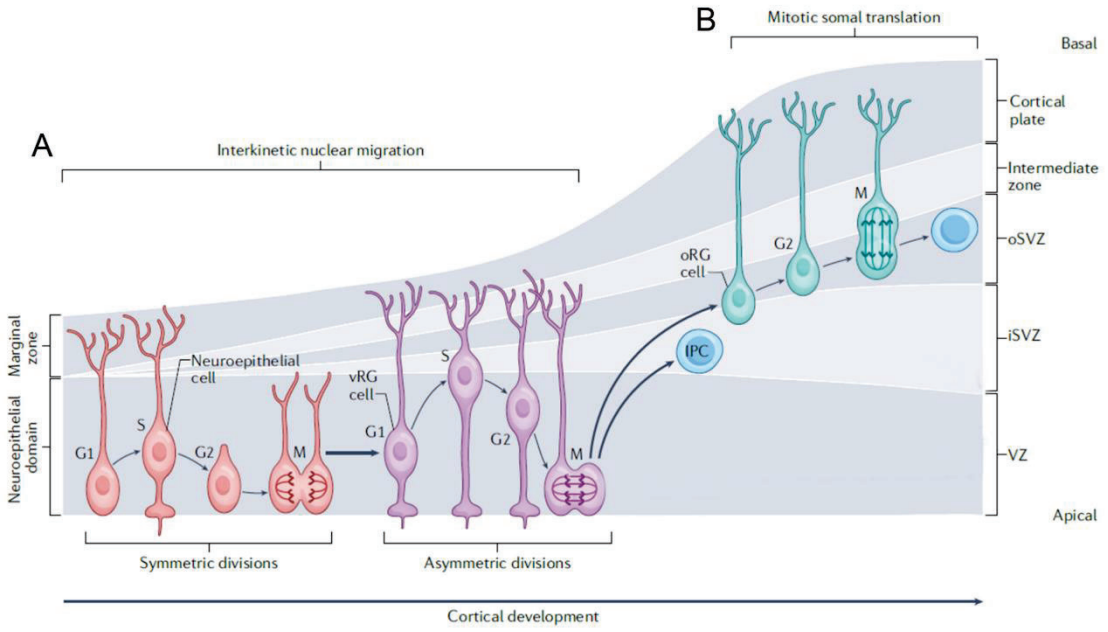


Figure I- 2 **Interkinetic nuclear migration (INM) is lost during cortical development**. In orange, bipolar neuroepithelial cells (NE) undergo symmetrical divisions to expand the progenitor pool. NE differentiates into radial glia cells (RG) that maintain apical-basal polarity and proliferate rough symmetric and asymmetric divisions. NE and RG divide through interkinetic nuclear migration (INM). Daughter cells from RG asymmetric division, intermediate progenitors, or outer/basal RG (oRG/bRG), migrate and populate the SVZ. In the SVZ, oRG, which loosed the apical anchorage and consequently the INM, divides through a process known as mitotic somal translocation, in which the cell body moves quickly in basal direction before dividing horizontally by mitosis. Adapted from (Andrews et al., 2022).

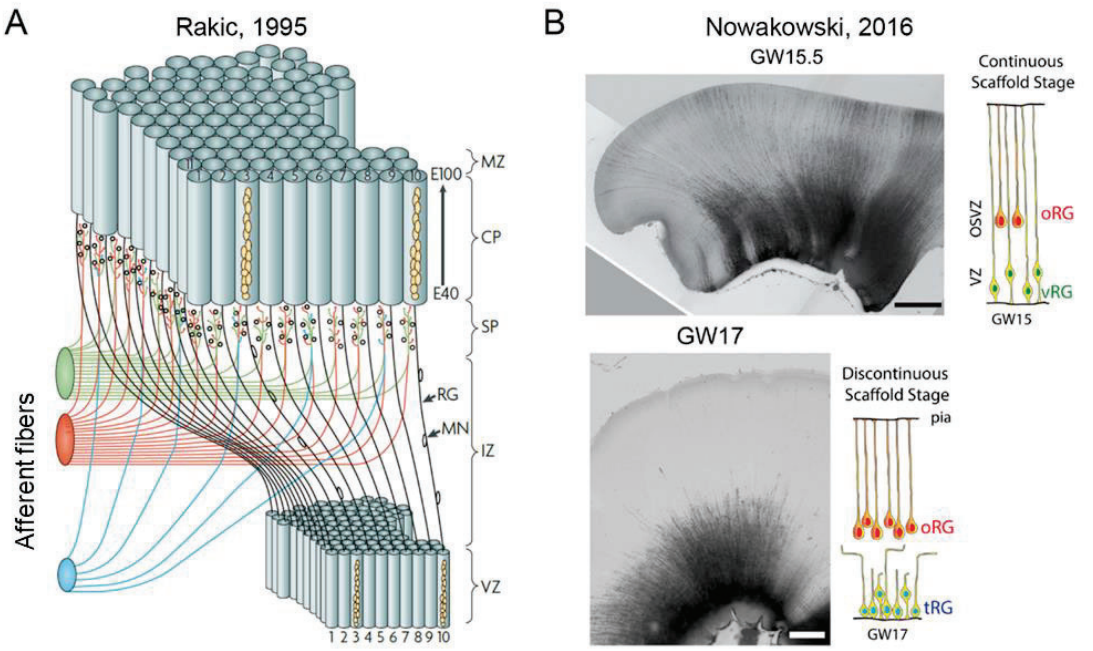
NE transforms into apical radial glia cells (RG/aRG) that progressively acquire characteristics of glial cells (including the expression of specific transcription factors and intermediate filaments, and the formation of glycogen granules) (Kriegstein, 2006). However, what triggers the transformation of NE to RG are the switch of tight junctions to adherent junctions, permitting the chemical and electrical interconnection (A.

Stoykova, n.d.; Aaku-Saraste et al., 1997; LoTurco et al., 1995). RG retain apical-basal polarity and can divide symmetrically (two identical cells) or asymmetrically giving rise directly to neurons or the production of transit-amplifying progenitor cells (intermediate progenitor cells, IPC), which can be neuronal (nIPC), astrocyte (aIPC) or oligodendrocyte (oIPC) restricted (Malatesta et al., 2000; Noctor et al., 2001). The combinatorial expression of transcription factors in each segment of the neuroepithelium determines the potential of RG to generate different types of neurons and glia. Subsequently, the newly generated neurons migrate radially through RG basal shafts, initiating cortical expansion. The RG scaffold stability is crucial for proper cortical development and neuron migration, and it is regulated by many extracellular cues (Ferent et al., 2020a). Indeed, RG is highly dynamic and plastic, and at the time that the cerebral cortex is expanding, is constantly interacting with neighbor RG. This interconnectivity presumably enables RG to undergo asymmetric division and to act as a scaffold for neuronal migration (Rakic, 2003; Tabata & Nakajima, 2003; Yokota et al., 2010).

Many hypotheses arise to explain cortical expansion through evolution. The longer accepted hypothesis was set in 1995 by Pasko Rakic (Rakic, 1995). He proposed the Radial Glia Unit Hypothesis, claiming that through symmetrical division prior to the initiation of neurogenesis, the pool of neural stem cells would rise the quantity of founder cells, thereby contributing to the exponential growth of radial cortical columns, and then, the number of neurons increase linearly within each RG column (Rakic, 1995) (Figure I-3A). In 2004 was described that cortical expansion gives rise to a second neurogenic pool in the subventricular zone (SVZ) composed by intermediate progenitor cells (IPC) (Haubensak et al., 2004; A. R. Kriegstein & Noctor, 2004). During development, each RG symmetric division requires endfoot apical anchorage regeneration, which restricts the RG state. Conversely, when this regenerative capacity is lost, the new generated cell translocates into the SVZ (Fujita et al., 2020). The loose of apical-basal anchorage generates apolar IPC that only undergo symmetric divisions (amplificative or differentiative), while those RG that lose the apical but retain their basal anchorage generate the basal or outer RG (bRG/oRG), which can proliferate by symmetric or undergo asymmetric divisions and support neuronal migration (Englund, 2005; Hansen et al., 2010). Due to their apical anchorage loss, bRG also lose the INM during mitosis and undergoes mitotic somal translation (Figure I-2B). The non-bRG daughter cell gradually loses RG markers, such as Pax6, and sequentially upregulate the expression of differentiation markers Tbr2 (IPC marker) and Tbr1 (neuron marker) (Englund, 2005; Hansen et al., 2010). Additionally, it has been described the presence of tri-potential IPC (Tri-IPC), which its hallmark is the expression of the transcription factor GS Homeobox

2 (Gsx2), and give rise oIPC, astrocytes or olfactory-bulb neurons (López-Juárez et al., 2013; Y. Zhang et al., 2020). Tbr2 gene encodes a member of the T-box family transcription factor that is used to identify neuron-restricted IPC, its ablation impairs bRG differentiation into IPC, and concomitant loss of cortical thickness and neuronal reduction in all cortical layers (Sessa et al., 2008).

In rodents, IPC and bRG have limited proliferative capacity and only 10% did not produce neurons (Noctor et al., 2004), while in primates, bRG undergo multiple divisions that end in the creation of an outer subventricular zone (oSVZ) (Hansen et al., 2010; Smart et al., 2002). Indeed, cortical neurons of rodents arise from the SVZ, and from the SVZ-oSVZ in primates (Noctor et al., 2004). A beautiful work performed by Nowakowski and colleagues have shown how the RG scaffold loses its continuity and establishes two different neurogenic zones in the human brain (Nowakowski et al., 2016a) (Figure I-3B).



igure I- 3 **Evolution of the RG scaffold.** (A) Representation of the first hypothesis established by Pasko Rakic between 1988-1995 to explain cortex formation and pattern distribution. The RG establishes columnar units where postmitotic neurons from the same site in the ventricular zone and generated at different times arrive successively at the cortical plate forming stacks – named ontogenetic columns. In the second wave, neurons migrate tangentially from differ brain zones and use the RG scaffold to arrive at the cortical plate. Adapted from (Rakic, 2009). (B) In the human brain, the continuity of RG scaffold is not maintained across the embryonic development, establishing a discontinued RG scaffold formed by truncated RG (tRG) and outer RG (oRG) that develop distinct gene expression profiles. The presence of oRG predominates below the gyri but not below the sulci during cortex gyrification. Adapted from (Nowakowski et al., 2016b).

The demonstration that cortical folding onset takes place after the majority of cortical neurons have migrated from their sites of origin to outer layers but prior to neuron

maturation and myelinization (Neal et al., 2007) agree with the heterogeneous bRG distribution patterns that is higher under incipient gyri (thicker oSVZ) than under incipient sulci (Figure I-4) (De Juan Romero & Borrell, 2015; Hansen et al., 2010; Reillo et al., 2011). All these data add additional layers of complexity to the initial Radial Glia Unit hypothesis, exposing the intricacy of the human brain.

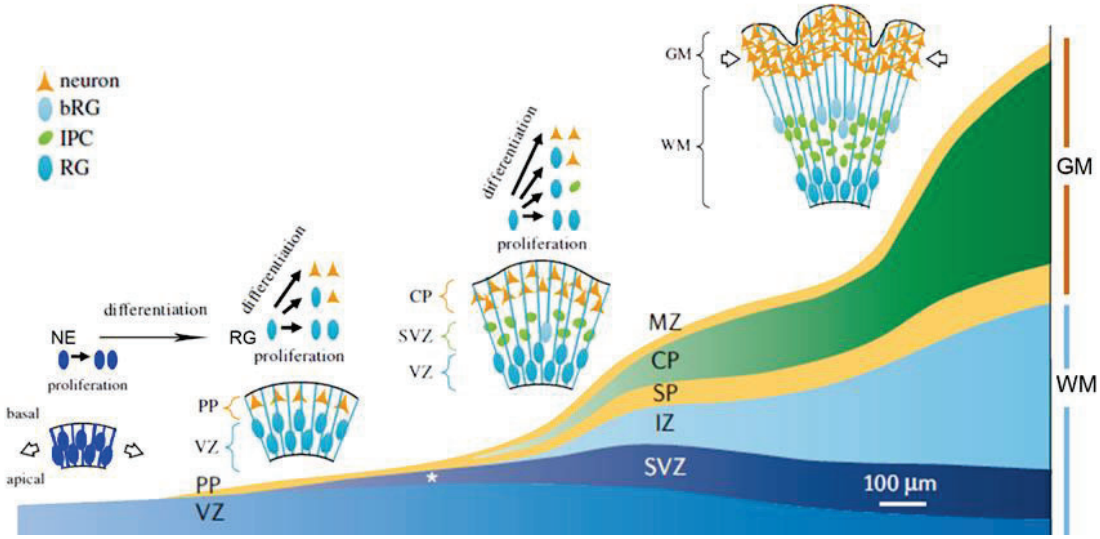


Figure I- 4 **Cell differentiation and cortex expansion during development in the gyrencephalic brain**. Schematic representation of the cortex expansion correlated with brain layers formation and neural cells differentiation progression. Cells: NE: neuroepithelial cell; RG: radial glia, bRG: basal RG; IPC: intermediate progenitor cells. Layers: VZ: ventricular zone; PP: pre-plate; SVZ: subventricular zone; CP: cortical plate; IZ: intermediate zone; SP: sub-plate; MZ: marginal zone. GM and WM identify grey and white matters. Adapted from (Arnold Kriegstein, 2006; Garcia et al., 2018).

1.1.2. RG lineage progression and characterization

The persistent challenge in cell biology revolves around the absence of distinctive and universal molecular markers for the precise identification of specific cell populations. In a groundbreaking study, La Manno and colleagues meticulously constructed a single-cell transcriptomic atlas and an in-situ mRNA sequencing map, unveiling the intricate molecular architecture of the developing mouse brain. Their work revealed the spatial and transcriptional diversity of RG, identifying 87 distinct subtypes (La Manno et al., 2021). Furthermore, other studies have disclosed significant transcriptional diversity and molecular variations in neural cell types at different developmental stages (Di Bella et al., 2021; Eze et al., 2021; Loo et al., 2019a). These findings imply that RG differentiation is based on a transcriptional continuum and a combination of cell intrinsic and extrinsic mechanisms, where cells can assume their final fate post-mitotically through non-cell autonomous factors present in their microenvironments (Beattie & Hippenmeyer, 2017; Rash et al., 2018).

Despite the lack of universal cell lineage markers, the principal cells can be identified by the combinatorial expression of intermediate filaments, such as nestin or GFAP, transcription factors, such as Sox2, Pax6, or Gsx2, and membrane proteins, such as neuron-glial antigen 2 (NG2) (Ferent et al., 2020a) (Dean et al., 2023; Iozzo & Schaefer, 2015). Those markers are expressed in specific moments for specific cell types, to undergo specific functions, so the combination of these molecular markers serve as identification. In Figure I-5, we provide a summary of the expression markers commonly employed to identify different neural cell types, and particularly, those that are used in this Thesis.

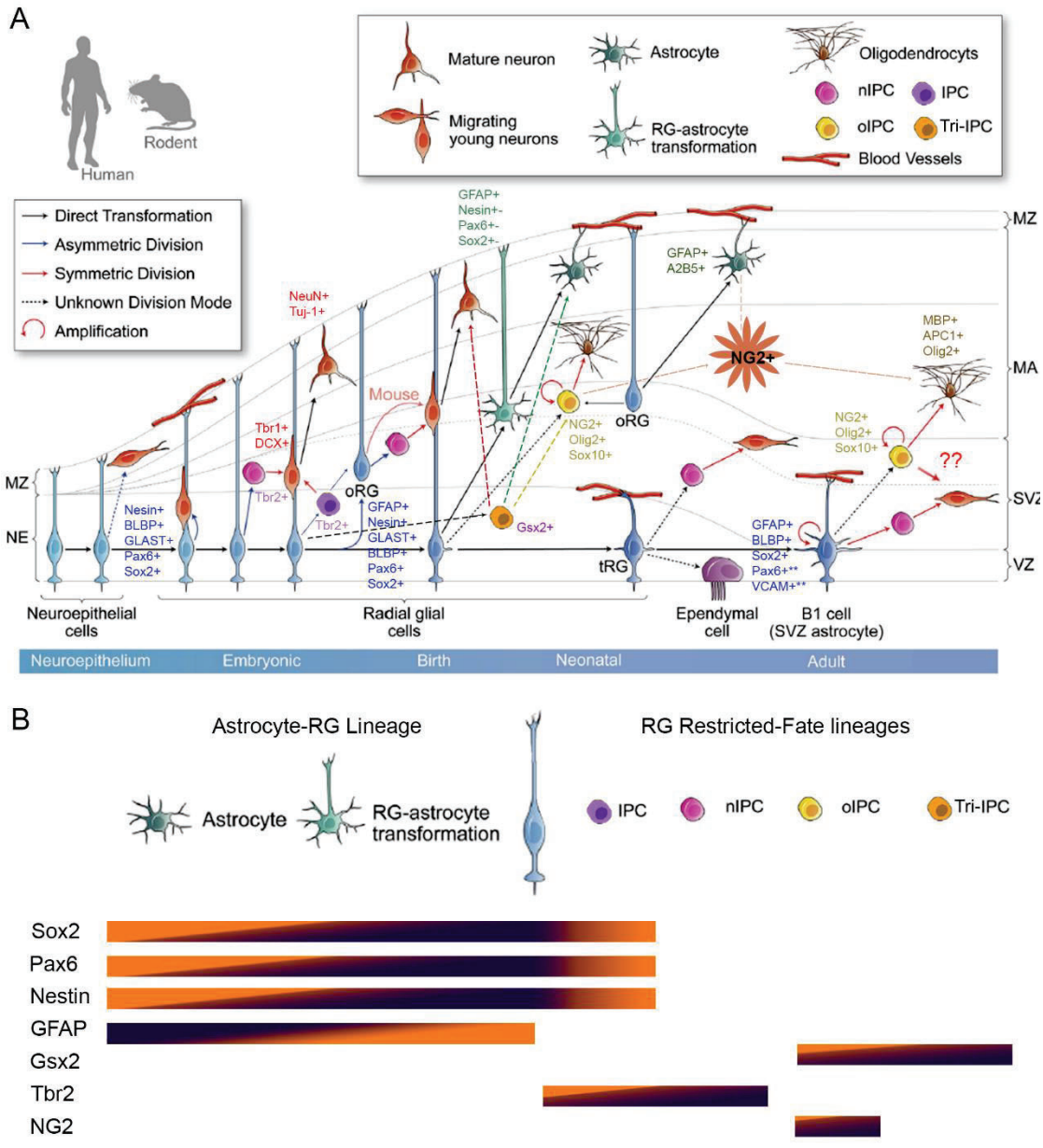


Figure I- 5 **Radial glia lineage differentiation in the developing and postnatal brain.** (A) Differentiation process of Neuroepithelial cells (NE) → Radial glia (RG) → neurons, IPC, astrocytes, or oligodendrocyte progenitor cells (OPC). Different molecular markers expressed during each transition allow to identify cell populations. (B) Common molecular markers used to identify distinct neural cell types, and particularly, those

that are used in this Thesis. Color gradients indicate more (blue) or less (orange) expression. Adapted from (A. R. Kriegstein et al., 2020).

1.1.3. RG-astrocyte transformation and adult brain regenerative capacity

The neurogenic-gliogenic switch in RG is tightly regulated and controlled by intrinsic and extrinsic environmental cues. The temporal competence of RG cells is determined by various intrinsic factors and the JAK/STAT signaling pathway (Janus Kinases and Signal Transducer and Activator of Transcription proteins), NOTCH signaling pathway (Notch homolog 1), and BMP-SMAD signaling pathway (Bone Morphogenetic Proteins and the second messenger Small Mothers Against Decapentaplegic) pathways collaborate synergistically to facilitate the transcription of astroglia genes (Figure 1-6) (Alexej Verkhratsky, 2023; Koo et al., 2023; Miller & Gauthier, 2007). During neurogenesis, HMGA (high mobility group AT-hook) genes modulate chromatin structure maintaining neurogenic capabilities in RG (high neurogenin-1,2 expression) and inhibiting gliogenesis by methylation of glial genes promoters. Immature neurons secrete neuregulin-1, its binding with ErbB4 receptor in RG release of the ErbB4 intracellular fragment and activate a repressor complex (Erb4i/N-CoR/RBPG) that block Notch signaling, maintaining the epigenetic silencing of pro-glial genes. Later on, the polycomb-group transcriptional repressor (PcG) complexes modify chromatin structure and increase epigenetic silencing of pro-neural genes (low neurogenin-1,2 expression) in RG, enabling gliogenesis (Bonni et al., 1997.; He et al., 2005; Sun et al., 2001; Urayama et al., 2013). With low neurogenin expression in RG, neurons determine the onset of the gliogenesis switch by increasing the secretion of cytokines of the interleukin-6 family, cardiotrophin-1 (CT-1), leukemia inhibitory factor (LIF) and ciliary neurotrophic factor (CNTF), which act as a trigger for the JAK-STAT pathway and recruit STAT3/p300/CBP co-activator complex. In these conditions, BMP ligands engaged with their corresponding receptors activate SMAD, allowing the formation of STAT3/p300/CBP/SMAD co-activator complex at the promoters of gliogenic genes (GFAP, calcium-binding protein S100β) (Bonaguidi et al., 2005; Markey et al., 2023) (Manzari-Tavakoli et al., 2022) (Hu et al., 2021; Kamakura et al., 2004). Notch activation release the active intracellular NICD fragment forming NCID/RBPJ/NF1A (nuclear factor 1a) complex, which binds to STAT3/p300/CBP/SMAD co-activator complex in gliogenic genes and initiates transcription (Ge et al., 2012; Namihira et al., 2009).

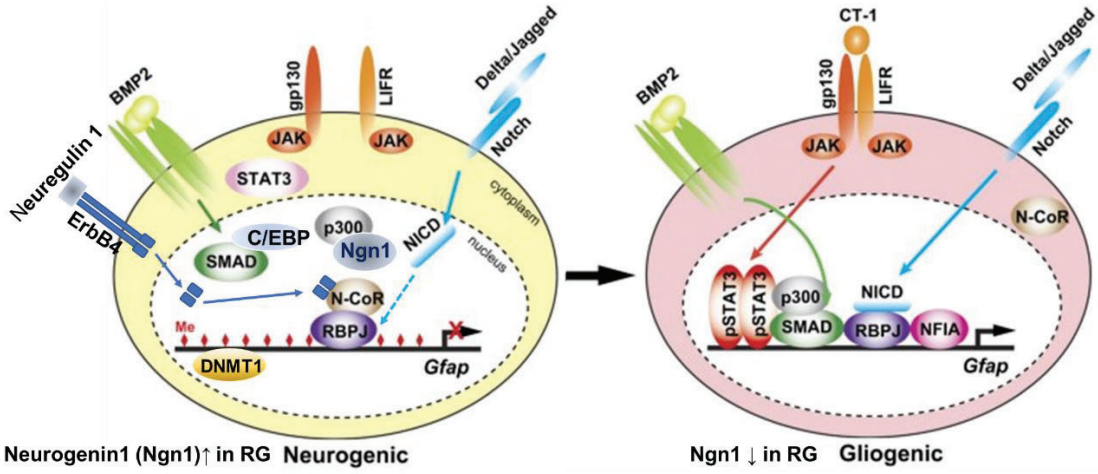


Figure I- 6 **Intrinsic and extrinsic cues that determine astrocytic development.** The temporal competence of RGCs is determined by various intrinsic factors and extrinsic signaling pathways involved in gliogenesis. Modified from (Shimazaki & Okano, 2016).

Gliogenic RG can generate oIPC, tri-IPC, or directly transform into astrocytes, type B1 cells/adult NSC, or ependymal cells (A. Kriegstein & Alvarez-Buylla, 2009). Type B1 cells are located in the VZ-SVZ and retain some RG properties including apical-basal polarity, with processes that contact the ventricle and blood vessels respectively. B1 cells are heterogeneous in terms of the cell types they generate, can generate at least ten different subtypes of OB interneurons depending on their RG origin, reason why they are considered adult NSC (Fuentealba et al., 2015; Merkle et al., 2014; Obernier & Alvarez-Buylla, 2019). The niche in which B1 cells reside regulate their activity, self-renewal, differentiation or quiescence (Llorens-Bobadilla et al., 2015). Niche signals include intrinsic and extrinsic factors from immediate cell neighbors, from the choroid plexus (CP), from cerebrospinal fluid (CSF), from the vasculature, and from local and distant neuronal sources (Murao et al., 2016; Obernier & Alvarez-Buylla, 2019). Moreover, it has been recently described a newly population of NSC in the basal side of the SVZ, which differ from apical type B1/adult NSC (Baur et al., 2022).

At the end of development most RG transform into astrocytes (Alvarez-Buylla et al., 2001; Malatesta et al., 2000b). However, not all parenchymal astrocytes in the adult brain are “terminally differentiated”, some of them are latent NSC that retain functional properties similar to RG cells and a “molecular memory” of their parental RG origin (Merkle et al., 2014). Although these astrocytic subpopulations share molecular markers and are morphologically resembling, a proportion of mature astrocytes may act as dormant NSC and transit into an NSC-like state favoring adult neurogenesis under specific extrinsic circumstances. The first steps on the signaling cascade regulating

neurogenic capacity of parenchymal astrocytes start to be elucidated (Magnusson et al., 2020; Yang et al., 2023; Zamboni et al., 2020).

1.1.4. The role of Ca2+ during corticogenesis

Ca^{2+} signaling in neuroglia and during brain development have been subject of recent reviews (Verkhratsky & Butt, 2023; McKinney et al., 2022; Verkhratsky & Nedergaard, 2018). However, the mechanisms through which Ca^{2+} is spatiotemporally regulated and directs early neurodevelopmental events are not fully understood.

As already described, RG is the primary NSC of the cerebral cortex and serves as a scaffold for neuronal migration along their radial fibers, while at the end of neurogenesis, RG can directly differentiate into astrocytes (Alvarez-Buylla et al., 2001). Among many other factors, RG proliferation, plasticity, structural scaffold maintenance, and cell migration depend on intracellular Ca^{2+} signaling. Particularly, bidirectional Ca^{2+} signaling in RG increased trough corticogenesis and regulate INM, proliferation, neurogenesis, and neuronal migration (McKinney et al., 2022; Rash et al., 2016; Weissman et al., 2004a). Ca^{2+} waves occur spontaneously, propagate trough the RG cells and require Ca^{2+} release from intracellular stores, as they persist in the absence of extracellular Ca^{2+} and are eliminated upon endoplasmic reticulum (ER) Ca^{2+} depletion (Owens & Kriegstein, 1998; Rash et al., 2016; Weissman et al., 2004b). The initiation of these Ca^{2+} transients require purinergic singling via metabotropic P2Y1 ATP receptors and is regulated through gap-junctions and hemichannels (Owens & Kriegstein, 1998; Weissman et al., 2004b), which at the same time regulate cell division and modulates INM (X. Liu et al., 2010; McKinney et al., 2022; Weissman et al., 2004b). Indeed, the inhibition of P2Y1Rs or gap junctions significantly reduces RG proliferation, promotes differentiation and nIPC migration to SVZ (X. Liu et al., 2008; Weissman et al., 2004b). The RG Ca^{2+} signaling dynamics is enclosed in a temporal-spatial framework where calcium sensitivity is progressively acquired through developmental stages (Weissman et al., 2004a). Additionally, RG exhibits specific Ca^{2+} bursts at distinct locations along the radial fiber, suggesting a role in guiding migrating neurons to depart from the radial fiber and establish spatial localization (Rash et al., 2016). However, the mechanisms underlying the intercommunication between migrating neurons and RG remain unknown. Furthermore, intracellular Ca^{2+} transients in RG can be triggered by mechanical signals from their microenvironment, involving bidirectional feedback likely mediated by the activation of mechanosensitive cation channels and Ca^{2+} influx from the extracellular space (McKinney et al., 2022; M. G. Park et al., 2017).

The intricate cross-talk between Ca^{2+} signaling and cellular metabolism involves key players such as mitochondria and the endoplasmic reticulum (ER) in the regulation of intracellular calcium concentration $[Ca^{2+}]_i$. Recent studies have highlighted the significance of Ca^{2+} signaling in the modulation of mitochondrial transport within RG. This regulatory mechanism emerges as a crucial factor for maintaining RG scaffold stability and overall RG maintenance (Rash et al., 2018).

Astrocytes, as a direct lineage end of RG, also inherit their Ca^{2+} sensitivity. Ca^{2+} waves are found in mature and immature astrocytes and are the major components of astrocytic signaling. Astrocytic Ca^{2+} signals go beyond generic cellular functions, such as gene transcription and metabolic regulation, to primarily serve as sensors, decoding information about surrounding cell activity. In response, astrocytes adapt their cellular physiology to meet the energetic and signaling demands, maintaining tissue homeostasis (Goenaga et al., 2023; Lim et al., 2021; Rasmussen et al., 2023). These regulatory outcomes are tailored to specific contexts. Ca^{2+} signals govern gene expression and excitation-metabolic coupling, influencing cell-specific functions. For instance, $[Ca^{2+}]_i$ microdomains in astrocytic branches immobilize mitochondria, enhancing local metabolic support (Jackson & Robinson, 2015). In the adult brain, astrocytic Ca^{2+} signals are implicated in slow wave sleep, and the genetic ablation of $InsP_3$ receptors type 2 results in increased micro-activations and abnormal brain rhythms (Bojarskaite et al., 2020). In turn, abnormal Ca^{2+} signals in astrocytes may constitute an underlying pathology common to multiple diseases, and initiate reactive astrogliosis (Heuser & Enger, 2021). The inhibition of astrocytic Ca^{2+} through $InsP_3$ receptors ablation or via pharmacological treatments inhibits reactive astrogliosis (Kanemaru et al., 2013). Another implication of intracellular calcium alteration was found on human OPC, where in demyelinating diseases such as multiple sclerosis, myelin repair is impaired due to $G\alpha_q$-coupled signaling which inhibits hOPC differentiation. Nonetheless, intracellular calcium oscillations directly regulate hOPC fate in a frequency dependent manner, which may overcome the inhibitory $G\alpha_q$-coupled signaling (Seidman et al., 2022).

The regulatory roles of Ca^{2+} are multiple and include, among others, cellular Ca^{2+} homeostasis, regulation of metabolism and bionenergetics, gene transcription, autophagy and proteostasis, motility and cellular morphological remodeling (McKinney et al., 2022; Parekh, 2008). In Figure I-7 we show a summary of the mechanisms that regulate intracellular calcium in neural cells.

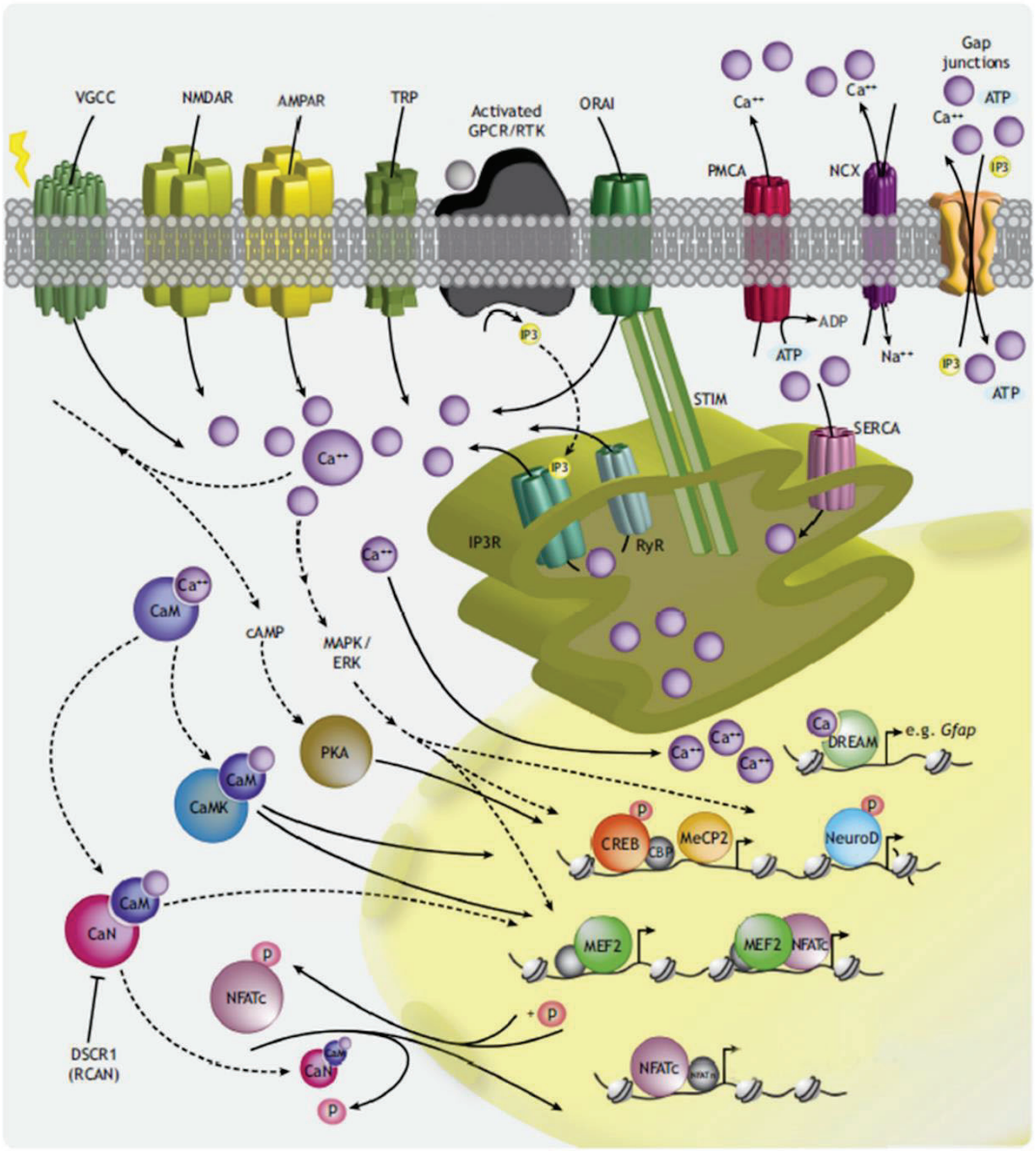


Figure I- 7 **Summary of Intracellular calcium signaling regulation in the nervous system**. Calcium regulation is divided into mechanisms regulating entrance and maintenance of $[Ca^{2+}]_i$, the $[Ca^{2+}]_i$ storage regulators, and Ca^{2+}-sensitive cytoplasmic proteins. Moreover, depending on the amount of $[Ca^{2+}]$, distinct mechanisms are activated. ATPases PMCA1-4, with low capacity for calcium efflux, regulate low resting cytoplasmic $[Ca^{2+}]_i$ levels. Then, sarco/endoplasmic reticulum (SR/ER) and mitochondrial pumps (e.g., SERCA1-3) transport Ca^{2+} into organellar stores (mitochondria and ER). Calcium influx from the extracellular space is mediated by various channels, including voltage-gated calcium channels (VGCCs), N-methyl-D-aspartate receptors (NMDARs), α-amino-3-hydroxy-5-methylisoxazole-4-propionic acid receptors (AMPARs), transient receptor potential (TRP) channels, and ORAI channels. VGCCs are activated by membrane depolarization, while ORAI channels enable calcium influx upon ER calcium store depletion. The $[Ca^{2+}]_i$ storage regulation is mediated by IP3R or RyR, depleting ER calcium and activating STIM calcium sensors (STIM1 and STIM2). This enables the interaction with ORAI channels (ORAI 1-3), leading to calcium influx. Indeed, when these mechanisms are active, small molecules can move to other cells through gap junctions. Finally, $[Ca^{2+}]_i$ regulation out from stores is regulated by calcium-sensitive proteins, such as calmodulin (CaM). This protein undergoes conformational changes during calcium binding, this initiate different signaling cascades, such as Ca^{2+}/Calmodulin Kinase II (CaMKII) cascade, or by modulating the function of voltage-gated potassium channels, like Kv7.4, depolarize the cell. Adapted from (McKinney et al., 2022).

Several signaling cascades (e.g. Ca^{2+} regulated gene transcription) require the participation of Ca^{2+}/calmodulin (CaM)-activated kinase II (CaMKII) or calcineurin (CaN) phosphatase to decode Ca^{2+} signal, however, their downstream mechanisms in glial cells are still poorly understood. CaMKII (α, β, γ, δ isoforms) is a ubiquitous, structurally complex, and multifunctional serine/threonine kinase protein complex. In the brain, CaMKII predominantly consists of the α and β isoforms, with CaMKIIβ expressed during embryonic life whereas CaMKIIα starts to be expressed after birth. In the absence of Ca^{2+}, the substrate binding site is blocked by the autoinhibitory regulatory segment. In response to increases in $[Ca^{2+}]_i$ concentration, Ca^{2+}-bound CaM (Ca^{2+}/CaM) competitively relieves this inhibition resulting in autophosphorylation, which makes CaMKII activity Ca^{2+}-independent. Moreover, CaMKIIβ (but not α and no data for γ and δ isoforms) can bind filamentous actin (F-actin), and accordingly, correct levels of CaMKIIβ are required for proper neuronal migration, partially trough their actin-binding and bundling activity (Nicole & Pacary, 2020). Although CaMKII is expressed and functional in astrocytes (mainly CaMKII γ and δ isoforms), their functions remain an open question (Haolong et al., 2013; Lim et al., 2021; X. Sun et al., 2013; Takeuchi et al., 2000; Yano et al., 1994). CaN is a Ca^{2+}/CaM-activated serine/threonine phosphatase ubiquitously expressed, including in astrocytes. CaN is a heterodymer composed by a catalitic subunit (CaNA) and a regulatory subunit (CaNB), with diferent isoforms. In response to chronic Ca^{2+} overload related to neuroinflammation, over-activation of CaN in astrocytes drives pathological NFAT/NFκB-mediated transcriptional remodeling. However, in physiological conditions CaN activity seems to be mostly related with post-transcriptional regulation of cell proteostasis and required for maintaining basal protein synthesis (Lim et al., 2023).

1.1.5. RG metabolism during corticogenesis

RG differentiation involve significant metabolic changes (Andrews & Pearson, 2024; Gkini & Namba, 2023a). The transition to RG asymmetric divisions implies the production of IP, neurons, and concomitant cortex expansion, and is correlated with vasculature development. In fact, vasculature development creates an O_2 gradient and two main zones: close to the vasculature (high O_2 concentrations) or close to the ventricle and the cerebrospinal fluid (low O_2 concentrations), what establishes differences with respect to metabolites availability (Figure I- 8) (Fame & Lehtinen, 2021; Ferent et al., 2020a). Note that O_2 levels were always lower than atmospheric levels. As development proceeds, the development of honeycomb vasculature networks is strictly and spatially controlled, and the progressive increase of O_2 availability is essential to normal development of RG

(Komabayashi-Suzuki et al., 2019; Ortega et al., 2017a). During cortical expansion germinal VZ and SVZ are established, VZ is less vascularized than SVZ, which sustained the expression of hypoxia inducible factor 1a (HIF1a) in the RG, indicating a higher glycolytic lactate production compared to bRG (Komabayashi-Suzuki et al., 2019; Ortega et al., 2017a). In the early stages of brain development, glycolysis is the dominant metabolic pathway, and the production of lactate after RG division coordinates vasculature and progenitor behavior and is essential for neurogenic niche and nIPC maintenance (Álvarez et al., 2016; Dong et al., 2022). The cataplerotic use of lactate is mediated by the mitochondrial phosphoenolpyruvate carboxykinase (PEPCK-M or PCK2), which catalyzes the GPT-dependent decarboxylation of mitochondrial oxaloacetate to produce phosphoenolpyruvate, which is then exported into the cytosol where it feeds the reverse glycolytic pathway (Álvarez et al., 2016). O_2 and glucose levels should be extremely well balanced, as maternal obesity and hyperglycemia impair maturation of RG fibers and delay cortical neurogenesis (Rash et al., 2018).

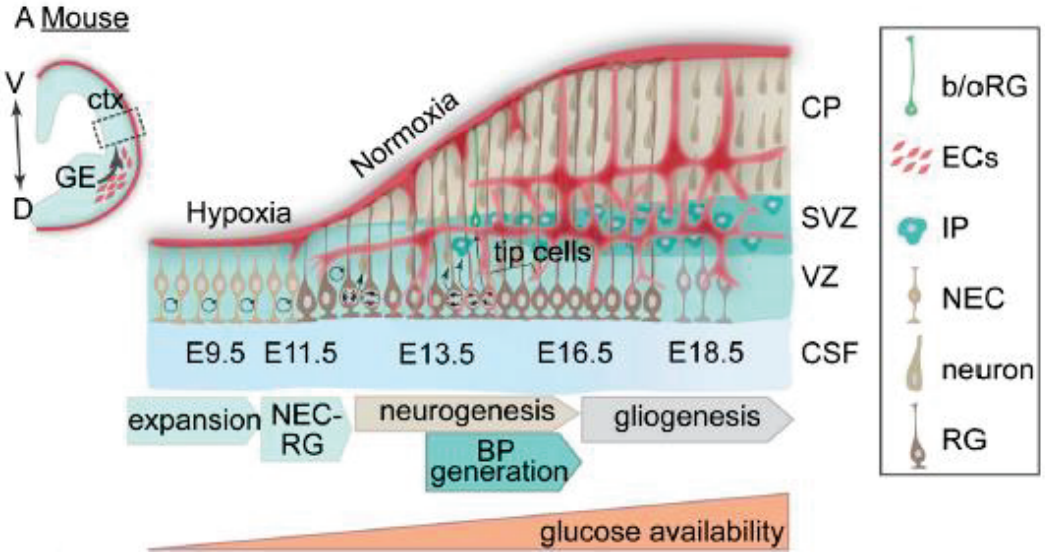


Figure I- 8 **Schematic representation of cortical vascularization during embryonic development**. Adapted from (Andrews & Pearson, 2023).

Glucose serves as the primary and extensively energy source for cells, uptake through glucose transporters and catabolized via glycolysis. The initial glycolytic step involves glucose phosphorylation by hexokinase, yielding glucose 6-phosphate, a pivotal molecule in various metabolic pathways. Through glycolysis, one glucose molecule is ultimately converted into two pyruvates, concurrently consuming two adenosine triphosphate (ATP) molecules to generate four ATP (Andrews & Pearson, 2024; Angelopoulos et al., 2022a; Gkini & Namba, 2023b). Following glycolysis, pyruvate

enters into the mitochondria, and via pyruvate dehydrogenase complex (PDH), transforms into acetyl-CoA through, a crucial precursor for the tricarboxylic acid (TCA) cycle. Under anaerobic conditions, pyruvate is alternatively converted into lactate, through lactate dehydrogenase (LDHA) which generates four ATP molecules per glucose molecule (two ATP as net gain). Under aerobic conditions, oxidative phosphorylation (OXPHOS), also known as mitochondrial electron transport chain, is the main source of energy (Gkini & Namba, 2023a; Kierans & Taylor, 2021). A summary of glucose metabolism is shown in Figure I- 9.

Even in the presence of O_2, aerobic glycolysis is notably prevalent in rapidly dividing cells, despite glycolysis generating much less ATP than OXPHOS does. Their faster kinetics is the reason why glycolysis is preferred to support cell growth and proliferation (Iwata & Vanderhaeghen, 2021). As cortex is expanding and vasculature is being defined, there is a shift towards increased reliance on OXPHOS (Iwata & Vanderhaeghen, 2021; Khacho et al., 2017). During neuronal differentiation, IPC exhibits higher OXPHOS activity than RG and their differentiation to neurons is linked to upregulation of genes involved in OXPHOS (Llorens-Bobadilla et al., 2015; Mandel et al., 2016).

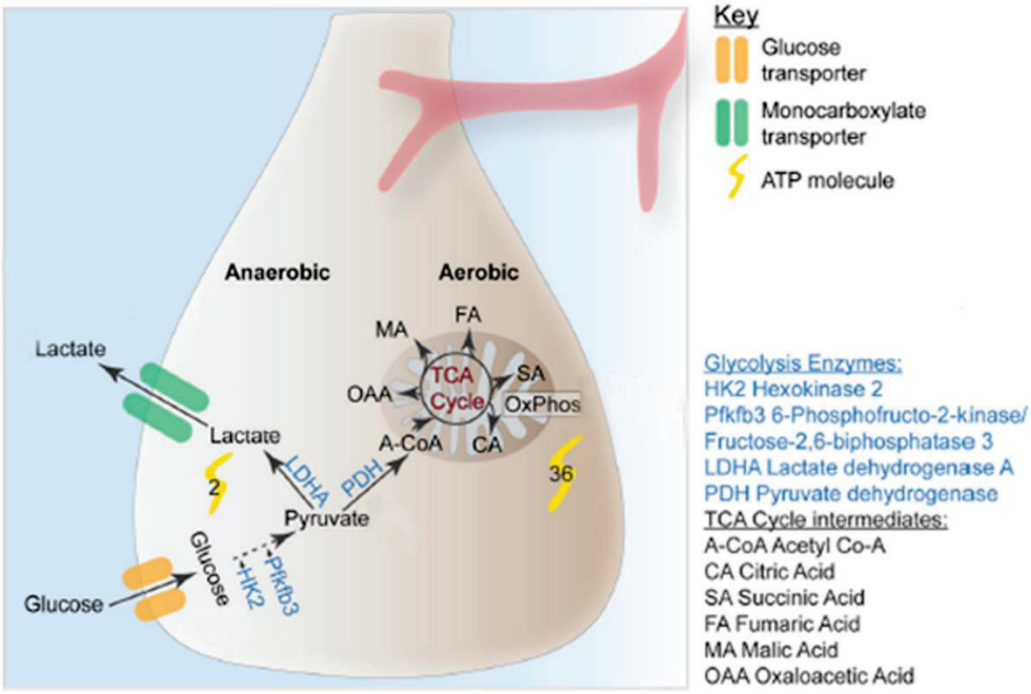


Figure I- 9 **Glucose metabolism in aerobic and anaerobic conditions.** In anaerobic conditions, pyruvate is converted into lactate through lactate dehydrogenase (LDHA) and transported out of the cell. This produces two ATP molecules. In aerobic conditions pyruvate enters the mitochondria through pyruvate dehydrogenase complex (PDH) and is transformed into acetyl-CoA that enters into the tri-carboxylic acid cycle (TCA cycle or Krebs cycle). In the mitochondria takes place oxidative phosphorylation (OXPHOS) that produces 36 ATP molecules per glucose. The conversion of glucose to pyruvate requires different enzymes

such as hexokinase 2 (HC2) and 6-phosphofructo-2-kinase/Fructose-2,6-biphosphatase (PFKFB3) that act sequentially. Adapted from (Andrews & Pearson, 2023).

During OXPHOS, ATP production in the electron transport chain (ETC) have two principal consequences: a change in redox (reduction – oxidation) state and the production of peroxides, superoxide, and hydrogen peroxide molecules, known as reactive oxygen species (ROS) (Angelopoulos et al., 2022b; Lautrup et al., 2019). The effectors of changes in redox balance are the pair formed by the oxidized (NAD^+) and reduced (NADH) forms of NAD (nicotinamide adenine dinucleotide), usually represented as NAD^+/NADH. In NSC, changes in NAD^+/ NADH balance via sirtuin-1 (Sirt1) are required for cell fate determination (Iwata & Vanderhaeghen, 2021; Prozorovski et al., 2008). In the mouse embryonic neocortex, mitochondrial ROS production is higher in IP than RG (Khacho et al., 2017). Oxidative stress levels regulate progenitor behavior and proper cortical neurogenesis (Chui et al., 2020; Hou et al., 2012; Ji et al., 2017), and mitochondrial ROS regulates astrocyte-neurons homeostasis (Vicente-Gutierrez et al., 2019). Therefore, maintaining ROS homeostasis trough neural development is crucial to prevent their accumulation and mitigate potential toxicity (Sheshadri & Kumar, 2016). The enzymes mitochondrial manganese superoxide dismutase (MnSOD) and glutathione peroxidase (GPX) are the main ROS scavengers. MnSOD acts as the primary defense mechanism against ROS accumulation. Upon entering the mitochondria, MnSOD becomes activated, catalyzing the conversion of superoxide radicals to O_2 and H_2O_2. These by-products are subsequently transformed into H_2O and eliminated by the enzyme glutathione peroxidase (GPX) (Nolfi-Donegan et al., 2020). Consequently, both MnSOD and GPX levels increase in response to oxidative stress (Sharma et al., 2021).

1.1.6. Mitochondrial morphology and dynamics

The mitochondria are the cellular organelle in charge of cellular respiration and metabolism regulation. Mitochondria has a dynamic double-membrane structure confined by the inner and outer membranes (IMM and OMM) separated by the intermembrane space (IMS). IMM is compartmentalized and forms tubular protrusions, called cristae, into the interior of the organelle (Iovine et al., 2021). Commonly referred to as the energy powerhouse of the cell, they display high plasticity in structure and size and remodel the IMM and OMM and spatial distribution to regulate bioenergetic efficiency depending on cell energy requirements (Baum & Gama, 2021; Iovine et al., 2021).

Mitochondrial dynamics includes three main processes: transport along the cytoskeleton, interaction with other subcellular structures, and a continuum of fusion and fission cycles, by which mitochondria repair and replace their components and rewire their general structure to adapt energy requirements (Chen et al., 2023; Quintana-Cabrera & Scorrano, 2023) (Iovine et al., 2021). Mitochondrial fusion is regulated by mitofusins 1 and 2 (Mfn1, Mfn2) in the OMM, and optic atrophy 1 (OPA1) proteins in the IMM. Opa1 is a dynamin-like protein that undergoes alternative splicing generating long OPA1 (l-OPA1) isoforms, their proteolytic cleavage by Oma1 and Tme1l1 proteases at site S1 generate short forms of OPA1 (s-OPA1). Opa1 cleavage is induced by different types of stress (mitochondrial dysfunction, oxidation) or by increased OXPHOS activity (Quintana-Cabrera & Scorrano, 2023). On the other hand, mitochondrial fission is regulated by the GTPase dynamin-related protein 1 (DRP1) and the fission factors FIS1, MFF, and MiD49 (Chen et al., 2023; Kraus et al., 2021) (Quintana-Cabrera & Scorrano, 2023).

Figure I-10 summarizes main effectors of mitochondrial dynamisms and cristae components. During mitochondrial fusion, Mnfs on the OMM homo- and hetero-oligodimerize with Mnfs in contact zones of adjacent mitochondria, leading OMM fusion. Mfn2 undergo different post-translational modifications that define their ability to trigger fusion (Quintana-Cabrera & Scorrano, 2023). In particular, Mfn2 ubiquitination is crucial for mitochondrial tethering with the ER, especially important for Ca^{2+} transfer from ER to mitochondria (De Brito & Scorrano, 2008). Subsequently, l-OPA1 homodimerize with proteins on the opposing target membrane to produce IMM fusion, allowing sharing matrix material between the fused mitochondria (Baum & Gama, 2021; Iovine et al., 2021; Kraus et al., 2021). OPA1 is sufficient to tether, dock and partially fuse membranes via its ability to interact with the lipid cardiolipin, a constituent component of IMM. Conversely, s-OPA1 only tether membranes. Thus, the ratio l/s-OPA1 is critical for fusion and cristae formation (S. Gao & Hu, 2021; Iovine et al., 2021; Quintana-Cabrera & Scorrano, 2023). Fission is mainly exerted by the cytoplasm protein DRP1, which translocate to the OMM upon activation through post-translational modifications (Baum & Gama, 2021; Khacho et al., 2017; Möpert et al., 2009). The ER sends membrane extensions that constrict mitochondria and indicate the contact sites where Drp1 will accommodate. The initial mitochondrial constriction is driven by actin cables and myosin IIA motor function. Actin/myosin II recruits Drp1 to the mitochondrial surface to trigger mitochondrial fission. Mechanically, actin is essential to undergo mitochondrial fission and is directly related to mitochondrial and ER Ca^{2+} exchange, serving mitochondrial

calcium as inductor of actin polymerization (Kraus et al., 2021; Quintana-Cabrera & Scorrano, 2023).

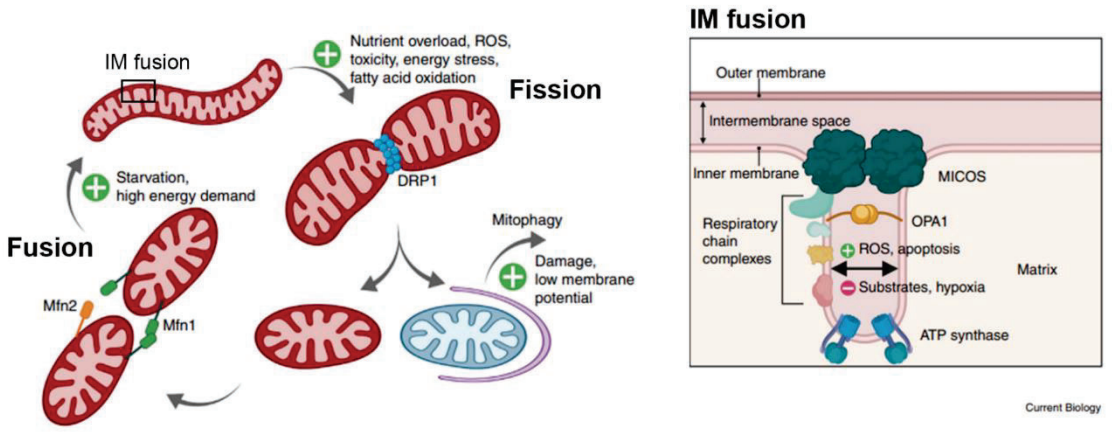


Figure I- 10 **Mitochondrial fusion and fission mechanisms.** Outer membrane (OM) fusion is promoted by starvation or high energy demand, and fission is induced by excessive ROS, nutrient overload or fatty acid oxidation. Inset corresponds to inner membrane (IM) fusion and cristae formation. Apoptosis and ROS induce cristae widening, and hypoxia and high metabolic demands induce cristae thinning. Overall, depending on the OXPHOS ratio and ETC function. Adapted from (Alan & Scorrano, 2022).

One outcome of mitochondrial dynamics is mitochondrial respiration, measured as mitochondrial membrane potential $\Delta\Psi_m$. Mitochondrial fission can generate mitochondria with different levels of membrane potential ($\Delta\Psi_m$), sorting mitochondria with low $\Delta\Psi_m$ or irreversible mtDNA damage to elimination by autophagy. When fusion predominates, $\Delta\Psi_m$ is more homogeneously distributed, in turn, $\Delta\Psi_m$ activates fission at sites where $\Delta\Psi_m$ is lower (Iovine et al., 2021; Quintana-Cabrera & Scorrano, 2023). There is a positive correlation between IMM surface and energy demand, as respiration is more a function of cristae density than mitochondrial volume, indeed, cristae morphology regulates bioenergetic efficiency (Chen et al., 2023; Nielsen et al., 2017). Due to reduced fission or increased fusion, mitochondria elongation is associated with higher respiration and ATP production. Mitochondrial elongation is frequently triggered by limited nutrient availability, emphasizing the adaptive nature of cells to adjust organellar shapes in response to respiratory needs (Iovine et al., 2021; Liesa & Shirihai, 2013; Quintana-Cabrera & Scorrano, 2023).

In the context of embryonic brain development, NSCs are linked to tubular mitochondria and glycolytic metabolism, whereas committed neural progenitors (NPCs) exhibit fragmented mitochondria and depend on OXPHOS (Baum & Gama, 2021; Iwata & Vanderhaeghen, 2021; Khacho et al., 2017). In a series of two articles, in 2020 and 2023,

Vanderhaeguen lab has described that the rates of mitochondrial fission during NSC mitosis are crucial regulators of cell fate commitment. First, those cells determined to remain as NSC displayed high levels of mitochondrial fusion, whereas future neuronal cells maintained higher levels of mitochondrial fission. Indeed, blocking mitochondrial fission interrupts the acquisition of neuronal fate and NSC undergo self-renewal. Second, temporal differences between neuron maturation in mice and humans can be modulated via mitochondrial manipulation, which affect NSC proliferation or neuron differentiation tempo (Iwata et al., 2020., 2023).

1.2. Mechanotransduction components

Mechanotransduction, the process that converts mechanical stimuli into biological signals, plays a pivotal role in the intricate regulation of neurogenic niches. At the cellular level, extracellular forces initiate this process by activating plasmalemmal receptors, which then transmit signals through the cytoskeleton and intermediate messengers to the nucleus. The nucleus, a mechanoresponsive organelle, undergoes deformation in response to tension, alters the composition of its nuclear envelope, and remodels chromatin, ultimately leading to changes in gene expression and cell behavior (Dupont & Wickström, 2022; Kalukula et al., 2022).

Recent advances in mechanobiology have unveiled various mechanotransduction effectors, such as mechanosensitive ion channels (MSC) (also called stretch activated channels and including transient receptor potential (TRP), acidic sensing (ASIC), and Piezo), Ca^{2+} signaling, and mitochondrial dynamics and metabolism. These effectors play crucial roles in early neurodevelopmental events, including cortical neurogenesis (Abuwarda & Pathak, 2020a; Fujita et al., 2020; Rash et al., 2016; Savic Azoulay et al., 2020; Segel et al., 2019). Mechanical stimuli, originating from neighboring cells, the extracellular matrix (ECM), fluid flow, osmotic forces, or within the cell itself, play a decisive role in determining cell fate (Petridou et al., 2017). In the developing brain, mechanical properties of the ECM have a significant impact on the regulation of NSC proliferation and differentiation (Javier-Torrent et al., 2021). In oligodendroglial progenitor cells (OPC), mechanical tensions induce its differentiation, and OPC niche stiffen during aging reduces proliferation and differentiation rates (Makhija et al., 2018; Segel et al., 2019).

Niches are intricate cellular, molecular, physical, chemical, and metabolic microenvironments that orchestrate the regulation of NSC proliferation, self-renewal, and differentiation (Bjornsson et al., 2015; Taupin, 2006). Consequently, the interplay between cell-cell and cell-ECM adhesion molecules and their mechanobiology

consequences emerges as potentially significant in the NSC niche environment (Stukel & Willits, 2016).

1.2.1. The mechanical brain

The brain tissue is extremely compliant and its mechanical response is highly nonlinear and viscoelastic, with a pronounced region-dependent asymmetry (Budday et al., 2017). However, the mechanical aspects influencing the brain extend beyond its general mechanics as an organ. The mechanical response is a result of the underlying microstructure, and provides us an insight into the brain structure, connectivity, and function. The brain tissue is composed of neuronal, glial, and endothelial cells, which proportion strongly varies among regions (in human, ~3.71 in the cerebral cortex and ~0.23 in the cerebellum) and across species (Figure I-11) (Azevedo et al., 2009; Herculano-Houzel, 2012) (Mota & Herculano-Houzel, 2014). Recent studies in human brain indicate that this heterogeneity is associated to their different cellular (in particular astroglia, microglia and oligodendroglia) and ECM composition (Hinrichsen et al., 2023; Linka et al., 2021). The brain's ECM is softer compared to other organs, and predominate non-fibrous elements, like tenascin C and proteoglycans that bind to anionic carbohydrate hyaluronan polymers (HA) and other glycosaminoglycans (Franze et al., 2013). ECM composition directly influences the mechanical properties of the microenvironment, which, in turn, orchestrates the commitment of differentiated cells. Through mechanotransduction, environmental mechanical signals, including ECM, activate different signaling cascades and regulate gene transcription. Integrins, transmembrane proteins connected externally to the ECM, play a crucial role in this process (Chighizola et al., 2019).

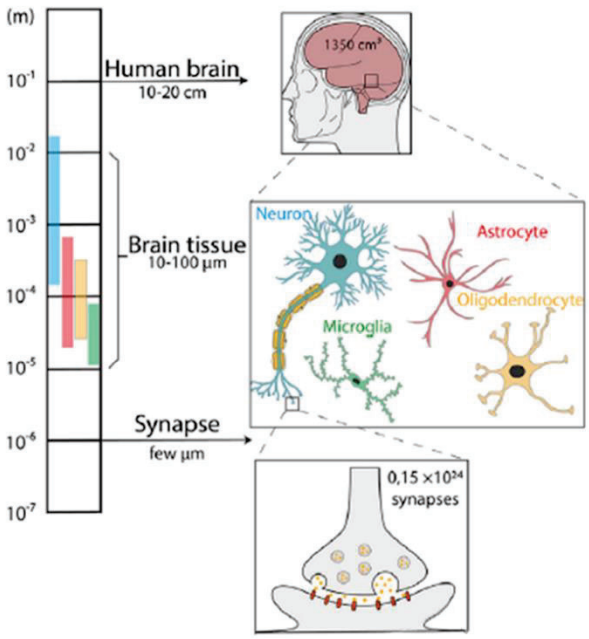


Figure I- 11 **Scaled view of brain and cellular components**. Adapted from (Procès et al., 2022).

This compliant brain is fully enclosed in the skull, providing an important barrier to external physical insults but limiting its effective growth (Saunders et al., 2016). To fit within the skull progressive larger brain through evolution, some species develop cortical folding, which is a mechanism that maximize the number of cortical neurons and minimize the length of their fibers (Zilles et al., 2013). Folding pattern complexities divide the type of brain in gyrencephalic, with cortical convolutions, and lissencephalic, without convolutions (Garcia et al., 2018).

1.2.2. Mechanical constraints and forces during brain development.

During brain development, proliferating cells organize into structures, differentiate, migrate, and neurons generate axons that connect with other cells. These processes generate mechanical forces that affecting cell behavior and organ patterning, impacting biochemical and genetic programs of development in still poorly known ways (Abuwarda & Pathak, 2020b). Figure I- 12 show the principal mechanotransduction components in the developing brain.

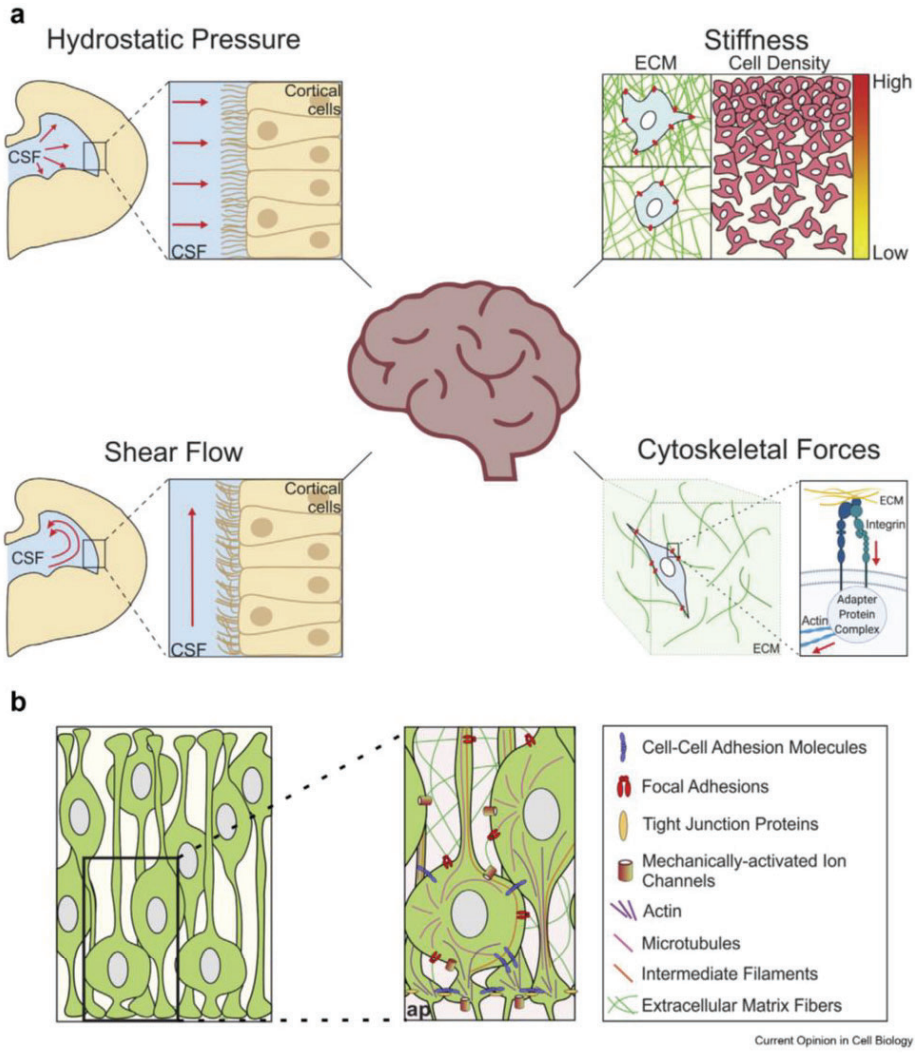


Figure I- 12 **Mechanotransduction in the developing brain.** (a) Mechanical cues affecting the developing brain experience a variety of mechanical cues. (b) The molecules and cellular structures involved in mechanotransduction in the developing neuroepithelium. ap = apical border, CSF = cerebrospinal fluid, ECM = extracellular matrix. Schematic view of fluid-based force. Extracted from (Abuwarda & Pathak, 2020b).

The principal fluid-based forces affecting brain development are hydrostatic pressure and shear flow generated by cerebrospinal fluid (CSF). Brain stiffness increases through development due to changes in ECM and increased cellular density. And finally, the cytoskeleton connects to the extracellular matrix through focal adhesions and is integral to cellular mechanotransduction. Substrate stiffness directly modulates NSC behavior, promoting differentiation into neurons on soft substrates and into astrocytes on stiff substrates (Saha et al., 2008). And ECM disruption due to degradation, transcriptional perturbations, or changes in mechanosignaling proteins, can significantly impact early brain development and lead to neuropathologic conditions in adulthood (Barnes et al., 2017; Dityatev et al., 2010; Franze et al., 2013; Soles et al., 2023). For instance, astrocyte stiffen due to pathological accumulation of GFAP intermediate filaments in astrocytes cause Alexander disease, a severe neurological disorder resulting from astrocyte dysfunction (L. Wang et al., 2018).

NSC microenvironment or niche, provide the necessary mechanical properties, metabolic requirements, and physiological conditions for maintaining proliferative capacity and differentiation potential (Moore & Lemischka, 2006). Niche composition involves NSC, their progeny, surrounding cells, proximity to blood vessels, and the extracellular matrix (ECM) (Faissner & Reinhard, 2015). As already described, NSC niche architecture is critical, and the apical-basal polarization and anchorage of NE and RG regulate their stemness and fate potentiality (Kriegstein, 2006). Disruptions in the ECM correlated with RG pial footing loss, retracted fibers, and aberrant neuron migration in laminin-mutant mice (Halfter et al., 2002). Moreover, a recent work demonstrated that niche stiffening during aging lead to an age-dependent decline in cell function and that adult OPCs seeded on embryonic OPC niches can restore their function (Segel et al., 2019).

In summary, the interplay between the mechanical properties of the ECM and the intrinsic characteristics of cells is pivotal for the healthy and normal development of the brain. The understanding of these relationships is the basis for the emerging concept of influencing cell fate through the modulation of niche mechanics (Segel et al., 2019).

1.2.3. Cellular cytoskeleton in glial cells.

The cellular cytoskeleton is a dynamic network of filaments that provide mechanical support for cell shape, organelle transport, and movement. The cytoskeleton primarily consists of three biopolymer-based filaments: actin-based microfilaments (MF), tubulin-based microtubules (MT) and intermediate filaments (IF) with different properties. MF and MT are polar and hydrolyze ATP and GTP respectively. This allows binding to molecular motors (myosin, kinesin or dynein) that convert chemical energy (ATP/GTP hydrolysis) into mechanical force and movement. On the contrary, IF are nonpolar, do not hydrolyze ATP or GTP and thus, they do not directly interact with molecular motors. IF are more flexible and difficult to brake than MF and MT, providing structural support and mechanical resistance to the cell (Block et al., 2015; Hookway et al., 2015; Robert et al., 2014). MF and MT are composed by three major subunits (α, β, and γ) hardly conserved. On the contrary, IF have organism and tissue specificity, which derive from approximately 70 different genes with multiple splice variants (Block et al., 2015; De Pascalis et al., 2018; Herrmann et al., 2009; Potokar et al., 2020). MF and IF are coupled to adjacent cells and the ECM trough adherent junctions and focal adhesions and trough desmosomes and hemidesmosomes respectively. An overview of the cell cytoskeleton and cell adhesions are shown in Figure I-13.

IF are classified into six groups, based on their amino acid sequence, protein structure and tissue-specificity (Potokar et al., 2020; Sanghvi-Shah & Weber, 2017). Here we will focus on intermediate filaments expressed in astrocyte cells, particularly GFAP and nestin as their expression is developmentally regulated. GFAP is commonly used as mature astrocyte marker, although it is also expressed in NSC, on the contrary, nestin is early expressed in neuroepithelial cells and is commonly used as NSC marker, although it is also expressed in immature and reactive astrocytes, and in other proliferative cells. Lamins, a type of nuclear IF, will be described in the following section.

GFAP (glial fibrillary acidic protein) belongs to type III group, which is characterized by its ability to for homopolymeric and heteropolymeric (with vimentin and nestin) filaments, although GFAP homopolymers have atypical organization and tend to cluster (Eliasson et al., 1999). There are seven GFAP splicing variants in murine and twelve in humans (Hol & Pekny, 2015; Middeldorp & Hol, 2011; van Asperen et al., 2022) and their major functions in cell mechanics include, among others, anchoring transporters, resistance to mechanical stress, maintenance and permeability of the blood-brain barrier, glial scar formation and response to hypoosmotic stress (Infante & Etienne-Manneville, 2022; Potokar et al., 2020). In addition, GFAP is mechanosensitive and interplay with cell adhesion, cell migration, cell invasion, and MF lifetime and turnover (De Pascalis et al., 2018; Potokar et al., 2020; Sanghvi-Shah & Weber, 2017).

Nestin belongs to the type VI and no splicing variants are described. Nestin can form homodimers and homotetramers *in vitro*, but do not form IF per se, consequently, nestin form heteropolymeric filaments with either vimentin or GFAP as obligatory partners (Eliasson et al., 1999; Hol & Pekny, 2015; Pekny et al., 1999; Steinert et al., 1999). In particular, different GFAP isoforms control IF network dynamics. Structurally, it seems that the small head domain of nestin appears to be the key structure that precludes nestin assembling in filaments on its own and have similarities with neurofilaments (Herrmann et al., 2009; Potokar et al., 2020). The major functions of nestin in cell mechanics include promoting vimentin disassembly, affecting trafficking and IF proteins delivery to daughter cells during division. Nestin also affects cell mobility, and its genetic ablation is sufficient to reduce astrocyte migration. Overall, nestin affects cell traction forces, modulate actin-myosin network and MT, affecting cell migration (De Pascalis et al., 2018).

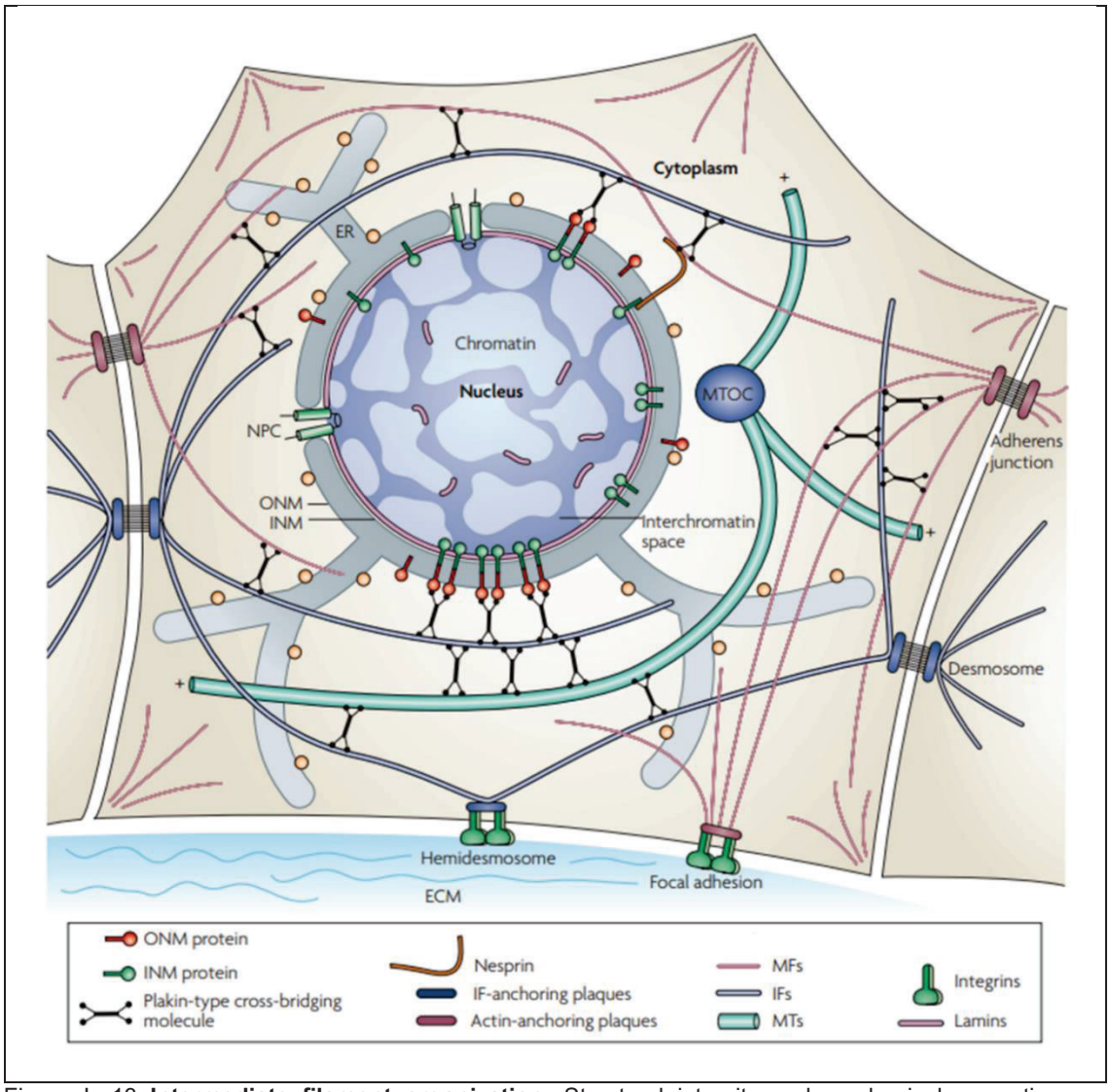


Figure I- 13 **Intermediate filament organization**. Structural integrity and mechanical properties are provided by microtubules (MT), microfilaments (MF), and intermediate filaments (IF) which are interconnected through plakin-type molecules, such as plectin. IF are coupled to cell-cell junctions (desmosomes), and to cell-ECM junctions (hemidesmosomes). IF are also coupled to the nucleus by plectin and nesprin-3 in the outer nuclear membrane (ONM). In the inner nuclear membrane (INM) there is a layer of IF formed by lamins, attached to nucleopores (NPC) and chromatin. The ONM and INM are interconnected, and the ONM is interconnected with IF and microtubules, which in turns, provide a mechanical continuum that interconnects ECM with chromatin. Adapted from (Herrmann et al., 2007).

Common to all IF, GFAP and nestin interact with different cytoskeleton crosslinkers, particularly, their interaction with plectin govern the collective cell migration of astrocytes through its participation with actin-myosin network dynamics (Bernal & Arranz, 2018; De Pascalis et al., 2018). Furthermore, the retrograde flow of actin attracts nestin, vimentin, and GFAP IF in front of the nucleus, facilitating the transmission of pushing forces that influence nuclear positioning (Dupin & Etienne-Manneville, 2011). The diversity in IF composition arises from variations in their primary amino acid sequences. These amino acids, in turn, interact with various cellular components, creating distinct binding sites for

regulatory factors. Additionally, IF acts as platforms, essentially serving as transitory docking sites, for functional proteins like kinases and transcription factors. These roles contribute to specific cellular properties, enhancing the adaptability and mechanosensitivity of individual cells (Herrmann et al., 2009).

1.2.4. The nucleus as a mechanosensitive organelle

The nucleus is the physical container of the eukaryotic genome. The chromatin, mainly formed by DNA and histones, store the genetic information, and regulate transcription. High degree of DNA packaging in heterochromatin silence gene transcription while low DNA packaging in euchromatin is associated with active transcription. In addition to its genetic functions, the nucleus is a large and stiff organelle that serve as a physical sensing device for cellular deformation, necessary to adapt cell behaviors to their environment and stage of development/differentiation (Kalukula et al., 2022; Maurer & Lammerding, 2019a; Niethammer, 2021; Swift et al., 2013). Nuclear mechanotransduction relay in the axis cell adhesion(1)-cytoskeleton(2)-nucleoskeleton(3), which is composed by (1) a dynamic clutch mechanism, based on talin depletion, that mediate force/rigidity relationship with the environment; (2) integral cytoskeleton components MF, MT and IF; and (3) the nuclear envelope (Elosegui-Artola et al., 2017a; Skinner & Johnson, 2017; Vahabikashi et al., 2022). A summary of nuclear mechanosensitive mechanisms is shown in Figure I-14.

The nuclear envelope is a specialized structure composed by the nuclear membrane, which is the physical separation between nucleus and cytoplasm; the nuclear lamina, which provide physical and structural support; and nuclear pore complexes (NPCs) that regulate exchange of large molecules (>30-kDa) across the nuclear envelope (Mestres et al., 2022a). The nuclear membrane consists in outer (ONM) and inner (INM) nuclear membranes separated by the perinuclear space (PNS), which is connected with the endoplasmic reticulum (ER). The nuclear lamina is a complex fibrillar meshwork of lamin IF and their associated proteins that is closely juxtaposed to the nucleoplasm face of the INM (Potokar et al., 2020; Vahabikashi et al., 2023). Mechanically, the linker of the nucleoskeleton and cytoskeleton (LINC) complex, comprised of nesprins at the ONM and SUN-domain proteins at the INM, couple cytoskeleton (MT, MF, and IF) with nucleoskeleton; and lamina-associated domains (LADs) connect chromatin to the lamina

and INM (Figure I-15) (Javier-Torrent et al., 2021; Vahabikashi et al., 2023)(Maurer & Lammerding, 2019b; Vahabikashi et al., 2022).

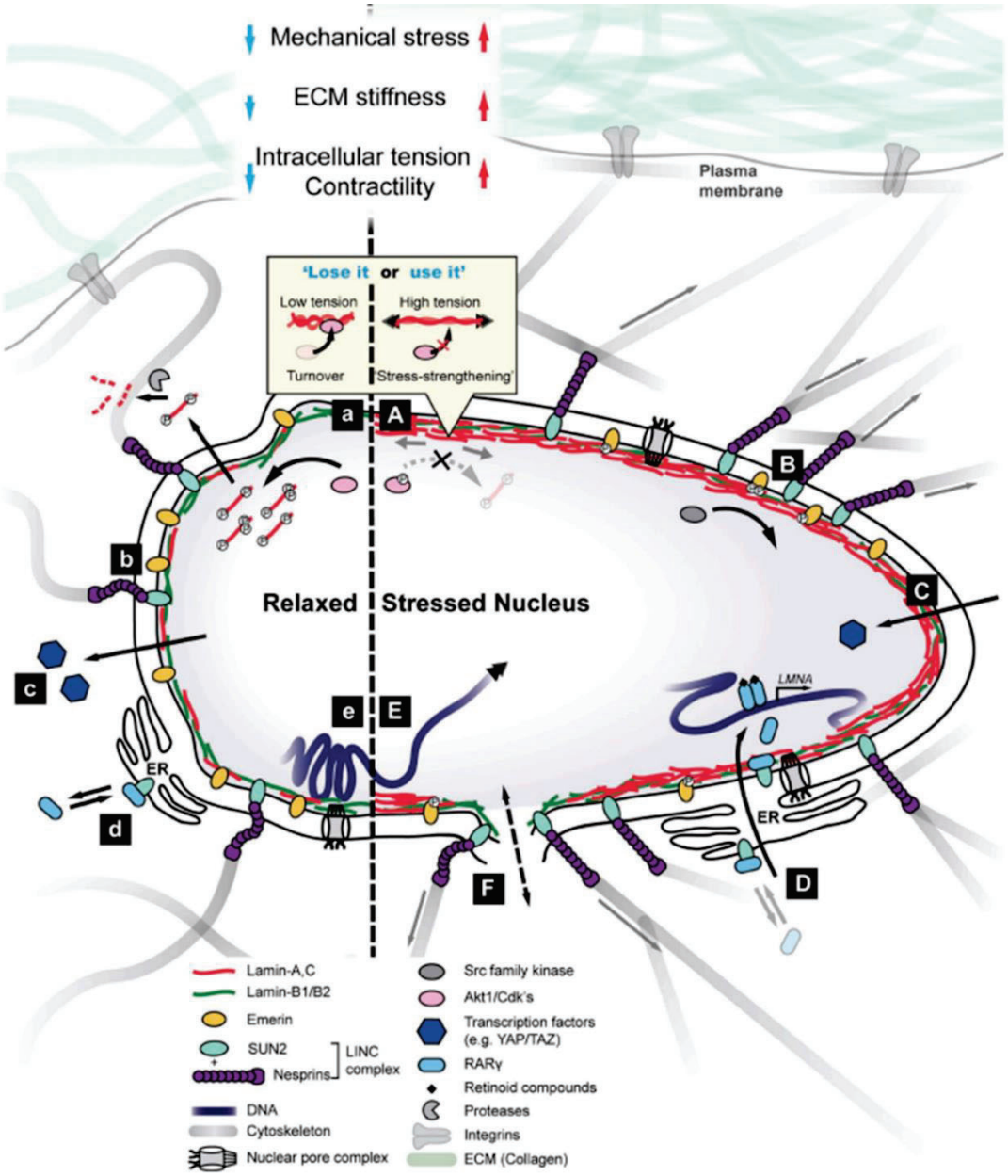


Figure I- 14 **Nuclear mechanosensitive mechanisms**. In the left side, the nucleus is relaxed (soft) and on the right side, the nucleus is mechanically stressed. Mechanosensitive transcription factors such as YAP and TAZ (Elosegui-Artola, 2021) translocate into the nucleus under stress to modulate gene transcription. Adapted from (Cho et al., 2017).

Lamins are nuclear Type V IF and are the only universally IF expressed in metazoans (Herrmann et al., 2009). Mammalian cells express A- and B-type of lamins, encoded by three genes. *LMNA* gene gives rise two lamin A-type isoforms, lamin A and lamin C, and *LMNB1* and *LMNB2* genes encoded lamin B1 and lamin B2 proteins respectively (Maurer & Lammerding, 2019b; Vahabikashi et al., 2022). The different lamins homotypically

assemble into separate meshwork that interact with each other, with lamin B1 in the outermost layer of the nuclear lamina right underneath the INM. Lamins are the most resilient component of the nucleus and a heavy-duty shock absorber. They are responsible of positioning and distribution of NPCs, the nuclear assembly and disassembly during cellular division – mediated by lamins phosphorylation and dephosphorylation –, and regulate nuclear shape, stiffness, and structure trough interaction with nuclear actin (S. Y. Liu & Ikegami, 2020; Maurer & Lammerding, 2019b; Vahabikashi et al., 2022).

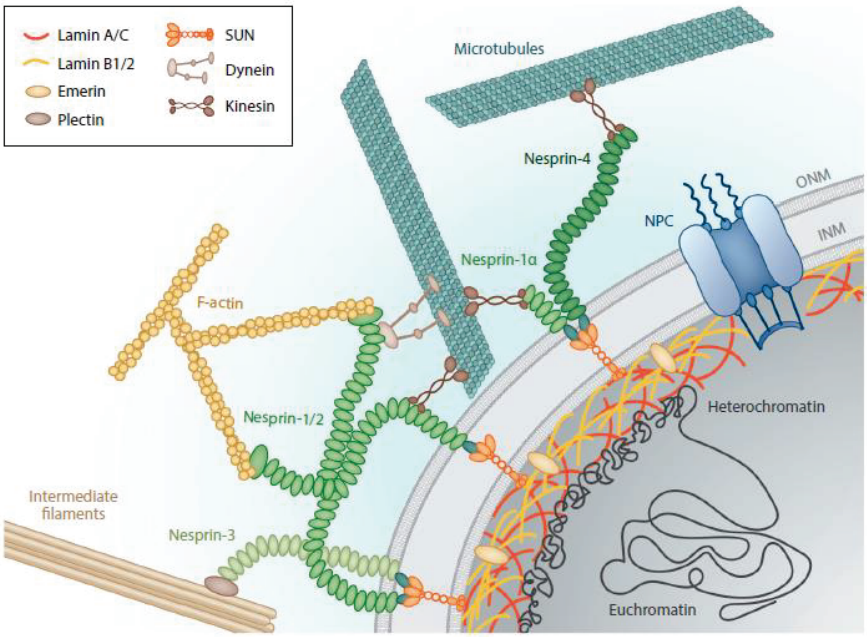


Figure I- 15 **Molecular machinery governing nuclear mechanotransduction**. The LINC complex, nesprins at the ONM and SUN proteins at INM, facilitates force transmission between the cytoskeleton and the nuclear interior. This complex interacts with cytoskeletal filaments, associated proteins (plectin), and the nuclear lamina. Nuclear lamins (A/C and B1/2) form independent yet interacting meshworks beneath the INM, playing a crucial role in maintaining nuclear shape and stiffness. Lamins interact with NPCs, chromatin, and various binding partners. NPCs facilitate molecular transport between the cytoplasm and nucleoplasm, highlighting the dynamic interplay of constituents involved in mechanotransduction within the nucleus. Extracted from (Maurer & Lammerding, 2019a).

Nuclear mechanical properties are strictly dependent on proportion of Lamins type A or type B in the composition of the nuclear lamina (Lammerding et al., 2006; Swift et al., 2013; Swift & Discher, 2014; Wintner et al., 2020). Particularly, lamin A-C and lamin B1 contribute to nucleus stiffness, while viscosity is specified mostly by lamin A-C (Wintner et al., 2020). Lamin B are constitutively and ubiquitously expressed throughout development. However, lamin B1 deficient cells show normal nuclear stiffness their nuclear lamina is prone to blebbing (Lammerding et al., 2006; Swift et al., 2013). Lamin A is more expressed in differentiated cells and vary across tissue and cell-types to adapt

nuclear stiffness to specific tissue microelasticity and extracellular associated stiffness (Swift et al., 2013). Lamin A-C stiffen the nuclear lamina, and lamin A/C-to-B1 ratio in the nuclear lamina increased in regions of high negative membrane curvature, such as at the poles of ellipsoid nuclei. Conversely, has been proposed that the role of lamin B1 is to stabilize nuclear shape by restraining outward protrusions of the lamin A-C network (Nmezi et al., 2019). Moreover, under mechanical stretch, lamin A-C is mechanoresponsive while lamin B1 is not (Nava et al., 2020; M. Wang et al., 2022). In summary, the expression level of lamin A-C determines nuclear stiffness and viscoelasticity properties, while lamin B1 provides nuclear stability and also contributes to nuclear stiffness.

In RG-astrocyte lineage cells, balanced levels of lamin B1 are required for maintaining nuclear integrity and undergo a proper corticogenesis, and astrocytic and neuron differentiation (Mahajani et al., 2017; Vergnes et al., 2004). Lowering lamin B1 expression is associated with concomitant loss of the neurogenesis capacity in the adult brain, and the restoration of lamin B1 expression favors NSC proliferation and neurogenesis (Bedrosian et al., 2021; bin Imtiaz et al., 2021a). Mature cortical glial cells have specific patterns of lamin expression. Astrocytes, oligodendrocytes, and neurons preferentially contain lamin C isoform as principal component of A-type lamin. Microglia lack lamin A-C, and OPC have intense lamin B1 expression and lack lamin C. Lamin B2 was weak in all glial cells than in cortical neurons (Takamori et al., 2018).

Abnormal lamin levels cause a plethora of pathologies, called laminopathies, most caused by autosomal-dominant point mutations in *LMNA* gene. They include cardiomyopathies, muscular dystrophies, lipodystrophies, peripheral neuropathies, and Hutchinson-Gilford progeria syndrome (HGPS) (Kang et al., 2018). Laminopathies course with abnormal gene expression and cell signaling, increased DNA damage, abnormal localization of telomeres, altered nuclear shape and altered response to mechanical stress. In HGPS, a very rare disease (1 in 20,000,000), all aging related features are displayed at an early stage (S. Y. Liu & Ikegami, 2020). For extensive information regarding laminopathies and abnormalities of the nuclear lamins see (Karoutas & Akhtar, 2021) and (Evangelisti et al., 2022).

In terms of mechanotransduction, nuclear deformation and nuclear transcriptional changes were mediated by distinct extracellular or intracellular downstream events, which through the adhesion-cytoskeleton-nucleoskeleton axis influence nuclear structural components, ending in chromatin regulation (Heo et al., 2016; Katiyar et al.,

2019; Kirby & Lammerding, 2018; Skinner & Johnson, 2017). Chromatin dynamics also influence nuclear mechanics itself, by changing its state (compacted or not) and tethering to the INM (Javier-Torrent et al., 2021; Nava et al., 2020; Wintner et al., 2020). Moreover, under rapid and dynamic external stretching, heterochromatin-mediated nuclei deformation drives calcium-dependent nuclear softening. In sustained mechanical stress, an extended and generalized mechanotransduction signal originated by cell-cell contacts reorganize structural and force carriers to prevent nuclei from excessive forces (Figure I-16) (Nava et al., 2020; Wintner et al., 2020).

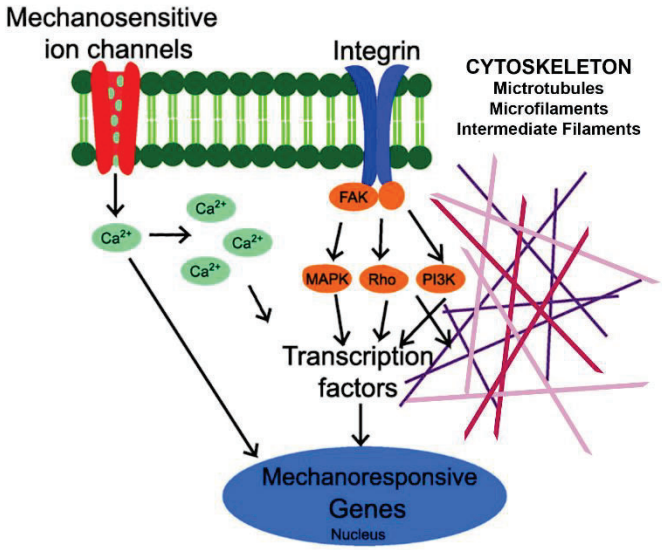


Figure I- 16 **Schematic overview of extrinsic modulators influencing transcription of mechanoresponsive genes**. Calcium entry through mechanosensitive ion channels and intracellular calcium regulation plays a pivotal role in modulating gene expression. On the other side, focal adhesion kinase (FAK) serves as a key mediator, influencing the transcription of mechanoresponsive genes through distinct integrin-related signaling pathways, including MAPK, Rho, and PI3K. Adapted from (Stukel & Willits, 2016).

1.2.5. Mechanosensing transcriptional co-activators in RG lineage progression.

Organ growth, in our case brain, is regulated by the interaction of many signaling pathways, among which Hippo pathway is central. The Hippo pathway is activated in response to external signals including apical-basal polarity, cell-to-cell adhesion, mechanical factors, and contact inhibition. Hippo pathway activation is controlled by two paralogous transcriptional coactivators, YAP and TAZ (YAP/TAZ), that switch between cytoplasmic and nuclear localization. When Hippo is activated (Hippo ON), YAP/TAZ is excluded from the nucleus and retained in the cytoplasm or degraded; when inactivated (Hippo OFF) YAP/TAZ entre the nucleus, interact with DNA binding factors (TEAD factors) and upregulate transcription of genes that promote cell growth, controlling cell

proliferation, tissue patterning and organ growth (Piccolo et al., 2014). Several studies have demonstrated the role of YAP/TAZ as co-transcriptional activators associated to mechanotransduction. For example, extracellular matrix stiffness induces YAP/TAZ nuclear translocation, and the corresponding Hippo pathway inactivation (Elosegui-Artola et al., 2017a; Nardone et al., 2017; Totaro et al., 2018).

The Hippo/YAPTAZ pathway engages intricate interactions with various regulatory mechanisms, including growth factors and hormones, hypoxia, and metabolism (see for further detail (J. Luo & Li, 2022), that orchestrate organ size and tissue growth, including brain.

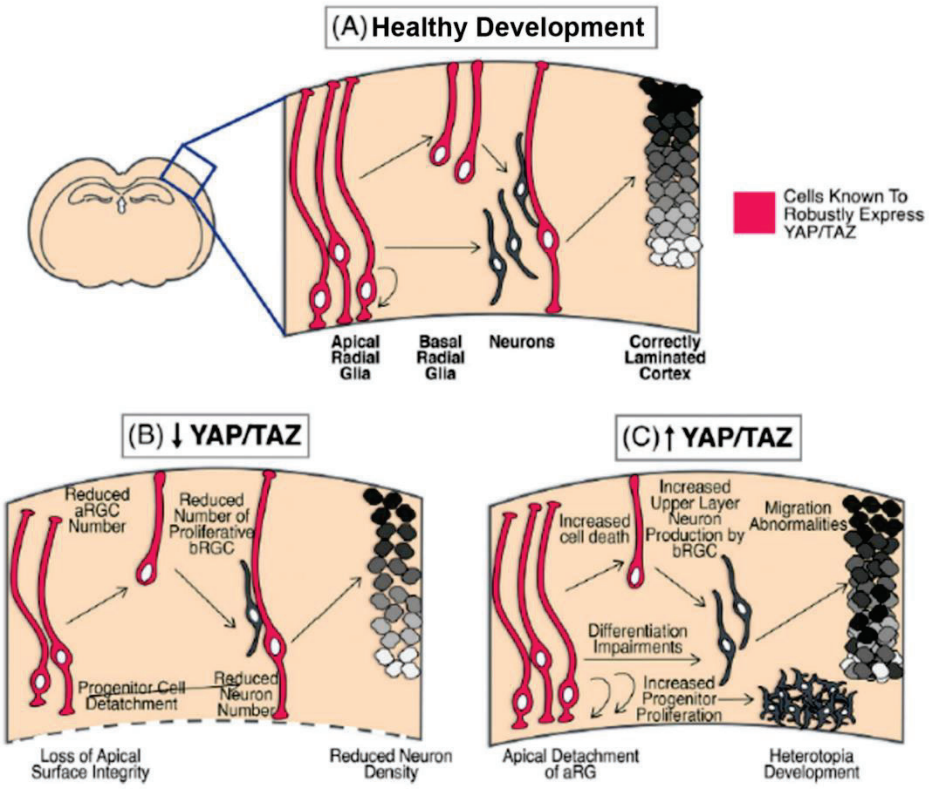


Figure I- 17 **YAP/TAZ expression during brain development.** In red cells known to highly express YAP/TAZ and the other cells in gray (does not exclude YAP/TAZ expression). (A) Normal cortex development with normal YAP/TAZ expression. (B) Cortex development with lower levels of YAP/TAZ than normal is associated to a loss of apical RG, and reduced bRG and neuron production. (C) Cortex development with increased levels of YAP/TAZ is associated to increased cell death, increased RG proliferation, bRG and neuron production, presence of heterotropias and aberrant neuron migration. Adapted from (Terry & Kim, 2022a).

In the developing brain, RG express YAP/TAZ with dynamic changes in its subcellular localization across development (Lavado et al., 2021; Mukhtar et al., 2020). YAP/TAZ is required for maintaining structural scaffold integrity and the proliferative potential of RG (Hughes et al., 2020; Lavado et al., 2021). Interestingly, in has been recently reported that YAP activity is sufficient and necessary to increase the pool size of bRG in

gyrencephalic and lissencephalic brains (Kostic et al., 2019a). Moreover, they also reported that YAP expression is driven by the Sox2 transcription factor, which was also observed in cancer stem cells (Kostic et al., 2019a; White et al., 2019). YAP/TAZ overexpression or downregulation in developing brains induce severe structural defects, such as apical junction loss and altered neurogenesis and NSC proliferation and differentiation (Figure I-17) (thoroughly reviewed in (Terry & Kim, 2022b). In the adult brain, Yap1 depletion reduces NSC activation, nonetheless, there is a tight upstream control because its overexpression did not induce NSC activation (Fan et al., 2023). Finally, depending on the temporal stage, the link YAP-SMAD1/5, canonical effectors of bone morphogenetic protein (BMP) signaling, induces RG self-amplification and astrocyte differentiation (Huang et al., 2016; Najas et al., 2020).

WNT signaling plays a key role in the regulation of neurogenesis and tissue homeostasis and is required for healthy brain development. The canonical WNT pathway relays in β-catenin. In the presence of Wnt ligands that are not phosphorylated β-catenin is stabilized in the cytoplasm. β-catenin accumulation induces their nuclear translocation, acting as a central effector of the canonical WNT/β-catenin signaling pathway. In the absence of extracellular Wnt ligands, β-catenin is target to proteasomal degradation through phosphorylation and ubiquitination (J. Gao et al., 2021a; J. Liu et al., 2022). The non-canonical WNT pathways are β-catenin independent, one is linked to the planar cell polarity axis (WNT/PCP) and the other is linked to intracellular Ca^{2+} (WNT/Ca^{2+}). WNT/PCP pathway regulates cell movement and polarity, while WNT/Ca^{2+} regulates cell fate and migration. Both pathways generally inhibit the canonical pathway (J. Gao et al., 2021a; J. Liu et al., 2022).

WNT/β-catenin are crucial for maintaining N-cadherin complex in adherent junctions during cortex expansion and RG proliferation (Figure I- 18) (Miyamoto et al., 2015). Knock out of *ctnnb1* gene produced an early loss of apical contact and RG scaffold disassembly, on the contrary, WNT/β-catenin activation enhanced cortex expansion (Machon et al., 2007; Wrobel et al., 2007). During brain development, the canonical WNT/β-catenin pathway progressively decreases following a biphasic pattern, with high activity during neurogenesis and neuron maturation, and low activity in early immature neurons (Bem et al., 2019; Heppt et al., 2020). Moreover, this β-catenin signaling dynamics influence cell-fate decisions (Rosenbloom et al., 2020). However, in the adult brain, Wnt/β-catenin signaling is not required to maintain hippocampal NSC homeostasis (Austin et al., 2021), and the non-canonical WNT/PCP and adhesion molecules are key in regulating the balance between activate (aNSC) and quiescent NSC (qNSC) in the SVZ niche (Chavali et al., 2018)

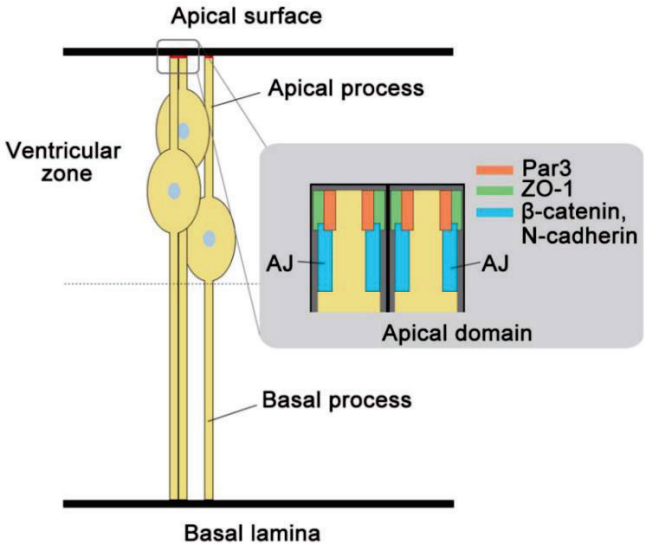


Figure I- 18 **Schematic overview of RG adherent junctions in the apical surface**. N-cadherin based adherent junction (AJ). Par3 and ZO-1, and β-catenin integrate AJ components. Extracted from (Miyamoto et al., 2015).

It has been demonstrated that YAP/TAZ are integral components of the β-catenin destruction complex and direct modulators of canonical WNT signaling (Figure I-19) (Azzolin et al., 2014).

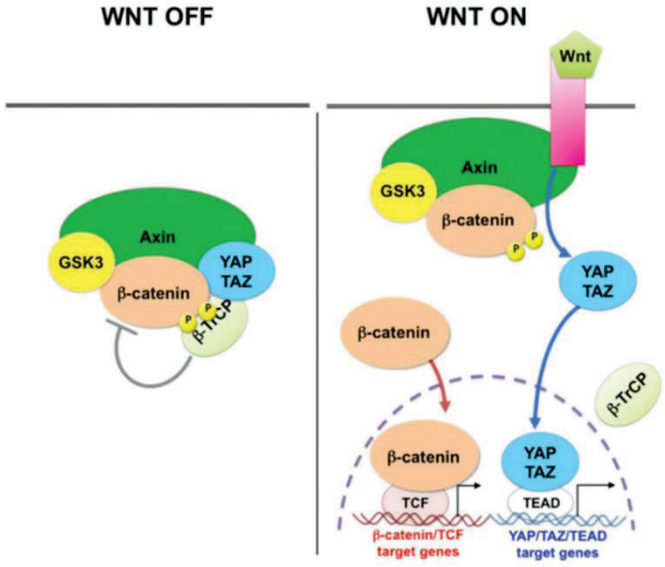


Figure I- 19 **YAP/TAZ and β-catenin destruction complex.** In the left, the inhibitory role in the WNT OFF. In the right, working as pathway effector in the WNT ON. Adapted from (Azzolin et al., 2014).

In the absence of WNT signaling (WNT OFF), YAP/TAZ plays a pivotal role in facilitating β-catenin degradation by recruiting β-TrCP. Conversely, when WNT signaling is active (WNT ON), YAP/TAZ disengaged from the destruction complex, allowing YAP/TAZ and β-catenin nuclear accumulation and activation of their target genes. This mechanism

ensures that WNT signaling induces a coherent and simultaneous activation of both YAP/TAZ and β-catenin signaling, relevant for organ size control, regeneration, and tumor progression (Azzolin et al., 2014).

1.2.6. Mechanoelectrical signals: Mechanosensitive ion channels

RG, neural progenitors, and neuroglial cells in general are electrically non-excitable (cannot generate action potentials), with low densities of Na^+ and Ca^{2+} permeable channels and large K^+ permeability and shunting, preventing membrane depolarization. While they can generate slow (electrotonic) potentials by fluctuations of free ions in the cytosol, especially Ca^{2+}, in response to chemical or mechanical stimulation. RG and astrocytes show Ca^{2+} transients and oscillations during early development, and the amplitude of intracellular Ca^{2+} events increase with age. The following sections present a summary of the principal mechanosensitive ion channels and calcium signaling mechanisms focused on RG and astroglial cells (review in: (Lim et al., 2021; Sawamura et al., 2017; Verkhratsky et al., 2014; Verkhratsky & Nedergaard, 2018).

Mechanosensitive ion channels (MSCs) serve as the earliest messenger in the transduction of mechanical stimuli into biologically relevant signals. Although the mechanisms of mechanosensitivity are a matter of discussion, it is assumed that MSCs change their conformation in response to mechanical stimuli (pressure, shear stress, osmolarity) generating ionic currents. The two main hypotheses, not mutually exclusive, are that MSCs are gated in response to curvature and mechanical stress within the lipid bilayer, “force-from-lipids” model, or gated by the force transmitted via ECM/membrane/cytoskeletal interactions, “force-from-filaments” model (Figure I-20) (Cox et al., 2019). Moreover, MSCs can be subdivided into inhibitory hyperpolarizing K^+ selective, and excitatory depolarizing non-selective cationic (permeable to Na^+, K^+, Ca^{+2}). Although direct mechanosensitivity was not demonstrated for all their components, MSCs that mainly respond to the mechanical microenvironment generated by ECM/membrane composition/cytoskeletal interactions include the family of DEG/ENaC/ASIC channels and some the transient receptor potential (TRP) channels. While those directly sensitive to lipid tension include two-pore-domain K^+ (K2P) channels, Piezo channels and some TRP channels (Ranade et al., 2015; Ruan et al., 2020; Suchyna, 2017; Turovsky et al., 2020).

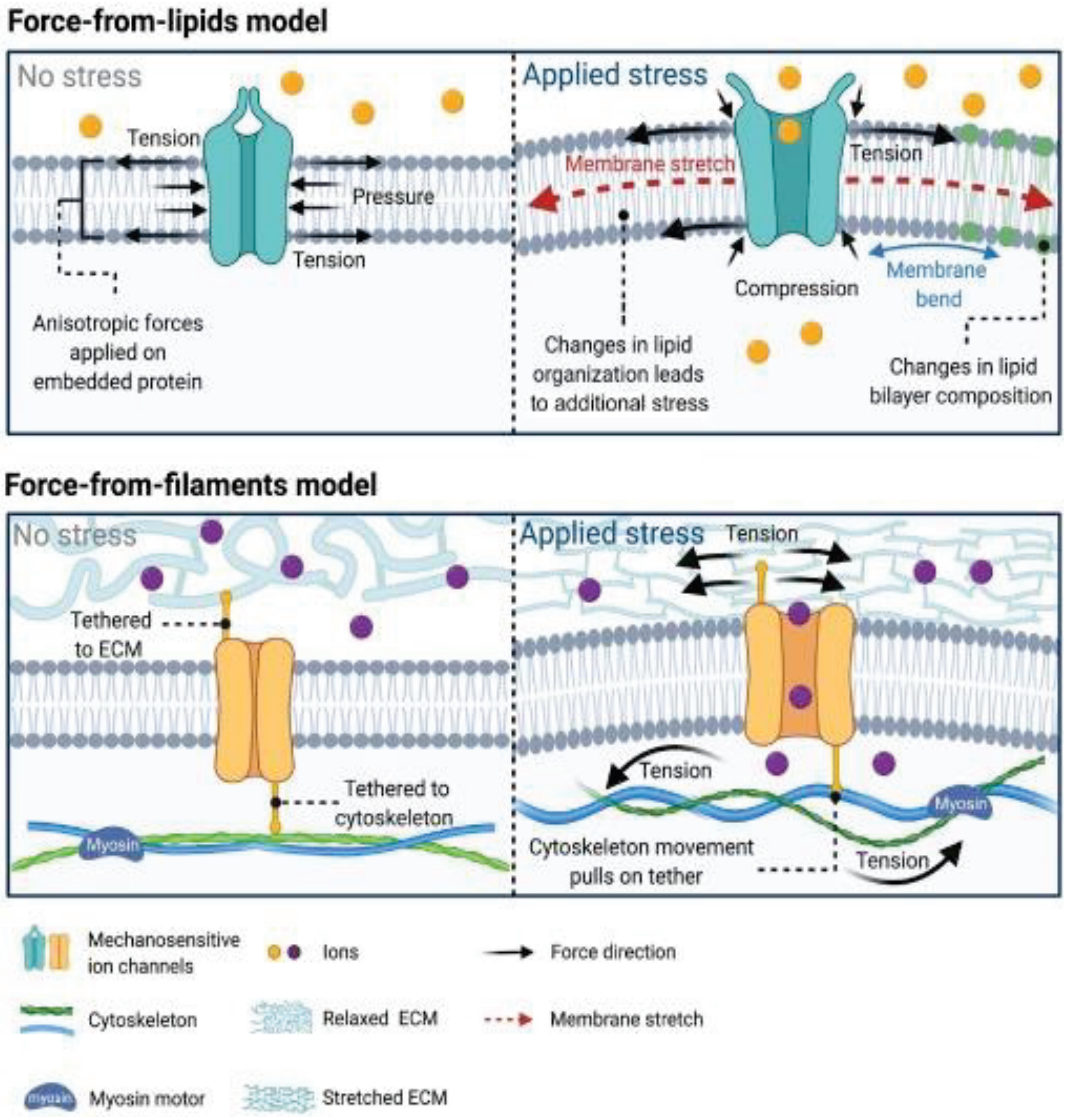


Figure I- 20 **Two models of mechanosensitive ion channel gating.** Gating mechanisms described for mechanosensing ion channels (MSC). The force-from-lipids model describes the effect of the anisotropic push and pull in the cell membrane influencing the state of the channels: closed without stress, and open with stress. Force-from-filaments model is also regulated by mechanical stress, this is applied via cytoskeleton or ECM binding. Adapted from (Momin et al., 2021).

Transient receptor potential (TRP) channels are evolutionary conserved non-selective polymodal cation channels that are generally classified into seven categories based on sequence homology (TRPA, TRPC, TRPM, TRPML, TRPN, TRPP, and TRPV). TRPs form tetrameric channels with different sensitivity for Ca^{2+}, K^{+} and Na^{+}, and act as environmental sensors for diverse stimuli, including intracellular pH, temperature, lipid and amphiphile membrane composition, and mechanical forces (Sawamura et al., 2017; Startek et al., 2019; Verkhratsky et al., 2014). The principal TRP members expressed in the CNS, and in particular in astrocytes, belong to TRPA, TRPC, TRPM and TRPV groups.

TRPA1 are multimodal channels with substantial Ca^{2+} permeability. TRPA1 channels are activated by low temperature (below 17ºC), spicy substances from plants (ex. allyl isothiocyanate, cinnamaldehyde, allicin, menthol, cannabinoids) and by proinflammatory agents, and have been involved in visceral mechanosensitivity. Its activation by specific agonists potentiated $[Ca^{2+}]_I$ transients and whole cell currents, while its inhibition resulted in significant decrease in basal $[Ca^{2+}]_I$.

TRPC1-7 form non-selective Ca^{2+} channels and between them, TRPC1/TRPC6/TRPC7 are activated directly by diacylglycerol (DAG) upon phospholipase C (PLC)-coupled receptor stimulation, functionally linking them to GPCRs and tyrosine kinase receptors (ex. mGluR1 and mGluR5). In addition, TRPC1 channels are involved in store-operated Ca^{2+} (SOC) entry and in the generation of $[Ca^{2+}]_i$ oscillations induced by depletion of endoplasmic reticulum (ER) Ca^{2+} stores, and its expression increases with age (Chen et al., 2020). TRPC1 and TRPC3 channels are expressed in neural progenitors and have been involved in cellular mobility and axonal migration (Louhivuori et al., 2015).

TRPM1-8 channels differ in modes of activation, cation selectivity and tissue distributions. Most of them were found in cancerous tissue and some were involved in temperature sensation, magnesium (Mg^{2+}) homeostasis and taste.

TRPV1-6 channels form Ca^{2+}-permeable cation channels that are activated by various chemicals (ex. capsaicin), thermal and noxious stimuli. TRPV1 channels carried cationic currents activated by acidification, and apparently, contributes to Ca^{2+}-dependent rearrangement of the cytoskeleton. TRPV4 channels are sensitive to osmotic pressure and their activation triggers cytosolic Ca^{2+} currents. It is postulated that TRPV4 acts in concert with aquaporin 4 (AQP4) in volume regulation in response to osmotic stress.

Piezo channels (Piezo1, 2) are evolutionarily conserved stretch-activated non-selective cation channels that display a rapid and labile voltage dependent inactivation, which became non-inactivating with excessive mechanical stimulation (Suchyna, 2017). The Piezo 3D structure suggests that can induce a distortion in the lipid bilayer, and mechanical sensitivity of Piezo 1 is modulated by resting membrane tension. In this sense, the cytoskeleton has a protective role against Piezo activation by modulating membrane tension (Jin et al., 2020; Ranade et al., 2015; Suchyna, 2017). Piezo1 was required for the development of mouse vasculature (Ranade et al., 2015), and *Piezo1* gene was the only expressed during mice corticogenesis (Bouron, 2020).

K2P channels are background K^+ channels widely expressed in the nervous system. These channels remain open (leaky) across the range of physiological voltages, playing a role in maintaining membrane potential (Lengyel et al., 2021; Y. Luo et al., 2021). TWIK-

related spinal cord K^+ channels (TRESK, *KCNK18*) strongly contribute to background K^+ currents, setting the resting membrane potential and adjusting membrane excitability. TRESK channel deletion in mice selectively enhances mechanical and cold sensitivity (Castellanos, 2020), and dominant negative TRESK mutations associated with migraine increase neuronal excitability trough inhibition of TREK (Royal et al., 2019). The TREK (TWIK-related K^+ channels) subfamily, TREK1, TREK2 and TRAAK (TWIK-related arachidonic acid-stimulated K^+ channel), are not always open and act as multimodal integrators of a wide variety of regulatory parameters, as intracellular pH, lipid membrane composition, temperature, some anesthetics gases, and tension of the plasma membrane, among others. TREK/TRAAK channels sense the asymmetry in the phospholipid bilayer and are differentially gated by monolayer tension. When open, TREK/TRAAK channels would cause an efflux of K^+, membrane hyperpolarization and a consequent decrease in cell excitability, counteracting or balancing the activity of excitatory mechanosensitive cation channels. TREK-1/TRAAK knockout mice show enhanced sensitivity to painful stimuli, including mechanical, and heat (Douguet & Honoré, 2019; Gnanasambandam et al., 2017; Suchyna, 2017).

Voltage-gated K^+ (Kv) channels are activated by membrane depolarization and cause membrane hyperpolarization, counteracting the activity of excitatory cation channels and functioning as a brake on membrane excitation. Some Kv channels (ex. Kv7) are also modulated by lipid bilayer composition and membrane tension, driving their lipid dependent gating. Kv7/M channels generate low-voltage activating, non-inactivating K^+ currents. Kv7 channels are highly sensitivity PIP_2, which acts as a cofactor tuning their voltage sensitivity, and to polyunsaturated fatty acids (PUFAs) (Duncan et al., 2019; Larsson et al., 2020). In addition, calmodulin (CaM) appears to be an essential auxiliary subunit of Kv7 channels and strongly modulates their function (Chang et al., 2018; Zhuang & Yan, 2021). Kv7 channels are crucial for setting the velocity and frequency preference of a subpopulation of rapidly adapting mechanoreceptors required for normal touch sensation (Heidenreich et al., 2012). Nevertheless, how mechanical forces are integrated in cells where mechanosensitive K^+ channels are co-expressed with excitatory mechanosensitive cation channels remains an open question (Jin et al., 2020; Ranade et al., 2015).

DEG/ENaC/ASIC channels are highly conserved and widely expressed voltage independent Na^+ channels. In mammals, canonical epithelial sodium channels (ENaCs) are heterotrimers from alpha (ENaCα), beta (ENaCβ), and gamma (ENaCγ) subunits, and are involved in the maintenance of blood pressure, electrolyte, and fluid balance. ENaC channels have a highly biased selectivity for Na^+ and are constitutively open in the

absence of an activating stimulus (Wichmann & Althaus, 2020). Acid sensing ion channels (ASICs) are homologs of ENaCα channels and predominantly expressed in the nervous system, both in neurons and glial cells. In contrast to ENaCs, ASICs (ASIC1-4) form homo- and hetero- trimers proton gated channels with different pH thresholds for channel activation, and quickly desensitize during prolonged extracellular acidification. In addition to extracellular protons, ASICs are mechanically gated by movement of their extracellular domains that are associated with the ECM. ASIC1, the most expressed in the CNS, also exhibits Ca^{2+} permeability in addition to Na^{+}, and its activation causes intracellular calcium rises (Bianchi, 2021; Deval & Lingueglia, 2015; Foster et al., 2021). Moreover, *Asic1* gene is the only ASICs gene expressed during mice corticogenesis (Bouron, 2020).

Connexins (Cx) are transmembrane proteins that form homo- or heterohexameric hemichannels or connexons. When one hemichannel docks to its counterpart on the adjacent cell form a gap junction. In astrocytes, the principal connexin subtypes are Cx26, Cx30 and Cx43. Cx43 is developmentally regulated and constitutes the most abundant and ubiquitously expressed in astrocytes. Astrocytic connexons and gap junctions allow rapid intercellular and intracellular exchange of ions and hydrophilic molecules (<1kDa) including second messengers, nucleotides, glucose, and various metabolites (ATP, glutamate, nicotinamide adenine dinucleotide (NAD), D-serine). The biophysical properties of connexons-based gap junction channels are regulated by pH, $[Ca^{2+}]_I$, and phosphorylation, and Cx26 and Cx30 are voltage-dependent. Astrocytic channels are critical for K^{+} and glutamate buffering and calcium wave propagation, while hemichannels are responsible for the release of gliotransmitters and neuromodulators to the extracellular milieu. The opening of hemichannels is highly dynamic. As a rule, hemichannels are close in healthy resting cells and can be activated by multiple signals including low $[Ca^{2+}]_e$, specific intracellular Ca^{2+} signals, mechanical signals, or exposure to inflammatory agents. In particular, CX43 hemichannel-mediated release of ATP has been involved in Ca^{2+} signal propagation in response to mechanical signals (Turovsky et al., 2020).

1.2.7. Calcium signaling toolkit in astrocyte lineage cells.

During brain development, intracellular Ca^{2+} transients control key neural process including neurogenesis, migration, and neural differentiation (Rash et al., 2016). Ca^{2+} influx trough different types of transport systems can be stimulated in response to intracellular and extracellular signals, including mechanical signals. Intracellular Ca^{2+} is an evolutionary conserved second messenger, and their precise regulation represents a nexus between environmental cues and transcriptional programs that are crucial for

development, homeostasis, and plasticity (Bouron, 2020). To keep resting cytosolic Ca^{2+} concentration ($[Ca^{2+}]_i$) very low (100-200nM in glial cells), Ca^{2+} is eliminated from the cytosol by sarcoplasmic reticulum calcium ATPase (SERCA) pump in the ER, and by calcium ATPases and sodium-calcium exchangers (NCXs) in the plasma membrane. Ca^{2+} can entry the cytosol from the extracellular milieu and from intracellular Ca^{2+} stores, principally endoplasmic reticulum (ER). In astroglial cells, Ca^{2+} entry from the extracellular milieu occurs through different Ca^{2+}-permeable channels dependent on environmental signals. Voltage-gated calcium channels (VGCCs) allow Ca^{2+} influx in response to neural activity; ligand gated calcium channels (LGCCs) are activated by neurotransmitter binding, and mechanosensitive cation channels (TRP, Piezo, etc.) are activated in response to mechanical forces in a polymodal way (Figure I-21) (Bouron, 2020; Jin et al., 2020; Lim et al., 2021; McKinney et al., 2022; Ranade et al., 2015).

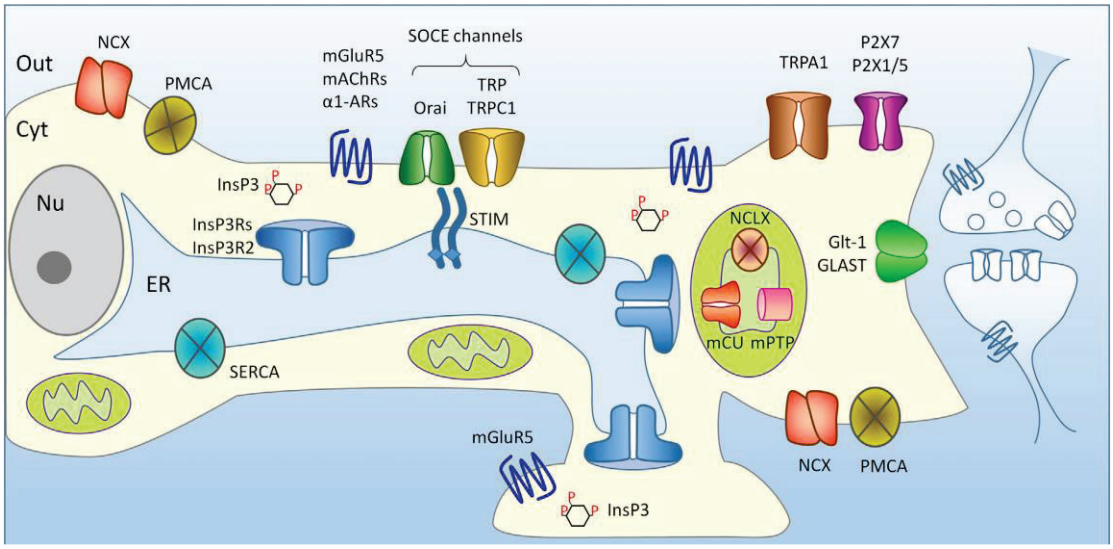


Figure I- 21 **Schematic representation of intracellular calcium regulation in astroglia**. The maintenance of resting $[Ca^{2+}]i$ involves the concerted action of plasma membrane Ca^{2+} ATPase (PMCA), sarco-endoplasmic reticulum Ca^{2+} ATPase (SERCA), and $Na+/Ca^{2+}$ exchanger (NCX). Metabotropic receptor activation leads to inositol-1,4,5-trisphosphate (InsP3) production, activating InsP3 receptors (InsP3Rs) on endomembranes, inducing ER Ca^{2+} release. Store-operated Ca^{2+} entry (SOCE) occurs upon ER depletion. In regions devoid of ER, Ca^{2+} signals are generated through various channels and receptors. Mitochondria contribute to cytosolic Ca^{2+} signals. Adapted from (Lim et al., 2021).

The main intracellular Ca^{2+} store is the ER, which is present in the soma and large astrocytic processes. Intracellular Ca^{2+} release channels in the ER include inositol triphosphate receptors (InsP3R), been InsP3R2 the predominant subtype in the forebrain. InsP3R are the main responsible of Ca^{2+} release from internal stores associated to metabotropic G-protein-coupled receptor (GPCR) signaling, which include $GABA_B$ receptors, glutamatergic mGluR3/5 receptors and P2Y purinergic receptors, among others. The Ca^{2+} content of the ER is constantly monitored by stromal interacting

molecule (STIM), which is activated upon ER Ca^{2+} store depletion, with subsequent activation of ORAI and TRPC1/3 channels in the plasma membrane, forming the store operated calcium entry (SOCE) system. TRPC1/3 channels have been identified as the primary pathway for Ca^{2+} release from intracellular stores in astrocytes, forming integral part of SOCE system (Belkacemi et al., 2017; Lim et al., 2021).

Mitochondria is not an intracellular store per se but acts as a Ca^{2+} sink, buffering large Ca^{2+} loads and preventing cells from Ca^{2+} overload. Ca^{2+} is moved across mitochondrial membrane by Ca^{2+} uniporter (mCU) according to the electrochemical gradient, which is dependent on mitochondrial inner membrane potential. Mitochondria may also release Ca^{2+} trough flickering of permeability transition pore (mPTP) or by mitochondrial Na^{+}/Ca^{2+} exchanger (NCX). Moreover, TRPC1 channels are also permeable for Na^{+} and their colocalization with NCX makes them good coordinator candidates for Na^{+} and Ca^{2+} signaling. Finally, elevations of $[Ca^{2+}]_m$ accelerates TCA cycle, coupling ATP generation with the metabolic demand triggered by Ca^{2+} activity (Lim et al., 2021).

1.3. Mechanical and Biomaterial-based strategies for brain regeneration

As aforementioned, only under specific extrinsic circumstances do certain astrocytes have the capability to dedifferentiate and adopt NSC functional properties. This raised the idea that by modulating such factors, it will be possible to enhance the endogenous brain regenerative capacity. Setting the path for future therapies for neurodegenerative diseases or acute brain insults, such as ischemia or traumatic brain injury (TBI). On this basis, many experimental approaches try to mimic the physiological niche to elucidate the mechanisms that regulate this process.

Ongoing evidence indicate that mechanotransduction significantly influences the differentiation and fate of NSC, progenitor cells, neurons, and glial cells (Lourenço & Grãos, 2016; Niari et al., 2022; Rouleau et al., 2023). Recent *in vitro* investigations reveal that substrate stiffness, surface properties or applied shear flow, affect neurons, astrocytes, and oligodendrocytes behavior and morphology (Lourenço & Grãos, 2016; Niari et al., 2022; Rocha et al., 2015). Notably, sustained mechanical strain rates of 10-15% inhibit OPC proliferation and promote oligodendrocyte differentiation, accompanied by changes in nuclear shape, chromatin organization, and increased histone deacetylation (Jagielska et al., 2017). The existence of stiff gradients that influence the biological functions of OPCs in terms of proliferation or maturation, aligns with the intricate meshwork typical of the brain's structural complexity. This suggests a diverse

spectrum of mechanical forces at play (Carvalho et al., 2022). In astrocytes, its adaptation to different stiffness induces significant behavioral and morphological changes, adopting spread and complex morphologies on stiff substrates, and star-like morphologies on soft substrates (Moshayedi et al., 2010; Rocha et al., 2015). Particularly, astrocytes cultured on soft substrates stiffened the hydrogel after 24h, correlated with an increase in collagen and chondroitin sulfate proteoglycans (CSPG) production, considered hallmarks of astrocyte reactivity. In 3D hydrogel constructs, these changes are mediated through Rho/ROCK signaling pathway. The inhibition of *RhoA* expression or ECM degradation with pharmacological treatments significantly reduced *Gfap* expression and recovered the normal astrocyte phenotype (Rocha et al., 2015).

Moving forward in biomaterial-based strategies, changes in substrate surface properties can be subdivided into two main groups: surface topography or surface modifications. Surface topography includes micro-patterned and nano-patterned surfaces, and surface modifications include biological, chemical, and physical modifications. Here we will provide an example regarding micro-patterned surface, for further information, it is nicely reviewed by (Niari et al., 2022) and (Rouleau et al., 2023). Previous work from our group revealed that poly methyl methacrylate (PMMA) sheets with 2µm lines topography (ln2PMMA) mimic the RG niche and induce astrocyte dedifferentiation into RG-like cells (Álvarez, Sena, et al., 2014; Mattotti et al., 2012). Ln2PMMA is a synthetic non-biodegradable, hydrophobic and negatively charged biomaterial that mimics RG surface properties and shape. Mouse cortical astrocytes grown in ln2PMMA express of Pax6, Sox2 and nestin, adopting a functional RG phenotype that supports neuronal migration (Figure I-22). Similar micro-topography imprinted in chitosan, a hydrophilic and positively charged polymer, do not induce RG phenotypes, highlighting that both, biophysical and chemical properties are crucial (Mattotti et al., 2017). In the same line, by applying shear flow in microfluidic 2D culture system, Park and colleges demonstrated that flow shear stress enhances the proliferative capacity of RG (M. G. Park et al., 2017). They proposed that this increment in proliferative capacity might be linked to increased Ca^{2+} entry through MSCs, possibly involving the activation of TRP channels. Moreover, a cell-free 3D scaffold of RG-mimetic lactate-releasing PLA aligned nanofibers implanted into the postnatal mouse brain induce the complete vascularization of the implant and the novo formation of neurovascular niches, sustaining endogenous neurogenesis, astrocitogenesis, oligodendrogenesis and synaptic reconnection with the preserved tissue (Álvarez et al., 2014).

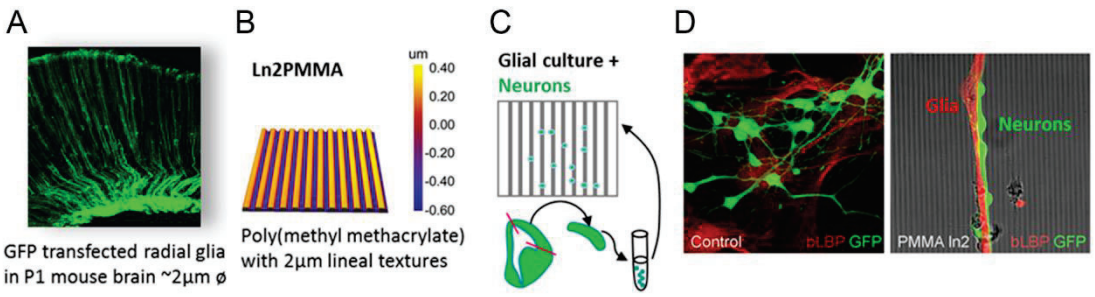


Figure I- 22 **Ln2PMMA mimic the RG niche and induce astrocyte dedifferentiation into RG cells**. (A) Cortical section of mice pups at postnatal day 1 (P1). RG cells transfected with green fluorescence protein (GFP) in neonatal pups. RG fibers diameter is approximately 2µm. Picture courtesy of Dr. JA Ortega. (B) ln2PMMA RG biomimetic substrate fabricated by nano-imprinting lithography (NIL). Micropattern lines are 2µm width and 1µm depth. (C) Coculture strategy of E16 transgenic GFP neurons grown on P0 glial cells. (D) Glial cells stained with BLBP (red) grown on control and ln2PMMA with neurons in green (Mattotti et al., 2012).

Collectively, these studies underscore the critical role of the microstructure of the microenvironment in generating mechanical cues that significantly impact NSC, and in particular RG lineage differentiation (De Belly et al., 2022; Rocha et al., 2022). Also serving as a proof of concept for the feasibility of regenerative strategies based on boosting endogenous astrocyte regenerative capacities.

1.4. The arising of modeling and multiparametric models

As has been seen across this introduction, RG differentiation is governed by a transcriptional continuum modulated by intrinsic and extrinsic factors. And implies multiple changes in morphology, metabolism and physiological signaling. The different cell-types, with different structure, molecular markers expression and metabolic requirements, perform distinctive tasks that are functionally integrated (Márquez-Zacarías et al., 2021). Cellular changes are translated to changes in the microenvironment, which in turn, are also implicated in the differentiation process. Furthermore, employing biomaterial-based strategies to explore differentiation or dedifferentiation processes introduces an additional layer of complexity, making challenging to discern the intricate interactions between these mechanisms. On this basis, the study of cell differentiation linked with mechanotransduction is a good approach to integrate environmental factors, molecular processes, and cell-fate (De Belly et al., 2022).

The first step of modeling differentiation process is to identify the target of the study. Defining the parameters of a cell type remained a subject of debate, and so far, no singular method has emerged that can comprehensively encompass the multimodal

nature of cell phenotypes, thereby establishing a standardized classification criterion (Yuste et al., 2020). Recently, it has been proposed that proper cell-type identification should rely on a probabilistic definition, incorporating data from different approaches, developmental stages, and species (Escartin et al., 2021; Yuste et al., 2020). To this end, the integration of various types of data requires modeling approaches.

Many models can be addressed, and one model is not necessarily better than another, but rather different. Starting by the assumption that modeling is based on establishing a mathematical relationship of the observations, we can distinguish between multiscale modeling, which include ordinary or partial equation-based approaches, and theory-driven machine learning approaches (Alber et al., 2019). Here, we will focus on multiscale modeling, for further detail see Alber et al 2019, which provides an interesting integrative approach between multiscale modeling and machine learning approaches (Alber et al., 2019; Almudevar et al., 2020) .

Mechanical models, based on mechanical properties, can be divided into schematic models, continuum models, and molecular dynamics (for further detail (Hobson & Stephens, 2020; Marinval & Chew, 2021). Deep learning and machine learning models are based on image data and high-throughput processing (Almudevar et al., 2020; Heckenbach et al., 2022a). Probabilistic models can be constructed using Bayesian estimation or Maximum Likelihood estimation (Almudevar et al., 2020; Sero & Bakal, 2017)). Finally, single-cell models can fall into two categories: models linking transcriptomics with electrophysiology, and models linking morphology with electrophysiology (Nandi et al., 2022).

The cell nucleus stands out among all the characteristics suitable for modeling, as it is applicable across all the aforementioned modeling methods. This organelle serves not only as the hub for transcriptional activity and DNA replication but also, as previously outlined, have specific mechanical properties. These properties play a crucial role during mechanotransduction processes to safeguard the genome (De Belly et al., 2022; Hobson & Stephens, 2020). An overview of nucleus-cell surface mechanic interactions is shown in Figure I-23.

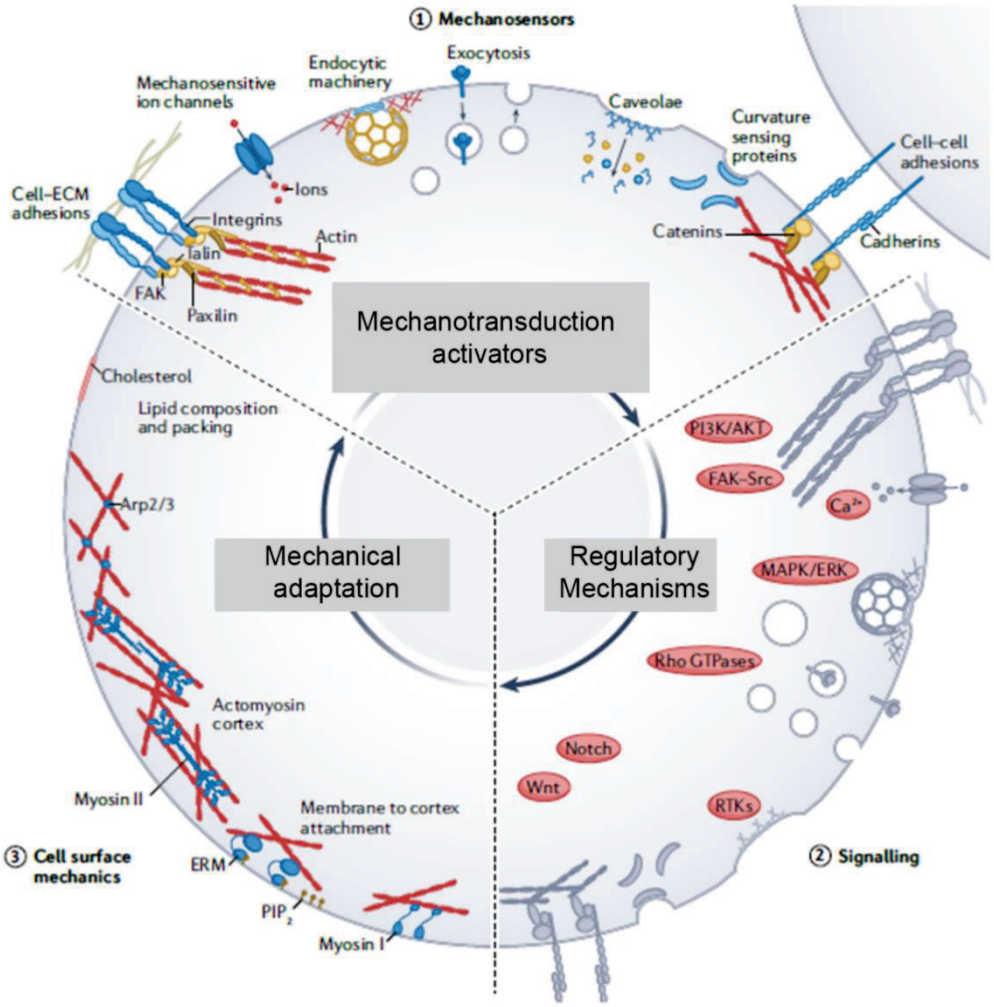


Figure I- 23 **From the outside to the cell function**. Schematic overview of mechanotransduction pipeline. (1) Mechanosensing mechanism by which the mechanical signal is sensed. (2) Different signaling pathways respond to the active mechanosensor. (3) Effect on cell function, controlling and remodeling protein production, and adapting cell structure to the new environmental constraints. Adapted from (De Belly et al., 2022).

On this basis, to characterize nuclear morphology of a specific cell population requires imaging assays, so first is mandatory to identify the cell population of interest. As aforementioned, there is not a unique and universal molecular marker. However, there are several powerful single-cell image assays that reasonably solved this challenge, although the most widely used method is still the combination of molecular markers (for further details of proposed methods see (Mattiazzi Usaj et al., 2021a). Technological advances permit to move from manual cell counts to rapidly process thousands of images, that can also include spatially and temporally associated data. The combination of data collection for individual cells with automated image processing, ends on high-throughput image screening (HSC) (Mattiazzi Usaj et al., 2021a). The automation of image processing necessitates a precise delineation of nuclei contours to ensure the

accurate identification of individual nuclei for subsequent analysis. Commonly accepted and, consequently, widely utilized are DNA-binding fluorophores like DAPI or Hoechst33342, which exhibit heightened fluorescence upon binding to DNA (Boutorine et al., 2013).

Once nuclei object is well defined, the automatization of image segmentation processes will provide quantitative parameters associated to nuclei morphology, called nuclear descriptors. Important to mention that the proper segmentation relay on nuclei object identification, therefore, if nuclei identification is not robust, it will drive to misleading results (Janssen et al., 2022). Nuclear descriptors fall into two categories, nuclear size, and nuclear shape. Nuclear size includes nuclear area, which is used to determine distinct nuclear shape descriptors. These are also subdivided into three subcategories: nuclear contour ratio (or nuclear circularity, or form factor), length-to-width ratio, and eccentricity. Note that nuclear area can be mediated by many other factors and that nucleus is a 3D structure, thus, it is recommended to combine nuclear size with shape descriptors. Other descriptors, such as boundary curvature and solidity, elliptic Fourier transform and nuclear symmetry are nicely described in (Janssen et al., 2022).

Once nuclear morphology is well described and defined, different approaches can be performed in order to answer different questions. Recently, nuclear morphology-based models have been proposed to serve as a senescence biomarker, or to unveil new molecular mechanisms of YAP1 nuclear translocation (Heckenbach et al., 2022a; Sero & Bakal, 2017). Also, nuclear morphology acquired from confocal pictures and combined with experimental assays, was used to create a finite element model that matches phenomenological data (Kennedy et al., 2021). In all models, the indispensable and crucial step that provides power to the model is the validation process. In a very recent paper, the combination of cell morphology, physiological data, and transcriptomic data, provides an amazing tool to classify cells more accurately (Nandi et al., 2022).

As a concluding remark, more and more studies emerge with incredible combinations of different data. There is a continuum in the research to provide more stable, robust, and reliable methods to be sure that what we are investigating is reproducible. A recent example is the proposition of two nondimensional parameters capable of characterizing nuclear morphology in dynamic environment, flatness index and isometric scale factor (Balakrishnan et al., 2021). All these studies show the tendency to unify methods, and it has been recently proposed that the combination of multiscale modeling, which provide causality, with machine learning, that provides correlation, could become the key to better understand biological, biomedical, and behavioral systems (Alber et al., 2019).

2. GOALS

RATIONALE

In the embryonic brain, radial glia (RG) are mechanosensitive bipolar cells, spanning the cerebral wall from the ventricular (apical) to the pial (basal) surfaces. RG are the principal neural stem cell (NSC) that sequentially gives rise to different intermediate progenitors, neurons, and glia, serving also as a scaffold for neuronal migration. At the end of corticogenesis, RG directly transforms into astrocytes. The RG lineage differentiation is associated to changes in shape, metabolism, and gene expression, and relies on a combination of cell intrinsic mechanisms and non-cell autonomous factors present in their microenvironment. Indeed, the direction of differentiation can be partially reverted after a lesion, when some astrocytes can de-differentiate into RG-like NSC with neurogenic capacities. Previous work in the group demonstrated that a synthetic micro3D scaffold of poly (methyl methacrylate) (PMMA) with 2µm linear grooves (ln2PMMA), which mimic RG surface properties and scaffolding structure, induces cultured cortical astrocytes to adopt a functional RG phenotype that support neuronal migration. However, the mechanotransduction mechanisms underlying the biomechanical induction of RG phenotypes are still largely unknown.

The main objective of this Doctoral Thesis is the identification of key mechanotransduction mechanisms in the RG embryonic niche affecting RG lineage progression, by using RG-mimetic biomaterial approach.

Objectives

1. *Implication of mechanosensitive ion channels (MSCs) and Ca2+ signaling in the biomechanical induction of RG.*
2. *Effect of ln2PMMA biomechanical signals in the metabolic signature and mitochondrial dynamics of glial cells.*
3. *Role of nuclear deformation in the biomechanical induction of RG.*
4. *Development of a statistical model based on nuclear morphology for RG identification, and its application to identify relationships between nuclear deformation and different mechanotransduction components.*
5. *Explore the conservation of RG nuclear morphology constraints across species*

3. MATERIALS AND METHODS

3.1. Animals and cell cultures

The Ethical Committee for Animal Experimentation of the University of Barcelona and the Generalitat de Catalunya with order nº: 9656 approved animal housing and all experimental procedures in accordance with Spanish and EU regulations.

Cortical primary cultures

Cortical glial cells were obtained from newborn (P0-P1) Swiss albino mice of both sexes. Briefly, after brain extraction, cerebral cortices were dissected out free of meninges in dissection buffer (PBS + 0.6% of glucose (Sigma), 0.3% bovine serum albumin (BSA) (Sigma)) and digested with 5 ml of trypsin (Life Technologies) with 500µl of DNAse I (Sigma) for 10 minutes at 37º. The tissue was mechanically dissociated in growing medium (GM) Dulbecco's Modified Eagle Medium (DMEM, Biological Industries), 10% normal horse serum (NHS, GIBCO), 1% penicillin-streptomycin (P/S, Biological Industries) and 1% L-glutamine (Biological Industries). After centrifugation and resuspension, passage 0 (Ps0) cells were plated in flasks and grown for 14 days. To remove contaminating microglial and oligodendroglia progenitor cells, cultures were shaken overnight at 37ºC followed by a change of medium the day before starting the experiment (adapted from (Schildge et al., 2013)). For all experiments, adherent Ps0 glial cells were dissociated with trypsin, counted, and plated on the different substrates (borosilicate glass coverslips or Ln2PMMA) at a density of 2-4x10^4 cells/cm^2 in 24 wells, and 2x10^6 cells in P60 culture plates, and grown for 1-14 DIV in Neurobasal™ (NB, Gibco), 3% NHS, 1% P/S and 1% L-glutamine (experimental medium, EM) (Ps1).

Human induced pluripotent stem cells (iPSCs)

Human induced pluripotent stem cells (iPSCs) were cultured in mTeSR medium on Matrigel-coated plates (ThermoFisher BD354277). The cells were fed with fresh mTeSR medium daily (Stem Cell Technologies - 85850). For thawing or splitting, iPSCs were resuspended in DMEM/F-12 media (FISHER SCIENTIFIC, Gibco, 11574546) and cultured in mTeSR supplemented with 10 µM ROCK inhibitor (RI) (Bio-Techne, ToCris, #1254) for 24-48 hours. Basic passaging was performed using EDTA (0.5 mM), while Accutase (Innovative Cell Technologies - AT 104-500) was used for human neural progenitor cells (hNPCs) or iPSC-derived brain organoids generation.

Human neural progenitor cells (hNPCs)

Human neural progenitor cells (hNPCs) were derived from the human iPSC cell line 18a, (Harvard Stem Cell Institute) following the protocol previously described by (Topol et al., 2015). Briefly, iPSCs were dissociated with accutase (Sigma-Aldrich) and replate in matrigel-coated plated and mTESR media with RI, to obtained a 70% confluency by the

following day (day 0), when mTESR was replaced by N2/B27 media [DMEM/F-12 with 1X N-2 (100X, 12013479, Gibco), 1X B27™ (50X, 11530536, Gibco), and 20ng/ml of recombinant human FGF-basic – (PHG0264, Fisher Scientific)] supplemented with dual SMAD inhibitors (0.1M LDN193189 and 10M SB431542) for 6 days. Media was changed on a daily-base, and from day 7, we also incorporated 1 µg/ml laminin (from day 7) to the media. By day 12 neural rosettes were dissociated utilizing STEMdiff™ Neural Rosette Selection Reagent (StemCell Technologies, #05832). The dissociated NPC were resuspended and replated in matrigel-coated plates with NPC media (DMEM/F-12 supplemented with N2 and B27).

Brain Organoids

Brain organoids were generated using induced pluripotent stem cells (iPSCs) derived from the 18a cell line obtained from the Harvard Stem Cell Institute. The protocol for brain organoid generation was adapted from (Lancaster & Knoblich, 2014). iPSCs maintenance involved standard procedures to reach confluence. iPSCs were dissociated using accutase and seeded into a 96-well plate at a confluence of 9000 cells per well to induce the formation of embryonic bodies (EB). The cells were maintained in mTeSR medium supplemented with 1:1000 ROCK inhibitor (RI) from day 0 until they were well-aggregated. After 48h (day 2) the media was changed and only RI was removed if cells were well-aggregated and measured at least 350µm. After removing RI, the EB were maintained in mTeSR until the formation of embryonic bodies (EB) reached a size of 500-600µm, which usually corresponds to day 5. Upon reaching the desired size, EBs were transferred to induction media consisting of DMEM/F-12 supplemented with 1% GlutaMAX™, 1% N-2, 1% penicillin/streptomycin, 1% non-essential amino acids (NEAA), and heparin (H3149-10KU, MERCK) at 1ug/mL (1:10000) and half of the media was changed every 2 days during two cycles (around day 7 and 9). When the neuroepithelium was evident, usually around day 9-10, organoids were embedded in Matrigel. Briefly, 9 µl drop of Matrigel was made on groove-shaped parafilm were rapidly organoids were embedded and incubated for 30 minutes at 37ºC. Organoids were next relocated to a P60 petri dish (10-15 organoids/dish) with 4 ml of differentiation media lacking vitamin A, with no agitation, counting as day 0 of differentiation. After 4 days, vitamin A was added to the differentiation media, and organoids were placed on an orbital shaker to allow better media perfusion in the growing organoid. Half of the media was changed every 3-4 days. The differentiation media consisted of DMEM/F-12 and Neurobasal™ (1:2) supplemented with 1% GlutaMAX™, 1% N-2, 1% penicillin/streptomycin, 1% NEAA, insulin (10µg/mL), and 1:100 2-mercaptoethanol in

DMEM/F-12. Vitamin A was introduced by adding 1% B27 supplement to the media. The culture conditions were maintained at 37ºC throughout the differentiation process.

Fetal tissue samples and human radial glia cell (RGC) cultures

Fetal tissue samples utilized by Ortega and colleagues at Zecevic's laboratory (University of Connecticut Health Center) were sourced from Advanced Bioscience Resources (ABR) and Human Developmental Biology Resource (HDBR), following parental consent and approval from the Ethics Committees of the respective Institutions. The fetal brains used in the study exhibited no signs of disease or abnormalities upon thorough neuropathological examinations. The developmental stage was determined based on gestational weeks after conception and ultrasound findings. The tissue was collected in oxygenated Hank's balanced salt solution (Invitrogen) and transported on ice. After dissection, cortical tissue was mechanically and enzymatically dissociated using 0.025% trypsin-EDTA (Invitrogen) and DNAse I (2 mg/mL, Sigma-Aldrich). The resulting cells were cultured in poly-D-lysine (Sigma-Aldrich) coated flasks containing proliferation medium (PM), consisting of DMEM/F12 (Invitrogen), B27 supplement (Invitrogen), basic fibroblast growth factor (bFGF; 10 ng/mL, Peprotech), epidermal growth factor (EGF; 10 ng/mL, Millipore), and penicillin/streptomycin (Invitrogen). After cell expansion, we utilized MACS® Technology to immunomagnetically sort human RGCs from fetal brain derived cultures with anti-CD15-antibody-coated microbeads (Miltenyi Biotech). Detailed description of the protocol followed is described in previous publications (Ortega et al., 2013, 2017b; Radonjić et al., 2016). Human RGCs were cultured on poly-D-lysine-coated and grown with PM for expansion for 1-3 days. For differentiation purposes, bFGF and EGF was removed from culture media.

For immunocytochemistry of human RGC cultures, we performed fixation with 4% paraformaldehyde for 30 minutes, blocked for 1 h in PBS with 0.1% normal goat serum (Gibco) and 0.1% Triton (Sigma-Aldrich), and incubated cells overnight at 4 °C with the primary antibodies Sox2 (Santa Cruz biotechnologies, sc-17320) and BLBP (Abcam, ab27171) for RGC identification; and GABA (Sigma, WH0026468M1) and TUJ1 (Dako, PRB-435P) for neuron identification. Next day, cells were incubated for 1h with the Alexa488- or Alexa555-conjugated secondary antibodies (1:500, Molecular Probes). Cell nuclei were counterstained with bisbenzimide (Hoechst 33342) (Sigma-Aldrich).

For immunohistochemistry, fetal forebrain blocks were fixed in 4% paraformaldehyde overnight, cryoprotected in PBS + 30% sucrose, and TissueTek OCT blocks were made by freezing in liquid nitrogen for subsequent sectioning 15-µm sections). Sections were blocked in Tris-NaCl-Tween buffer (TNT) [0.1 M, pH7.5 Tris-HCl (Thermo Fisher

Scientific); 0.15 M NaCl (Thermo Fisher Scientific); and 0.05% Tween] with 0.5% blocking reagent (Roche) and incubated overnight at 4 °C with primary antibodies. Next day, sections were incubated with Alexa555 or Alexa 488 (Molecular Probes)-conjugated secondary antibodies and then briefly with bisbenzimide (Sigma-Aldrich) for nuclear counterstaining.

3.2. PMMA micropatterning, characterization and sterilization

Goodfellow Ltd. (UK) supplied PMMA sheets (125 µm thick). The Nanolithography Laboratory of the Institute of Microelectronics of Barcelona (IMB) - National Center of Microelectronics (CNM) CSIC prepared Ln2PMMA substrates as a service. Micropatterning consist in linear grooves of 1µm deep/tall and 2µm wide, introduced by nano-imprinting lithography (NIL) and characterized as previously described (Mills et al., 2007; Mattotti et al 2012). For cell culture, Ln2PMMA substrates were cut to fit in 60 mm cell culture dishes or 24 multi-well culture plates, sonicated for 10 minutes in sterile water, sterilized in 70% ethanol for 15-20 min, rinsed with sterile water for 20 min, left dry and then used uncoated. We used borosilicate glass cover slips as control substrates, since there were no major differences in cell morphology and expression of differentiation markers between no patterned PMMA, glass and culture plastic (Mattotti et al 2012).

3.3. Immunofluorescence

For immunofluorescence, cells were fixed in 4% PFA in 0,1M phosphate buffer (pH of 7.2) for 20'. Then, samples were transferred to a new multi-well plate, washed with PBS, 3 times for 5', and blocked for 2h using phosphate buffered saline (PBS) with 3% normal serum (horse and/or goat, Gibco), 0.05% Triton (Sigma-Aldrich), and 0.2M glycine. Then, samples were washed 3 times with PBST (PBS + 0.05% triton) and incubated with primary antibodies overnight at 4ºC with incubation buffer (PBST + 1% normal serum) (listed in Table 1). The next day, samples were washed with PBST (5' x4) and incubated for 2h at room temperature in their appropriate anti-mouse, anti-rabbit or anti-goat Alexa488, Alexa555, or Alexa 649-conjugated secondary antibody (1:1000, Life Technologies). Then, samples were washed with PBST x2 and incubated 15' with Hoechst 33342 (1 µl/mL, life technologies, 1:20000) in PBS, to counterstain cell nuclei. Lastly, samples were washed with PBS, 5' x2, and mounted with in-house Mowiol preparation (Calbiochem, standard protocol). Antibodies used to characterize neural populations are shown in Table M-1, and those used in sections 4.1, 4.2 and 4.3 are shown in Table M-2.

Table M- 1 Antibodies used to characterize neural populations.

Primary antibody	Dilution	Reference	Molecule and Cell type marker

Rabbit anti glial fibrillary acidic protein (GFAP)	1:3000	DakoCytomation - Z0334	Intermediate filament, mature astrocyte marker
Rabbit anti NG2	1:600	Millipore - AB5320	Proteoglycan, OPC marker
Rabbit anti Pax6	1:500	Abcam - ab195045	Transcription factor, RG marker
Mouse anti Pax6	1: 500	Santa Cruz - sc-81649	Transcription factor, RG marker
Rabbit anti Sox2	1:3000	Abcam - ab97959	Transcription factor, general stem cell marker
Rabbit anti GSX2	1:500	Thermofisher - 15504202	Transcription factor, Tripotential intermediate progenitor
Mouse anti Nestin	1:3500	BD Pharmigen - 556309	Intermediate filament, RG / immature astrocyte marker

Table M- 2 Antibodies used in section 4.1, 4.2 and 4.3.

Primary antibody	**Dilution**	**Reference**	**Subcellular location and function**
Rabbit anti Ki67	1:500	Abcam – ab15580	No-histone protein, cell cycle marker.
Rabbit anti PH3	1:500	Millipore	Histone protein, mitosis marker.
Mouse anti Lamin A/C	1:3000	Thermofisher -	Ubiquitous, nuclear lamina
Rabbit anti Lamin B1	1:3000	Abcam - ab16048	Ubiquitous, nuclear lamina
Rabbit anti YAP/TAZ	1:1000	Cell Signaling - 8418	Transcription factor, ubiquitous, transcription factor
Rabbit anti β-Catenin	1:3000	Abgent – AX10009	Key downstream component (protein) of the canonical Wnt signaling pathway.
Rabbit anti Cleaved Caspase 3 (asp175)	1:500	Cell Signaling – #9664	Caspase-3 (CPP-32, Apopain, Yama, SCA-1) is a critical executioner of apoptosis, as it is either partially or totally responsible for the proteolytic cleavage of many key proteins, such as the nuclear enzyme poly (ADP-ribose) polymerase (PARP)

3.4. Western Blot

For western blot, total protein extracts were obtained from newborn mice cortical glial cultures. We directly added lysis buffer to the plates, scrapped the cells, homogenized with a sonicator and then quantified using the BCA protein assay kit (Thermo Scientific™-Pierce™, #23225). The lysis buffer used contains 100 mM NaCl, 100 mM Tris-HCl pH

7.5, 1%NP4O, 1% Triton X-100, 0.1% SDS, 1mM PMSF and proteases and phosphatases inhibitors. Samples were diluted in water with 1x Laemli Buffer (10% SDS, 25% β-mercaptoethanol, 50% Glicerol, 250mM Tris-HCl, 1 mg/mL Bromophenol Blue), to a final concentration of 1-2µg/µL. We heat the sample at 37ºC for 30 minutes with a posterior 5'' spin for condensation and loaded 14-20µg of protein in the gels. Proteins were separated by SDS-polyacrylamide gel electrophoresis (SDS-PAGE), choosing acrylamide percentage depending on protein molecular weights (7%-15%), and transferred to a nitrocellulose membrane (Bio-Rad). The membranes were stained with ponceau, rinsed with TBST buffer (150 mM NaCl, 10 mM Tris-HCl, 0.1% Tween-20) and blocked for 1h with non-fat milk or 5% BSA, for detection of phosphorylated proteins. Primary antibodies were incubated with slow agitation overnight at 4ºC in TBST+5% BSA. Primary antibodies used and their working concentrations are shown in Table M-3. The next day membranes were washed and incubated 1 hour with the corresponding HRP secondary antibodies (1:5000, Invitrogen) in TBST+5% non-fat milk or 5% BSA. Protein signals were detected by the ECL chemiluminescent system (Amersham, GE Healthcare, Buckinghamshire, UK). Densitometry analyses were performed with ImageJ Software (National Institutes of Health, USA) and standardized to actin, α-tubulin, GAPDH or vinculin.

Table M- 3 Antibodies used in section 4.1 and 4.2.

Mechanosensing Cation Channels			
Primary antibody	**Dilution**	**Reference**	**Channel and protein type**
Rabbit anti TRPA1 (extracellular)	1:200	#ACC-037	Transient receptor potential cation channel subfamily member 1. Ankyrin-like with transmembrane domains protein 1.
Rabbit anti TRPA1	1:1000	Abcam – ab62053	
Rabbit anti TRPC1	1:200	Alomone - #ACC-010	Short transient receptor potential channel 1, Transient receptor protein 1, TRP1
Rabbit anti TRPC1	1:1000	Abcam – ab192031	
Rabbit anti TRPC6	1:200	#ACC-017	Short transient receptor potential channel 6, Transient receptor protein 6, TRP6
Rabbit anti TRPP1 (PKD2)	1:200	Alomone - #ACC-052	Polycystin-2, Polycystic kidney disease 2 protein, PC2
Rabbit anti TRPV4	1:200	Alomone - #ACC-034	Transient receptor channel vanilloid, OTRPC4, VRL-2, VR-OAC, TRP12

Rabbit anti ASIC1	1:200	Alomone - #ASC-014	Acid-sensing ion channel 1, Amiloride-sensitive brain sodium channel, BNaC2, ACCN2
Goat anti ASIC1	1:1000	Abcam – ab205387	
Rabbit anti ASCI2a	1:200	Alomone - #ASC-012	ACCN1, Acid-sensing ion channel 2, Brain sodium channel 1, BNaC1, BNC1, Amiloride-sensitive cation channel neuronal 1, Mammalian degenerin homolog, MDEG
Rabbit anti ASIC3	1:200	Alomone - #ASC-018	Acid-sensing ion channel 3, Amiloride-sensitive cation channel 3, ACCN3, DRASIC
Rabbit anti K_{2P}2.1 (TREK-1)	1:200	Alomone - #APC-047	Potassium channel subfamily K member 2, Outward rectifying potassium channel protein TREK-1, Twik-related K^+ channel 1, K_{2P}2.1, TPKC1
Rabbit anti K_{2P}4.1 (TRAAK)	1:200	Alomone - #APC-108	Potassium channel subfamily K member 4, K2P4.1, TWIK-related arachidonic acid-stimulated K^+ channel protein, Two pore K^+ channel KT4.1
Rabbit anti K_{2P}10.1 (TREK-2)	1:200	Alomone - #APC-055	Potassium channel subfamily K member 10, K_{2P}10.1, TWIK-related K^+ channel 2
Rabbit anti K_{2P}18.1 (TRESK extracellular)	1:200	Alomone - #APC-122	Potassium channel subfamily K member 18, TWIK-related spinal cord K^+ channel, K_{2P}18.1
Rabbit anti K_V7.4	1:200	Alomone - #APC-164	K_V7.4, Potassium voltage-gated channel subfamily KQT member 4, KQT-like 4, KvLQT4, DFNA2
Rabbit anti ENaCα (extracellular)	1:200	Alomone - #ASC-030	Amiloride-sensitive sodium channel subunit alpha, Alpha-NaCH, Epithelial sodium channel α subunit, Alpha-ENaC, Nonvoltage-gated sodium channel 1 subunit alpha, SCNEA
Rabbit anti ENaCβ (exctracellular)	1:200	Alomone - #ASC-019	Amiloride-sensitive sodium channel subunit beta, Beta-NaCH, Epithelial sodium channel β subunit, Beta-ENaC, Nonvoltage-gated sodium channel 1 subunit beta, SCNEB
Rabbit anti ENaCγ (extracellular)	1:200	Alomone - #ASC-011	Amiloride-sensitive sodium channel subunit gamma, Epithelial sodium channel γ subunit, Gamma-ENaC, Gamma-NaCH, Nonvoltage-gated sodium channel 1 subunit gamma, SCNEG

Rabbit anti Connexin 43 (Cx43)	1:200	Alomone - #ACC-201	CX43, Gap junction α1 protein, GJA1, GJAL, Gap junction 43 kDa heart protein
Rabbit anti TRPV1	1:1000	Abgent – AP13988a	Capsaicin receptor; Transient receptor potential cation channel subfamily V member 1.
METABOLISM ANTIBODIES			
General Metabolism			
Primary antibody	**Dilution**	**Reference**	**Structure and family**
Rabbit anti SIRT1	1:1000	Upstate®, Sigma-Aldrich, 07-131	Belongs to the sirtuin family. Class I subfamily. Contains 1 deacetylase sirtuin-type domain.
Rabbit anti pPDH (PhosphoDetect PDH-E1α (Ser293))	1:1000	Calbiochem – AP1062	Synthetic phosphopeptide corresponding to amino acids surrounding the Ser 293 phosphorylation site of human pyruvate deshydrogenase-E1α
Rabbit anti PCK2	1:1000	Abcam – ab70359	Belongs to the phosphoenolpyruvate carboxykinase [GTP] family.
Rabbit anti PFKFB3	1:1000	In-house	See (Riera et al., 2002).
Rabbit anti GPX	1:750	Abcam - ab108427	Belongs to the glutathione peroxidase family.
Rabbit anti MnSOD	1:10000	Enzo - ADI-SOD-11	Manganese superoxide dismutase
Rabbit anti VDAC	1:1000	Cell Signaling - #4866	Voltage-dependent anion channel (VDAC)
Mitochondrial Markers			
Primary antibody	**Dilution**	**Reference**	**Mitochondrial function**
Rabbit anti MFN2	1:750	Abcam - ab124773	Mitofusin 2. Essential transmembrane GTPase, which mediates mitochondrial fusion.
Mouse anti OPA1	1:2000	BD-612607	Optic atrophy type 1. Dynamin-related GTPase required for mitochondrial fusion and regulation of apoptosis.
Rabbit anti DRP1	1:500	Abcam - ab184247	Belongs to the dynamin family. Functions in mitochondrial and peroxisomal division
Rabbit anti FIS1	1:750	Santa Cruz - sc-376469	Fis1 localizes to the outer mitochondrial membrane and participates in mitochondrial fission.
LOADING CONTROLS			
Primary antibody	**Dilution**	**Reference**	Experimental Function
Rabbit α-tubulin	1:15000	Abcam – ab4074	Protein load control
Rabbit anti actin	1:2000	Santa Cruz – sc-8432	Protein load control

Mouse anti vinculin	1:750	Santa Cruz – sc-59803	Protein load control
Mouse anti GAPDH	1: 500	Abgent AM1020b	Protein load control

3.5. Lactate assays

The L-lactate concentration release in culture media was assessed through an enzymatic reaction involving the oxidation of L-lactate to pyruvate by lactate dehydrogenase (5 mg of the enzyme (Roche)/mL, 550 U/mg) in the presence of NAD (Sigma-Aldrich, St. Louis, MO). In this assay, the quantity of NADH generated correlates with the L-lactate levels in the samples, and D-lactate is not detectable using this enzymatic system. We performed four different experiments to set up conditions related to acquisition method (fluorescence or absorbance), sensitivity during standardization (determination of optimal concentration), and normalization method (protein quantification or number of cells) before the definitive attempt. We extracted medium from eight different samples from 24 multi-well plates. Medium samples were diluted 1:20 with a reaction mix containing 0.3M hydrazine sulfate (Merck, USA), 0.87M glycine (AppliChem, USA), pH 9.5; 2.5M NAD+ (Sigma-Aldrich), and 0.19M EDTA (Merck). Lactate dehydrogenase was introduced at a final concentration of 6.9 U/ml. The NADH concentration was determined using the Fluostar Optima BMG Labtech system, measuring absorbance (340 nm) at 0 and 20 minutes after the initiation of the reaction. The reaction endpoint was set at 20 minutes, and the corresponding values were utilized in the calculations. Standardization was achieved using various concentrations of sodium L-lactate (0, 0.5, 1.25, 2.5, 5, 10, 15 and 20) (Sigma-Aldrich). Total lactate concentration was normalized by the total number of cells, calculated from nuclei counterstained with Hoechst 33342.

3.6. Image processing

Mitochondrial morphology characterization

Mitochondrial morphology was analyzed from confocal pictures (Zeiss LSM880 confocal microscope, and Plan-Apochromat 40x/1.3 Oil DIC UV-IR M27 objective) of samples in vivo stained with MitoTracker™ CMXRos and immunostained with specific neural markers. For each sample, 20-37 z-stacks (z-scaling pixel of 0.36µm) were acquired from different sample zones, fitting as many cells as possible within the focal plane. Cut cells and cells in the borders were discarded. Then, we applied nuclei segmentation algorithm and correlated each cell with its specific neural markers expression (see cell nuclei segmentation section). Mitochondrial morphology parametrization of identified cells was addressed by using open-source plugin Mitochondria Analyzer for FIJI/ImageJ (Chaudhry et al., 2020). We performed 3D mitochondrial segmentations based on

fluorescence signal of MitoTracker™ CMXRos probes. First, we established a threshold by using the tool of Threshold Optimization. We randomly selected two different cells from control and ln2PMMA substrates to establish a common threshold (block size of 1,25, C-value of 5, scale max slope through stack and Gamma 0.9). Cells were analyzed individually and delimited by Fiji's freehand tool. We obtained results per cell (a single raw with mean and average values from per mitochondria data) and per mitochondria (the tool generates a CSV file per cell). Among descriptors, we focused on total mitochondria, total volume, sphericity, branches per mitochondria (connectivity), mean of total branches length (total length/total branches), and mitochondrial intensity per volume. This last descriptor was obtained from each CVS file, by calculating the sum of all mitochondrial intensity and divided by total mitochondrial volume (per cell). We presented differences using per cell basis data.

Cell nuclei segmentation

For image acquisition, we used an LSM 880 spectral confocal microscope (Carl Zeiss, Germany) and Plan-Apochromat 40x/1.3 Oil DIC UV-IR M27 objective. In a reduced number of experimental conditions, we also used 25x and 63x objectives. Images were mounted with the ZEN (blue edition) software to obtain projections. We adjusted the number of optical confocal sections depending on the experiment and markers. For each marker, the same settings for acquisition and projection were used for all the experiments. A range of six to nine images from two to four different samples were used for each study. Images were randomly taken at different sample areas but avoiding those of high confluence (middle of the sample). As we have previously described, at areas of high confluence, intercellular interactions overcome mechanical signals from ln2PMMA substrate and cells tend to differentiate into astrocytes, as in control substrate (Alvarez et al., 2014).

For cellular and nuclear parameters extraction from each image, we used a custom-made high-throughput-like image analysis algorithm in Matlab developed by Dr. Carlos Borau (University of Zaragoza). The algorithm and segmentation outcomes were developed during my final master thesis (José Pablo Soriano Esqué Director Soledad Alcántara Horrillo José Manuel García Aznar, 2017). This app allowed us to simultaneous correlate lineage markers with nuclei morphology, at the single-cell level. Nuclei segmentation was performed in z-stack orthogonal maximum projections (cell-lineage assignments) or from average projection (intensity fluorescence assays), as we found no significant differences between both types of analysis (Fig. M-1).

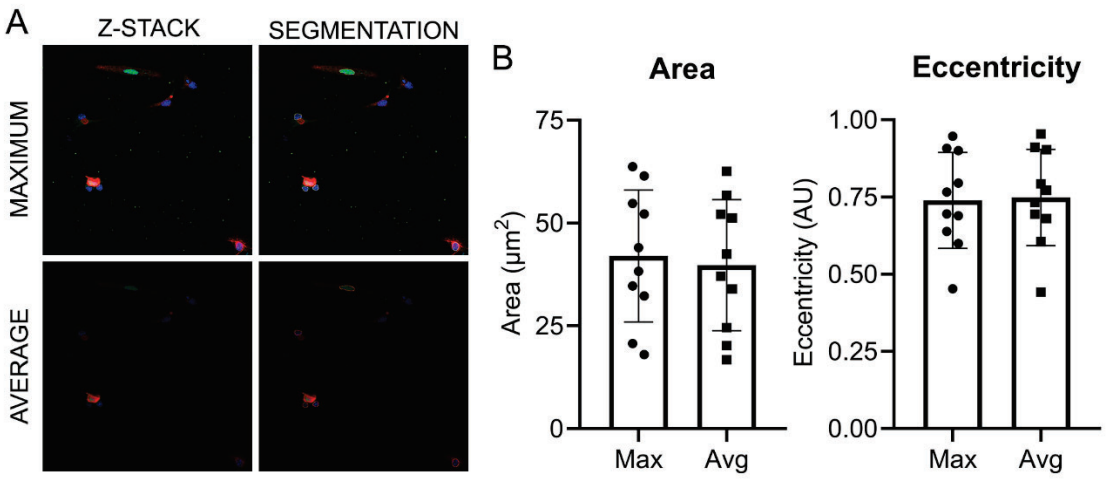


Figure M- 1 **Nuclei segmentation results from maximum and average projections were similar**. (A) Immunofluorescence images with maximum and average z-stack projections and their corresponding nuclei segmentation. (B) Nuclear area and eccentricity bar plots of segmented nuclei from maximum and average projections. Points represent individual nucleus. We used the Unpaired T-test for statistical analysis: area, p=0.76; eccentricity, p=0.89.

The developed tools allowed for semiautomatic processing of immunofluorescence images through the application of specific functions for each wavelength channel. These functions implement advanced segmentation methods combining simple thresholding with more refined techniques such as a modified version of the top-hat algorithm (Bai et al., 2008). Segmented pixels in the blue channel (Hoechst staining) were used for the extraction of the nucleus perimeter, area, and eccentricity. Eccentricity (*E*) is a non-dimensional measure that indicates the range of nuclear shape from circular (*E*=0) to a linear segment (*E*=1) shape. Technically, the program calculates the eccentricity of the ellipse that has the same second moments as the nuclear region, returned as a scalar, which is the ratio of the distance between the foci of the ellipse and the length of its major axis.

We also explored which nuclear staining allowed us detecting as many nuclei as possible with the default settings of the program (as tweaking the parameters is a time-consuming process). Many nuclear morphology studies use lamin B1, a nuclear intermediate filament, to extract nuclear morphologies (van Tienen et al., 2019), but in immunostaining assays it is usual to counterstain with Hoechst to label nuclei. Hence, we analyzed which nuclear staining was better for segmentation (Fig. M-2A). We segmented 16% more nuclei when using Hoechst staining than when using lamin B1 in control, and 18% more in ln2PMMA substrate, taking as reference the 50% (Fig. M-2B). For the same nucleus, we found no differences in area and eccentricity obtained from both nuclear labels (Fig. M-2C). Thus, we always used Hoechst for nuclear segmentation.

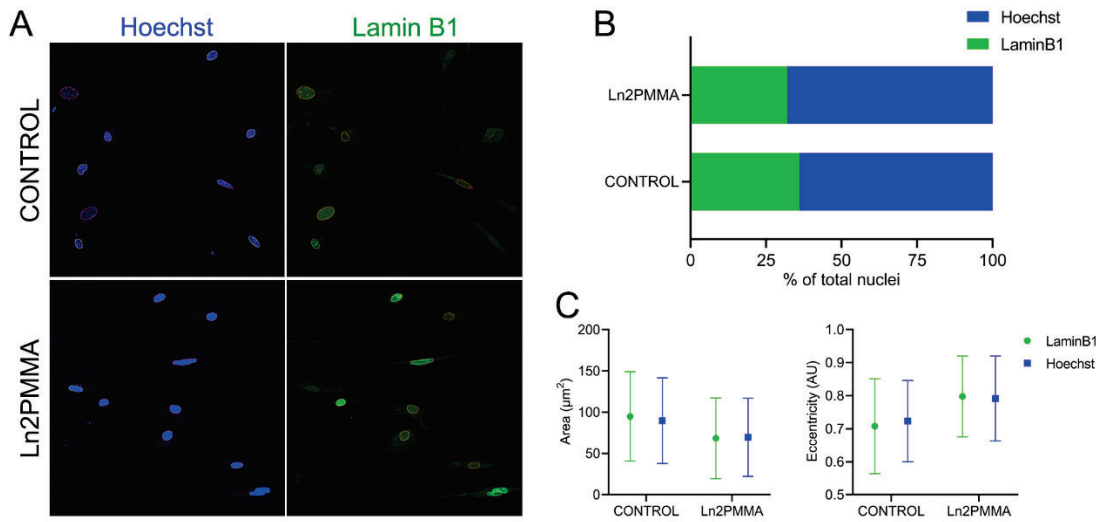


Figure M- 2 **Nuclei counterstained with Hoechst is better for nuclei segmentation**. (A) Immunostaining images from glial cultures cultured 3DIV in control and ln2PMMA substrates. Nuclei immunolabeled with lamin B1 (green) and counterstained with Hoechst (blue). (B) Relative percentage of segmented nuclei. In control total nuclei n=88: segmentation with Hoechst n=61, with lamin B1 n=47. In ln2PMMA total nuclei n=22: segmentation with Hoechst n=17; with lamin B1 n=13. (C) Graphs showing nuclear area and eccentricity (mean± SD) obtained from Hoechst and lamin B1 labeled nuclei. Unpaired T-test control area p=0.71, and ln2PMMA area p=0.27; control eccentricity p=0.54, and ln2PMMA eccentricity p=0.89.

Lastly, our app included an optional color correction to enhance visualization, if required, and the option to extract nuclear and perinuclear intensities from the desired channel. When a nucleus is segmented, the algorithm extracts the total intensity within the nuclear region, as well as within the surrounding (perinuclear) region that has the same area as the original nucleus, as proposed by (Elosegui-Artola et al., 2017a) for the analysis of cytosolic to nuclear protein translocation. We used this approach to calculate nuclear and cytoplasmic intensity ratios in transcriptional cofactors analysis (YAP/TAZ and β-catenin) (Fig. M-3A) and nuclear fluorescence intensity of lamin A-C and lamin B1 nuclear proteins (Fig. M-3B). Intensity extraction from two different markers within the same nucleus required specific attention to avoid fluorescence overlap and the use of the same segmentation in both channels.

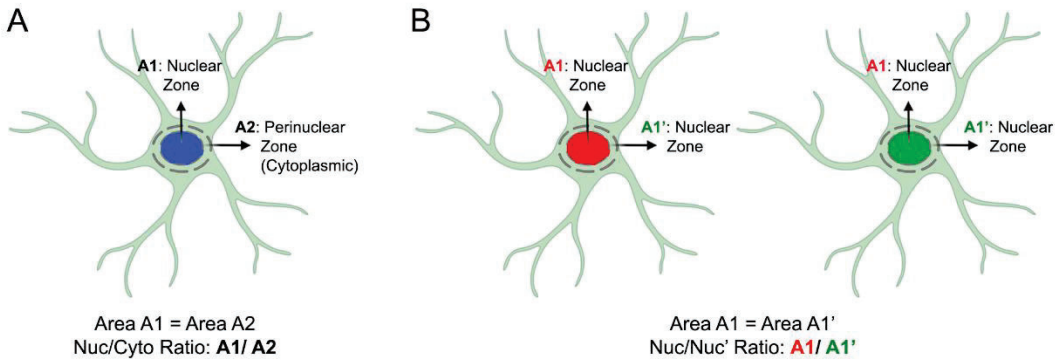


Figure M- 3 **Schematic of nuclear and perinuclear fluorescence intensity extraction.** (A) Nuclear and perinuclear intensity fluorescence can be applied to any channel. (B) Nuclear intensity from two different channels.

In Fig. M-4 we show the nuclei analysis app and examples of the main features used (Markers improvement assignments and Nuc/Cyto fluorescence intensity extraction). Additionally, general nuclei orientation was computed using the methods described in (Movilla et al., 2018), obtaining an alignment index per image ranging from 0 (total random orientation) to 1 (completely aligned structures). Total nuclei per image was also considered to detect correlations between densely packed nuclei and their morphological features. The App included all microscopes from our facilities with their relative objectives to combine data if required (Table M-4).

Table M- 4 Microscope conversions used to scale image segmentation parameters.

	µm/pixel	Zoom
Nikon Eclipse 800	444.84/1360	20x
Zeiss Axiovert 200M	161.4/1024	20x
Zeiss Apotome Axio Imager.M2	354.66/2056	20x
Leica TCS-SL (Confocal)	375/1024	40x
Zeiss LSM 880 (Confocal)	212.55/1024	40x

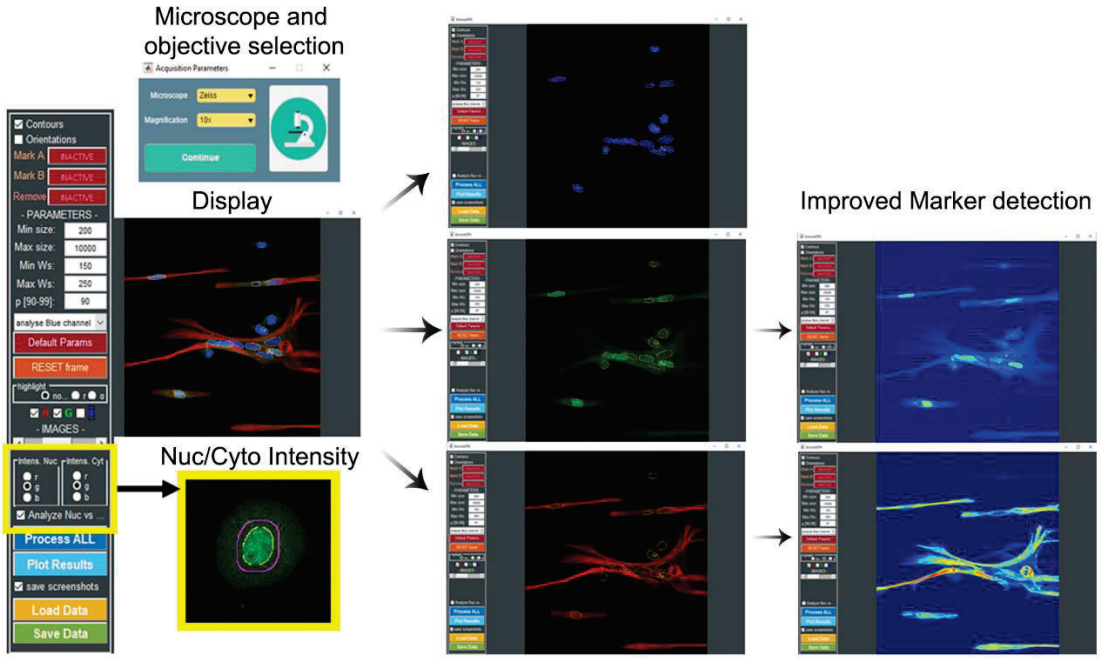


Figure M- 4 **Nuclei segmentation App pipeline**. The left panel includes markers selection (A or B), nuclei segmentation parameters, channel segmentation selection and channel improved visualization. Also include optional nucleus and cytoplasmic intensity fluorescence data extraction (yellow square).

3.7. Logistic regression model construction

A logistic regression model was constructed and estimated to examine the relationship between nuclear morphology parameters and the expression of radial glia (RG) cell markers. The model was built using R (A language and Environment for statistical Computing, R Core Team, Vienna, Austria). Data were obtained from confocal images of primary mouse cortical astrocyte cultures grown for 3DIV in control and ln2PMMA substrates, and immunofluorescence stained with cell-type specific molecular markers, as described above in image processing. Dr. Jesús Asín, of the Statistical Methods Department of the University of Zaragoza, has developed the model and guided me in the parts of this section.

Image Variable definition

For model construction, we used as input the vector of covariates that includes nuclear morphology parameters of area (as a measure of size) and eccentricity (as a measure of shape), the cell density (calculated as total nuclei number/area of the confocal picture) and the type of substrate, control or ln2PMMA.

The dataset used for fitting the model was obtained from 15 different immunofluorescence assays of glial cells grown in control and ln2PMMA, obtaining 3855

nuclei with its nuclear morphology parameters and its cell-type assignment. To normalize the effect of cell density we took 7 to 12 pictures per condition from low, medium, and high confluence zones.

Type and definition of response

We defined a binary response, being RG or Non-RG nuclei, based on the expression of cell-type specific molecular markers.

The cell-type molecular markers are gradually more or less expressed depending on the lineage stage. For that reason, was necessary to combine different markers. To define RG, we based on generalized RG-associated markers (nestin, Sox2, Pax6). So, we defined RG based on the expression of the transcription factor Pax6+, alone or in combination with nestin+/-, GFAP+/- or Sox2+/-, and the combination Sox2+ with nestin+. To define non-RG cells, we used double negative nuclei from assays where Pax6/nestin, Pax6/GFAP, and Sox2/nestin were used, and nuclei from cells that express markers for fate-committed cells, such as NG2+, Gsx2+ or Pax6-/GFAP+. Finally, all nuclei belonging to cells with no conclusive cell-type markers were considered confusing cells. Table M-4 summarizes the cell-type marker combinations used to assign the different categories.

Table M- 5 Summary of cell-type markers used to define RG, Non-RG and confusing cells. Promising combinations were considered as 1 and non-promising combinations as 0 for the binary response. Markers with /-- indicate that were used alone.

Promising N=374	**Non-Promising N=786**	**Confusing N=1295**
Pax6+/Nestin+	Pax6-/Nestin-	Nestin-/Sox2+
Pax6+/Nestin-	Pax6-/GFAP+	Pax6-/Sox2+
Pax6+/Sox2+	Pax6-/Sox2-	Nestin+/--
Pax6+/Sox2-	Nestin-/Sox2-	Sox2+/--
Nestin+/Sox2+	Nestin-/NG2+	GFAP+/--
Pax6+/GFAP+	Nestin+/NG2+	Nestin+/NG2-
Pax6+/GFAP-	Nestin-/GFAP-	Nestin+/GFAP+
Pax6+/--	Nestin-/GFAP+	Nestin+/GFAP-
	Pax6-/GFAP-	Nestin+/Sox2-
	NG2+/--	Nestin+/Pax6-
	Gsx2+/--	

Type of model

To assess the probability of RG based on nuclear morphology parameters, we employed a Generalized Linear Model (GLM), that allowed us to work with non-normal data to establish probabilities associated with the response. The use of non-linear relationships allowed us for more flexibility to accommodate the variables but, at the same time, increase the complexity of the model. The linear prediction is defined in the following equation:

$$P(success) = \frac{\exp(\beta_0 + \boldsymbol{g(Eccentricty,\ Area\ and\ Cell_Density)})}{1 + exp(\beta_0 + \boldsymbol{g(Eccentricty,\ Area\ and\ Cell_Density)})}$$

Due to the nature of our data and the type of response, we used the function logit link to define the relationship between the linear predictor (the weighted sum of predictor values) and the expected value of the response variable, i.e., the probability of RG (1=success) in the conditions due by Eccentricity (E), Area (A) and Cell Density (Cd). The logit link function maps the linear predictor to the odds of success in binomial distributions, as shown in the following equation:

$$logit\big(P(success)\big) \sim \boldsymbol{g(E,\ A\ and\ Cd)} = (\mathrm{poly}(\mathbf{E},\ \mathrm{k_E}) + \mathrm{poly}(\mathbf{A},\ \mathrm{k_A})) * (\mathbf{Material} + \mathbf{Cd})$$

K term represents the polynomial degree, i.e., for $K_E = 3, \mathrm{poly(E, 3)} = \sum_{i=1}^{3} \beta_{Ei} * E^i$ and the symbol * indicates the interaction of the type of substrate and cell density with nuclear morphology parameters. *E* corresponds to Eccentricity, *A* to Area and *Cd* to Cell density.

Selected model

The GLM was constructed based on likelihood maximum estimation. The likelihood function represents the probability of observing the given data as a function of the model's parameters. It measured how well the model explained the observed data. The key principle of this function was to make the observed data as likelihood as possible, ensuring that the model accurately reflected the underlying probability distribution of the data, capturing the complex relationships between the nuclear morphology parameters and the probability of being RG cells. Different models of increased complexity were initially fitted, we selected those with better Akaike Information Criterion (AIC), and the final model included statistically significant effects at 0.05 significance level. Lower AIC values indicate better-fitted models with appropriate complexity. The terms of the selected model are shown in Table M-5.

Table M- 6 Terms that define RG based on nuclear morphology parameters in control and ln2PMMA substrates. Estimated coefficients, standard error of coefficients, z-value, and p-value (Pr(>|z|)) for every term of the model.

Term	Estimate	Std. Error	z value	Pr(>|z|)
(Intercept)	-5,82E+03	7,62E+02	-7.634	0
Ln2PMMA	-9,45E+02	5,66E+02	-1.669	0.095
Area	1,51E+02	2,58E+01	5.829	0
Area^2	-1,05E+00	2,22E-01	-4.755	0
Area^3	1,81E-03	5,49E-04	3.296	0.001
Control * Eccentricity^3	-2,31E+02	8,84E+02	-0.261	0.794
Ln2PMMA * Eccentricity^3	2,57E+03	7,32E+02	3.509	0
Ln2PMMA * Area	-7,33E+00	4,74E+00	-1.546	0.122
Eccentricity^2 * cell density	5,15E+00	2,49E+00	2.068	0.039
Eccentricity^3 * cell density^2	-2,75E-03	1,50E-03	-1.834	0.067
Area * cell density	-1,46E-01	4,13E-02	-3.522	0
Area * cell_density^2	8,80E-05	2,37E-05	3.722	0
Area^2 * cell density	8,91E-04	2,78E-04	3.2	0.001
Area^2 * cell density^2	-6,22E-07	1,84E-07	-3.384	0.001

The presence of terms that depend on substrates meant that this model defined two paths to define RG nuclear morphology, which depended on substrates, one for control (1) and another for ln2MMA (2).

(1) $$\text{logit}(\,\mathrm{P}\big(\mathrm{y}=1\big|(\mathrm{X},\mathrm{Control})\big)=\beta_0+\beta_A\mathrm{A}+\beta_{\mathrm{A}^2}\mathrm{A}^2+\beta_{\mathrm{A}^3}\mathrm{A}^3+\beta_{E^3C}\mathrm{E}^3+\beta_{E^2*Cd}\mathrm{E}^2*\mathrm{Cd}+\beta_{E*Cd^2}\mathrm{E}*\mathrm{Cd}^2+\beta_{A*Cd}\mathrm{A}*\mathrm{Cd}+\beta_{A*Cd^2}\mathrm{A}*\mathrm{Cd}^2+\beta_{A^2*Cd}\mathrm{A}^2*\mathrm{Cd}+\beta_{A^2*Cd^2}\mathrm{A}^2*\mathrm{Cd}^2$$

(2) $$\text{logit}(\,\mathrm{P}\big(\mathrm{y}=1\big|(\mathrm{X},\mathrm{Ln2PMMA})\big)=\beta_0+\beta_{0Ln2}+\beta_A\mathrm{A}+\beta_{\mathrm{A}^2}\mathrm{A}^2+\beta_{\mathrm{A}^3}\mathrm{A}^3+\beta_{E^3Ln2}\mathrm{E}^3+\beta_{ALn2}A+\beta_{E^2*Cd}\mathrm{E}^2*\mathrm{Cd}+\beta_{E*Cd^2}\mathrm{E}*\mathrm{Cd}^2+\beta_{A*Cd}\mathrm{A}*\mathrm{Cd}+\beta_{A*Cd^2}\mathrm{A}*\mathrm{Cd}^2+\beta_{A^2*Cd}\mathrm{A}^2*\mathrm{Cd}+\beta_{A^2*Cd^2}\mathrm{A}^2*\mathrm{Cd}^2$$

The expression *logit (…)* indicated the application of the linear predictor to the associated probability to the response *y=1*, using the variables *X* in control or ln2PMMA. *β* corresponds to estimated coefficients*, A* corresponds to area, *E* to eccentricity and *Cd* to cell density. Specific terms depending on substrate were indicated as C for control and Ln2 for ln2PMMA.

The presence of quadratic and cubic terms reflected the complexity of the reality behind nuclear deformation and the expression of specific molecular markers. The z-value indicated the direction effect on the response, affecting positively when positive and negatively when negative. The impact of the term relied on Pr(>|z|) value, which determined the statistical significance of the term. Note that some terms in Table M-5

have associated p-value over 0.05, but those terms appear in order to distinguish the effect on substrate, in the case of cubic effect of E and A, then they still lightly affected to the response.

In general, as many terms are used to build a model, better will be the approximation. However, the complexity of the terms and their interactions will dramatically increase. The final step consisted in a step-by-step refinement and depuration of the model, reducing its complex terms until the lower AIC was reached.

Table M- 7 Summary of AIC and AUC of the selected model. AIC is general for the model and AUC is sectioned for control and ln2PMMA substrates with lower and upper confidence intervals.

	AIC	AUC	Lower IC	Upper IC
All	1300.325	0.73	0.7	0.76
Control		0.67	0.62	0.71
Ln2		0.77	0.73	0.81

A receiver operating characteristic (ROC) curve is a graphical plot that illustrates the performance of a binary classifier model at varying threshold values, and the area under the curve (AUC) is used to address the classification ability of the model. We obtained a general model AUC of 0.73, and the subsequent AUC's associated to ln2PMMA (0.77) and control (0.67) (Fig. M-5). AIC and AUC's summary are shown in Table M-6, including sensitivity and specificity with usual threshold 0.5.

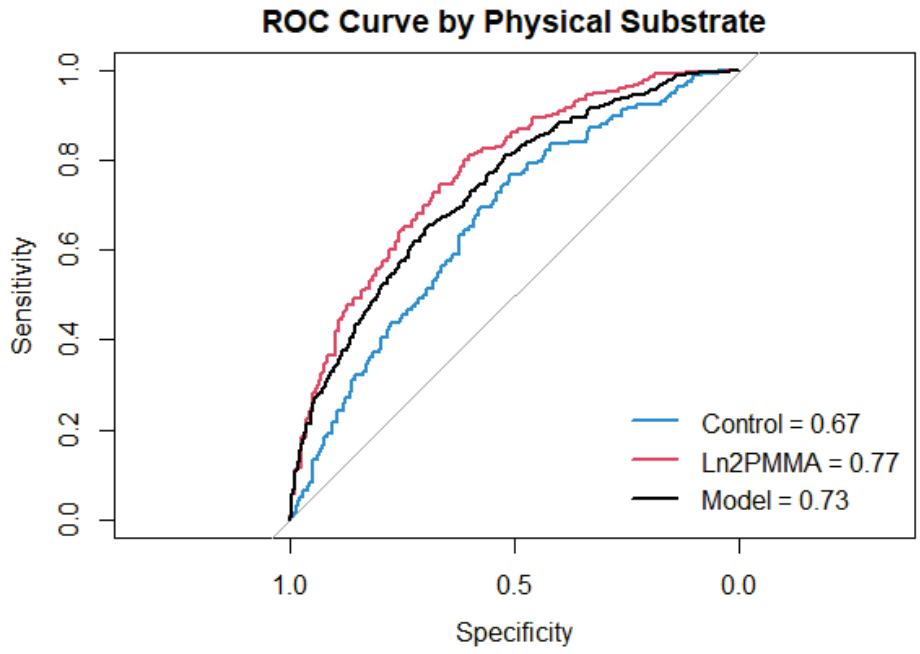


Figure M- 5 **ROC curves of the model**. The model ROC curve is shown in black, Control in blue and ln2PMMA in red. Values represent the AUC.

Describing the equation and model validation

We calculated the odds ratio function of equations (1) and (2) to depict which variables were conditioned in function of substrates. The odds ratio is an association measurement between two conditions, variables, or functions.

$$(3)\ Odds\ ratio = \frac{Odds\ (RGM)}{Odds\ (Control)} = \frac{\exp\left(\beta_{0Ln2}+\beta_{E^3{}_{Ln2}}\mathrm{E}^3+\beta_{ALn2}A\right)}{\exp\left(\beta_{E^3{}_C}\mathrm{E}^3\right)}$$

β corresponds to estimated coefficients, *A* corresponds to area, *E* to eccentricity and subscripts C and Ln2 correspond to substrates.

For an easily exportation and interpretation when applied to data, we calculated the log-odds ratio. By this calculation we clarified two questions. First, we quantified the proportion of change induced by ln2PMMA substrates with respect to control. Second, at log-odds ratio equaled to 0, we determined a threshold at which nuclei deformation was not conditioned by substrates, being considered the frontier of an intrinsic mechanical factor associated to glial nuclei that was required to adopt RG nuclear morphologies. This function was used to nuclear data without their associated probability.

For validation, we used new data from glial cells grown at 3DIV from two different biological samples and two replicates of nuclei immunostained with nestin/GFAP and

Pax6/nestin. We compared the total number of predicted RG with the experimental observation of RG markers. In further results, every time we used vehicle treatments could be considered as additional validations.

Model Application

For model application, the new dataset must fit into the range used for model construction. Figure M-6 provides a visual workflow of model application procedure.

Thus, before model application, it was required to explore the new data to detect extrapolation, in those cases, the dataset, or the extrapolated part of data were excluded. Then, we obtained the associated predictions for each nucleus. Finally, we applied the model in two different ways. The first consisted in calculating the predicted RG percentages by directly applying the model to data, see left bottom panel in Figure M-6. The outcome results were represented in density plots associated to fitted probabilities, ranging from 0 to 1 in the x-axis, and then obtaining AUC's at probability of 1/3 (33%) and 1/2 (50%). The second allowed us to observe which nuclei were within the region above the log-odds ratio equal to 0 (F(0) or RG mechanical factor threshold), defined by the model in function of area and eccentricity. This was pictured as surface plots in function of area (x-axis) and eccentricity (y-axis) representing the log-odds ratio function at different thresholds (F(0), F(-0.1), and F(-0.25)) and the calculation of data proportions above thresholds.

The main scripts are provided in the following link: https://github.com/PepPau/RGM-model-main-scripts.git. These scripts form the foundational code for training, generating, exploring, and applying the RGM model. However, scripts for uploading experimental datasets, variations of the latest script versions, and alternative options for plotting and data visualization are not included.

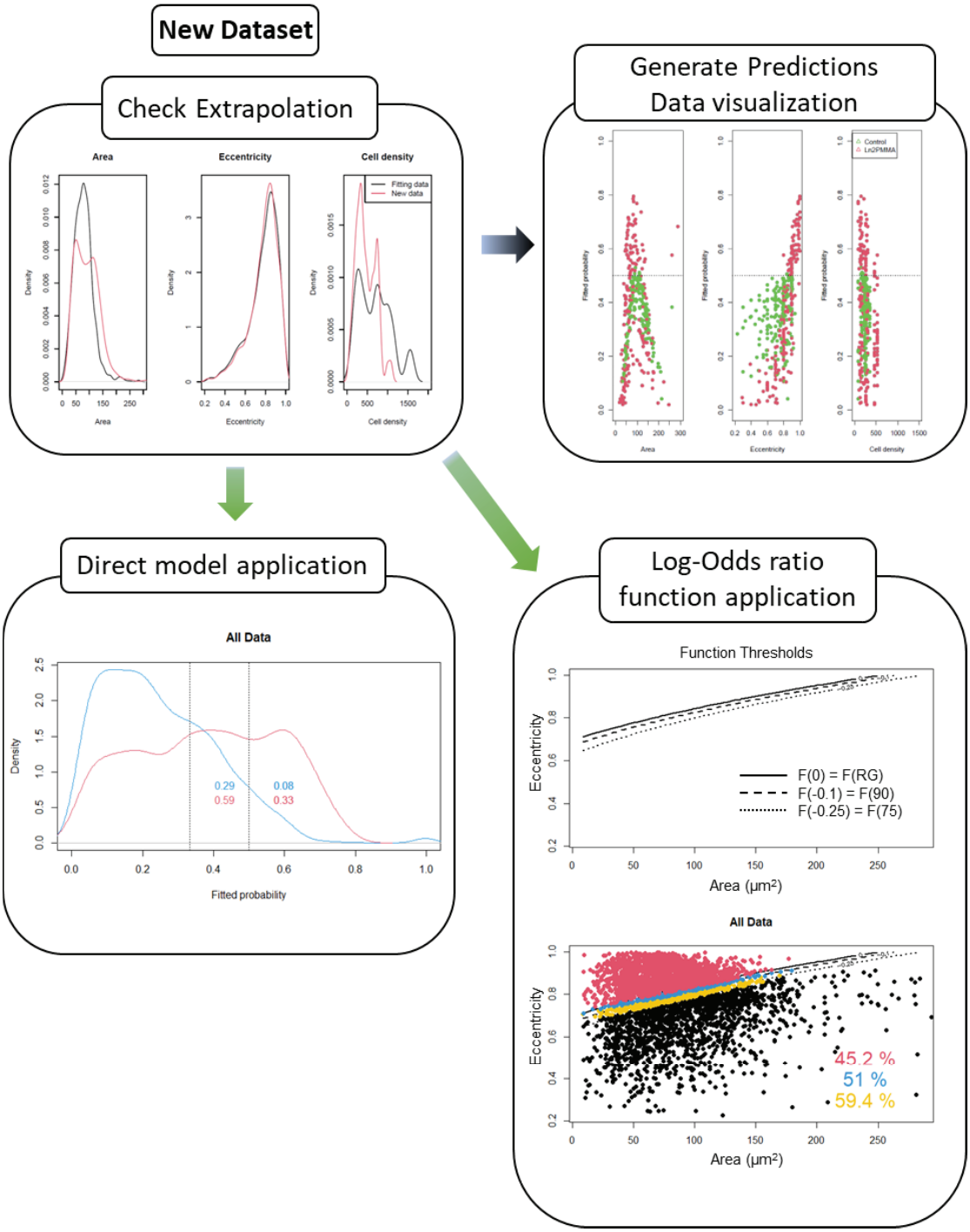


Figure M- 6 **Workflow for the use and application of the RGM model to new datasets**. Check extrapolation plot fitting data (black) and new data (red). The red curves should fit in black x-axis ranges. 1st (black arrow) Generate predictions and visualize predictions in function of variables. 2nd (green arrows) direct model application, and log-odds ratio function application. Both provide associated percentages at different thresholds.

3.8. Publicly available single-cell transcriptomics data analysis

To analyze mRNA expression at different developmental stages, we used mouse cerebral cortex single-cell transcriptomics data from a previous study by Di Bella et al. (Di Bella et al., 2021), deposited on the GEO database with accession number GSE153162. We used SCANPY (Wolf et al., 2018) to apply quality control filters based on the distribution of counts and genes found on each dataset. We discarded all cells with less than 500 UMIs or more than 50000, all those with less than 800 detected genes and those with more than 7000, and all the cells with more than 15% of mitochondrial content. In total we retained 81792 out of the initial 82415 cells. Subsequently, we discarded an additional 2431 cells that had been identified as doublets by the scrublet package (Wolock et al., 2019). To retain only cells from relevant developmental stages for our study, we discarded all the cells from E10, E11 and E12. After this selection, we were left with 67961 cells. We then normalized the data using the normalize_total function from SCANPY with a target of 10000 counts per cell, and then we log-transformed the data. We applied dimensionality reduction keeping the first 10 principal components, clustered the data using the Louvain algorithm for community detection (Levine et al., 2015) (r=0.2) and selected clusters expressing RG-astrocyte lineage markers (Sox2, Pax6, Hes5) and no expression of neuronal (Neurod2, Tubb3, Neurod6, Meg3). We applied again principal component analysis (PCA) on the 14469 selected cells, clustered them on the space of the first 11 principal components and removed those clusters expressing neuronal or oligodendrocyte (Olig1, Olig2, Pdgfra) lineage makers, except for a cluster which expressed both Olig1 and mature astrocyte markers (Aqp4, Slc1a2). After this selection, we retained 9343 that we confidently labeled as RG-astrocyte lineage cells, on which we examined the expression of our proteins of interest.

3.9. Pharmacological treatments

Pharmacological inhibition of Ca^{2+}/Calmodulin-Dependent Protein Kinase II (CaMKII) signaling (KN93 at 5μM) and non-selective mechanosensing cation channels (GsMTx-4 at 1.22μM) was performed for 3h in 3DIV glial cultures grown in control and ln2PMMA substrates without previous serum deprivation. We also treated samples with their respective vehicles: DMSO for KN93 and PBS for GsMTx4. Samples were fixed and prepared for immunocytochemistry assays as described in section 3.3. We used two different experiments and samples were immunostained using different cell type-specific and lamins antibodies. Image processing and nuclei segmentation was performed as detailed in section 3.4. We generated two datasets: (1) astrocyte-RG lineage dataset

(N=6839) and (2) lamins A-C/B1 ratio dataset (N=1759). The number of samples were equilibrated across immunostainings and treatment conditions. The number of cells for dataset (1) were: DMSO, N=1832; KN93, N=1931; PBS, N=1349; and GsMTx5, N=1727. The number of cells for dataset (2) were: DMSO, N=483; KN93, N=506; PBS, N=372; and GsMTx5, N=398.

3.10. Calcium Imaging

For single-cell intracellular calcium recordings, glial cultures samples at 3-4DIV were mounted into a microfluidic chamber (Open Diamond Bath Imaging Chamber for Round Coverslips from Warner Instruments) and loaded with Oregon Green BAPTA-1M (OGB-1 AM, Life Technologies), a calcium-sensitive fluorescent dye, for 30' at 37ºC and 5% CO_2. A working solution of OGB-1 AM (10 µM) was prepared in EM to prevent cell detachment, which occurred when PBS was used. For calcium imaging experiments, the bath solution was composed of the following: 140 mM NaCl, 5.4 mM KCl, 1 mM $MgCl_2$, 10 mM HEPES, and 10 mM glucose with the pH adjusted to 7.4. This solution was used both calcium free and with the addition of 2 mM $CaCl_2$.

Ca^{2+} activity was recorded for 10 minutes and divided into two stages: initially in calcium free conditions (~ 2 minutes) to establish a baseline, and subsequently in the presence of 2 mM calcium. We used an IX71 inverted microscope (Olympus) with an XLUMPLFLN 20XW x20/1 water immersion objective (Olympus). OGB-1 AM was excited during 50 ms at 488 nm using a Polychrome V light source (Till Photonics) equipped with a Xenon Short-Arc lamp (Ushio) and a 505 nm dichroic beam splitter (Chroma Technology). The emission at 510 nm was filtered by a D535/40 nm emission filter (Chroma Technology) and finally collected by a C9100-13 EM-CCD camera (HAMAMATSU). The emission spectrum of the indicator changes in amplitude and peak wavelength when it is bound to the Ca^{2+} ions. The variations in the intensity of fluorescence are indicative of the quantity of free calcium that the fluorescent indicator can bind. These changes in fluorescence can be quantified using cameras to estimate the levels of calcium within the cell. Images were acquired at room temperature with an imaging interval of 1 second. Immediately after recordings, we draw a circle in the recorded area on the back of the sample. Then, samples were washed, and transferred to a multi-well plate, and then incubated in EM at a temperature of 37ºC for a period ranging from 30 to 60 minutes to equilibrate the cells. Then we fixed and prepared the samples for immunocytochemistry assays as described in section 3.3. We used eight different samples for each substrate. Samples were immunolabeled with Pax6 and nestin expression markers. The excessive handling of the samples during the experimental procedure led to the loss of cells from three

samples. Additionally, for another sample, it was not possible to align the area captured during recording with the corresponding section visualized during immunolabeling in the confocal microscope. We used an LSM 880 spectral confocal microscope (Carl Zeiss, Germany) and LD LCI Plan-Apochromat 25x/0.8 Imm Korr DIC M27 objective. Microscope cross-correlation was extremely time consuming and represented the hardest part of this experiment. Moreover, 20x microscope objective for calcium recordings did not match with confocal objectives, so we applied a 0.7 zoom out to fit recorded focal planes. Calcium recording and confocal images required orientation correction and, in ln2PMMA, flipping images due to differences during sample mounting (cells are face up). Further improvements should be considered to gain precision, efficiency, and rigor for future replications. Image processing and nuclei segmentation was performed as detailed in section 3.4.

For calcium data acquisition, we used a custom-developed image analysis algorithm in Matlab developed by Dr. C Borau (University of Zaragoza). This extracts nuclear and perinuclear calcium signals maintaining the same distance between ROIs in any direction around 360º. We used ImageJ snaps colocalized with confocal immunolabeled pictures that allowed us to assign specific nuclear morphologies, cell expression markers and calcium signals. Figure M-7 illustrates an example of microscope cross-correlation.

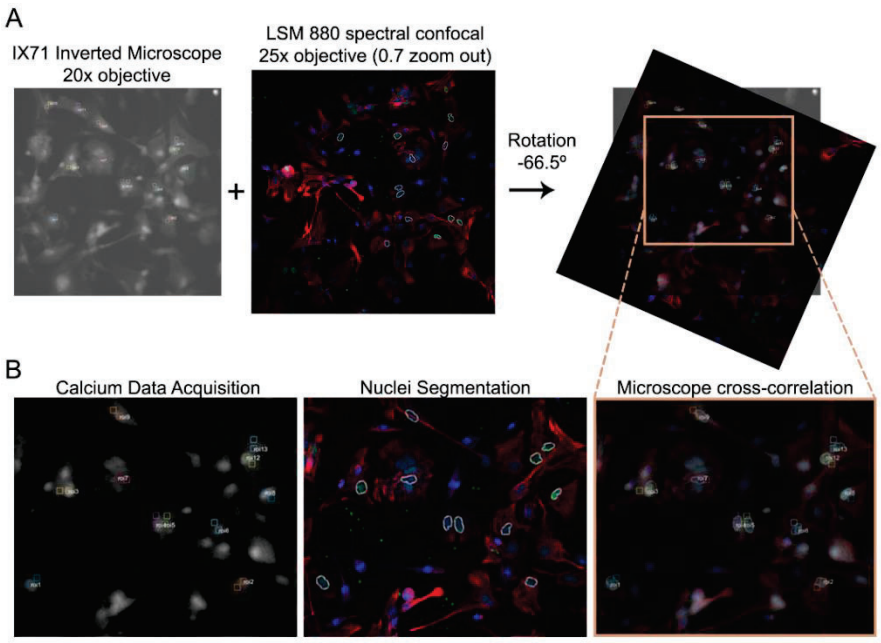


Figure M- 7 **Live calcium imaging and immunolabel microscopy cross-correlation**. (A) Default images acquired during calcium recordings and confocal acquisition. (B) Zoom detail showing calcium data acquisition display linked to nuclei segmentation and molecular markers (nestin in red, Pax6 in green, and Hoechst in blue for nuclei detection).

To determine relative intracellular calcium levels (fluorescence intensity), we extracted the background signal from the calcium signal of each cell and time point. Background was obtained determining 10 ROIs from zones without cells and the average was

calculated for each time point. This analysis was performed using Excel. Prior to this, background required detailed examination to avoid recording artifacts (Fig. M-8).

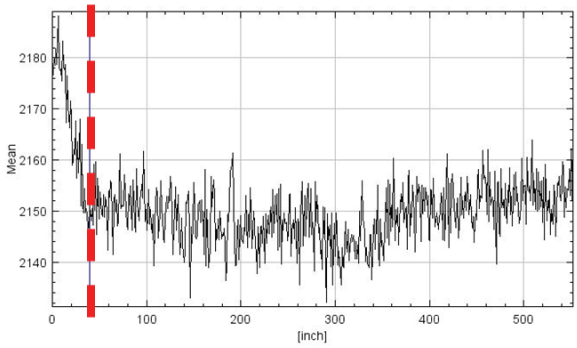


Figure M- 8 **Example of recording artifacts**. Example of background signal with initial recording artifacts. Data discarded from 0 to the red dashed line to eliminate recording artifacts.

Then, to determine calcium activity patterns from each cell, we first smoothed the signal with Savitzky-Golay filter, which consists in define each point by doing a polynomial regression of the order two (of our choice) of the next 6 points (window size, of our choice). Figure M-9 shows an example of raw signal compared to filtered signal.

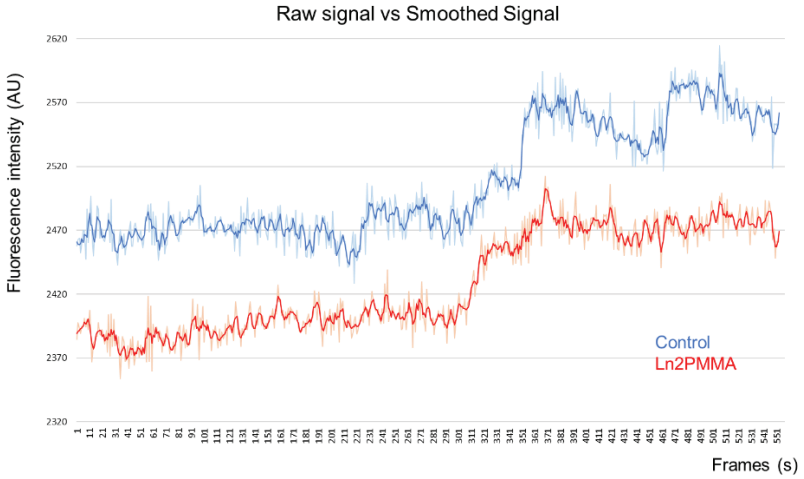


Figure M- 9 **Example of raw signal and smoothed signal by applying Savitzky-Golay filter.** Data corresponds to a random cell from control and ln2PMMA substrates.

Then we extract the first 50 frames of recorded signal, to reduce signal artifacts, and we used the signal-to-baseline ratio (SBR), also described as $\Delta F/F_o$. First, we calculated F_o, which is the measure of baseline, then ΔF, which is the moment-by-moment deviation from the baseline. This is described in the following equations:

$$(1)\ F_0 = \frac{\sum_{i=1}^{50} F_{Baseline}(t)_i}{50}$$

$$(2)\ \frac{\Delta F}{F_0} = \frac{F_i(t) - F_0}{F_0}$$

To perform analysis and plots we applied an increase of 100% to the resultant signal, i.e. % = $\frac{\Delta F}{F_0}$ x100.

3.11. Statistical analysis

Statistical analyzes were performed using Minitab® 17.1.0 (LEAD Technologies, INC), IBM SPSS (Version 26), GraphPad Prism version 8.0. R Core Team (2021) and R: A language and environment for statistical computing. R Foundation for Statistical Computing, Vienna, Austria. We performed the normality test by default and different post-hoc tests depending on the nature of the data. For two sample comparisons we used t-test or Mann-Whitney. For three or more sample comparisons we used one-way or two-way analysis of variance (ANOVA, with Tukey adjustment) or Kruskal-Wallis with multiple comparison test (with Benjamini-Yekultieli and Krieger FDR correction). To determine differences between populations we performed chi-square tests for 4 groups or multiple regression approach in contingency tables for more than 4 groups (adapted from Beasley & Schumacker, 1995) To demonstrate statistical significance, we deemed it sufficient to utilize thresholds such as $p < 0.05$ and $p < 0.01$. While we frequently observed values lower than $p = 0.001$ in numerous instances, we found that adopting a threshold of $p < 0.01$ was satisfactory for identifying meaningful biological distinctions.

4. RESULTS

4.1. Implication of MSCs and Ca^{2+} signaling in the biomechanical induction of RG.

One way of examining the mechanobiology of the NSC niche and its effect on neural linage progression is the use of biomaterial-based strategies (Collins et al., 2022; Ozgun et al., 2022). Using different RG biomimetic materials, our group has previously demonstrated that the induction of functional RG depends on specific substrate surface properties, local physical constraints, and metabolic adaptations. Ln2PMMA is a synthetic non-biodegradable, hydrophobic and negatively charged scaffold of poly (methyl methacrylate) (PMMA), with 2µm linear grooves that mimic RG surface properties and shape. Mouse cortical astrocytes grown in ln2PMMA adopt a functional RG phenotype that support neuronal migration (Álvarez, Sena, et al., 2014; Mattotti et al., 2012). RG phenotype hallmarks in ln2PMMA were bipolar morphology, alignment with the grooved topography, and the expression of RG markers, such as transcription factors Pax6 and Sox2, and the intermediate filament nestin. (Álvarez, Sena, et al., 2014; Mattotti et al., 2012). Ln2PMMA demonstrated the ability to induce the dedifferentiation of astrocytes into functional RG. However, the precise mechanisms underlying this process still remain unexplored.

4.1.1. Temporal sequence of ln2PMMA biomechanical induction of phenotypic changes in glial cultures

We prepared astrocyte enriched glial cultures grown on control (glass) and ln2PMMA substrates at different days in vitro (DIV), as described in methods section 3.1 (Fig. R-4.1-1A). Fixed cells were immunostained for detection of GFAP, considered an astrocyte marker, and for RG markers nestin and Pax6, and counterstained with Hoechst 33342 for nuclei labeling (Fig. R-4.1-1B). We determined the alignment of nestin and GFAP positive cells using a discrete Fourier Transformation (FT) method described in (Movilla et al., 2018), which provided insights into the spatial distribution and orientation. The alignment index ranges from 0 for total random orientations, to 1, for completely aligned structures. As expected, nestin+ and/or GFAP+ glial cells cultured on control substrates exhibited a spread and randomly oriented morphology, while the same cells cultured on ln2PMMA aligned with the topography and adopted RG phenotypes (Fig. R-4.1-1C). The alignment was evident from 1DIV, and it was maintained over time, indicating a rapid cell response to the mechanical signals from the substrate. As expected, the proportion of Pax6+ cells increased in ln2PMMA (3-7 DIV $p<0.05$), while the proportion of GFAP+ cells ($p<0.05$ at 3DIV) decreased with respect to control substrate (Fig. R-4.1-1B, D). The differences in the proportion of astrocyte and RG cells vary over time in vitro. This reflects the initial response to the mechanical properties of the substrate (1DIV), the phase of

maximal response to mechanical signals (3-7DIV), and the maturation phase, when increasing confluence and cell-cell signaling overcome mechanical signals from the substrate (14DIV).

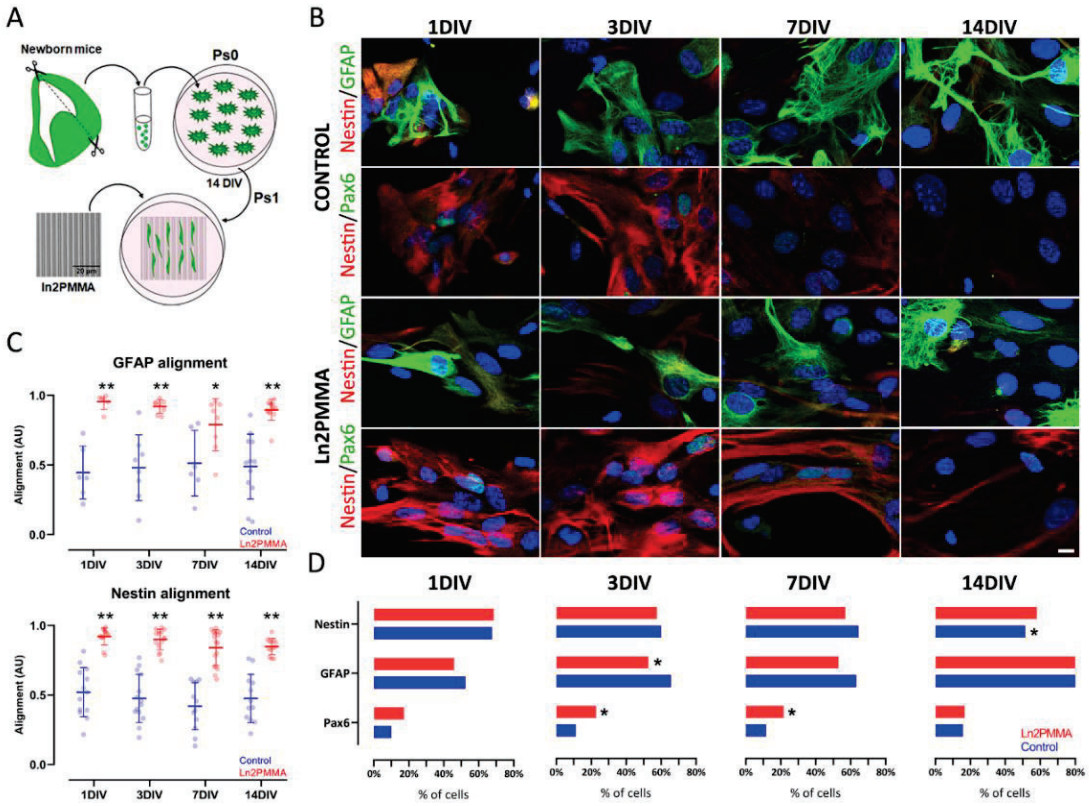


Figure R-4.1- 1 **Ln2PMMA induce astrocytes alignment and dedifferentiation.** (A) Scheme of astrocytes obtention and culture protocol. (B) Glial cells at different time points (1DIV, 3DIV, 7DIV and 14DIV), nuclei are stained with Hoechst (blue) and cells immunolabeled with nestin (red) and GFAP or Pax6 (green) in control and ln2PMMA. (C) Cytoplasmic alignment of nestin+ and GFAP+ cells. (D) Percentage of nestin, Pax6 and GFAP positive cells in control and ln2PMMA substrates at different time points (1DIV, 3DIV, 7DIV and 14DIV). To compare cell alignment, we used multiple t-test with Benjamini-Krieger-Yekultieli FDR correction, and chi-square test to compare cell populations, *p<0.05, **p<0.01. Scale bar, 10µm.

4.1.2. Expression of mechanoelectrical transduction components during mouse RG linage progression.

Mechanoelectrical transduction, by changing the open/close state of mechanosensitive ion channels (MSCs) at the plasma membrane, is the earliest event upon mechanical stimulation. Activation of MSCs is direct and changes plasma membrane potential, causing depolarization by opening cationic non-selective channels (permeable to Na^+, K^+, Ca^{2+}), or hyperpolarization by opening K^+-selective stretch-activated channels (Douguet & Honoré, 2019). This ion flux can modify intracellular Ca^{2+} dynamics, a key control system for neurodevelopmental processes including RG proliferation, neurogenesis, migration, and neural differentiation (McKinney et al., 2022).

To identify potential mechanoelectrical transduction candidates during RG-astrocyte lineage development in mouse, in collaboration with Dr. Leonardo Garma, we performed a metanalysis of publicly available transcriptomics dataset (Di Bella et al., 2021). To do so, we normalized data with respect to mean gene expression at E13 using the normalize_total function from scanpy (Wolf et al., 2018) and applied a two-step dimensionality reduction to select clusters expressing RG-astrocyte lineage markers (Sox2, Pax6, Hes5, Olig1, Aqp4 and Slc1a2) and no expression of neuronal markers (Neurod2, Tubb3, Neurod6, Meg3). Then, we analyzed the expression of 167 MSCs, Ca^{+2} related ion channels, and associated genes that are mechano-related with Ca^{2+} signaling. It included transient receptor potential, acid sensing, voltage-gated Ca^{+2} and K^{+} channels, connexins and pannexins, K^{+} two pore domain channels, epithelial Na^{+} channels, mitochondrial Ca^{+2} channels, CaMKII genes, etc. First, we analyzed their presence in the dataset (160/167), then we calculated their average, mean variance and total expression at each development stage (Annex I). In general, the expression of MSCs and related genes in RG-astrocyte lineage cells was low or very low and some genes failed to meet the selection criteria, so we considered their expression as zero. Finally, we calculated the difference between E13-E14 with respect to P1-P4 and the results were represented in a dot plot indicating expression % (size of dots) and the relative expression (color code), and genes were organized from left to right as its expression increase across time (Fig. R-4.1-1).

First, we focused on CaMKII (Ca^{2+}/calmodulin-dependent protein kinase II), a multimeric serine/threonine-specific protein kinase that plays a central role in decoding space-temporal Ca^{2+} signals to activate specific developmental events (Lambris, 2016.; Nicole et al., 2018). Our metanalysis revealed consistent expression of all CaMKII isoforms (*Camk2a, Camk2b, Camk2d and Camk2g*) during RG-astrocyte lineage cells development (E13-P4). Camk2a and Camk2b were expressed at low levels through development, while Camk2d and Camk2g expression were always higher than Camk2a/b isoforms and increased with time, coinciding with the peak of glycogenesis (Fig. R-4.1-1, Annex). Moreover, there was a concomitant increase trough development in ER and mitochondrial Ca^{2+} channels genes (Tmbim1 -4 -6, Tmco1) that play a key role in calcium homeostasis in part by preventing calcium stores from overfilling. Although most of the MSCs were expressed at low levels, the most relevant changes were found for inhibitory potassium two pore domain and calcium-activated channels (Kcnk1 -2 -10, Kcnn2) and excitatory transient receptor potential channels (Trpc1, Pkd2), which expression increased trough RG-astrocyte lineage progression. In addition, there was a shift from Cx45 (Gjc1) to Cx43 (Gja1) gene expression trough development.

Taking together, our metanalysis suggest that the mechanoelectrical machinery is expressed in RG-astrocyte lineage cells though development, and that lineage progression involves an increase in genes related to Ca^{2+} signaling and homeostasis, and in genes of inhibitory potassium channels responsible to keep the hyperpolarized resting membrane potential characteristic of astrocytes.

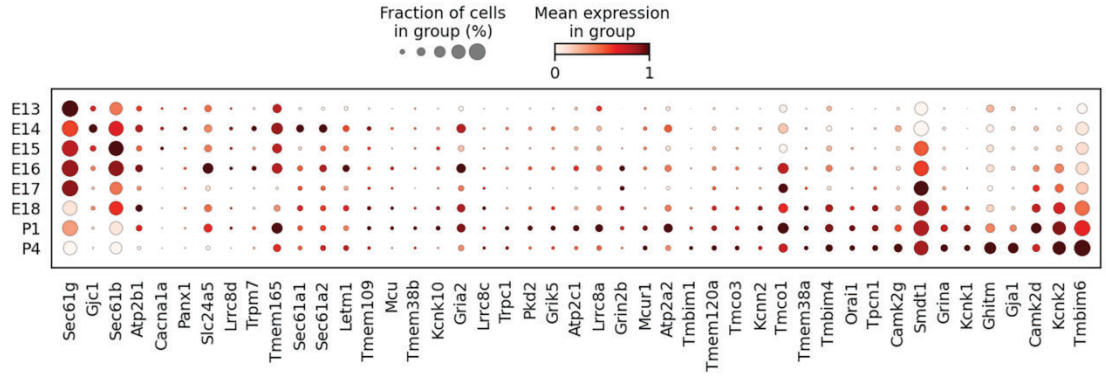


Figure R-4.1- 1 **Changes of MSCs and Ca^{2+} signaling-related genes during mouse cerebral cortex development in astrocyte-RG cell lineages.** Combined Dot plot and Heatmap representing percentage of cells expressing each gene (dot size) and the average of expression at each developmental stage (color). Expression is normalized by individual gene maximum expression (0 to 1).

4.1.3. Identification of MSCs potentially relevant in ln2PMMA biomechanical induction of RG.

To identify potential candidates in our experimental model, we analyzed by WB the differential protein expression of eighteen different MSCs, in glial cells grown for 3DIV on control and ln2PMMA substrates. We used the mechanosensitive ion channel antibody explorer kit (Alomone #AK-234) that include transient receptor potential cation channels (TRPA1, TRPC1, TRPC6, TRPP1 (PKD1), TRPV4), acidic sensing proton gated ion channels (ASIC1, ASIC2a, ASIC3), epithelial sodium channels (ENaCα, β, γ), two-pore-domain potassium channels (TREK-1, TREK-2, TRAAK, TRESK, voltage-gated potassium channel subunit Kv7.4 (Kv7.4). We also included the transient receptor potential vanilloid receptor 1 (TRPV1) and the pore forming connexin 43 (CX43).

We found that ASIC1, TRPC1, TRESK and Kv7.4 were significantly upregulated, while TRPA1 and TREK-2 were significantly downregulated in glial cells grown on ln2PMMA with respect to control substrate. Although not reaching statistical significance, we also found an upregulation tendency for TREK1 (p=0.059) in ln2PMMA. TRPV4 expression was not detected, and no significant protein expression changes were found for the remaining 10 MSCs analyzed. A summary of the results is shown in Figure R-4.1-2.

These results suggest that astrocyte to RG dedifferentiation proceeds through a complex shift in the expression of excitatory and inhibitory MSCs. Unfortunately, the antibodies used here were not suitable for immunofluorescence, and we could not analyze the expression of MSCs candidates at the cellular level.

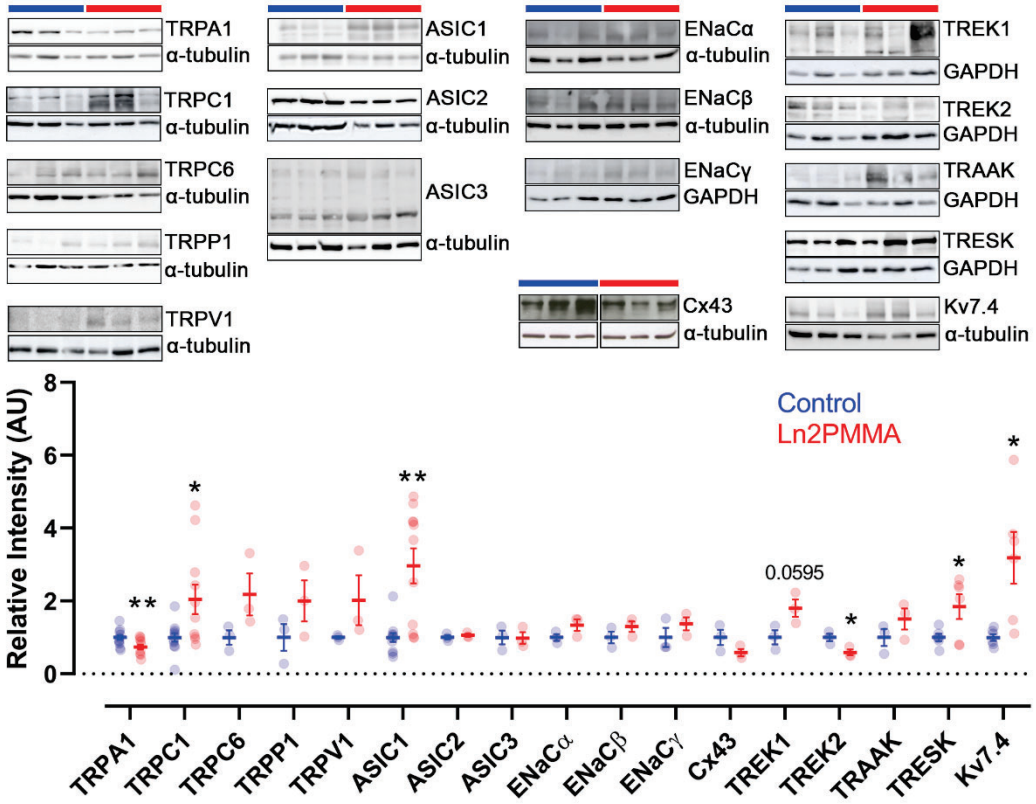


Figure R-4.1- 2 **MSCs protein expression changes induced by ln2PMMA biomechanical signals**. WB and densitometry plot of MSCs protein expression in glial cultures grown on control and ln2PMMA substrates for 3DIV. Individual dots correspond to different samples. N>5 in TRPA1, TRPC1, ASIC1, TRESK, and Kv7.4. All others had at least N=3 from different experiments. Individual unpaired t-tests were performed, two-tailed p value. *P<0.05 and **P<0.01.

4.1.4. Pharmacological validation of MSCs and Ca^{2+} signaling implication in the biomechanical induction of RG.

The changes in MSCs expression observed in response to ln2PMMA mechanical signals does not inform whether the different MSCs are in open or close conformation (Fig. R-4.1-3A). Therefore, we performed a pharmacological approach to inquire the functional state of MSCs and Ca^{2+} signaling during ln2PMMA mechanical-driven RG induction. After 3DIV grown on control or ln2PMMA substrates, glial cells were treated for 3h with GsMTx-4 (1.22 µm), KN93 (5 µm) or vehicle (PBS and DMSO respectively), fixed and prepared for immunostaining (Fig. R.4.1-3B). KN93 molecule binds to its Ca^{2+}/CaM binding site, preventing Ca^{2+}/CaM-dependent activities, including CaMKII activation (Wong et al., 2019) (Fig. 4.1-3C). GsMTx-4 is a spider venom peptide that physically

penetrates into the cell membrane, modifying its structure and mechanical properties (Fig. 4.1-3D). Through differential deformation of the outer and inner lipid bilayer membrane, GsMTx-4 inhibits excitatory (cationic non-selective) MSCs, while activates inhibitory (K^+-selective) MSCs (Gnanasambandam et al., 2017; Suchyna, 2017).

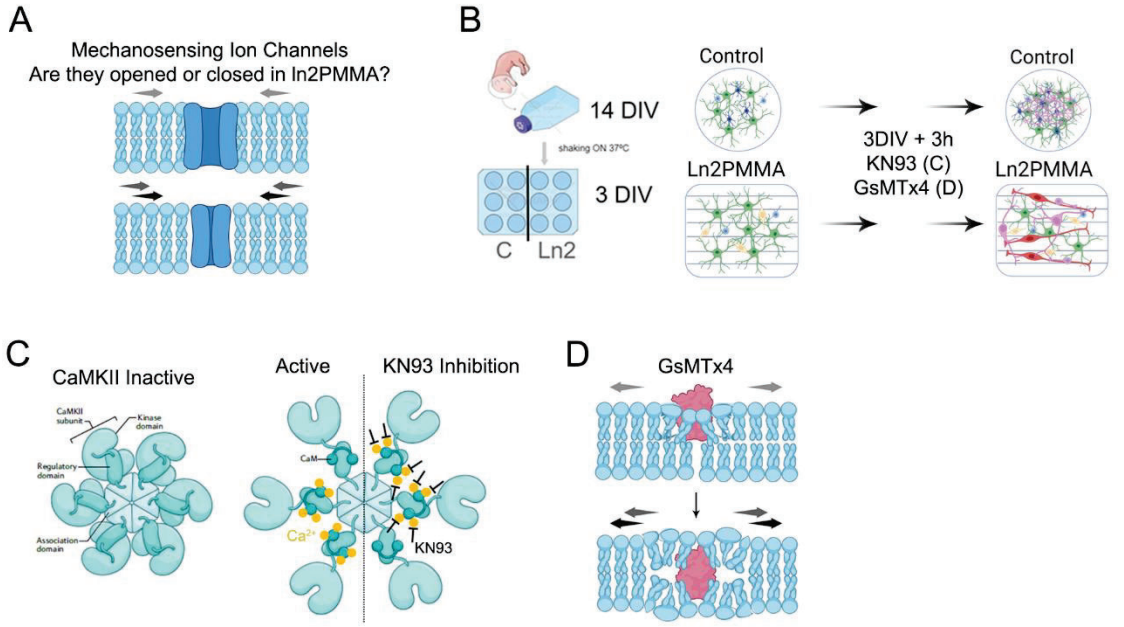


Figure R-4.1- 3 **Experimental approach to explore the role of Ca^{2+} signaling in ln2PMMA mechanical adaptation.** (A) Schematic hypothesis of the mechanosensing ion channels state. (B) Schematic of the experimental approach. (C) KN93 mechanism of action. Yellow dots represent calcium ions and black T represents KN93 molecules. (D) GsMTx4 action mechanism. Arrows indicate tension direction. Illustration of CaMKII (C) adapted from Yasuda et al., 2022.

First, by immunostaining glial cells with cleaved caspase 3, the active form of the enzyme that initiates the apoptosis process (Enari et al., 1997), we corroborated that KN93 and GsMTx4 treatment does not induce apoptosis at the doses used here (Fig. S1). After confirming the lack of deleterious effects, glial cultures were immunostained for the detection of RG (nestin and Pax6) and astrocytes (GFAP) (Fig. R-4.1-4A-B).

Consistent with our previous findings, the population of nestin+ cells were similar in both vehicle-treated substrates, GFAP+ astroglia was significantly lower, and Pax6+ RG significantly higher in ln2PMMA with respect to control substrate, both vehicle-treated. The differences between substrates in the proportion of GFAP+ and Pax6+ glia was abrogated by 3h treatment with either GsMTx4 or KN93 (Fig. R-4.1-4C-D). KN93 treatment significantly increased the proportion of GFAP+ astrocytes in ln2PMMA ($p<0.05$), approaching the values observed in control substrate. Conversely, although not reaching statistical significance, Pax6+ RG cells tended to decrease in KN93-treated ln2PMMA, while they tended to increase in KN93-treated control substrate (Fig. R-4.1-

4C). On the other side, GsMTx4 treatment in control substrate cultures significantly reduced the proportion of GFAP+ astrocytes ($p<0.01$) with respect vehicle-treated, while GsMTx4-treated ln2PMMA cultures had a significant reduction in Pax6+ RG with respect to vehicle-treated ($p<0.01$) (Fig. R-4.1-4D).

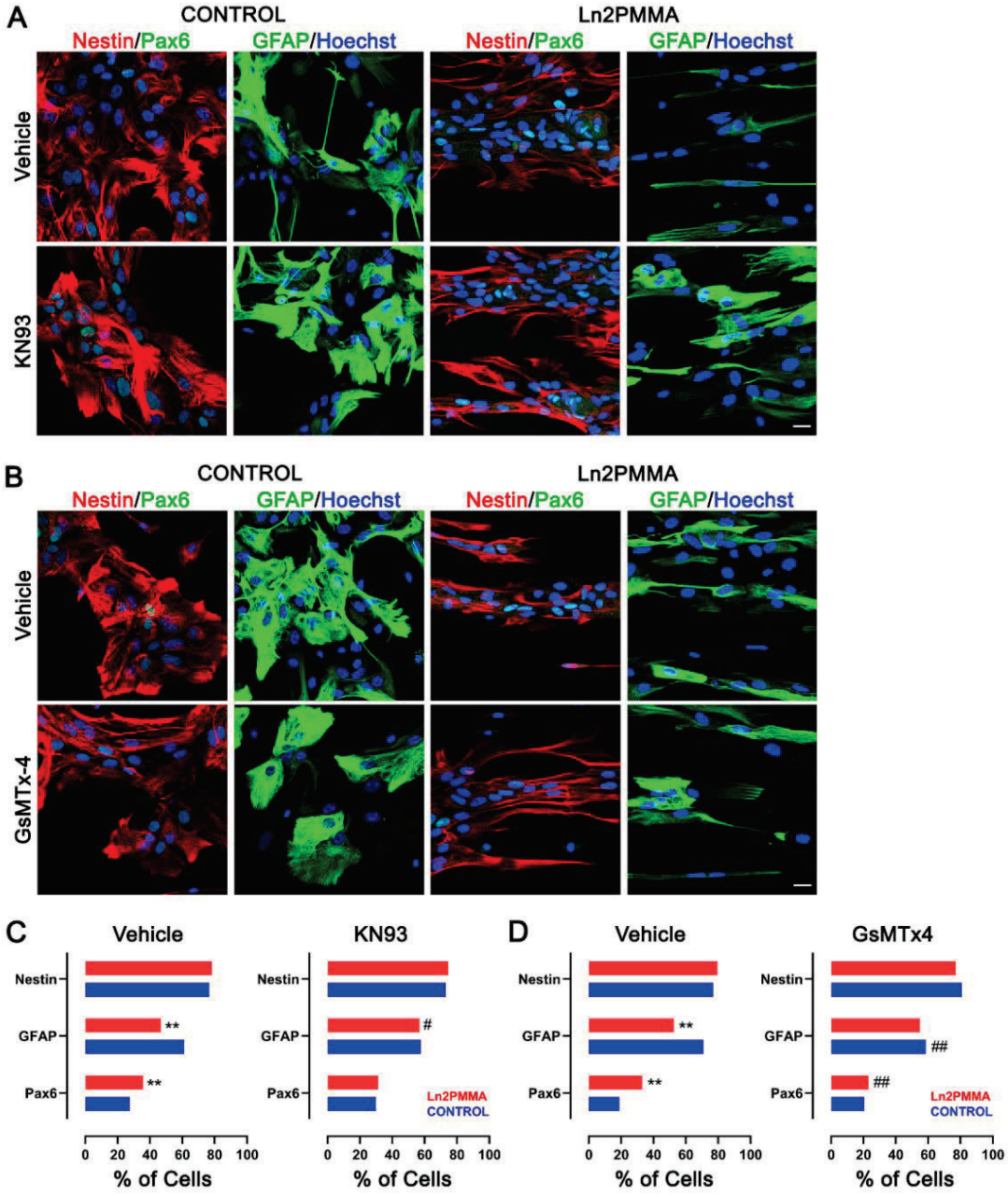


Figure R-4.1- 4 **Pharmacological validation of mechanosensitive cation channels and downstream Ca2+ signaling implication in the biomechanical induction of RG.** (A, B) Confocal pictures of glial cells grown on control and ln2PMMA substrates immunostained for RG (Nestin and Pax6) and astrocyte (GFAP) molecular markers, and Hoechst 33342 for nuclei (blue); treated with (A) vehicle (DMSO, 5μM) and CaMKII inhibitor KN93 (5μM), or (B) vehicle (PBS 1.22μM) and stretch gating channels inhibitor GsMTx4 (1.22μM). (C, D) Plots showing the percentage of cells expressing nestin, Pax6 and GFAP in control and ln2PMMA substrates treated with (D) vehicle and KN93 (E) vehicle and GsMTx4. Significant differences with respect

control substrate **p<0.01 chi-squared test; with respect vehicle treatment #p<0.05, ##p<0.01. Scale bar, 20µm.

Taken together those data indicate a direct role for calcium signaling in ln2PMMA biomechanical induction of RG and suggest that low Ca^{2+}/CaM signaling favors GFAP+ astrocyte phenotypes, while a higher Ca^{2+}/CaM signaling, but within a relatively narrow window, favored Pax6+ RG phenotypes. Similarly, our data support a precise balance between excitatory and inhibitory MSCs in ln2PMMA biomechanical induction of RG, although their precise interpretation, related to the direction of membrane potential changes, is complex, due to the divergent effect of GsMTx-4 on excitatory and inhibitory MSCs.

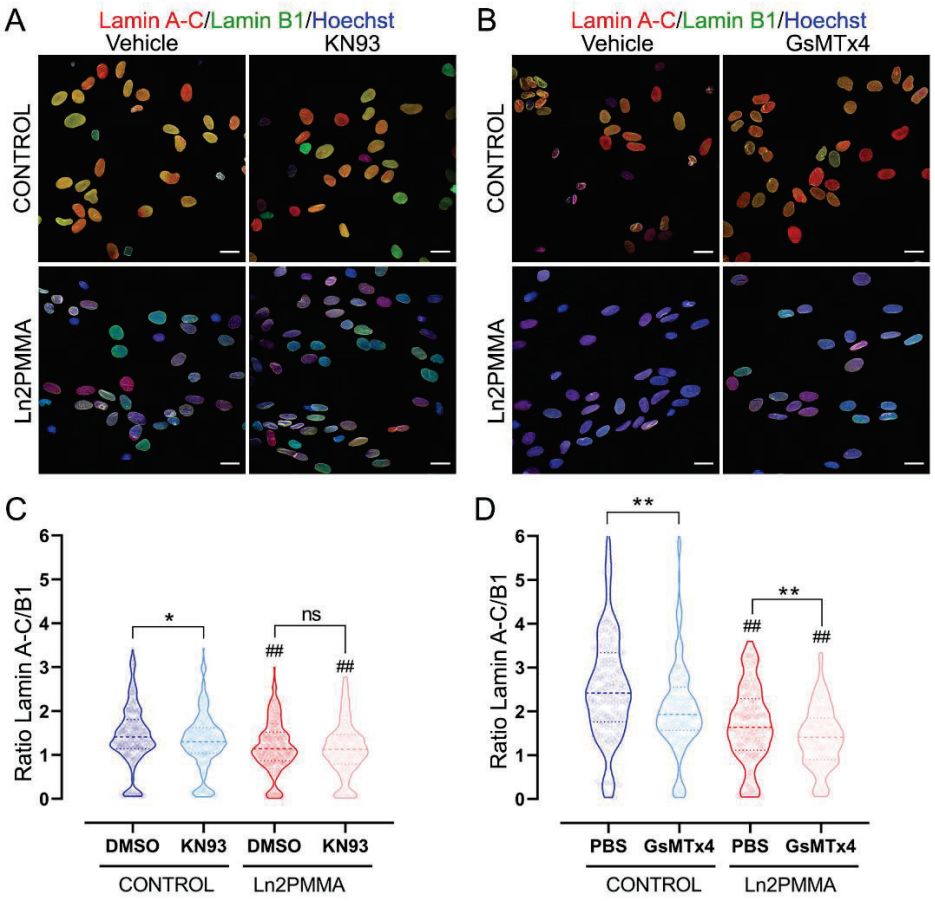


Figure R-4.1- 5 **Ln2PMMA substrate, KN93 and GsMTx4 treatments reduced lamins A-C/B1 ratio.** Confocal images of glial cells grown for 3DIV on control and ln2PMMA substrates immunostained for lamins A-C (red) and B1 (green), and Hoechst 33342 for nuclei (blue); treated with (A) vehicle (DMSO, 5µM) and CaMKII inhibitor KN93 (5µM), or (B) vehicle (PBS 1.22µM) and MSCs inhibitor GsMTx4 (1.22µM). (C, D) Violin plots showing lamin A-C/B1 ratios from glial cells grown in control and ln2PMMA treated for 3h without deprivation (C) with vehicle (DMSO, N=483) and KN93 (5µM) (N=506), and (D) with vehicle (PBS, N=372) and GsMTx4 (1.22µM) (N=398). Data from two different biological samples for each condition. Statistical analysis; Kruskal Wallis, * comparison DMSO vs KN93 in the same substrate (*p<0.05); # comparison between substrates in the same treatment condition (##p<0.01).

Nuclear lamins are generalized mechanosensors that monitor changes in the cell mechanobiology and regulate chromatin organization and gene expression, to adapt cell fate and behavior to their physical microenvironment (Niethammer, 2021). Recent work demonstrated that nuclear lamin A-C expression in lung cancer cells is mediated by Ca^{2+}/CaMKII activation, and that treatment with Ca^{2+}/CaMKII inhibitors reduced lamin A-C expression (Kim et al., 2022). If that was also true for glial cells, blocking Ca^{2+}/CaMKII activation by KN93 will reduce lamin A-C nuclear expression. Therefore, we analyzed lamins A-C and B1 expression in glial cells grown on control and ln2PMMA substrates, and whether pharmacological 3h treatment with KN93 and GsMTx4 inhibitors reduced lamins A-C/B1 ratio. To do that, we extracted lamins A-C/B1 nuclear intensity ratio from confocal images (Fig. R-4.1-5A-B), as described in the methods section 3.5 (Fig. M-3B). In all cases, lamins A-C/B1 ratio was lower in ln2 PMMA than in control substrate and, as predicted, we observed a significant reduction in lamins A-C/B1 ratio in KN93 treated cultures with respect to vehicle-treated conditions, although not reaching statistical significance in ln2PMMA substrate. Unexpectedly, the reduction in lamins A-C/B1 ratio was more pronounced in GsMTx4 treated cultures in both substrates (Fig. R-4.1-5C-D).

In summary, these data indicate that 3h pharmacological interference of the mechanoelectrical signal is sufficient to abrogate substrate-induced changes in cell type-specific molecular markers, remodeling nuclear lamins composition. Moreover, both KN93 and GsMTx4 treatments seem to reduce Ca^{2+}/CaM signaling, and thus, the lower lamins A-C/B1 ratio in ln2PMMA substrate might reflect a mechanically-induced decrease in Ca^{2+}/CaM signaling.

4.1.5. Evaluation of intracellular Ca^{2+} dynamics in glial cells grown on control and ln2PMMA substrates.

Our results point to a shift in MSCs expression and reduced Ca^{2+}/CaM signaling, as integrant of the ln2PMMA mechanoelectrical signaling transduction (Fig. R-4.1-6). Therefore, we aimed to directly assess whether glial cells grown on ln2PMMA substrate changed their intracellular Ca^{2+} ($[Ca^{2+}]_I$) levels and dynamics. For that, we performed fluorometric calcium imaging, in collaboration with Dr. Rosalba Sortino at Gorostiza's Lab, using the Ca^{2+} indicator Oregon Green™ 488 BAPTA-1, AM (OGB), which binds to free $[Ca^{2+}]_I$ in live cells. After Ca^{2+}-imaging recording slides were fixed and immunostained for Pax6 and nestin detection, to correlate individual cells activity with RG marker expression (Fig. R-4.1-7A-B).

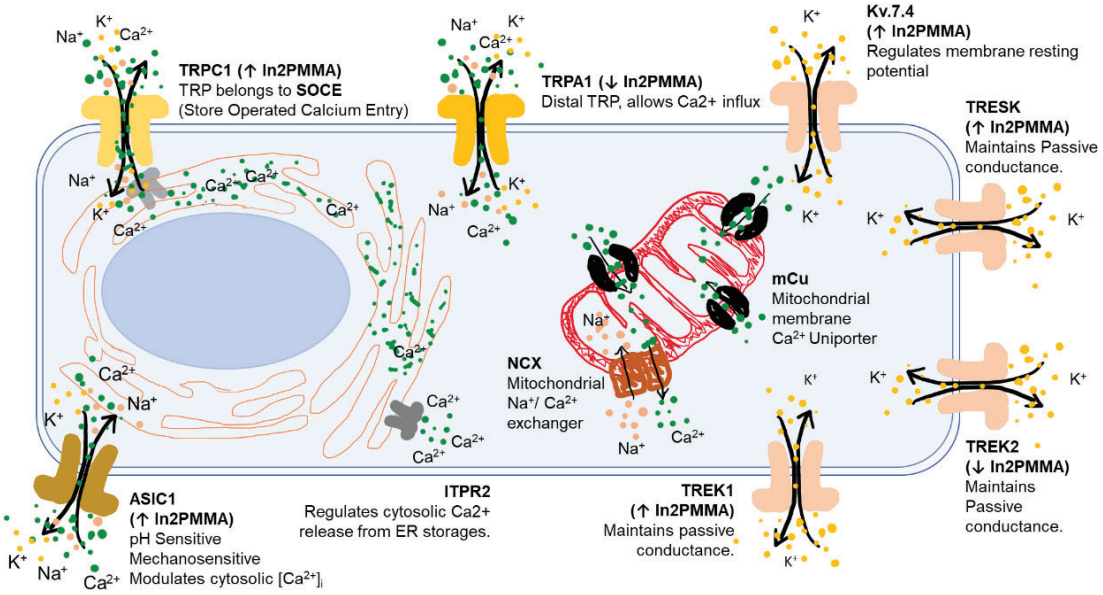


Figure R-4.1- 6 **Summary of MSCs candidates to mediate In2PMMA bioelectrical signaling in glial cells.** Arrows indicate the direction of significant differential expression observed in In2PMMA substrates.

As nuclear calcium dynamics is one of the most potent regulators of gene expression (Bading, 2013), we defined a ROI mask of identical size in the nuclear region of each cell. To determine relative differences in $[Ca^{2+}]_I$ between live cells grown in control and In2PMMA substrates, we normalized the signal by sample background subtraction, and plotted the mean signal in function of time. With this analysis, Ca^{2+} signal was significantly lower in glial cells grown on In2PMMA than in those grown on control substrate ($p<0.01$), both, in absence and presence of 2mM extracellular Ca^{2+} ($[Ca^{2+}]_e$) (Fig. R-4.1-7C). When segregating by cell type (Fig. R-4.1-7D-F), the higher $[Ca^{2+}]_I$ was found in Pax6+ RG, Nestin+/Pax6- glial cells had intermediate $[Ca^{2+}]_I$ and nestin-/Pax6- non-RG cells had significantly lower $[Ca^{2+}]_I$ than the other two glial cell types, in both materials and $[Ca^{2+}]_e$ conditions ($p<0.01$).

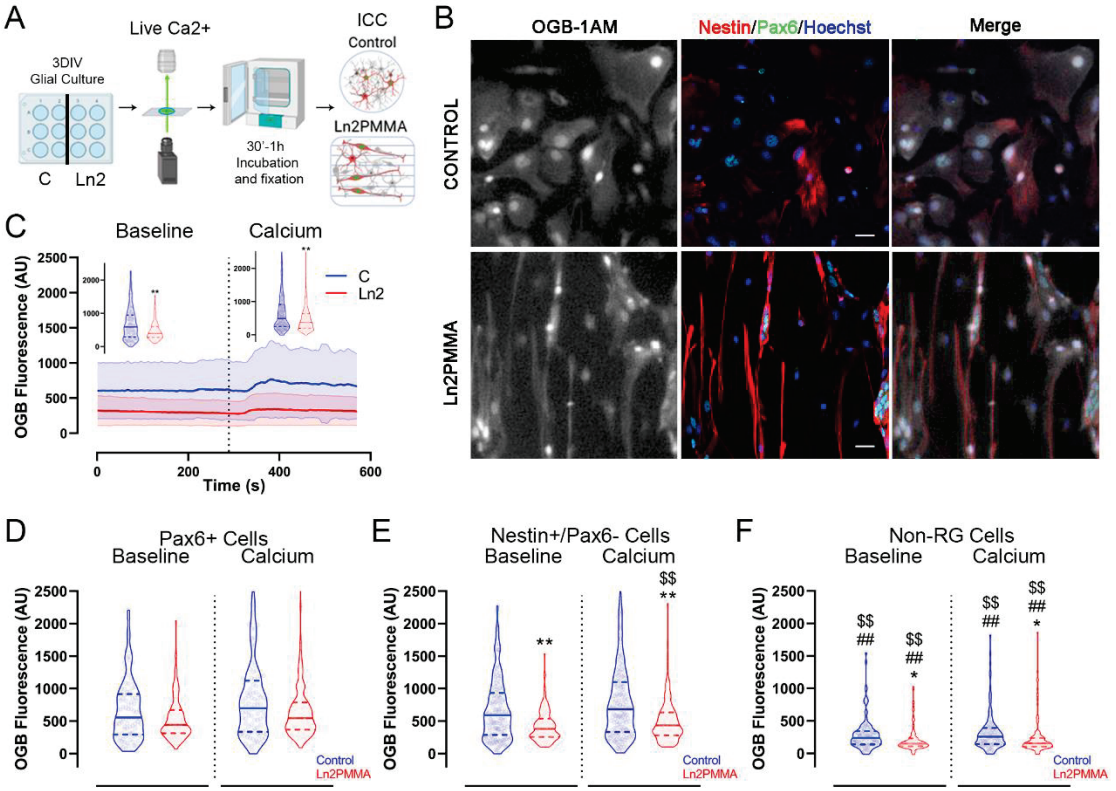


Figure R-4.1- 7 **Evaluation of intracellular Ca^{2+} concentration in glial cells grown on control and ln2PMMA substrates.** (A) Experimental design. (B) microscopy images of glial cells grown for 3-4 DIV on control and ln2PMMA substrates live-loaded with OGB (white) and immunostained after fixation for RG markers Pax6 (green) and nestin (red), using Hoechst 33342 for nuclei (blue) detection. (C) Intracellular Ca^{+2} levels were analyzed by background subtraction (F(t)-background) method and represented as signal mean +/- 95% CI (shadow area) in control (blue) and ln2PMMA (red) substrates. Baseline are extracellular Ca^{+2} free and calcium has 2 mM $CaCl_2$. The violin plots in C represent the average fluorescence intensity in each nucleus. (D-F) Violin plots representing the average fluorescence intensity in each nucleus of (C) Pax6+ RG (Control=63, Ln2PMMA=91), (D) nestin+/Pax6- glia (Control=125, Ln2PMMA=106), (E) nestin-/Pax6- non-RG (Control=69, Ln2PMMA=75). Statistical analysis: Kruskal Wallis and multiple comparison test * p<0.05, **p<0.01 differences between control and ln2PMMA; $$p<0.01differences with respect to Pax6+ RG; ##p<0.01differences with respect to nestin+/Pax6- glia. Four different samples for each condition. Scale bar: 25µm.

Then, to analyze intracellular Ca^{2+} dynamics and the presence of spontaneous transient Ca^{2+} rises or oscillations (calcium transients), with independence of the basal $[Ca^{2+}]_I$, we calculate $\Delta F/F_o$ (basal/resting value) as described in the methods section 3.9 (equations 1 and 2). This analysis showed that glial cells grown on ln2PMMA substrates had significantly less spontaneous Ca^{2+} transients, both, in absence and presence of extracellular Ca^{2+} (active cells in control 73.10%, N=242; in ln2PMMA 61,7%, N=266, p<0.01; Fig. R-4.1-8A). When segregating by cell type, we confirmed cell type-specific differences in response to ln2PMMA mechanical signals, linking the significant $[Ca^{2+}]_I$ reduction in Nestin+/Pax6- and nestin-/Pax6- glial cells with a parallel decrease in spontaneous Ca^{2+} transients (Fig. R-4.1-8B-D).

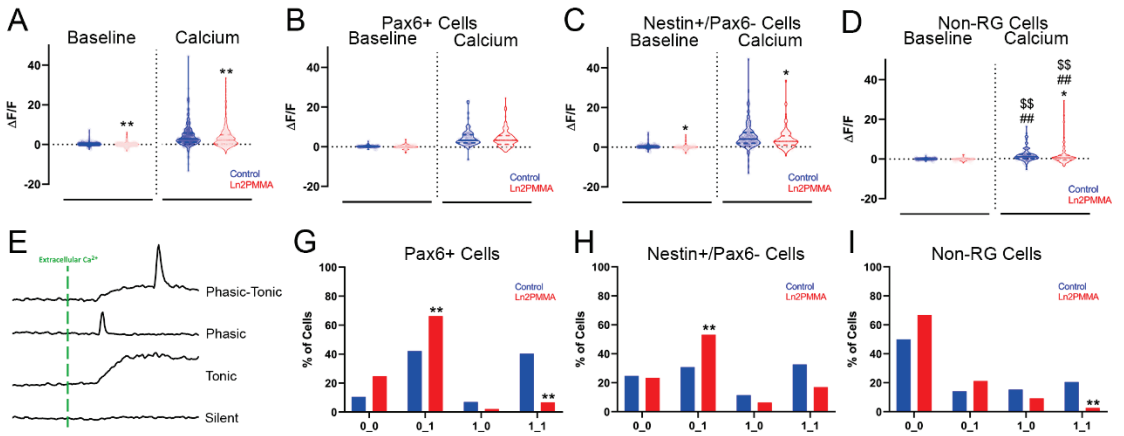


Figure R-4.1- 8 **Ln2PMMA substrate modify spontaneous calcium activity in glial cells.** (A) Violin plots showing spontaneous nuclear Ca^{2+} transients (average $\Delta F/F_o$) at baseline (calcium-free extracellular medium) and calcium (2mM extracellular calcium) conditions in glial cells grown on control and ln2PMMA. Points represent individual cells. (B-D) Violin plots showing spontaneous nuclear Ca^{2+} transients in (B) Pax6+ RG, (C) nestin+/Pax6- glial cells, and (D) nestin-/Pax6- non-RG cells. (E) Scheme of the four different patterns of Ca^{2+} activity identified above $\Delta F/F_o \geq 3\%$ threshold. Calcium activity patterns distribution (%) in Pax6+ RG cells (F), nestin+/Pax6- glial cells (G), and non-RG cells (H). Statistical analysis: (A-D) Kruskal Wallis and multiple comparison tests; (G, H and I) Chi-square test and multiple comparison post-hoc test. Differences between control and ln2PMMA * $p<0.05$, ** $p<0.01$; differences respect to Pax6+ RG \$\$$p<0.01$; differences respect to nestin+/Pax6- glial cells ## $p<0.01$. Four different samples for each condition.

To deeper this analysis, we identified the presence of peaks above the $\Delta F/F_o \geq 3\%$ threshold and classify Ca^{2+} activity in four different patterns: cells without peaks above threshold (silent), cells with rapid transient peaks (only phasic), cells with slow prolonged rises (only tonic), and cells with both types of activity (phasic-tonic) (Fig. R-4.1-8E). Consistent with the generalized fall in $[Ca^{2+}]_I$ in ln2PMMA, 45% of cells analyzed were Ca^{2+} silent versus 24% in control ($p<0.01$). By cell type (Fig. R-4.1-8F-H), the predominant pattern in nestin-/Pax6- non-RG cells were silent, while predominated tonic and tonic-phasic activity patterns in Pax6+ RG and nestin+/Pax6- glial cells. In all cases, cells grown on ln2PMMA significantly reduced the phasic component of the Ca^{2+} signal, increasing the percentage of cells showing only the tonic component or become silent.

In summary, these results support that mechanical signal from ln2PMMA substrate significantly reduced $[Ca^{2+}]_I$, spontaneous transient Ca^{2+} events and Ca^{2+}/CaM signaling, in all glial cell types but to a much lesser extent in Pax6+ RG. Particularly, ln2PMMA substrate reduced the phasic component of the Ca^{2+} signal, increasing the proportion of cells with tonic patterns of activity. Whether these changes were directly associated with the expression of particular MSCs in different cell types required further investigation.

4.2. Effect of ln2PMMA biomechanical signals in the metabolic signature and mitochondrial dynamics of glial cells.

Differentiation is usually associated with metabolic rewiring including switches between glycolytic and oxidative phosphorylation (OXPHOS) and changes in oxidative state (Chui et al., 2020). Moreover, cell mechanics and adaptation to mechanical signals also accompanied a crosstalk between mechanotransduction and metabolism (reviewed in Romani et al., 2021). However, little is known about the mechanisms coupling mechanosensitive responses and metabolism during RG-astrocyte lineage progression.

4.1.1. Characterization of the metabolic signature of glial cells grown on ln2PMMA and control substrates.

During brain development, RG undergo symmetric (self-renewal) and asymmetric (neurons or intermediate progenitors) divisions. After RG division, and depending on cell-fate, there is a metabolic shift, from glycolysis to OXPHOS metabolism, along with mitochondrial morphological changes. Particularly, after NSC division, dysregulation of NAD+ promotes SIRT1 expression which enhances NSC-neuronal commitment (Iwata et al., 2020a). In figure R-4.2-1A we show a schematic view of glycolysis with different intermediate components and end products.

To investigate the metabolic state in glial cells grown on control and ln2PMMA substrates, we explored by Western blot and the expression of key metabolic enzymes (in green Fig R-4.2-1A) involved in glycolytic and OXPHOS pathways (Fig. R-4.2-1B-C). Phosphofructo-2-kinase/fructose-2,6-biphosphatase isoform 6 (PFKFB3) is the rate-limiting enzyme of glycolysis and is also required for cell cycle progression, linking glucose metabolism to cell proliferation (Lv et al., 2015a). On the contrary, pyruvate dehydrogenase (PDH) favors pyruvate conversion to Acetyl-CoA for energy production in OXPHOS metabolism and is inactivated by phosphorylation (pPDH) (Halim et al., 2010). In glial cells grown on ln2PMMA, PFKFB3 significantly increased, while pPDH significantly decreased with respect to those grown on control substrate. We also found a mild although non-significant increase in the anabolic enzyme mitochondrial phosphoenolpyruvate carboxykinase 2 (PCK2), and no relevant changes in the NAD+-dependent histone deacetylase sirtuin-1 (SIRT1) (Fig. R-4.2-1B, C). The concomitant rise in PFKFB3 and fall in pPDH in ln2 PMMA suggest activation of the glycolytic metabolism and increased influx of acetyl-coA from glycolysis into the TCA cycle. However, when analyzing L-lactate release, we only found a very mild and non-significant increase in L-lactate concentration in culture media from glial cells grown on ln2PMMA with respect control substrates (Fig. R-4.2-1F).

We then analyzed the expression of the two main modulators of the ROS scavenging system, finding a significant reduction in glutathione peroxidase (GPX) in ln2PMMA, without changes in manganese superoxide dismutase (MnSOD) (Fig. R-4.2-1D, E). Data suggesting a reduction in ROS production of in Ln2PMMA.

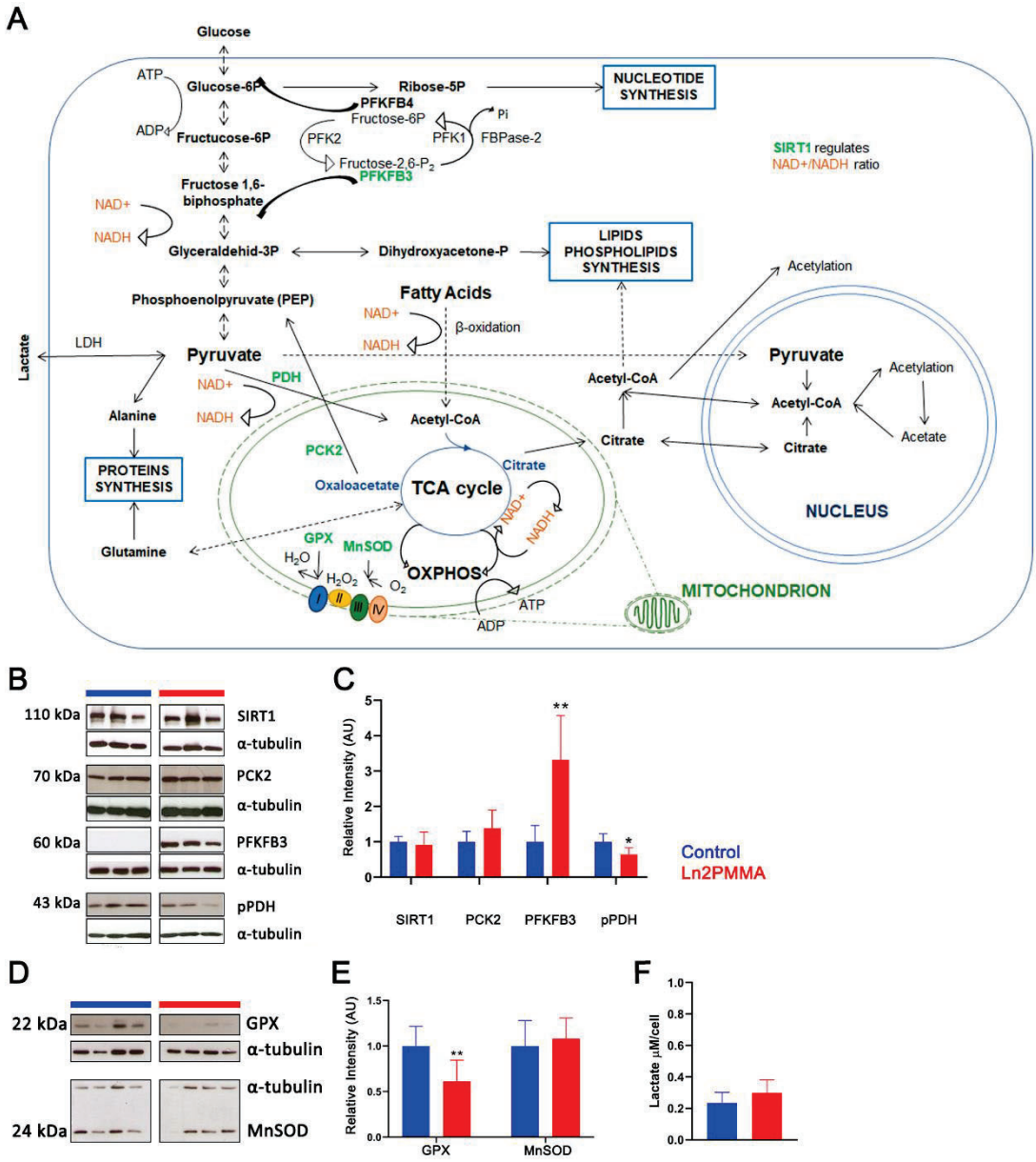


Figure R-4.2- 1 Ln2PMMA induced a shift in key metabolic enzymes in glial cells. (A) Schematic of glycolysis and intermediate processes with different enzymes analyzed in this section. Dashed lines indicate alternative paths, non-specific of glycolysis. (B) Western Blot of key enzymatic makers to evaluate the metabolic state of glial cells grown on control and ln2PMMA substrates and (C) densitometry with intensity values normalized by α-tubulin. (D) Western Blot of oxidative stress associated markers and (E) densitometry with intensity values normalized by α-tubulin. (F) Quantification of L-lactate concentration in medium from glial cells grown for 3DIV on control and ln2PMMA substrates (eight different samples of each condition). For Western Blot analysis we performed 3 different experiments with 9 different samples and full membranes are shown in figure S2. Statistical analysis: unpaired T-Test, *p<0.05, **p<0.01. TCA: tricarboxylic acid cycle. OXFHOS: oxidative phosphorylation.

The interpretation of these data is challenged by the heterogeneity of our glial cultures. Therefore, we explored whether the expression changes in metabolic enzymes were concentrated in particular cellular subpopulations. Unfortunately, pPDH and PFKFB3 antibodies were not suitable for immunostaining. Therefore, we immunostained glial cultures for PCK2 and nestin (RG) detection. PCK2 was expressed in subsets of nestin+ and nestin- cells in both substrates (Fig. R-4.2-2A). Despite the non-significant PCK2 rise in WB, we found a significant increase in the percentage of cells expressing PCK2 in ln2PMMA ($p<0.01$), which mainly corresponded to nestin+ cells (Fig. R-4.2-2B). Suggesting that ln2PMMA mechanical signals increase oxidative glycolysis and anabolic capacity at least in some subsets of glial cells.

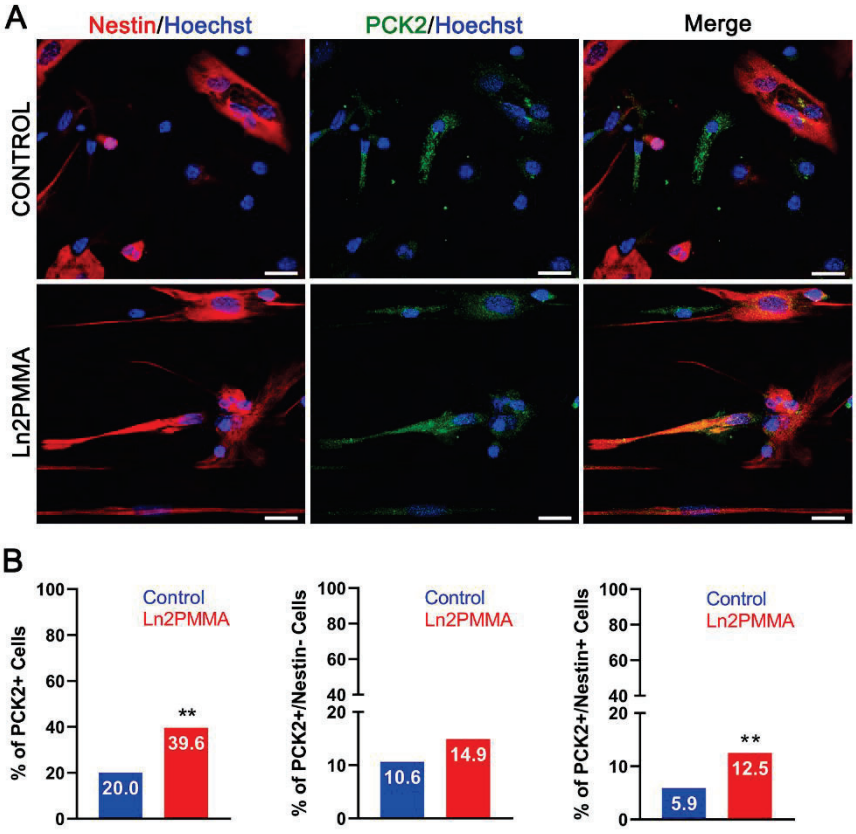


Figure R-4.2- 2 Ln2PMMA increase PCK2 expression in glial cells. (A) confocal images of glial cells grown for 3DIV in control and ln2PMMA substrates immunolabeled for PCK2 (green) and nestin (red). (B) Barr plots showing the percentage of PCK2+ cells and their colocalization with nestin. Chi-square test with post-hoc multiple comparisons, **p<0.01. Scale bar 20µm.

In summary, although much more work is required, these results suggest that metabolic adaptation to ln2PMMA mechanical signals involved a mild increase in PFKFB3-dependent glycolysis and PCK2-dependent anabolism in glial cells. Changes that are characteristics of increased stemness and correlate with the rise in RG in glial cells in ln2PMMA.

4.1.2. Analysis of mitochondrial dynamics in glial cells grown on ln2PMMA and control substrate.

Mitochondria are dynamic organelles that adapt their network dynamics and metabolic functions to mechanical, physical, and metabolic cues, and are crucial actors in cell differentiation (Baum & Gama, 2021). Particularly, in a recent study, mitochondrial morphology and network state determines the different tempo of neurogenesis in the rodent and human brain (Iwata et al., 2023b). On this basis, we inquired whether mechano-driven metabolic shifts of glial cells grown on ln2PMMA substrates modulate mitochondrial dynamics. In figure R-4.2-3A we pictured the main effectors of mitochondrial fusion and fission machinery: mitofusin 2 (MFN2) and optic atrophy protein 1 (OPA1) regulate fusion; and dynamin-related protein 1 (DRP1) and mitochondrial fission 1 (FIS1) regulate fission.

Next, we analyzed by Western blot the expression of MFN2, OPA1, DRP1, FIS1, and the voltage-dependent anion channel (VDAC), which is the most abundant protein in the mitochondrial outer membrane and thus, can served as surrogate mitochondrial normalizer (Figure R-4.2-3B-C). In ln2PMMA, the expression of MFN2 significantly increased while total OPA1 (including l-OPA1 and s-OPA1 isoforms) decreased with respect to control substrate, indicating differential changes in the inner and outer mitochondrial fusion machinery. DRP1 and VDAC expression remained constant between substrates, suggesting that fission machinery and total mitochondrial mass were unaffected in ln2PMMA. Unfortunately, we could not detect FIS1 expression.

Then, we evaluate whether the differential changes observed in the mitochondrial fusion machinery in ln2PMMA affected mitochondrial shape and network. We performed live mitochondria staining with MitoTracker™ Red CMXRos probes (Fig. R.4.2-3D) and morphometric analysis using ImageJ Mitochondrial Analyzer Plugin (Chaudhry et al., 2020) as described in the methods section 3.6 (Mitochondrial morphology characterization). Our morphometric analysis revealed that glial cells in ln2PMMA have significantly less mitochondria but accounting for higher mitochondrial volume per cell. Moreover, mitochondria are more elongated and ramified (Fig. R.4.2-3E), indicating a higher interconnected mitochondrial network. Furthermore, MitoTracker™ CMXRos uptake by mitochondria is dependent on mitochondrial membrane potential ($\Delta\Psi m$) and accumulates in active mitochondria. We found that MitoTracker™ CMXRos fluorescence intensity per mitochondrial volume was significantly lower in ln2PMMA than in control substrate (Fig. R.4.2-3E), indicating lower $\Delta\Psi m$. These results align with the increase in glycolytic enzymes and reduction of antioxidant enzymes previously described in ln2PMMA glial cultures.

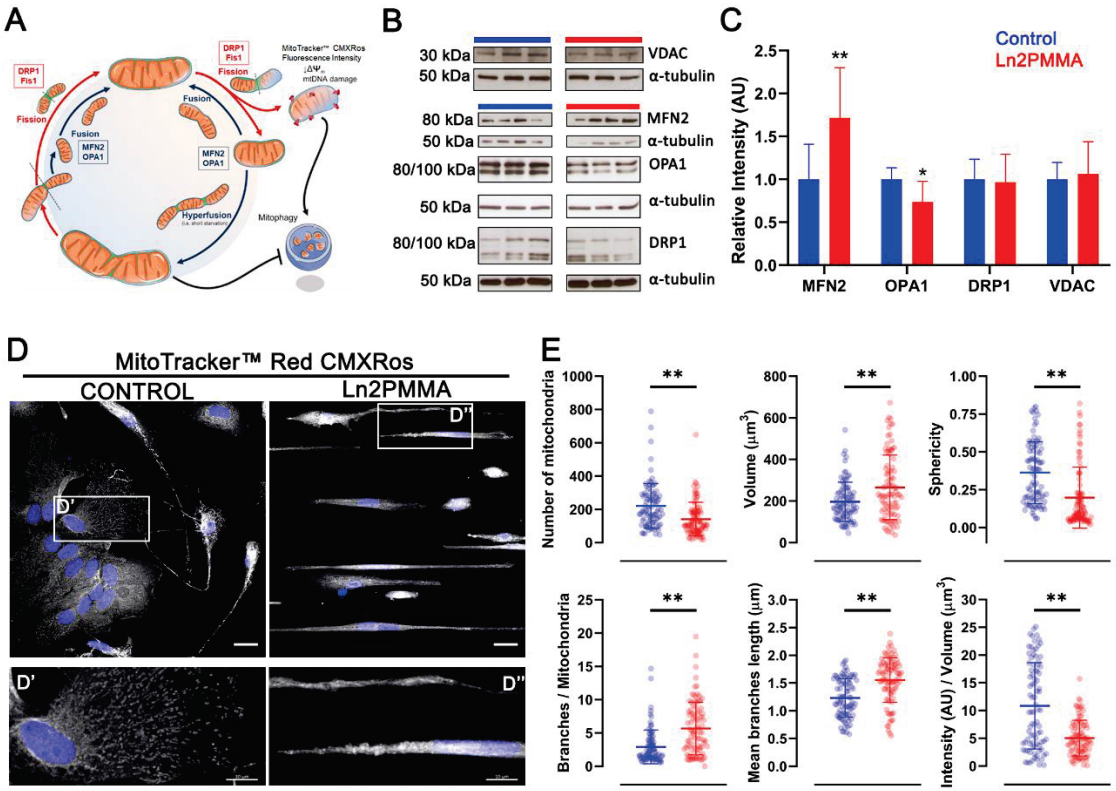


Figure R-4.2- 3 Ln2PMMA biomechanical adaptation induced a generalized mitochondrial network remodeling in glial cells. (A) Schematic of mitochondrial dynamics (fusion and fission) adapted from (Quintana-Cabrera & Scorrano, 2023). (B) Western Blot of VDAC and fusion and fission machinery proteins from glial cells grown on control and ln2PMMA substrates (full membranes are shown in figure S2), and (C) densitometry with intensity values normalized by α-tubulin. (D) Glial cells lived labeled with MitoTracker™ Red CMXRos, 30' at 37º before fixation (top). Squares show zoom detail of mitochondrial morphologies in control and ln2PMMA (bottom). (E) Individual plots showing mean and SD of different mitochondrial morphology parameters. Each individual point represents the mitochondrial data of a cell. Number of cells from two experiments: Control=88, ln2PMMA=92. For Western Blot analysis, at least 3 different experiments with 9 different samples. Statistical analysis: unpaired T-Test, *p<0.05, **p<0.01.

To explore whether those mitochondrial changes were linked to specific cell types, we immunolabeled MitoTracker™ Red CMXRos-live stained glial cultures grown on control and ln2PMMA substrates with nestin and Pax6 markers (Fig. R-4.2-4A-B). In control substrate, nestin-/Pax6- non-RG cells have significantly fewer mitochondria, which were more elongated, interconnected and with lower ΔΨm than Pax6+ RG and Nestin+/Pax6- glia, with the last two cell types sharing similar mitochondrial shape and network connectivity. The ln2PMMA mechanical adaptation effects on mitochondrial shape and connectivity already described were restricted to Pax6+ RG and Nestin+/Pax6- glia (Fig. R-4.2-4C).

Altogether, our data indicated that the biomechanical adaptation to ln2PMMA force RG lineage cells to a profound metabolic rewiring that involved mitochondrial dynamics and

network reorganization, to support the shift towards the more glycolytic and anabolic metabolism characteristic of stem cells.

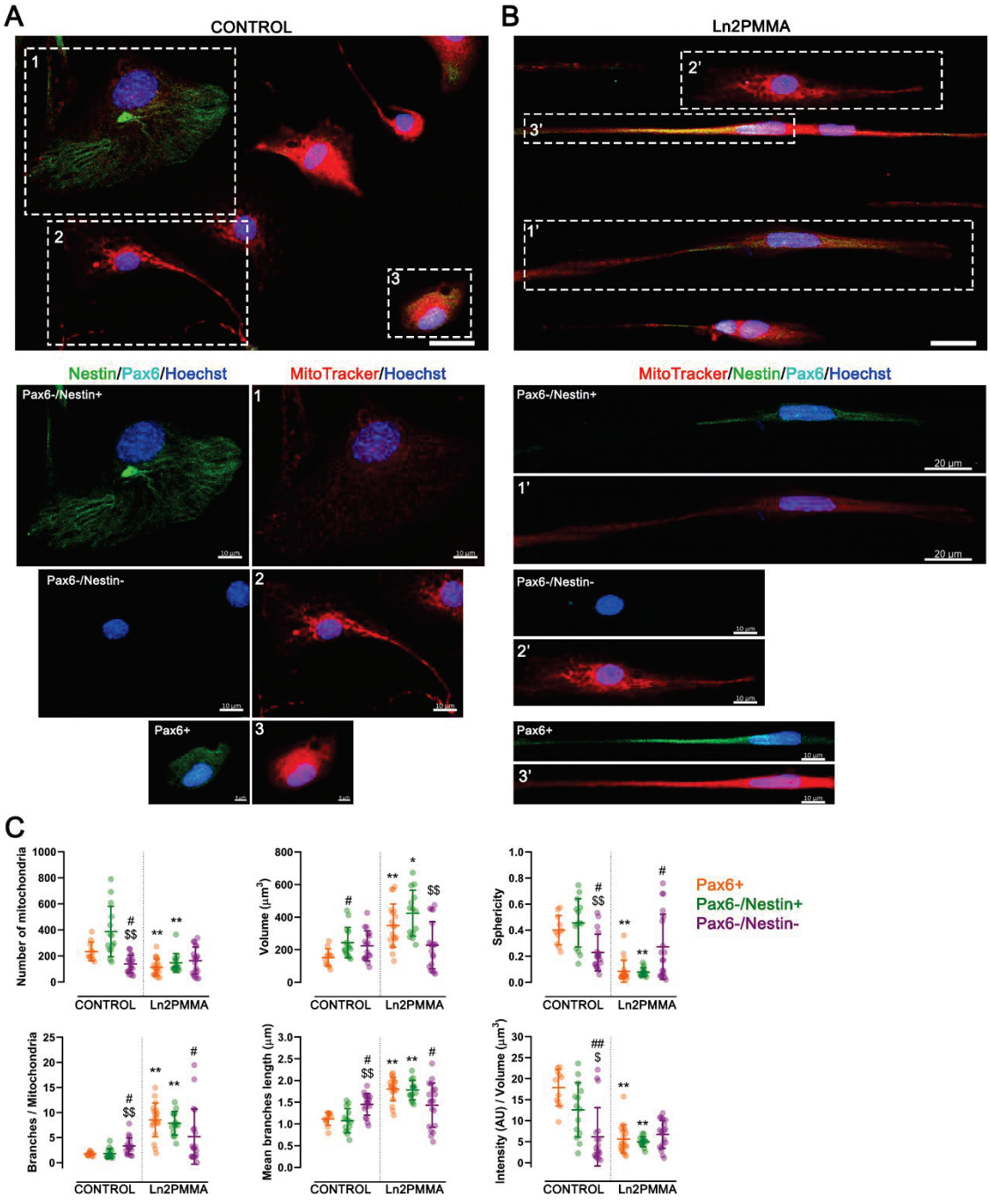


Figure R-4.2- 4 **Ln2PMMA induce mitochondrial reshape and network rewiring in RG lineage cells**. Glial cells live-labeled with MitoTracker™ Red CMXRos (red), and immunolabeled with Pax6 (turquoise) and nestin (green) markers. Nuclei were counterstained with Hoechst 33342 (blue). (A) Control and (B) ln2PMMA substrates. Cells within dashed rectangles are displayed down the main figure with a 33% zoom. (1) Pax6+ RG, (2) nestin+/Pax6- cells, and (3) nestin-/Pax6- non-RG cells. Scale bar from the principal images 20um. (C) Individual plots showing mean and SD of different mitochondrial morphology parameters from three different cell types: Pax6+ RG (orange), nestin+/Pax6- cells (green), and nestin-/Pax6- non-RG cells (fuchsia). Each individual point represents the mitochondrial data of a cell. Control: Pax6+ (N=11), nestin+/Pax6- (N=14), and nestin-/Pax6- (N=18). Ln2PMMA: Pax6+ (N=19), nestin+/Pax6- (N=14), and nestin-/Pax6- (N=19). Kruskal Wallis with multiple comparison test. Differences between substrates for the

same cell type: *p<0.05, **p<0.01. Differences between cell-types within substrates: # compared to Pax6+: #p<0.05, ##p<0.01; and $ compared to nestin+/Pax6-: $$p<0.01.

4.3. Role of nuclear deformation in the biomechanical induction of RG.

In the following section, we explored whether nuclear deformation was associated with mechanical-driven RG induction in ln2PMMA substrates. We linked nuclear morphology parameters with cell type-specific molecular markers by using a custom-made image segmentation application, to easily process large amounts of data and generate a kind of single-cell high-throughput database. This database was later analyzed and used to build a logistic regression model to reliable predict RG based on specific nuclear morphology parameters.

4.3.1. Nuclear morphology analysis.

We then investigated whether, in parallel to cell bodies, nuclei were also aligned with the topography. For that, we quantified three nuclear parameters: area (μm²), eccentricity (from 0 round to 1 elongated shapes), and orientation (converted from 360º to 90º scale) (see methods section 3.5; Fig. R-4.3-1A, B). This analysis showed that in ln2PMMA, glial cells nuclei were significantly more eccentric and aligned with the grooved topography than in the control substrate at all-time points (1-14DIV) (Fig. R-4.3-1C-F). The nuclear area was also significantly different in glial cells grown in ln2PMMA with respect control substrate, with changes that were dynamic over time (Fig. R-4.3-1C-F).

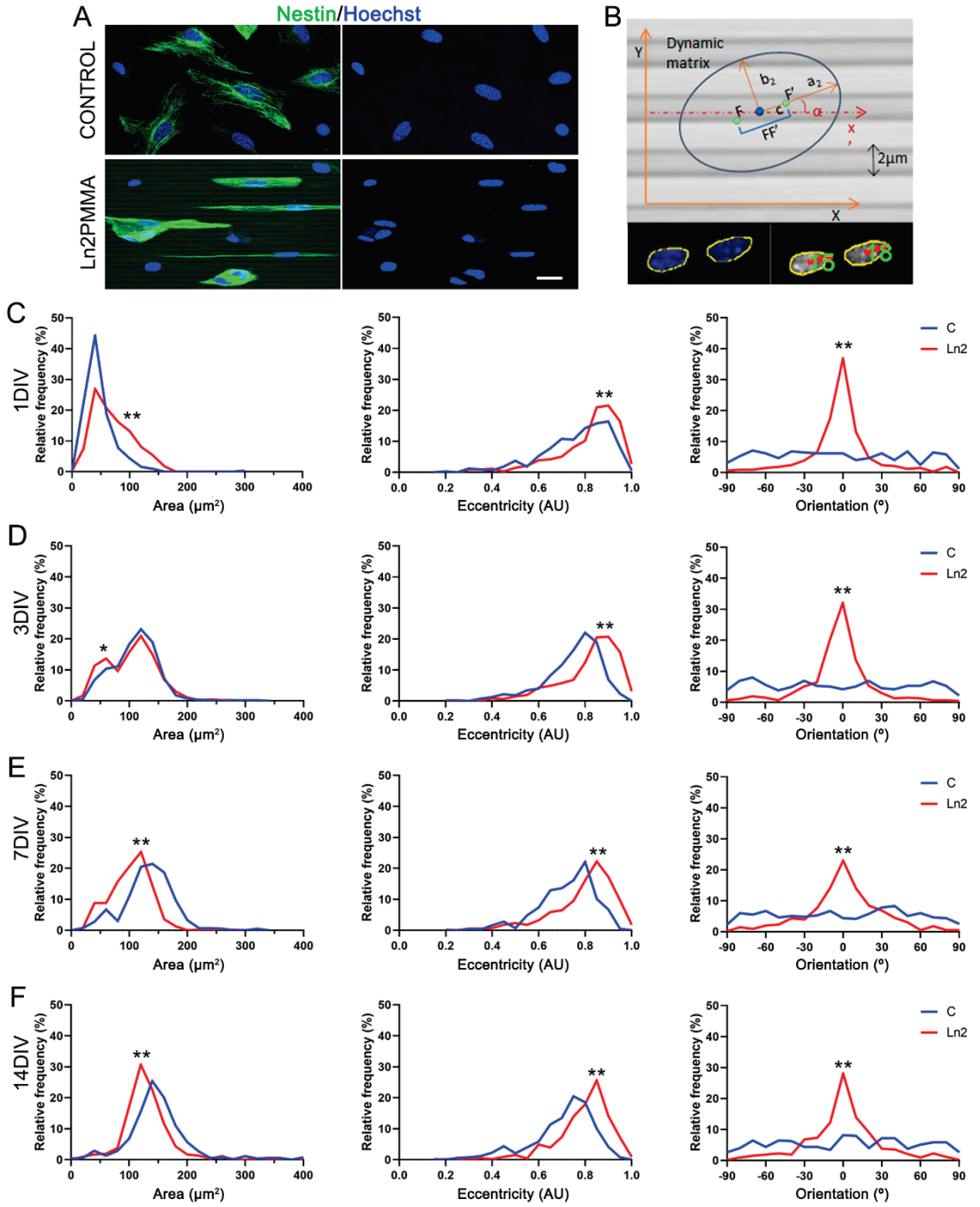


Figure R-4.3- 1 **Time-dependent changes in nuclear morphology and alignment in control and ln2PMMA glial cultures.** (A) Glial cells in control and ln2PMMA labeled with nestin (green) and Hoechst to stain nuclei (blue). (B) Nuclear morphology parametrization scheme. Graphs showing relative frequency of nuclear morphology parameters (area, eccentricity, and orientation) of glial cells cultured on control (blue) and ln2PMMA (red) over time: (C) 1DIV, (D) 3DIV, (E) 7DIV and (F) 14DIV. Mann-Whitney test *p<0.05 and **p<0.01. Scale bar, 20µm.

To evaluate whether these nuclear changes were substrate dependent, cell type-specific, or both, we performed a linear regression analysis of nuclear area and eccentricity associated with nestin, GFAP and Pax6 positive cells over time in culture (Fig. R-4.3-2). For all cell types analyzed, nuclear area increased over time (positive slopes), although

significantly faster in control than in ln2PMMA substrate ($p<0.01$, Figure R-4.3-2). Moreover, nuclear growth rates were cell type-specific in control (slopes were significantly different $p<0.01$). On the contrary, the nuclear growth rates were similar in ln2PMMA, despite they differed in the initial nuclear areas (intercepts were significantly different $p<0.01$, Fig. S3A). For each cell type, nuclear eccentricity was significantly different in ln2PMMA (intercepts $p<0.05$) but not in control and tended to decrease with time (negative slopes), although with no significant differences between substrates (Fig. R-4.3-2, Fig. S3B).

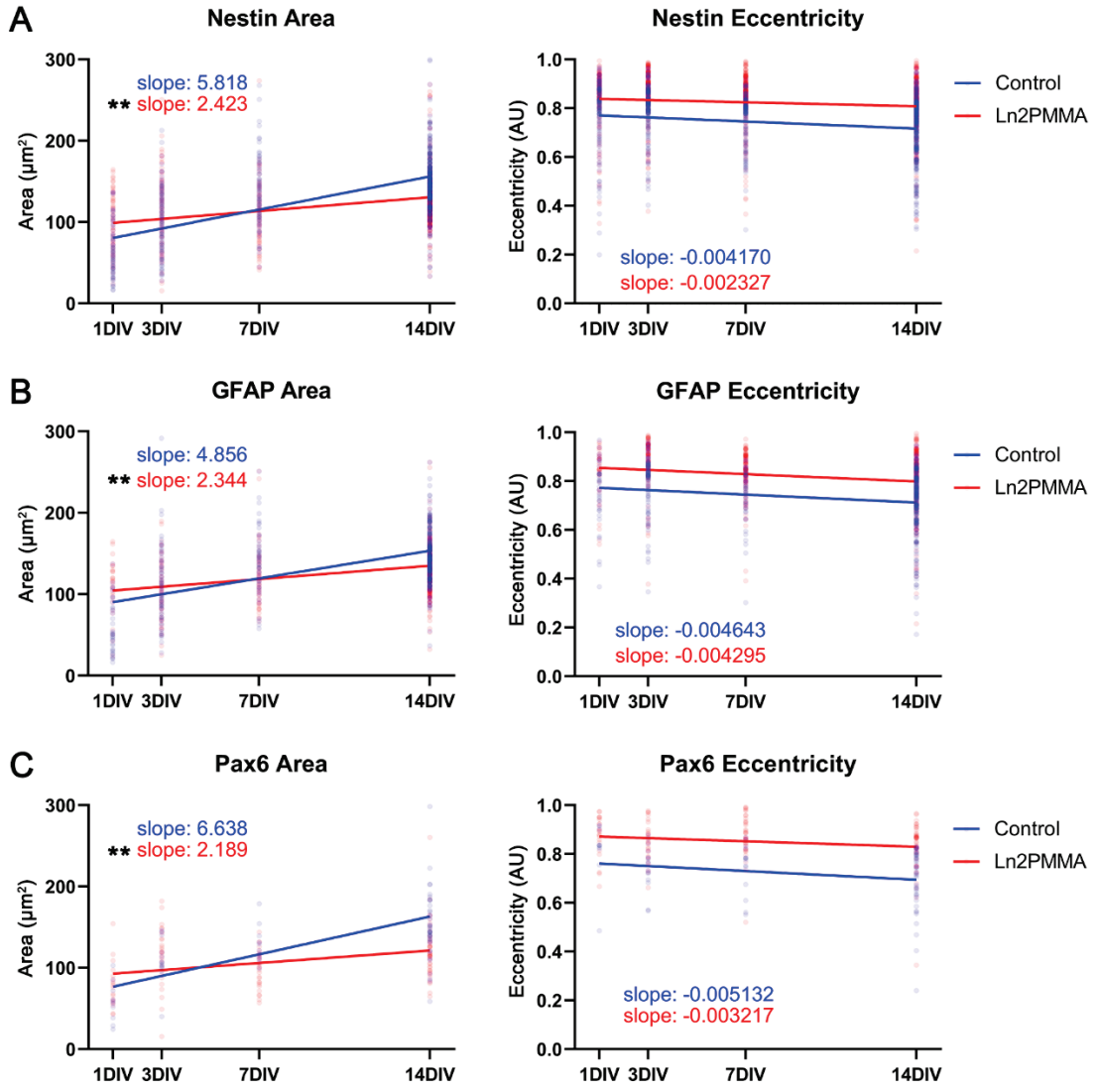


Figure R-4.3- 2 **Nuclear shape follows cell type-specific dynamics over time in control and ln2PMMA.** Linear regression plots show changes in nuclear area and eccentricity over time in culture (1, 3, 7, and 14DIV) in control (blue) and ln2PMMA (red) substrates. (A) nuclei from nestin+ cells, (B) nuclei from GFAP+ cells, and (C) Pax6+ nuclei. ANCOVA test **p<0.001. Eccentricity graphs; slopes p=ns, all intercepts p<0.01.

Taking all together, these data indicated that ln2PMMA grooved microtopography was early sensed by glial cells, promoting cellular and nuclear orientation. Moreover, ln2PMMA induced cell type-specific nuclear conformational changes along the RG-astrocyte lineage.

To broad the glial cell types analyzed in our cultures at 3DIV, we used Sox2 as a general stem cell marker, NG2 to identify oligodendrocyte precursor cells (OPC), and Gsx2 for tri-potential intermediate progenitors (tri-IPC) identification, in addition to GFAP, Pax6 and nestin markers (Fig. R-4.3-3A). We also TBR2 as neuron-restricted progenitors marker but, unfortunately, although the antibodies worked well in WB, all of them gave very unspecific immunostaining in our cultures, and we could not introduce this cell-type in the analysis (Fig. S4). As expected, there were significantly less GFAP+ cells ($p<0.05$) and more Pax6+ cells ($p<0.05$) in ln2PMMA with respect to control substrate (Fig. R-4.3-3B), but no significant differences were found for the rest of cell-type markers analyzed. When examining markers co-expression, nestin and GFAP colocalized in 50% of the cells, and 80% of Pax6+ cells also expressed Sox2, while only 30% of Sox2+ cells also expressed Pax6. This data highlights the necessity of using multiple cell-type markers to accurately identify the different types of glial cells.

To explore the global effect of ln2PMMA on the nuclear area and eccentricity associated to each glial cell type, we performed multivariate kernel density estimation, a nonparametric technique for populations density estimation. This analysis showed density probability regions for each cell marker based on shared area and eccentricity (Fig. R-4.3-3C). No differences between marker distributions were found using the Peacock test, thus, we used paired T-test for individual statistical observations of area and eccentricity between substrates (Table S1). This analysis showed that nuclei from nestin+, GFAP+, Pax6+ and Sox2+ cells were significantly deformed in ln2PMMA, while nuclei from NG2+ and Gsx2+ cells did not significantly change their morphology.

Taking all together, our data suggest that mechanical signals from ln2PMMA substrate converge to the nucleus, prompting them to assume elongated and aligned configurations, in a subset of mechanosensitive glial cells belonging to the astrocyte-RG lineage (cells expressing GFAP, nestin, Pax6, and Sox2). In contrast, cells expressing NG2 and Gsx2 were less responsive to mechanical signals from the substrate and may represent more committed developmental side-paths.

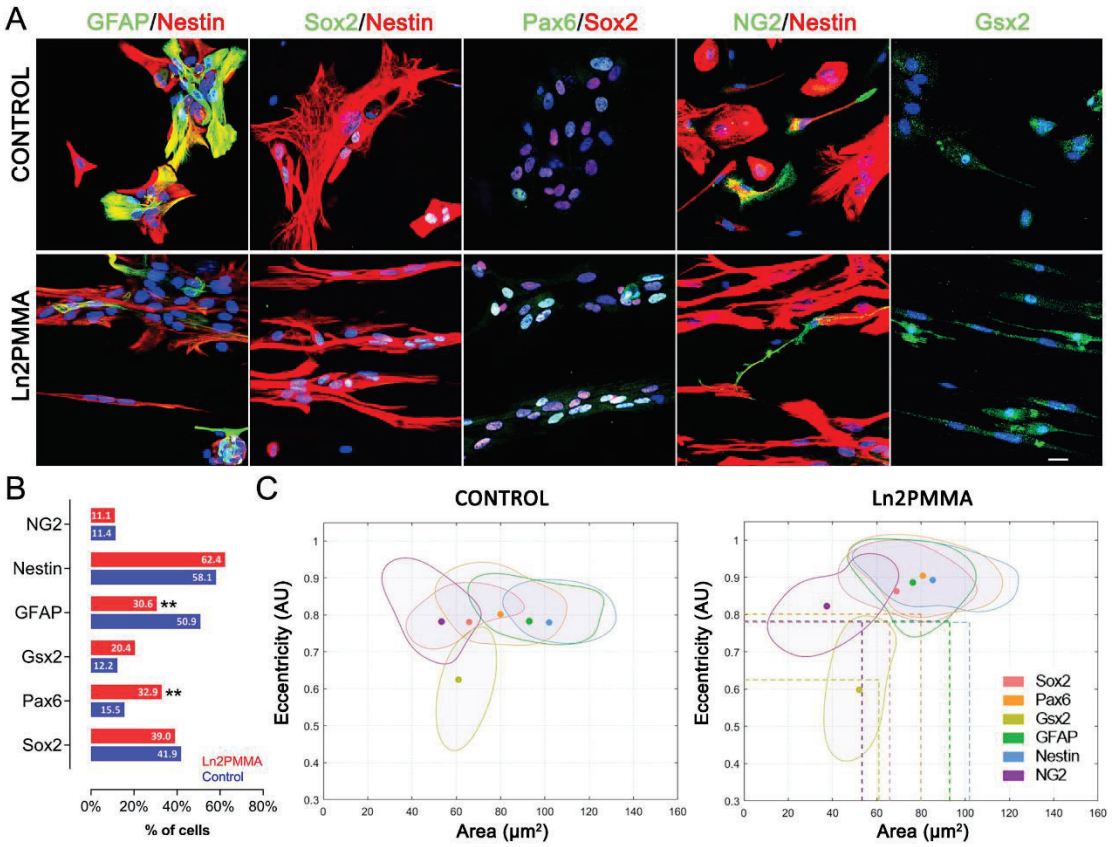


Figure R-4.3- 3 **Cellular composition and multivariate kernel density estimation of nuclear morphology changes in glial cultures grown for 3DIV on control and ln2PMMA**. (A) Glial cells grown on control and ln2PMMA labeled with the cell type-specific markers GFAP, nestin, Pax6, Sox2, NG2 and Gsx2. Nuclei are stained with Hoechst (blue). (B) Barr plot summarizing the percentage of GFAP, nestin, Pax6, Sox2, NG2 and Gsx2 positive cells observed in control and ln2PMMA. (C) Graphs showing multivariate kernel density estimation of specific area (x-axis) and eccentricity (y-axis) for each cell type. Centroids represent median values. In Ln2PMMA plot, dashed lines correspond to area-eccentricity centroids observed in control substrate, each color corresponds to each cell type. ** p<0.01 Chi-square test. Scale bar, 10µm.

4.3.2. Development of a logistic regression model for fitting RG probability based in nuclear morphology parameters.

Glial cell culture on control substrate is highly disadvantageous for the maintenance of functional RG cell phenotypes, while culture on ln2PMMA substrate, which mimic RG architecture in vivo, is highly favorable for the presence of functional RG cell phenotypes (Mattotti et al., 2012). Additionally, cell-cell interactions are essential determinants of cell shape, proliferation, differentiation, and growth. During development, the community effect is a mechanism by which interactions among groups of precursor cells facilitate their coordinated differentiation (Saka et al., 2011). In the following subsections we break down into the development and interpretation of a statistical regression model based on nuclear morphology changes induced by ln2PMMA. The structure of the model effects emphasizes the contribution of cell density, which only interacts with nuclear morphology

parameters (area and eccentricity). Additionally, it underscores the significance of the cell-substrate interaction (ln2PMMA) in directing the progression of the RG lineage.

Model Selection

To evaluate whether nuclear deformation constitutes a hallmark in RG phenotype induction in ln2PMMA, we constructed several logistic regression models to explain the success defined by nuclei been specific of RG, including as predictors nuclear area, eccentricity, and cell culture density (the community effect). The models hinge on a binary response, RG or not RG, determined by the presence or absence of molecular markers associated with the RG phenotype. We used general linear models (GLM) and the logit function, which links the binary response with the linear predictor, and estimates the probability of an event to happen. In our case, the event to happen was to determine if RG cells had a specific nuclear morphology, using glial cultures grown in control and ln2PMMA substrates for 3DIV.

From the basis that the main variables used in our models were the nuclear measurements of area and eccentricity, we developed multiple models of increasing complexity, by adding, suppressing, or conditioning these variables with substrate type or cell density. The best model was selected following the AIC criterion, as lower AIC values indicate better-fitted models with less complexity. We refined the selected model by a step-by-step procedure, to eliminate complex and non-significant terms. In table R-4.3-1 we summarize different approaches, which are divided into two groups depending on the use of the nuclear bounding box or not. The bounding box is an imaginary rectangle that tightly encloses the shape of each nucleus.

Table R-4.3- 1 Summary of the different models developed. The selected model is highlighted in bold.

	AIC	AUC	lowIC	uppIC
With Bounding Box	1376.774	0.66	0.63	0.69
Without Bounding Box				
Without Substrate	1303.976	0.73	0.7	0.76
Without Cell density	1313.062	0.72	0.69	0.75
With Cell density only with interactions	1302.395	0.74	0.71	0.77
With cell density only with interactions and step-by-step refinement	1300.325	0.73	0.7	0.76

The first model using bounding box obtained an AIC=1376.774, then we discard bounding box and all the resultant models obtained lower AIC's, suggesting the exclusion

of this variable. By suppressing the factor cell density as independent variable and using it only in interaction, we lower the AIC to 1302.395. When analyzing one by one the terms of this model, not all were statistically significant, indicating its relatively low relevance in the response. During step-by-step refinement, most of the non-significant terms were suppressed. For those terms only relevant in a particular substrate interaction, some non-significant terms in the counterpart substrate were also maintained. This refinement successfully reduced the AIC to 1300.325. However, this improvement came at the cost of a reduction in AUC, indicating a trade-off between model complexity and predictive accuracy.

Table R-4.3-2 shows the most relevant terms in the selected model. The sign of the estimated value indicates the direction on the prediction, positive values increase, while negative values decrease the probability to determine a specific RG nuclear morphology. The z-value corresponds to the weight of each term in the model, the larger it was in absolute terms, the higher the impact. Finally, as mentioned before, the main indicator that determines the relevance of any term relies in the p value, represented as Pr(>|z|).

Table R-4.3-2 Relevant terms in the selected model grouped by its substrate dependence. Estimated coefficients, standard error of coefficients, z-value, and p-value (Pr(>|z|)) for every term of the model. The full table is shown in the methods section.

Term	Estimate	Std. Error	z value	Pr(>|z|)
Dependent on substrates				
Ln2PMMA	-9,45E+02	5,66E+02	-1.669	0.095
Control * Eccentricity^3	-2,31E+02	8,84E+02	-0.261	0.794
Ln2PMMA * Eccentricity^3	2,57E+03	7,32E+02	3.509	0.000
Ln2PMMA * Area	-7,33E+00	4,74E+00	-1.546	0.122
Independent on substrates				
Eccentricity^2 * cell density	5,15E+00	2,49E+00	2.068	0.039
Area * cell density	-1,46E-01	4,13E-02	-3.522	0.000

Ln2PMMA is a biomimetic substrate designed to replicate at the micrometric scale the anisotropic 3D organization of the RG niche in vivo, prompting cultured astrocytes to transform into functional RG cells (Mattotti et al., 2012). When analyzing the relevance of the different terms in the selected model, the term associated to ln2PMMA substrate by itself did not yield statistical significance at the 5% significance level. However, in interaction with eccentricity it exhibited a substantial positive impact on the response (Pr(>|z|) <0.01), particularly in identifying a specific RG nuclear morphology. As eccentricity increased, the probability of being a nucleus specific to RG cells became more defined. In our modeling approach, it was crucial to maintain the effect of ln2PMMA

substrate by itself, as the term appeared during model construction, and in interaction with other variables. Similarly, we withheld the interaction between the control substrate and eccentricity, even though it was not statistically significant and had a negative effect on the response (z-value=-2.61E+02). Nevertheless, the presence of cubic eccentricity in interaction with both substrates supported the relevance of increased eccentricity induced by ln2PMMA substrate in favoring a defined nuclear shape for RG. Its noteworthy that we conditioned cell density as an interacting variable, and the model only considered relevance its interaction with area or eccentricity. This corroborates that at high confluence, there was an increase of cell-cell interactions, affecting nuclear morphologies and this is not substrate dependent.

In the selected model, cell density only has significant interactions with area (Pr(>|z|) <0.01) or eccentricity (Pr(>|z|) <0.05) in quadratic or cubic expressions. The presence of substrate-dependent terms allowed splitting the model in two equations, one for control substrate (1) and another for ln2MMA substrate (2).

$$(4)\ \text{logit}(\ \mathrm{P}\big(\mathrm{y}=1\big|(\mathrm{X},\mathrm{Control})\big)=\beta_0+\beta_A\mathrm{A}+\beta_{\mathrm{A}^2}\mathrm{A}^2+\beta_{\mathrm{A}^3}\mathrm{A}^3+\beta_{E^3C}\mathrm{E}^3+\beta_{E^2*Cd}\mathrm{E}^2*\mathrm{Cd}+\beta_{E*Cd^2}\mathrm{E}*\mathrm{Cd}^2+\beta_{A*Cd}\mathrm{A}*\mathrm{Cd}+\beta_{A*Cd^2}\mathrm{A}*\mathrm{Cd}^2+\beta_{A^2*Cd}\mathrm{A}^2*\mathrm{Cd}+\beta_{A^2*Cd^2}\mathrm{A}^2*\mathrm{Cd}^2$$

$$(5)\ \text{logit}(\ \mathrm{P}\big(\mathrm{y}=1\big|(\mathrm{X},\mathrm{Ln2PMMA})\big)=\beta_0+\beta_{0Ln2}+\beta_A\mathrm{A}+\beta_{\mathrm{A}^2}\mathrm{A}^2+\beta_{\mathrm{A}^3}\mathrm{A}^3+\beta_{E^3Ln2}\mathrm{E}^3+\beta_{ALn2}A+\beta_{E^2*Cd}\mathrm{E}^2*\mathrm{Cd}+\beta_{E*Cd^2}\mathrm{E}*\mathrm{Cd}^2+\beta_{A*Cd}\mathrm{A}*\mathrm{Cd}+\beta_{A*Cd^2}\mathrm{A}*\mathrm{Cd}^2+\beta_{A^2*Cd}\mathrm{A}^2*\mathrm{Cd}+\beta_{A^2*Cd^2}\mathrm{A}^2*\mathrm{Cd}^2$$

The expression *logit (…)* indicates the application of the linear predictor to the associated probability to the response *y=1*, i.e. success defined by been RG, using the variables *X* in control or ln2PMMA substrates. Remember that *β* corresponds to estimated coefficients*, A* corresponds to area, *E* to eccentricity and *Cd* to cell density. Specific terms depending on substrate are indicated as C for control and Ln2 for ln2PMMA.

Interpretation and behavior of model variables

We then analyzed the behavior of model terms by plotting terms effects in function of eccentricity and area, in both substrates and at different cell densities (Fig. S4 and S5). Using control equation and control substrate data, RG nuclei probability shows a nearly-linear increase in function of eccentricity, although never gets over 50%. Using ln2PMMA equation and ln2PMMA data, RG probability shows an evident positive quadratic relationship with nuclei eccentricity, with a negligible probability for rounded nuclei and an abrupt slope increase at eccentricities >0.7, reaching probabilities >60% for nuclear areas ranged q25-q75 (Fig. S4 and S5). When analyzing RG probability in function of area, both equations show a cubic behavior, with a maximum of probability for nuclear

areas in the range of 50-120μm^2 that increased for eccentricities >0.7, and a probability minimum in the range of 120-250μm^2.

To facilitate model terms interpretation and define more accurately the emerging RG nuclear morphology region, we generated surface plots showing area, eccentricity, and adjusted probability curves at different cell densities. Using the range of eccentricity (0.7-1) and area (0 to 150 μm^2) predetermined by the observed behavior in 2D (Fig. S5). Level curves allowed us to observe an "RG region" where the probability to predict RG nuclei was at least 50%. This "RG region" include areas of 90-110 μm^2 and eccentricity ≥0.95 in control (Fig. R-4.3-4A), and areas of 50-150μm^2 and eccentricity ≥0.85 in ln2PMMA (Fig. R-4.3-4B). Despite the relevant threshold differences, in both substrates, the size of the "RG region" decreases and shifts to higher eccentricities as increases the cell density.

Together with these results, emerged a "RG region" in which RG probability raises for medium sized and highly elongated nuclei. Moreover, for the same nuclear morphology, the probability of being predicted as RG nuclei by the selected model differs between substrates and is dynamically modulated by cell density.

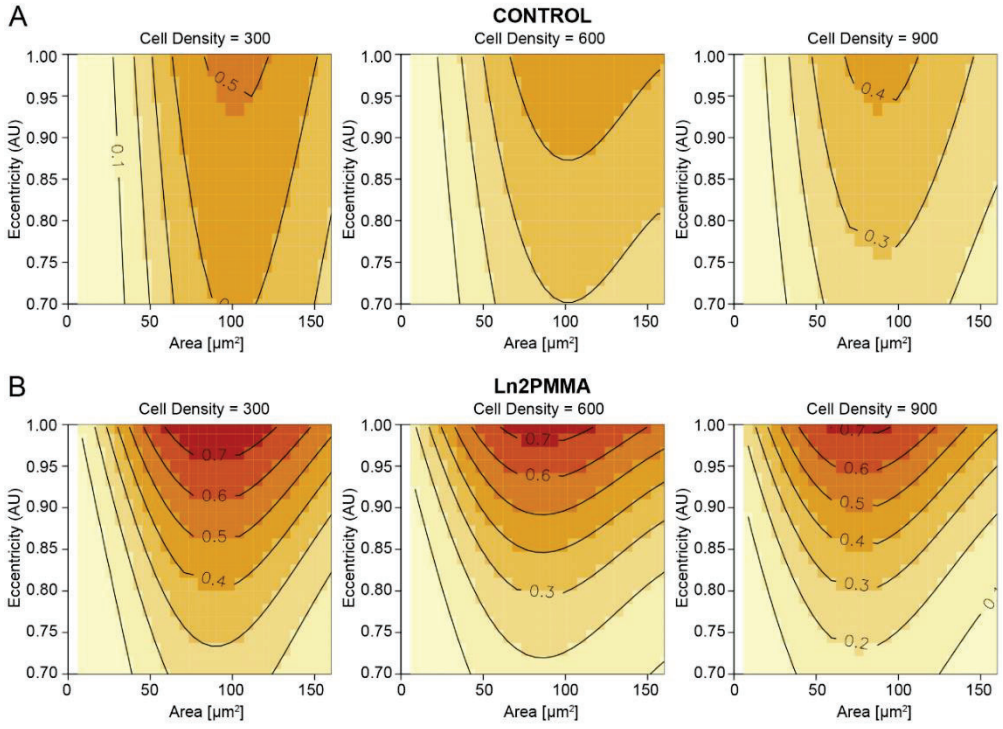


Figure R-4.3- 4 **The model delimitated a specific RG nuclear morphology**. Surface plots of eccentricity (x-axis) and area (y-axis). Line curves represented the adjusted probability to be defined as RG at three different cell densities, 300, 600 and 900 cells/mm^2 in control (A) and ln2PMMA substrates (B).

Model equation selection

The selected model was initially described as a single equation, that varies depending on the substrate. This results in two material-dependent equations that predict different RG probabilities for nuclei with exactly the same morphology. A dichotomy that raised the question of whether there was a defined RG-specific nuclear morphology. Thus, we evaluated the matching between the model predictions and the proportion of experimentally observed RG, based in the combinatorial expression of accepted RG molecular markers (Pax6, nestin and Sox2). For that, we first used the control equation to draw the model fitted probabilities density plot for datasets in control and ln2PMMA used for model construction. We calculated the area under the curve (AUC) at two thresholds, 33% and 50% probability, for better description of distribution symmetry (skewness) and its localization along the probability axis (Fig. R-4.3-5). At 50% threshold, the control equation predicted 2% of RG in control and 11% in ln2PMMA, values far below the experimental observations of 15.1-22.4% cells expressing RG markers in control, and 30.5-32.9% in ln2PMMA (Fig. R-4.3-5). In contrast, the application of the equation defined for ln2PMMA predicted 10% of RG in control and 33% in ln2PMMA much closer to the experimentally observed RG values in both substrates (Fig. R-4.3-6). When segregating by RG molecular markers, the ln2PMMA equation predictions precisely matched with ln2PMMA data, varying 0.1% (Pax6+), 2.5% (Sox2+/nestin+) and 0.2%(Sox2+/Pax6+) and deviate more from control data 5.1% (Pax6+), 12% (Sox2+/nestin+) and 5.5% (Sox2+/Pax6+) (Fig. R-4.3-6).

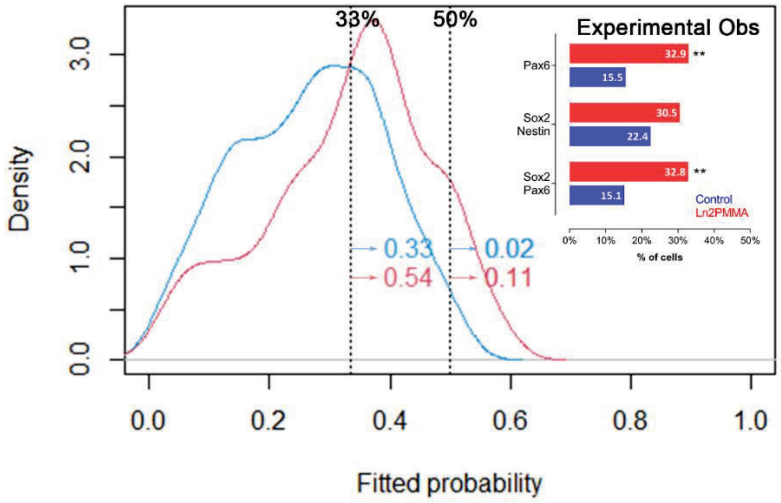


Figure R-4.3- 5 **Application of control equation to data used for fitting**. Density plot with model fitted probabilities, control substrate data in blue and ln2PMMA substrate data in red. Dashed line delimitates thresholds at 33% and 50% of probability. The numbers correspond to the AUC from each threshold and the arrows indicate the direction of calculated AUC. Bars plot shows the proportion (numbers in white) of cells expressing the RG markers in representative datasets used to build the regression model. *p<0.05, **p<0.01, Chi-square test.

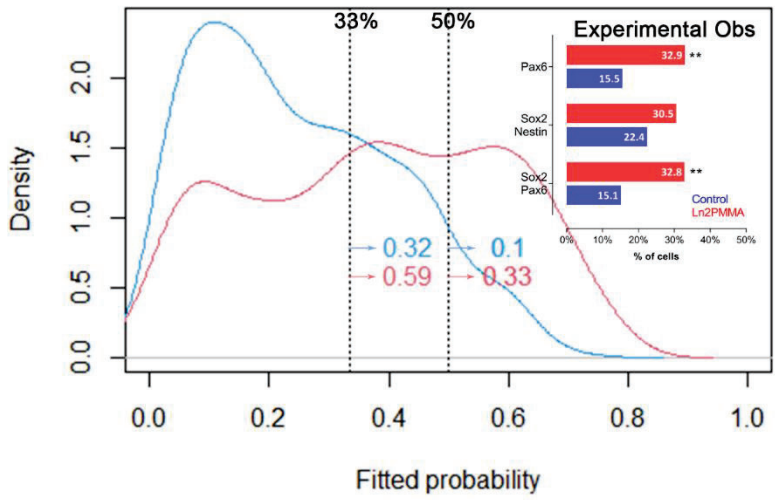


Figure R-4.3- 6 **Application of ln2PMMA equation to data used for fitting**. Density plot with model fitted probabilities, control substrate in blue and ln2PMMA substrate in red. Dashed line delimitates thresholds at 33% and 50% of probability. The numbers correspond to the AUC from each threshold, arrows indicate the direction of calculated AUC. The bars plot shows the proportion (numbers in white) of cells expressing the RG markers in the same representative datasets used to build the regression model described in R-4.1- 3. Chi-square test, *p<0.05, **p<0.01.

The higher accuracy of model predictions when using ln2PMMA equation correlates with its associated 0.77 AUC, with respect to the 0.66 AUC of control equation. This unexpected substrate-independent accuracy of ln2PMMA equation in predicting RG made us consider the unique equation that identifies a specific RG nuclear morphology, discarding the control equation. As ln2PMMA mimics the architecture of RG niche in the embryonic brain (Mattotti et al., 2012), from now, we named the model exclusively based in ln2PMMA equation as Radial Glia Mimetic (RGM) model.

RGM model application to the datasets used for fitting the model

Initially, to define the model binary response (RG or not RG), we established categorical assignments based on cell type-specific expression patterns described in the literature. Then, we used the RGM model to investigate whether model assignments match with the initial categories. By performing the same density plots with model fitted probabilities described above, we analyzed the RG probability of cells with all single and double molecular marker combinations used in the model. Fig. R-4.3-7 shows density plots ordered by decreasing RG percentage prediction.

The molecular marker combinations with RGM model predictions for RG > 0.5 AUC at 50% probability were for cells expressing Pax6+/GFAP+ > Pax6+/nestin+ > Pax6+ > Pax6+/Sox2+ > nestin+/Sox2+ (Fig. R-4.3-7A-E). Confirming Pax6 transcription factor and Nestin+/Sox2+ combination as bona fide RG markers. The second conclusion is that, in our culture conditions, the expression of nestin, GFAP, or both, is not informative

about the astrocyte-RG differentiation state, as RG predictions at 50% of probability threshold were quite similar for nestin+/GFAP+ > nestin+ > GFAP+ cells (8-10% in control and 43-49% in ln2PMMA) (Fig. R-4.3-7F, G, I). Moreover, nestin-/GFAP- > NG2+/nestin- > Gsx2+ cells have only residual probability to be RG (2-6% in control and 0-8% in ln2 PMMA) (Fig. R-4.3-7N-P). Results that evidence the important role of GFAP and nestin intermediate filaments in defining astrocyte-RG cell lineage but not the exact developmental point. In this sense, the RG probability of NG2+ cell population is bimodal, depending on nestin co-expression. RG probability of NG2+/nestin+ cells are similar than for nestin+ cells, probably representing the initial step of the developmental side branch leading to NG2+/nestin- committed OPC (Nishiyama et al., 2009) (Fig. R-4.3-7G, H, M, O). Similarly, the RGM model identifies Gsx2+ cells, which represent tri-potential intermediate progenitors (Zhang et al., 2020), as a developmental side-branch out of the astrocyte-RG developmental trajectory.

In summary, the RGM model application revealed that, in our glial culture system, only cells expressing nestin/GFAP intermediate filaments have the capacity to move along astrocytic-RG lineage and dedifferentiate into an RG phenotype in response to the mechanical stimulus. Moreover, the acquisition of the RG phenotype is associated with nuclear deformation and the acquisition of a particular RG-specific nuclear shape.

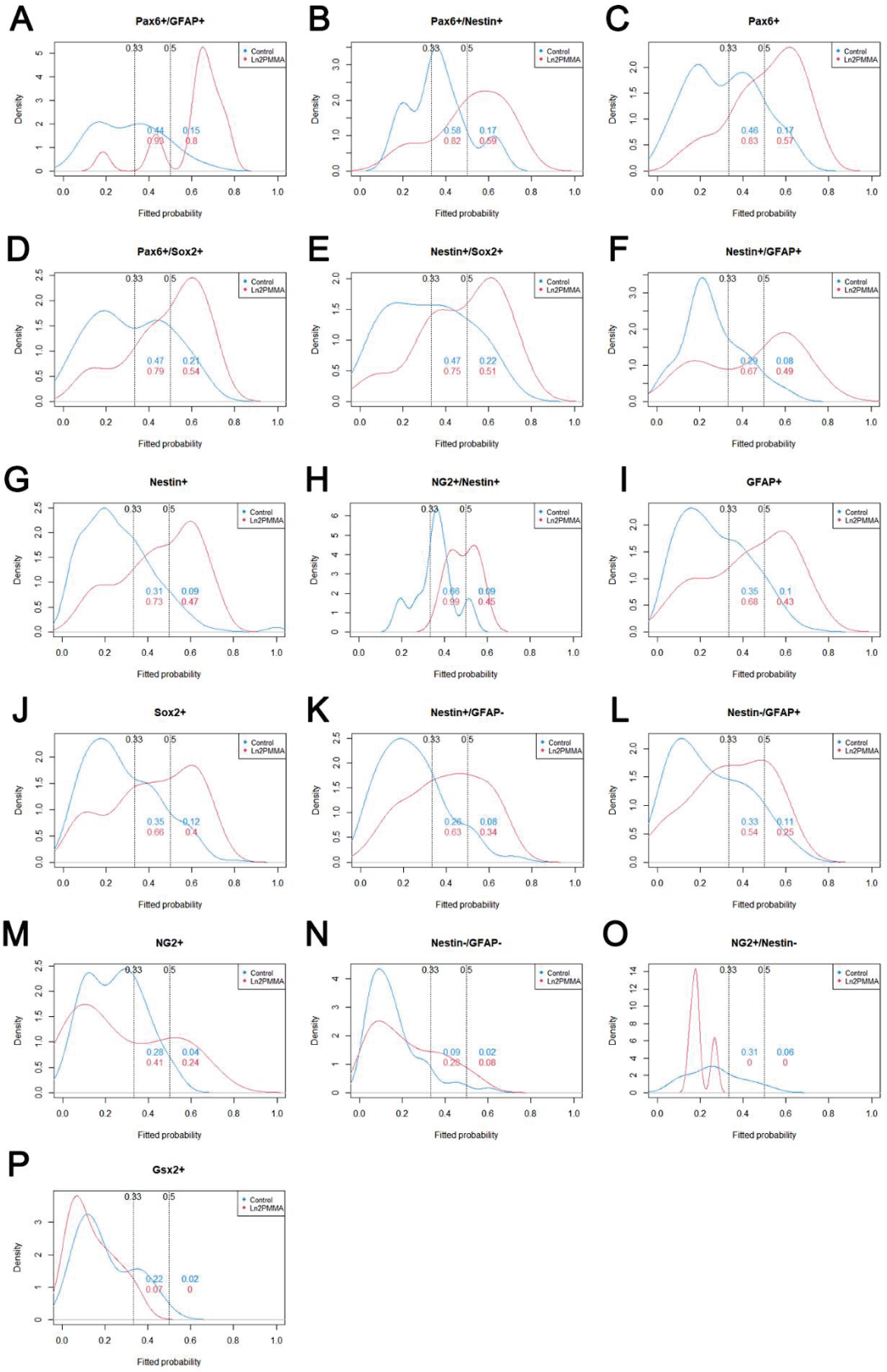


Figure R-4.3- 7 **RGM model application to glial subpopulations expressing different lineage marker combinations.** Density plots with model fitted probabilities with control substrate in blue and ln2PMMA substrate in red. Dashed line delimitates thresholds at 33% and 50% of probability. The numbers correspond to the AUC from each threshold. Plots are ordered from left-right and up-down by decreasing RG prediction

at 50% probability threshold. (A) Pax6+/GFAP+ (N=42), (B) Pax6+/Nestin+ (N=50), (C) Pax6+ (N=305), (D) Pax6+/Sox2+ (N=103), (E) Nestin+/Sox2+ (N=69), (F) Nestin+/GFAP+ (N=68), (G) Nestin+ (N=1070), (H) NG2+/Nestin+ (N=16), (I) GFAP+ (N=362), (J) Sox2+ (N=425), (K) Nestin+/GFAP- (N=138), (L) Nestin-/GFAP+ (N=84), (M) NG2+ (N=68), (N) Nestin-/GFAP- (N=152), (O) NG2+/Nestin- (N=12), (P) Gsx2+ (N=38).

The LogOdds ratio function F(0) identified intrinsic mechanical nuclear constrains in RG

The somehow surprising finding was that our RGM model accurately identfied RG nuclear morphologies in glial cultures independent of culture substrate. This, raises the possibility of cell-intrinsic mechanical factors limiting the range of nuclear shapes in functional RG cells. If that was true, the model terms specifically associated with ln2PMMA might represent those RG cell-intrinsic nuclear constraints, favored by mimicking the cellular architecture of RG in the embryonic brain using ln2PMMA substrate (RGM) (Mattotti et al., 2012). In particular, the effects linked to substrates appear modifying the relationship with area and eccentricity, in this last case with its cubic effect.

To identify those RGM constraints, we calculated the odds ratio function from RGM (ln2PMMA) over control. The odds ratio is commonly used to measure relative changes between probabilities. The odds ratio function was defined as follows:

$$(6)\ Odds\ ratio = \frac{Odds\ (RGM)}{Odds\ (Control)} = \frac{\exp\left(\beta_{0Ln2} + \beta_{E^3{}_{Ln2}}\mathrm{E}^3 + \beta_{ALn2}A\right)}{\exp\left(\beta_{E^3{}_C}\mathrm{E}^3\right)}$$

When calculating the odds ratio, all common terms between equations are canceled out. Therefore, the *Odds ratio* function, that appears in the expression (3), only depends on area and eccentricity, which are cell-intrinsic parameters. By applying *Log* to the *Odds ratio*, we gained symmetry, linearity, the variance was stabilized, and made it compatible with coefficients defined by the linear regression. To explore *LogOdds ratio* function behavior, we performed a surface plot at different levels of the function (equation 4 and Fig. R-4.3- 8A).

$$(7)\ LogOdds\ ratio(A,E) = Log(=$$

$$(8)\ LogOdds\ ratio(A,E) = \beta_{0Ln2} + \beta_{E^3{}_{Ln2}}\mathrm{E}^3 + \beta_{ALn2}A - \beta_{E^3{}_C}\mathrm{E}^3$$

We define the isolines of *LogOdds ratio* function, i.e. the lines in the plain defined by area and eccentricity that fit the same value of the function. We denoted the isoline with *LogOdds ratio(A,E)* =0 as F(x). When the function *LogOdds ratio* equaled 0, it defined a line F(0) that delineated the boundary at which the RGM equation consistently elevated the probability of a nucleus being classified as RG across all levels, with no differences between the probabilities associated with control and ln2PMMA substrates. In essence,

F(0) line might outline an inherent mechanical factor within the cells, establishing a theoretical threshold for RG nuclei region. As the *LogOdds ratio* function only relies on nuclear morphology parameters area and eccentricity, we draw the allowed nuclear morphologies within the RG region delimitated by F(0) (Fig. R-4.3-8B).

To explore whether potential RG nuclei used for fitting drop into the region above F(0) surface, we plotted the nuclear centroids from cells expressing GFAP, Nestin, NG2, Pax6, Sox2 or Gsx2 markers, and grown on control and ln2PMMA substrates (Fig. R-4.3-8C-D). We found that nuclear centroid from glial cells with developmental potential to be RG drop below F(0) in control substrate, according with the known low probability to find functional RG in this condition. However, in ln2PMMA, where the probability of finding functional RG is higher (Mattotti et al., 2012), nuclear centroids from cells with the same developmental potential to be RG drop in the region above F(0), the theoretical RG region. Importantly, even in the presence of those physical signals from ln2PMMA favoring functional RG phenotypes, nuclei from tri-potential intermediate progenitors expressing Gsx2 (Zhang et al., 2020) move even further from F(0) threshold (Fig. R-4.3-8C-D). Together these data support the existence of cell intrinsic nuclear mechanical constraints within functional RG cells, and only those cells with the adequate developmental potential can transit across the nuclear shape threshold, to become RG in response to permissive or favorable physical signals.

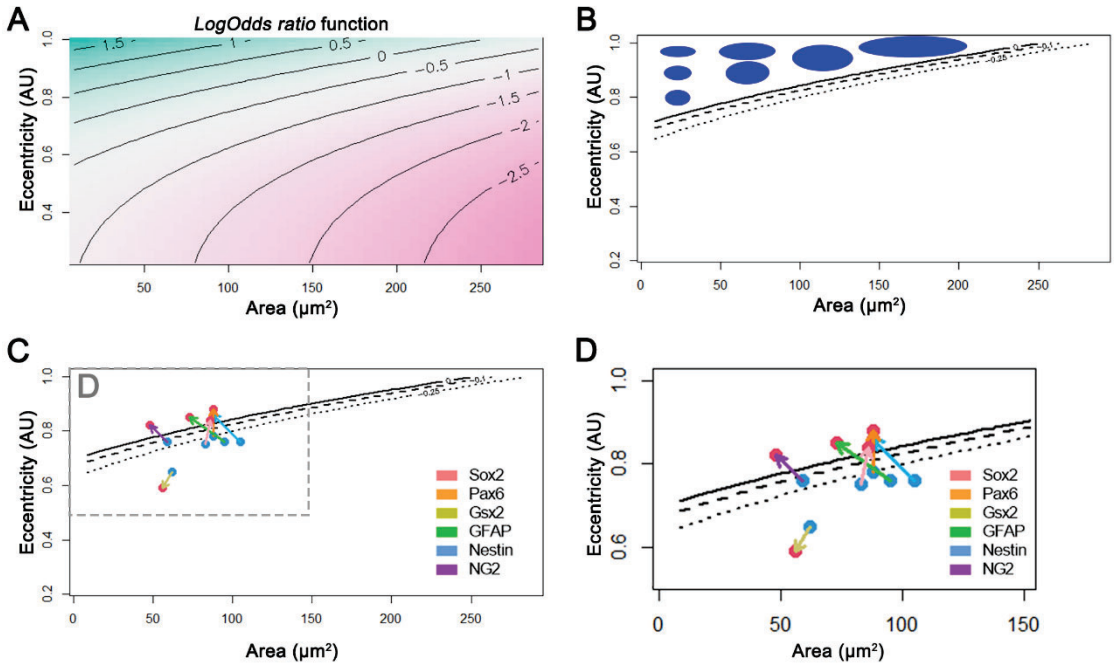


Figure R-4.3- 8 ***LogOdds ratio* function defined a threshold for RG nuclear morphologies.** (A) Surface plot in function of area (x-axis) and eccentricity (y-axis) representing different levels of the *LogOdds ratio* function. B) Selected levels of *LogOdds ratio* function: F(0) = RG threshold (straight line), F(-0.1) (dashed line), and F(-0.25) (dotted line). Scaled theoretical allowed RG nuclear morphologies at area 30µm^2 - eccentricities at 0.78, 0.85 and 0.95; at area 75µm^2 – eccentricities at 0.85 and 0.95; at area 120µm^2 –

eccentricity at 0.9; and at area 175 μm^2 – eccentricity at 0.98. (C) Centroids of nuclei expressing GFAP, nestin, Pax6, Sox2, NG2, and Gsx2. (D) Zoom detail of (C). Blue dots correspond to control and red dots to ln2PMMA substrate. Colored arrows indicate the direction of displacement. Color code links markers with arrows (legend).

Plotting nuclear centroids offered a broad overview of the data displacement along the defined *LogOdds ratio* function surface levels (Fig. 4.3-9D) and indicated a nuclear size region in which this transition occurs. Although it imprecisely captured the comprehensive behavior of all the nuclei. Considering Pax6 as bona fide RG marker, we delimited the range of nuclear areas of Pax6+ cells experimentally observed in our cultures (min=34.75μm^2 and max=139μm^2) within the F(0) threshold and included these size limits as additional spatial constrictions. Then, we plot individual nuclei from cells with developmental potential to be RG (nestin+, GFAP+, PAX6+) on the surface plot representing the *LogOdds ratio* function at F(0) threshold and at F(-0.1), i.e. the isoline with *LogOdds ratio* in 0.9 (Fig. R-4.3-9A-C).

The first conclusion is that the proportion of nuclei fitting into the region delimited by threshold at F(0) and F(-0.1), and the interval of experimental RG nuclear areas roughly match with model predictions at 33% of probability for the corresponding substrates and markers (nestin, GFAP and Pax6) shown in Figure R-4.3-7. Secondly, the effect of ln2PMMA mechanical constraints on the glial cell population with developmental potential to be RG is the nuclear transit trough F(0) threshold of the *LogOdds ratio* function, accumulating them into the defined RG nuclear zone. In summary, by calculating the *LogOdds ratio* function, our model mathematically identified an RG cell-intrinsic mechanical factor that sets limits for the possible nuclear morphologies present in functional RG. Whether this nuclear mechanical constraint is also conserved in living brain RG, or their functional consequences required further investigation.

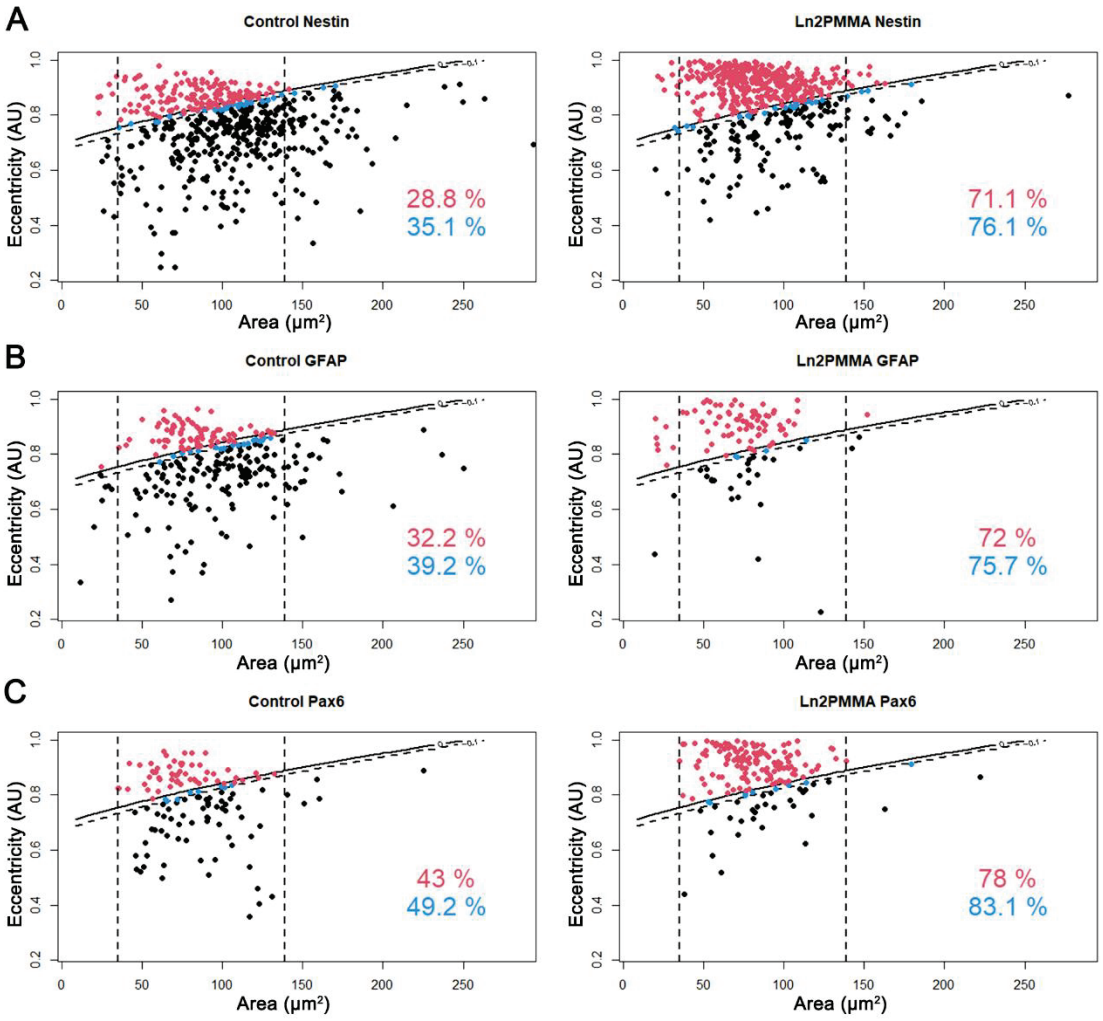


Figure R-4.3- 9 **Fitting of potential RG nuclei on the RG region delimitated by F(0) surface.** Surface plot in function of area (x-axis) and eccentricity (y-axis) representing the *LogOdds ratio* function at F(0) = RG threshold (straight line) and F(-0.1) (dashed line). Dots represent cells stained with different astrocyte-RG lineage markers after 3DIV: (A) Nestin+ (N=1070), (B) GFAP+ (N=362), (C) Pax6+ (N=305) Red correlates dots and percentages at threshold F(0) and blue at F(-0.1). Vertical dashed lines delimitate the nuclear area range of Pax6+ cells within F(0) threshold.

Model Validation

To validate the RGM model, we used a new independent dataset of glial cells grown for 3DIV on control and ln2PMMA substrates. This data set corresponds to the time course experiment described in Figs. R-4.1-1 and R-4.3-1 and will also be used in the next section. As already described in figure R-4.1-1D, the proportion of Pax6+ cells in control substrates are 11.2% and in ln2PMMA substrates 22.7% (Fig. R-4.3-10A). As for fitting data in figure R-4.3-7, RGM predictions matched better with experimental observations in ln2PMMA than in control substrate. The differences were 1.7% in ln2PMMA and 5.2% in control, which are in the range of fitting datasets, serving for valid replication. To visualize nuclear shape shifts on and out of the RG region delimited by F(0) surface, we plotted nuclear morphology parameters on the surface plot of the *LogOdds ratio* function

(Figure R-4.3-10B). The percentages of nuclei above F(0) matched with previous results, and in ln2PMMA the proportion of nuclei within the mathematically defined RG nuclear morphology constraints doubled.

Next, we moved to test RGM model to predict probabilities associated to neuron nuclei and used them as a negative control for model validation. We analyzed pictures from neuronal primary cultures and from long-term non-purified astrocyte heterogeneous cultures (Fig. R-4.3-10C). As expected, distributions were right-skewed, and the vast majority of nuclei fitted the range between 0 and 0.2% of probability to be RG (Fig. R-4.3-10D). When we applied the F(0) of the LogOdds ratio function, only 14.6% of nuclei shared common area and eccentricity with RG mathematical nuclei morphology constrains (Fig. R-4.3-10E). Nonetheless, despite the relatively high percentage, a careful analysis of the graph showed that the tendency of those nuclei was to drop out from the RG region, acquiring smaller and rounder morphology.

The new 3DIV dataset, and the negative control results are suitable for model validation. Note that in the following subsections, nuclei analyzed from all experimental conditions performed at 3DIV with control and ln2PMMA substrates in basal conditions will corroborate these results.

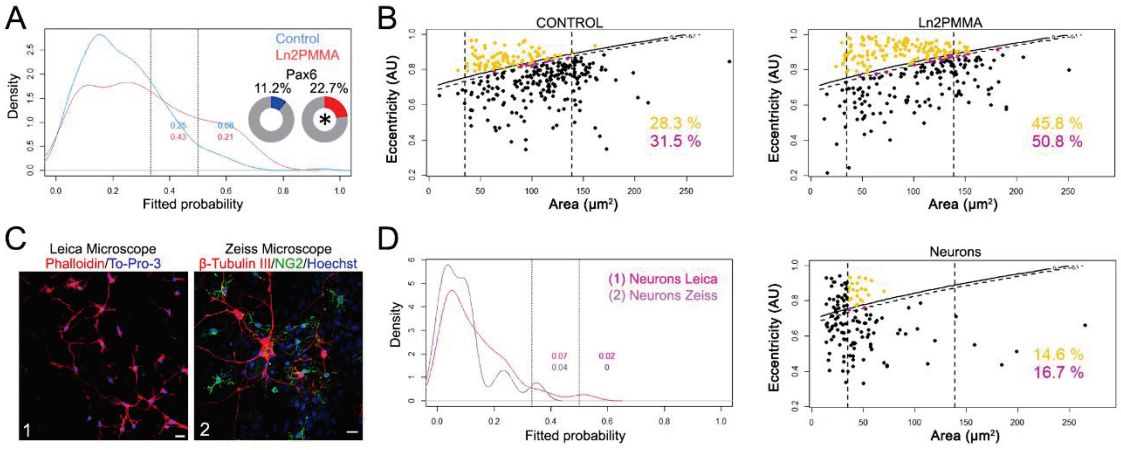


Figure R-4.3- 10 **Validation of RGM model.** (A) Density plots with RGM model fitted probabilities for cells grown in control (blue) and ln2PMMA (red) substrates at 3 DIV. Pie charts correspond to the observed proportion of Pax6+ cells. Chi-square test, *p<0.05. (B) Surface plots in function of area (x-axis) and eccentricity (y-axis) representing the *LogOdds ratio* function at F(0) = RG threshold (straight line) and F(-0.1) (dashed line) in control and ln2PMMA substrates. Dots represent glial cells nucleus, N=608. (C) (1) Primary neuronal cultures, obtained from E16 (embryonic day 16) cerebral cortices, grown on borosilicate glass coated with poly-D-Lysine for 3DIV (phalloidin/To-Pro-3). Images acquired in Leica TCS-SL Spectral confocal microscope. N=126 (2) Long non-purified astrocyte heterogeneous cultures. Neurons appeared on non-purified astrocyte cultures after culture amplification of 30DIV, and experimental culture of 7DIV. Images acquired with Zeiss LSM880-40x confocal microscope. Cells marked with β-tubulin III (Tuj1) and NG2. Nuclei counterstained with Hoechst 33342. N=18 (D) Density plots with RGM model fitted probabilities for neurons from primary cultures (1, fuchsia) and from long non-purified astrocyte cultures (2, light purple). (B) Surface plots in function of area (x-axis) and eccentricity (y-axis) representing the *LogOdds ratio* function at

F(0) = RG threshold (straight line) and F(-0.1) (dashed line). Dots represent each neuron nucleus. (B,E) Vertical dashed lines delimitate the range of Pax6+ nuclear areas (A_{min}=34.75µm^2 /A_{max}=139µm^2).

Confounding effect of the cell cycle progression in RGM model predictions

One relevant observation in the density plots with model fitted probabilities shown above was the systematic presence of a peak in the 0.1-0.2 fitted probability, and accounting for around 10-20% of cells. As our glial cultures are in the growing phase (1-14DIV), we asked whether nuclear changes associated to cell cycle progression may account for this systematic peak, and thus confounding RGM model predictions. To label the proportion of active cycling cells at 3DIV we used the general proliferation marker Ki67, and the M phase-specific marker phosphohistone H3 (PH3) (Fig. R-4.1-11A-B). The use of these markers revealed that the cycling population was similar between substrates conditions, with a slightly, although not statistically significant, increase in ln2PMMA (17,6%) with respect to control substrate (13,2%), and similar traits were found for PH3 (control: 6.1; ln2PMMA: 10.7%). When analyzing the density plots with model fitted probabilities, we found that >80% of Ki67+ and >77% of PH3+ nuclei were placed in the range of 10-20% of probability in both substrates (Fig. R-4.1-11C). These data unravel the presence of a systemic confounding effect of nuclear shape changes associated to cell cycle progression. Further refinements must be done to remove this cell cycle associated confounding effect and improving our RGM model.

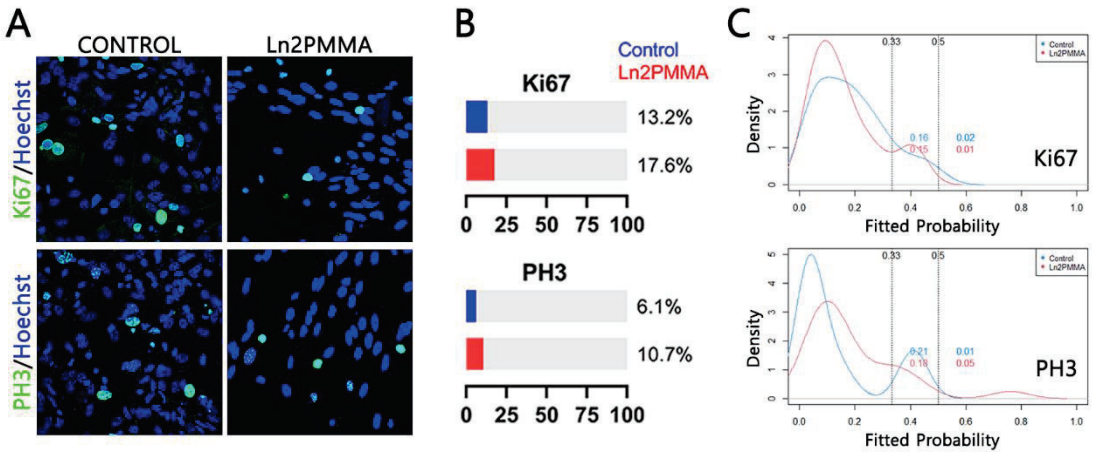


Figure R-4.3- 11 **Actively cycling cells present a specific non-RG nuclei morphology pattern.** (A) Glial cultures stained with Ki67 and PH3 proliferation markers, and Hoechst to stain nuclei in control and ln2PMMA substrates. (B) Bars graphic representing the percentage of Ki67+ (control N=108, ln2PMMA N=54) and PH3+ (control N=42, N=18, ln2PMMA N=24) cells. (C) Density plots with model fitted probabilities for Ki67 and PH3 positive cells in control (blue) and ln2PMMA (red) substrates. Dashed line delimitates thresholds at 33% and 50% of probability. The numbers correspond to the AUC from each threshold. Chi-square test used to compare distributions in (B).

4.3.3. Application development to easily apply RGM model

Dr. Carlos Borau (University of Zaragoza) developed a Matlab application to easily apply RGM model once nuclei were segmented. The application interface is depicted in Figure R-4.3-12A, featuring deployable options enabling users to select the substrate equation.

In Figure R-4.3-12B, we showcase the application display tailored for cells stained with nestin and Sox2 markers. Within this context, we presented predictions for neurons and nestin/Sox2 (Figure R-4.3-12A-B), allowing for a comprehensive comparison of results and application outcomes. This analysis focuses on nuclei exhibiting morphologies that either align or deviate from the RGM-predicted patterns.

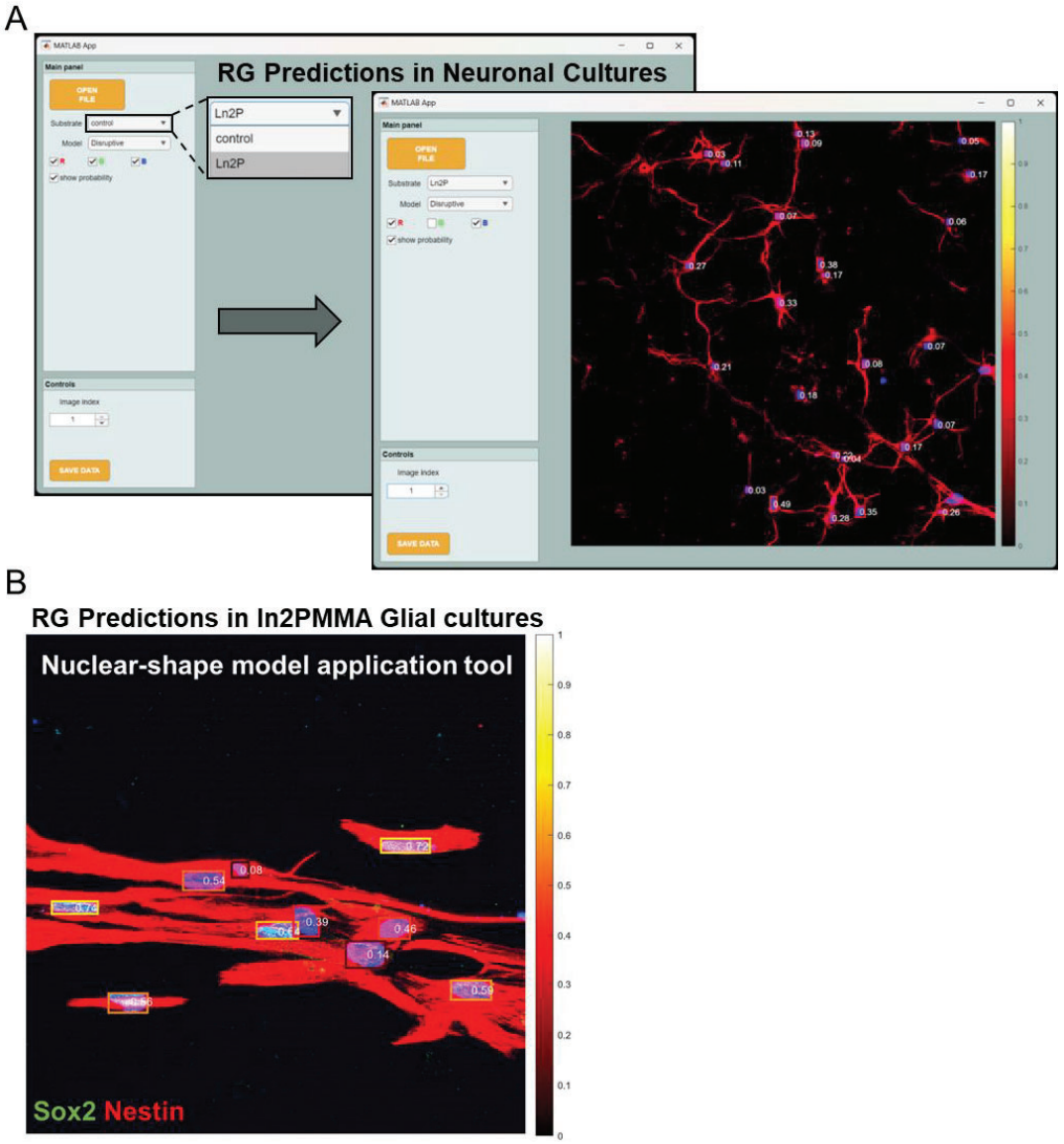


Figure R-4.3- 12 **RGM application workflow, interface, and visual outcomes.**

4.4. RGM model application to identify relationships between nuclear deformation and different mechanotransduction components

In the previous sections, we have generated many datasets based on nuclei morphology parameters of all analyzed cells. In consequence, in the following section we will apply the RGM model to different experimental conditions to link RG nuclei morphology with time, cell-nuclear co-factors, calcium signaling (CaMKII) and metabolism (mitochondrial morphology).

4.4.1. RGM model application to predict RG in glial cell cultures across time.

As we described above, at seeding time, attaching glial cells early detect the mechanical properties of the substrate. As time in culture increases from 1DIV to 14 DIV, glial cells adapt to the mechanical signals from the substrate and neighboring cells and recapitulate, until somehow, the developmental phases of RG-astrocyte lineage differentiation, changing their cell morphology and pattern of gene expression. Through RGM application to nuclei morphologies of time course dataset, we investigated whether nuclear morphology changes accompanied this process (Fig. R-4.4-1). The proportion of Pax6+ cells in control substrates ranged 9.9-15.7%, with no significant differences over time in culture, as previously described in figure R-4.1-1D. On these control cultures, the RGM model predicted 0.2-0.5 RG probability. Although the fraction of fitted probability over 0.5 (threshold 0.5 for fitted probability) remained constant, the probability curves shifted to the left with increasing time in culture, indicating increased adaptation to the non-RG permissive substrate and a decrease in the cell proportion with potential to be RG (cells within 0.33-0.5 thresholds for fitted probability) (Fig. R-4.1-11A-D).

In ln2PMMA substrate the proportion of Pax6+ cells varied with time and culture maturation. At 1DIV, the proportion of Pax6+ cells in ln2PMMA were not significantly higher than on control substrate, significantly increased at 3-7 DIV and then decreases at 14DIV to that of control substrate (Fig. R-4.4-1A-D), because of increasing cell density and maturation (Álvarez, Sena, et al., 2014). As a remainder, this 3DIV dataset was already described and used for model validation (Fig. R-4.1-10A). One important observation is that, although significant increases in the proportion of Pax6+ cells were only found at 3-7 DIV, the RGM model prediction for RG at 1DIV was similar than at 3DIV, and the prediction at 7DIV similar than at 14DIV. This might indicate that substrate-driven influence guide nuclei deformation. As consequence of ln2PMMA mechanical adaptation, this promoted the adoption of an RG nuclei morphology at early stages, preceding changes in Pax6 gene expression. Later, as maturation and cell-cell

interactions overcome ln2PMMA mechanical signals Pax6+ nuclei exit from RG region before the drop in Pax6 expression.

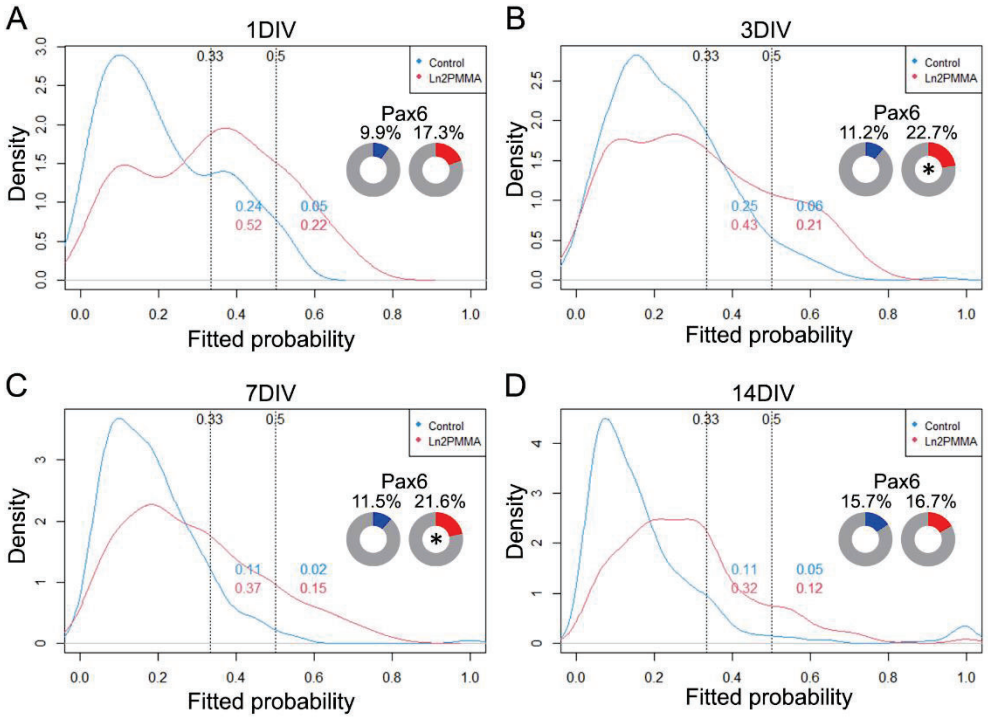


Figure R-4.4- 1 **Validation of RGM model.** Density plots with RGM model fitted probabilities for cells grown on control (blue) and ln2PMMA (red) substrate, at 1 DIV (A), 3 DIV (B), 7DIV (C) and 14 DIV (D). Pie charts correspond to the observed proportion of Pax6+ cells at each time point. Chi-square test, *p<0.05, **p<0.01.

To visualize nuclear shape shifts on and out of the RG region delimited by F(0) surface, we plotted nuclear morphological parameters on the surface plot of the *LogOdds ratio* function (Fig. R-4.4- 2). At 1DIV, when seeding cells are adapting to mechanical substrate signals, around 50% of glial cells in control and 60% in ln2PMMA drop into the RG region delimited by F(0) surface (Fig. R-4.4- 2A). This percentage rapidly dropped in the non-RG permissive control substrate (1-3DIV 21.9%; 3-7DIV 19.3%, and 7-14DIV 2.8%), while remained high in ln2PMMA RG-promoting substrate (1-3DIV 13.6%; 3-7DIV 5.2%, and 7-14DIV 15.6%) (Fig. R-4.4- 2A-D). In both cases, there is a clear shift to bigger nuclear sizes with time in culture, more evident at 14DIV and probably associated with progressive cell cycle exit and cell differentiation.

Taken all together, by exploring nuclear morphology at different time points in culture, our RGM model unraveled that nuclear morphology changes in response to mechanical signals precede subsequent changes in gene expression.

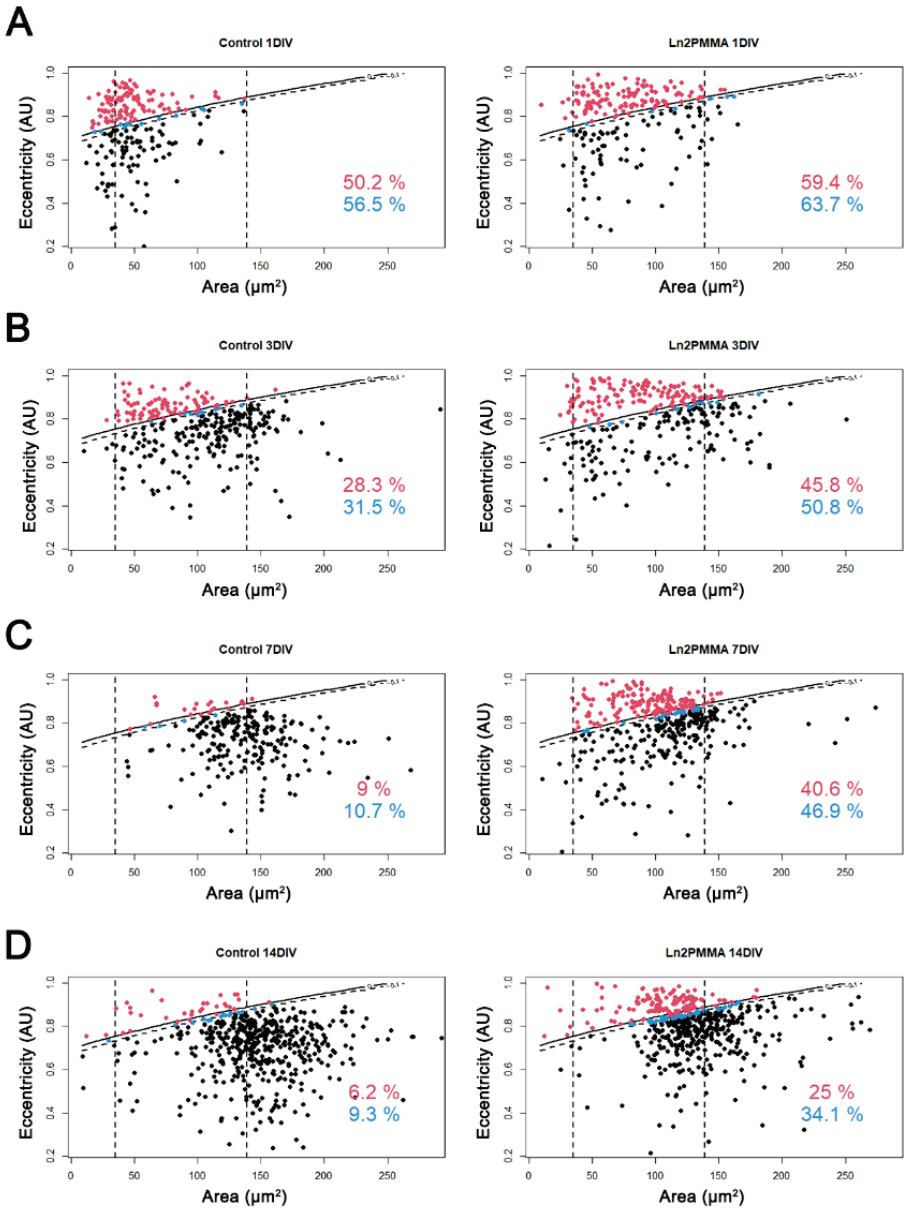


Figure R-4.4- 2 **Time-dependent changes in glial nuclei fitting in the RG region delimitated by F(0) surface.** Surface plot in function of area (x-axis) and eccentricity (y-axis) representing the *LogOdds ratio* function at F(0) = RG threshold (straight line) and F(-0.1) (dashed line). Dots represent glial cell nucleus at time points: (A) 1DIV (N=409), (B) 3DIV (N=608), (C) 7DIV (N=634), and (D) 14DIV (N=1059). Red correlates dots and percentages at threshold F(0), and blue at F(-0.1). Vertical dashed lines delimitate the nuclear area range of Pax6+ cells within F(0) threshold.

4.4.2. RGM model application to evaluate the relationship between lamins A-C/B1 ratio and nuclear deformation.

In a previous section, we showed that glial cells in ln2PMMA have lower lamins A-C/B1 ratio in glial cells. It has been described that lowering lamin A-C expression decreases nuclear stiffness and facilitates nuclear deformation in response to mechanical signals (Kim et al., 2022; Lammerding et al., 2006). Differential expression of lamin isoforms A-C, B1, and B2 (*Lmna*, *Lmnb1* and *Lmnb2* genes respectively) has also been associated with cellular mechanical adaptations during developmental progression and are cell-type specific (Mestres et al., 2022b; M. Wang et al., 2022). Therefore, we analyzed lamin A-C/B1 ratio as a mechanotransduction mechanism candidate to be involved in nuclear deformation during biomechanical induction of RG.

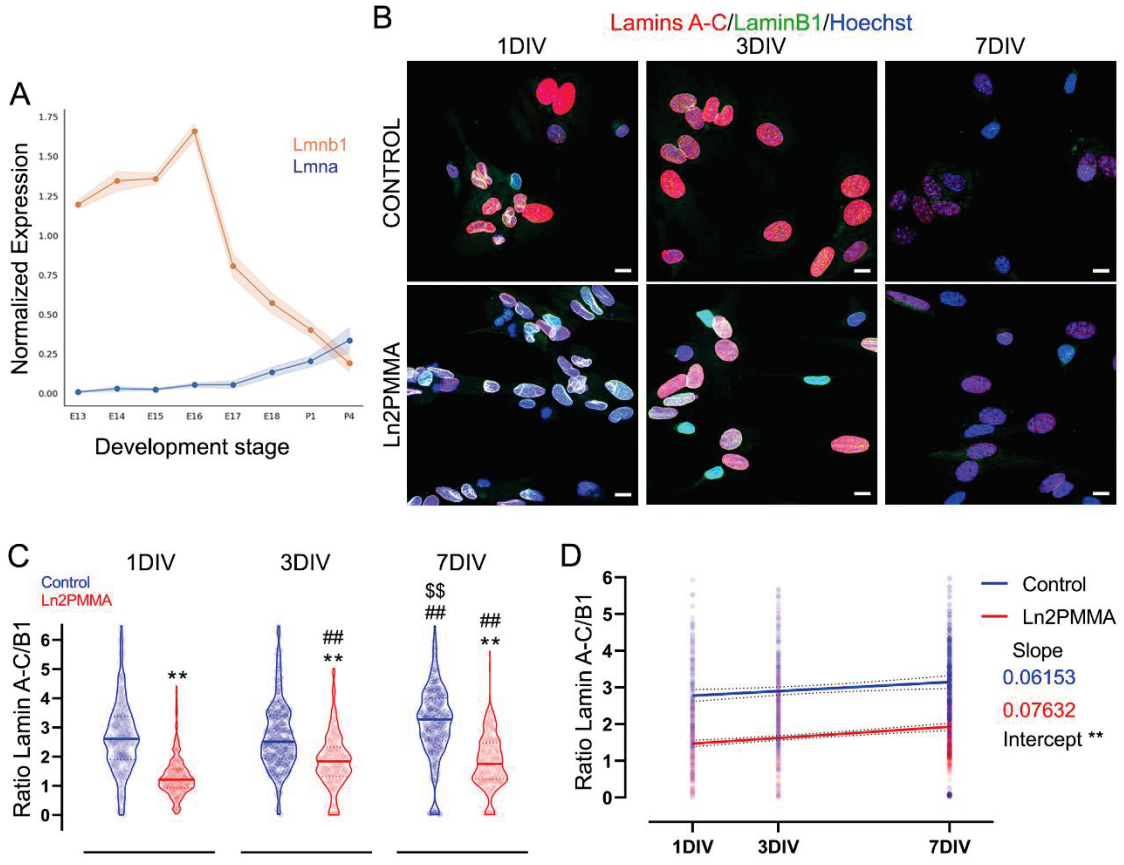


Figure R-4.4- 3 **Changes in lamin A-C/B1 ratio over time.** (A) Plot, showing negative correlation between *Lmnb1* and *Lmna* gene expression during brain development, normalized by the average of *Lmna* gene expression at E13 (data from Di Bella et al., 2021). Dots correspond to the mean value and shadowed area correspond to 95% CI. (B) Confocal images of glial cells grown for 1, 3, and 7DIV on control and ln2PMMA substrates and immunostained for lamin A-C (red) and B1 (green). Hoechst 33342 (blue) was used for nuclei staining. (C) Violin plots showing lamin A-C/B1 ratio in control and ln2PMMA at 1DIV (N=487), 3DIV (N=553), and 7DIV (N=532), using two different biological samples for each condition. (D) Linear regression analysis of the same dataset shown in (B). Scale bar 10µm. Statistical analysis for (C) Kruskal Wallis, * differences with respect to control (*p<0.05 and **p<0.01); # differences with respect to 1DIV on the same substrate (##p<0.01); $ differences with respect to 3DIV on the same substrate ($$p<0.01). Statistical analysis for (D) ANCOVA **p<0.01.

First, in collaboration with Dr. Leonardo Garma we performed a metanalysis of publicly available transcriptomics datasets (Di Bella et al., 2021; Loo et al., 2019b) to evaluate the expression of lamin genes in astrocyte-RG lineage cells during mouse cerebral cortex development as previously described in section 4.1.2. We found an inverse correlation between *Lmna* and *Lmnb1* expression from E16 onwards (Fig. R-4.4-3A), leading to a sustained increase in *Lmna/Lmnb1* ratio during late embryonic and early postnatal brain development. Therefore, we immunostained our glial cultures with lamin A-C and lamin B1 antibodies and analyzed the nuclear lamins A-C/B1 ratio at 1DIV, 3DIV and 7DIV (Fig. R-4.4-3B-C). Consistently, nuclear lamins A-C/B1 ratio was significantly lower on ln2PMMA than in control, differences that were maintained over time. A linear regression analysis demonstrated a significantly lower intercept in ln2PMMA and increased lamin A-C/B1 ratio over time, with similar slopes in both substrates (Fig. R-4.4-3D). Indicating a rapid nuclear response to ln2PMMA mechanical signals, without affecting the differentiation effect of increasing culture time.

Then, we applied the RGM model to explore whether lamin A-C/B1 ratio was associated with specific nuclear shapes and RG probability. The RG probability on control substrate was low and evenly decreased over time in culture, while there was higher and peaked at 3DIV in glial cultures grown on ln2PMMA (Fig. R-4.4-4A). Reproducing the time-dependent behavior described in the previous section. When analyzing RG prediction in function of nuclear lamins A-C/B1 ratio, we find no specific association (Fig. R-4.4-4B), although lamin A-C/B1 ratio tends to increase as RG probabilities decreased. Next, we investigated the relationship between lamins A-C/B1 ratio intervals and the *LogOdds ratio* function at F(0), which we considered a mathematical representation of the nuclear shape constrictions intrinsic of functional RG (Fig. R-4.4-4C-D). As expected, the percentage of nuclei above F(0) and within Pax6+ nuclear area range (A_{min}=34.75 μm^2, A_{max}=139 μm^2) notably diminished in control substrate over time (1DIV: 43.5%, 3DIV: 20.9%, and 7DIV: 8.7%, Fig. R-4.4-4C). Conversely, the percentage of nuclei above F(0) was higher and peaked at 3DIV in ln2PMMA (1DIV: 48.9%, 3DIV: 52.6%, and 7DIV: 30.3%, Fig. R-4.4-4D). In both substrates, nuclei tend to be rounder, bigger and with higher lamins A-C/B1 ratio over time in culture. Although nuclei with all lamins A-C/B1 ratio values can be found in the RG nuclear region delimited by F(0) surface and Pax6+ nuclear area range, nuclei with lower lamins A-C/B1 ratio lean to populate this RG area for longer time.

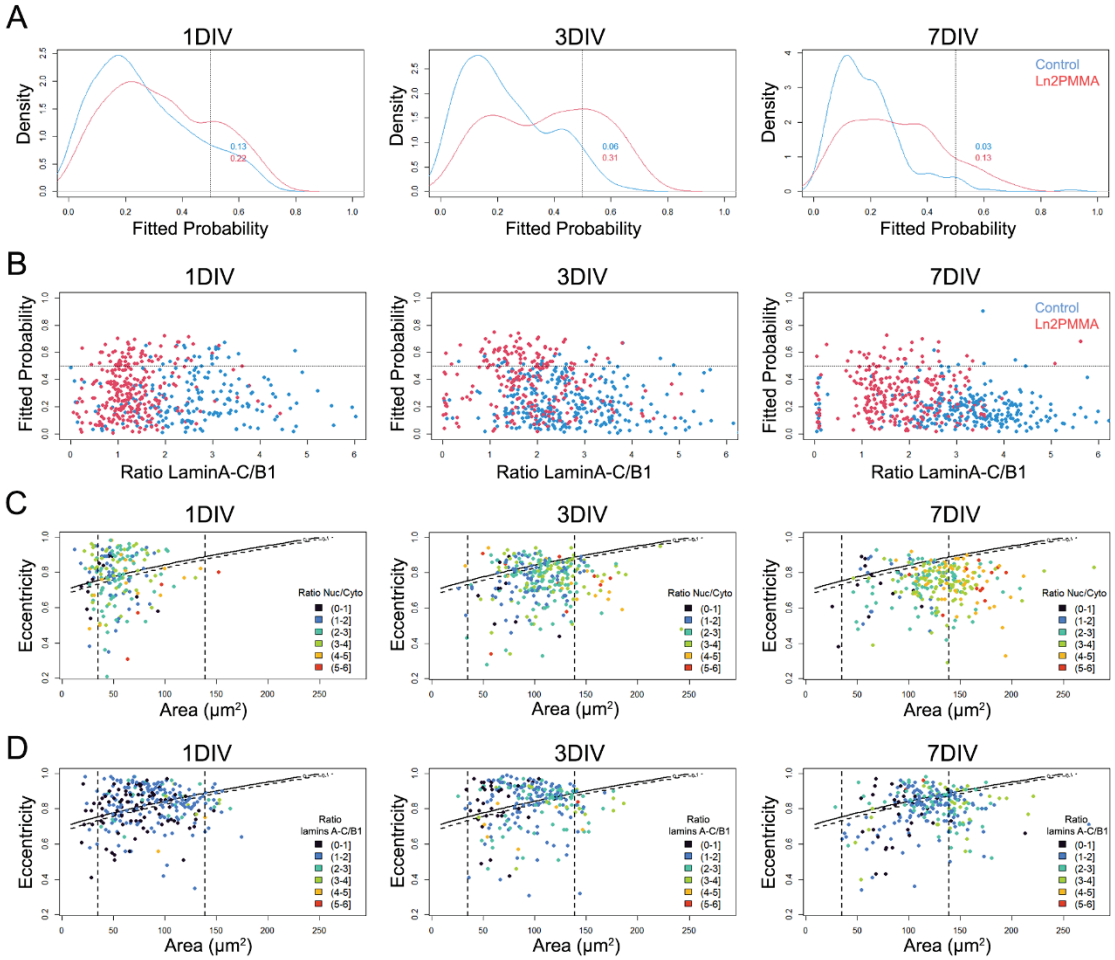


Figure R-4.4- 4 **The increase of lamins A-C/B1 ratio negatively correlates with RG mechanical factor over time.** (A) Density plot with model fitted probabilities of glial cells cultured on control and ln2PMMA at 1DIV (N=487), 3DIV (N=553), and 7DIV (N=532) of two different biological samples of each condition, and immunostained for lamins A-C and B1. Dashed line delimitates 50% of probability. The numbers correspond to AUC of nuclei with more than 50% probability to be RG. Control substrate in blue and Ln2PMMA substrate in red. (B) Scatter plots of fitted probabilities for different lamins A-C/B1 ratio. Dashed line delimitates 50% of probability. Control substrate in blue and Ln2PMMA substrate in red. (C-D) Surface plots in function of area (x-axis) and eccentricity (y-axis) representing the log-odds ratio function at F(0) = RG threshold (straight line) and F(-0.1) (dashed line). Vertical dashed lines delimitate the range of Pax6+ nuclear areas. Color code correlates with lamin A-C/B1 ratio intervals in control substrate (C) and Ln2PMMA substrate (D).

In summary, glial cells grown on ln2PMMA substrate rapidly reduced their lamins A-C/B1 ratio when compared to those grown on control. In both materials, lamin A-C/B1 nuclear ratio progressively increased over time in culture, and negatively correlated with the permanence in the predicted RG nuclei region. This was consistent with the progressive increase in *Lmna/Lmnb1* ratio throughout brain development, where a progressive decrease of RG occurs. Although lamins A-C/B1 ratio was not a direct predictor of RG probability, our data suggest that, for competent glial cells, ln2PMMA mechanical signals might facilitate nuclear deformation and fitting into the RG region by lowering lamins A-C/B1 ratio.

4.4.3. RGM model application to evaluate the relationship between mechanosensitive transcriptional cofactors and nuclear deformation.

Mechanical regulation of gene expression involves changes in the activity and subcellular localization of transcriptional coregulators, such as β-catenin, yes-associated protein (YAP) and the transcriptional coactivator with PDZ-binding motif (TAZ) (Elosegui-Artola et al., 2017a; J. Liu et al., 2022; MacDonald et al., 2009; Sen et al., 2022; Wagh et al., 2021) (Elosegui-Artola et al., 2017b; J. Liu et al., 2022; MacDonald et al., 2009; Sen et al., 2022; Wagh et al., 2021). During brain development, β-catenin and YAP/TAZ activity are directly involved in different aspects of RG organization and neural progenitor expansion) (Austin et al., 2021; J. Gao et al., 2021b; Kostic et al., 2019b; Lavado et al., 2021; Rosenbloom et al., 2020; Wrobel et al., 2007). Therefore, we asked whether mechanical signals from In2PMMA substrate affect β-catenin and YAP/TAZ expression and its subcellular distribution. To address this, we characterized by Westen Blot the protein expression of β-catenin and YAP/TAZ in glial cultures grown for 3DIV on control and In2PMMA substrates (Fig. R-4.4-5A). We found a significant increase in total β-catenin protein in In2PMMA, associated with higher levels of degraded forms, without changes in full length β-catenin (Fig. R-4.4-5B). In contrast, no significant changes were found in the amount of YAP/TAZ proteins between substrates (Fig. R-4.4-5C).

Force application to the nucleus induces nuclear pore opening and import of transcription factors, such as YAP/TAZ and β-catenin, therefore, affecting gene expression (Maurer & Lammerding, 2019a). To evaluate whether In2PMMA mechanical signals affect nucleo-cytoplasmic trafficking, glial cell cultures grown on control and In2PMMA substrates at 1DIV, 3DIV and 7DIV were immunostained with β-catenin and YAP/TAZ antibodies. We determined their nuclear/cytoplasmic intensity ratio (Nuc/Cyto ratio) from confocal images (see methods section Fig. M3) and performed linear regression analyses to evaluate dynamic changes over time (Fig. R-4.4-5D-G). At 1DIV, β-catenin Nuc/Cyto ratio was similar in both substrates and decreased over time in control, with significantly higher negative slope than in In2PMMA substrates (Fig. R-4.4-5F, Fig. S6A). Data indicating a progressive reduction of β-catenin nuclear import over time in glial cells grown on control substrate, while In2PMMA induced a transient increase in β-catenin nuclear import at 3DIV, coincident with the peak of RG induction, and significantly slowing down this process. On the contrary, YAP/TAZ nuclear-cytoplasmic distribution was similar in both substrates, without major changes over time (Fig. R-4.4-5G). Nevertheless, In2PMMA induced a mild and transient increase in nuclear YAP/TAZ at 3DIV (Fig. S6B), as described for β-catenin.

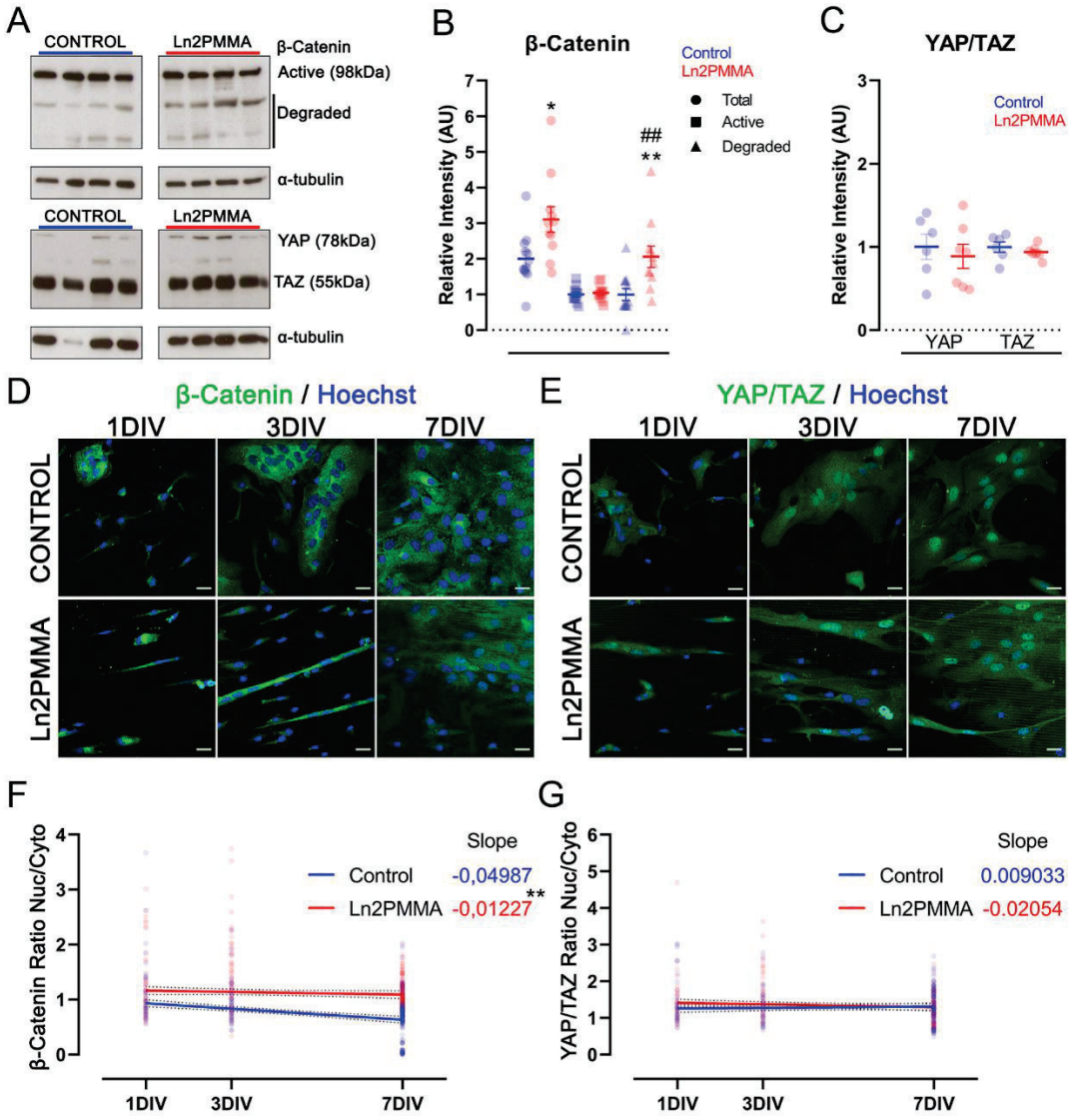


Figure R-4.4- 5 **Ln2PMMA effect on β-catenin and YAP/TAZ expression and subcellular distribution.** (A) representative Western blots (two experiments with 6 different samples at last) showing β-catenin and YAPTAZ protein expression in glial cells cultured for 3DIV in control and ln2PMMA. (B) Quantitative representation of the western blots densitometry (intensity values normalized to α-tubulin) with points representing individual samples. (D-E) Confocal images of glial cells cultured for 1DIV (N=487), 3DIV (N=553), and 7DIV (N=532) in control and ln2PMMA, immunostained for β-catenin (green) (D) YAP/TAZ (green) (E), and counterstained with Hoechst (blue) to identify nuclei. Linear regressions of nucleus-cytoplasm (Nuc/Cyto) ratio for β-catenin (F) and YAP/TAZ (G), with one biological sample for each condition and time point. Statistical analysis of densitometry: Mann-Whitney for total β-catenin, YAP, and TAZ *p<0.05 ln2PMMA vs control; Kruskal Wallis for β-catenin active and degraded, **p<0.01 (same substrate); ##p<0.01 (ln2PMMA vs control). Linear regression: ANCOVA, first slopes were tested, if different, then intercepts, **p<0.01. Scale bar: 20µm.

To address whether β-catenin dynamic changes were associated to specific nuclear morphologies, we applied the RGM model and calculated the associated RG probabilities for specific β-catenin Nuc/Cyto ratios at each time point (Fig. R-4.4-6A-C). Even though the β-catenin Nuc/Cyto ratio was higher in ln2PMMA than in control, no specific β-catenin Nuc/Cyto ratio was associated with higher RG probability,

independently of the substrate. Nevertheless, RG probability decreased as decreased Nuc/Cyto ratio (Fig. R-4.4-6A). To substantiate this, we investigated the relationship between β-catenin Nuc/Cyto ratio intervals and the *LogOdds ratio* function at F(0), as a mathematical representation of the nuclear shape constrictions intrinsic of functional RG (Fig. R-4.4-6D-I). We found nuclei with all β-catenin Nuc/Cyto ratio intervals in the RG nuclear region delimited by F(0) surface and Pax6+ nuclear area range, with no clear correlation with concrete nuclear morphologies.

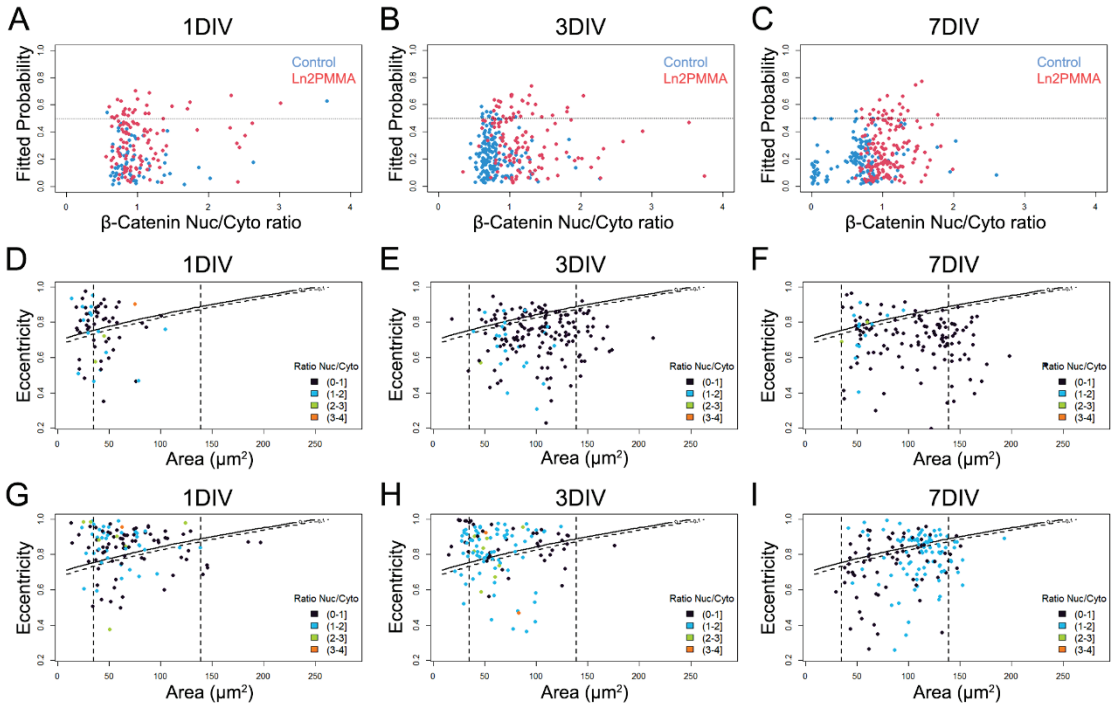


Figure R-4.4- 6 **β-catenin nucleo-cytoplasmic ratio does not corelated with specific nuclear morphologies.** Data corresponding to glial cells cultured for 3DIV in control and ln2PMMA at 1DIV (A, D, G, N=487), 3DIV (B, E, H, N=553) and 7DIV (C, F, I), N=532) corresponding to one biological sample for each condition and time. (A-C) Density plot with model fitted probabilities for nuclei with different β-catenin nucleo-cytoplasmic (Nuc/Cyto) ratio intervals. Dashed line delimitates 50% of probability, control substrate in blue and Ln2PMMA in red. (D-I) Surface plots in function of area (x-axis) and eccentricity (y-axis) representing the log-odds ratio function at F(0) = RG threshold (straight line) and F(-0.1) (dashed line). Vertical dashed lines delimitate the range of Pax6+ nuclear areas (A_{min}=34.75μm^2 /A_{max}=139μm^2) and color code correlates with lamin A-C/B1 ratio intervals. (D-F) Control substrate, percentages above F(0) at 1DIV: 26.2%, 3DIV: 21.9%, and 7DIV:16.1%. (G-I) Ln2PMMA substrate, percentages above F(0) at 1DIV: 60.2%, 3DIV: 53.5%, and 7DIV:35.6%.

In summary, with respect to the control substrate, glial cells grown on ln2PMMA expressed more nuclear β-catenin over time in culture. Although no particular β-catenin Nuc/Cyto ratio was correlated with RG nuclear morphology, Pax6 is a direct transcriptional target of β-catenin/TCF complex, and genetic ablation of β-catenin inhibits Pax6 expression and RG development (Gan et al., 2014). These data point to sustained β-catenin nuclear import as part of the mechanotransduction cascade that favor Pax6

expression in competent cells during ln2PMMA mechanical-driving RG induction. YAP and TAZ mechanosensitive factors are integral components of the β-catenin destruction complex (Azzolin et al., 2014), and required for maintaining the proliferative capacity and structural organization of radial glial cells during brain development (Lavado et al., 2021). Therefore, even though we found only a mild and transient increase in nuclear YAP/TAZ in ln2PMMA, we cannot rule out a coordinated involvement of YAP/TAZ/β-catenin signaling in the ln2PMMA mechanotransduction cascade that drives functional RG induction.

4.4.4. RGM model application to evaluate the relationship between Ca^{2+} signaling and nuclear deformation.

We have previously described that Pax6+ RG had higher $[Ca^{2+}]_{I,}$ and spontaneous transient Ca^{2+} events than non-RG cells, and that ln2PMMA substrate significantly reduced $[Ca^{2+}]_{I,}$ transient Ca^{2+} events and Ca^{2+}/CaM signaling in all glial cell types, but to a much lesser extent in Pax6+ RG. Now, we explored whether our RGM model can appropriately identify cells with specific calcium behaviors by selecting nuclei with a predicted RG probability above 50% (referred as RG p>0.5), and whether intrinsic nuclear physical constraints are relevant by selecting nuclei above F(0) from the *LogOdds ratio* function (Fig. R-4.4-7).

First, we applied the model to live Ca^{2+} imagen dataset. All nuclei with RG probability p>0.5 were within the F(0) category in both substrates, but not all nuclei within the F(0) category were selected by the model as RG (Fig. R-4.4-7A). Moreover, as previously described (section 4.3.2), nuclei with RG probability p>0.5 does not belong to a single cell-type marker category (Fig. R-4.4-7B). When comparing $[Ca^{2+}]_I$ measured by OGB fluorescence intensity, cells with RG p>0.5 had significantly higher levels of $[Ca^{2+}]_I$ and spontaneous Ca^{2+} transients than their counterpart cells with RG p<0.5, regardless the substrate type, and the presence or absence of $[Ca^{2+}]_e$ (Fig. R-4.4-7C, E). Result that confirmed the validity of our RGM model to correctly identify functional RG with similar reliability that Pax6 marker. However, when comparing data from nuclei above and below F(0), these differences were attenuated or even disappeared (Fig. R-4.4-7D, F), according with the lack of RG probability associated to the *LogOdds ratio* function F(0), which only defines a region with possible nuclear shapes.

Second, we analyzed the nuclear morphology dataset resulted from the 3h pharmacological treatments described in section 4.1.4 and figure R-4.1-4. We found that KN93 treatment significantly reduced the nuclear area in both substrates (control p ≤

0.01, ln2PMMA p ≤ 0.01) without affecting nuclear eccentricity. Conversely, no nuclear differences were observed in GsMTx4 treated cells, precluding further analysis.

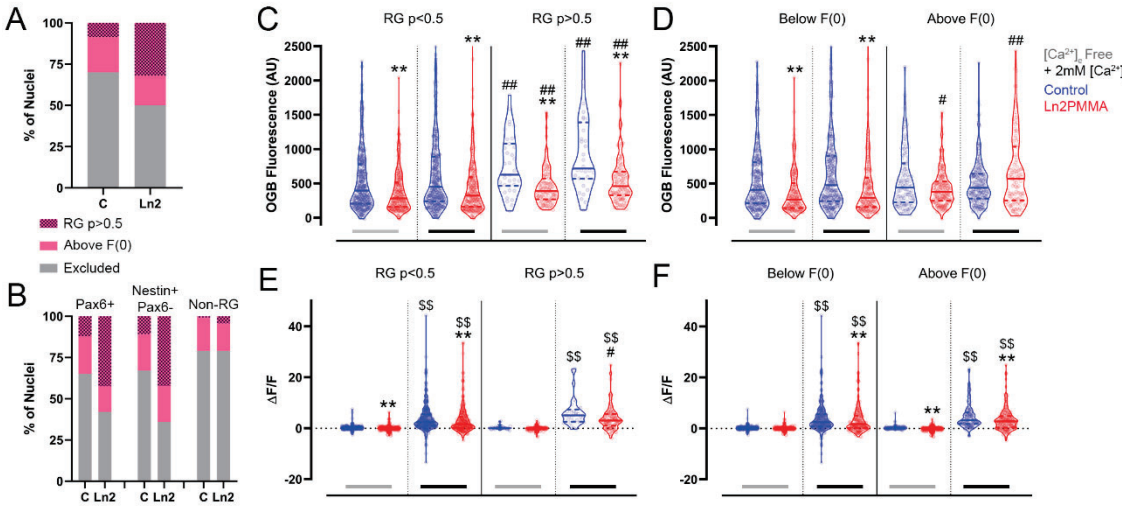


Figure R-4.4- 7 **RG defined by RGM model matched with intracellular Ca^{2+} concentration and activity patterns profiles defined by expression markers.** (A) Bar plot representing percentages of predicted nuclei with probabilities above 50% (RG p>0.5), nuclei above F(0) from the *LogOdds ratio* function and excluded nuclei. Data from glial cells grown on control and ln2PMMA 3DIV, in the absence or presence of $[Ca^{2+}]_e$. (B) Bar plots representing percentages of (A) segregated by cell-type. (C,D) Violin plots representing the average fluorescence intensity in each nucleus of (A), (C) RG p>0.5 (Control=35, Ln2PMMA=130), RG (p<0.5) (Control=367, Ln2PMMA=296); (D) nuclei above F(0) (Control=121, Ln2PMMA=199), nuclei below F(0) (Control=281, Ln2PMMA=200). (E,F) Violin plots showing spontaneous nuclear Ca^{2+} transients (average $\Delta F/F_o$). Points represent individual cells. Data from (A). Statistical analysis: Kruskal Wallis and multiple comparison test with Benjamini and Yekultieli correction, **p<0.01 differences between control and ln2PMMA; ##p<0.01 differences between nuclei with RG p>0.5 and p<0.5, within substrates in absence or presence of $[Ca^{2+}]_e$; $$p<0.01differences between the absence or presence of $[Ca^{2+}]_e$ within substrates and RG probability. Four different samples for each condition.

Hence, we applied our RGM model to dataset from KN93-treated cells to investigate whether nuclei change in RG (p>0.5) and above F(0) paralleled with the observed changes in astrocyte and RG proportions. As described, KN93 treatment significantly lowered lamins A-C/B1 ratio, increased the proportion of GFAP+ astrocytes in ln2PMMA and tended to increase Pax6+ RG in control and to lower them in ln2PMMA substrates (Fig. R-4.1-4C). RGM model application over GFAP+ population predicted a 15% decrease in nuclei with RG (p>0.5) within this population in ln2PMMA and a 3% increase in control substrate (Fig. R-4.4-8A-B). Correspondingly, we found less nuclei (13.7%) in the RG region delimited by *LogOdds ratio* function F(0) in ln2PMMA and more nuclei (15%) within this region in control substrate (Fig. R-4.4-8E-F). RGM model application over Pax6+ population predicted rises of 15% in nuclei with RG (p>0.5) in control and of 4% in ln2PMMA substrates (Fig. R-4.4-8C-D). Concomitantly, the percentage of Pax6+ cells with nuclei above F(0) increased 13.6% and 2,5% in (Fig. R-4.4-8C-H). In summary,

all these data indicated that 3h pharmacological inhibition of $Ca^{2+/}$CaM signaling in glial cells is sufficient to revert mechanoelectrical signals from the substrate, favoring the differentiation of GFAP+ astrocytes and the exit of their nuclei from the RG region in ln2PMMA, while similar $Ca^{2+/}$CaM inhibition in control substrate partially mimic ln2PMMA biomechanical signals, favoring nuclei entering into the RG region and astrocyte dedifferentiation to RG. Nuclear changes are probably linked to $Ca^{2+/}$CaM signaling direct regulation of nuclear lamins composition.

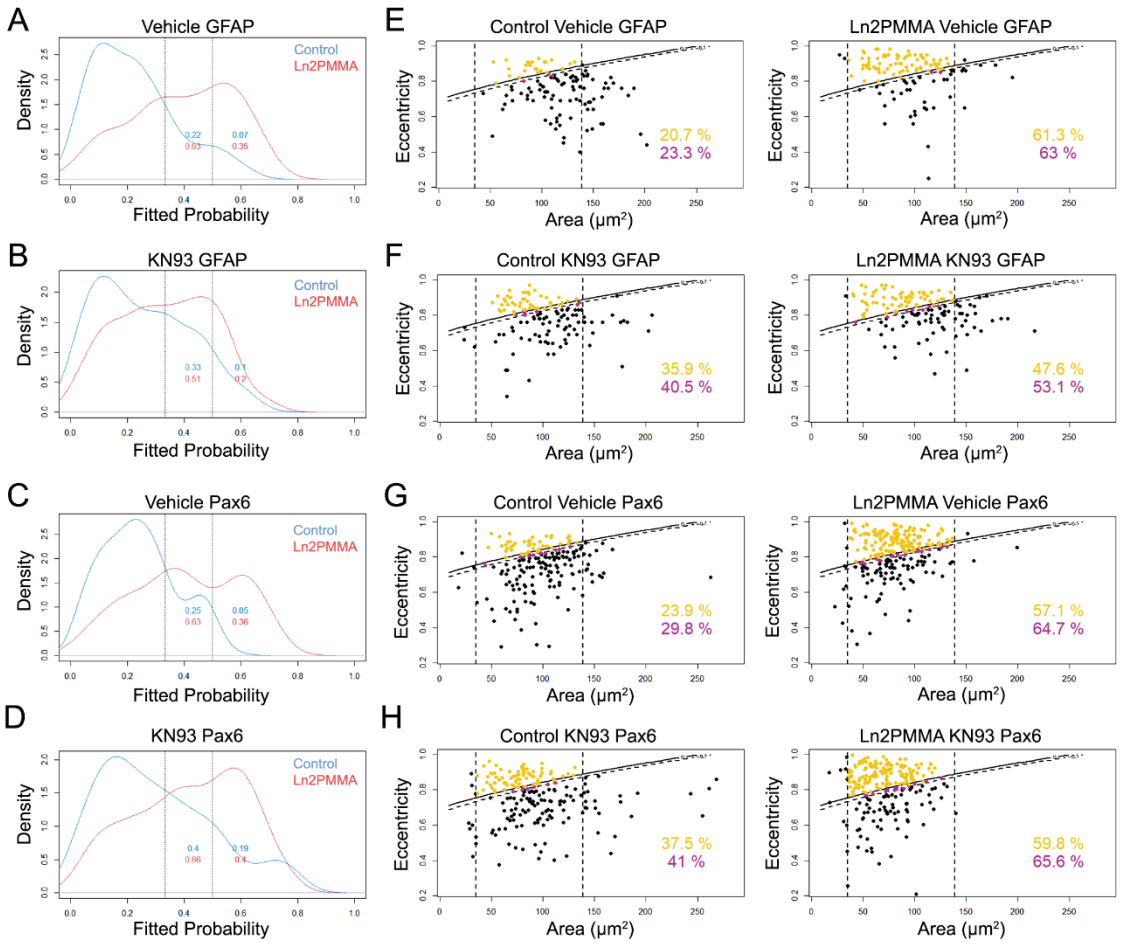


Figure R-4.4- 8 **KN93 treatment induce cell-type specific changes in nuclear morphology.** (A-D) Density plots with model fitted probabilities, control substrate in blue and ln2PMMA substrate in red. Dashed line delimitates thresholds at 33% and 50% of probability. The numbers correspond to the AUC from each threshold. (A) Vehicle-treated GFAP+ cells nuclei (Control N=116, ln2PMMA N=119), (B) KN93-treated GFAP+ cells nuclei (Control N=131, ln2PMMA N=147), (C) Vehicle-treated Pax6+ nuclei (Control N=188, ln2PMMA N=252), (D) KN93-treated Pax6+ nuclei (Control N=200, ln2PMMA N=241). (E-H) Scatter plots of area (y-axis) and eccentricity (x-axis), straight line, points and text in yellow correspond to F(0); dashed line, points and text in purple correspond to F(-0.1) of the *LogOdds ratio* function. Vertical dashed lines delimitate the range of Pax6 nuclei areas (Amin=34.75µm^2 /Amax=139µm^2). Three different experiments for Pax6 staining condition and two different experiments for GFAP staining.

4.4.5. RGM model application to evaluate the relationship between mitochondrial dynamics and nuclear deformation.

Previously, using MitoTracker™ Red CMXRos staining we showed that mitochondrial dynamics and metabolism was profoundly affected by ln2PMMA substrate, in particular in Pax6+ Nestin+ glia. Glial cells in ln2PMMA have significantly less mitochondria but higher mitochondrial volume, with more elongated, ramified and interconnected mitochondrial network, and lower ΔΨm (less fluorescence of MitoTracker™ Red CMXRos per mitochondrial volume) (Fig. R.4.2-3, -4). Now, as performed in the previous subsection, we explored whether our RGM model can appropriately identify cells with specific mitochondrial characteristics by selecting nuclei with a predicted RG p>0.5, and whether intrinsic nuclear physical constraints are relevant by selecting nuclei above F(0) from the *LogOdds ratio* function to data from figure R-4.2-4. (Fig. R-4.4-9).

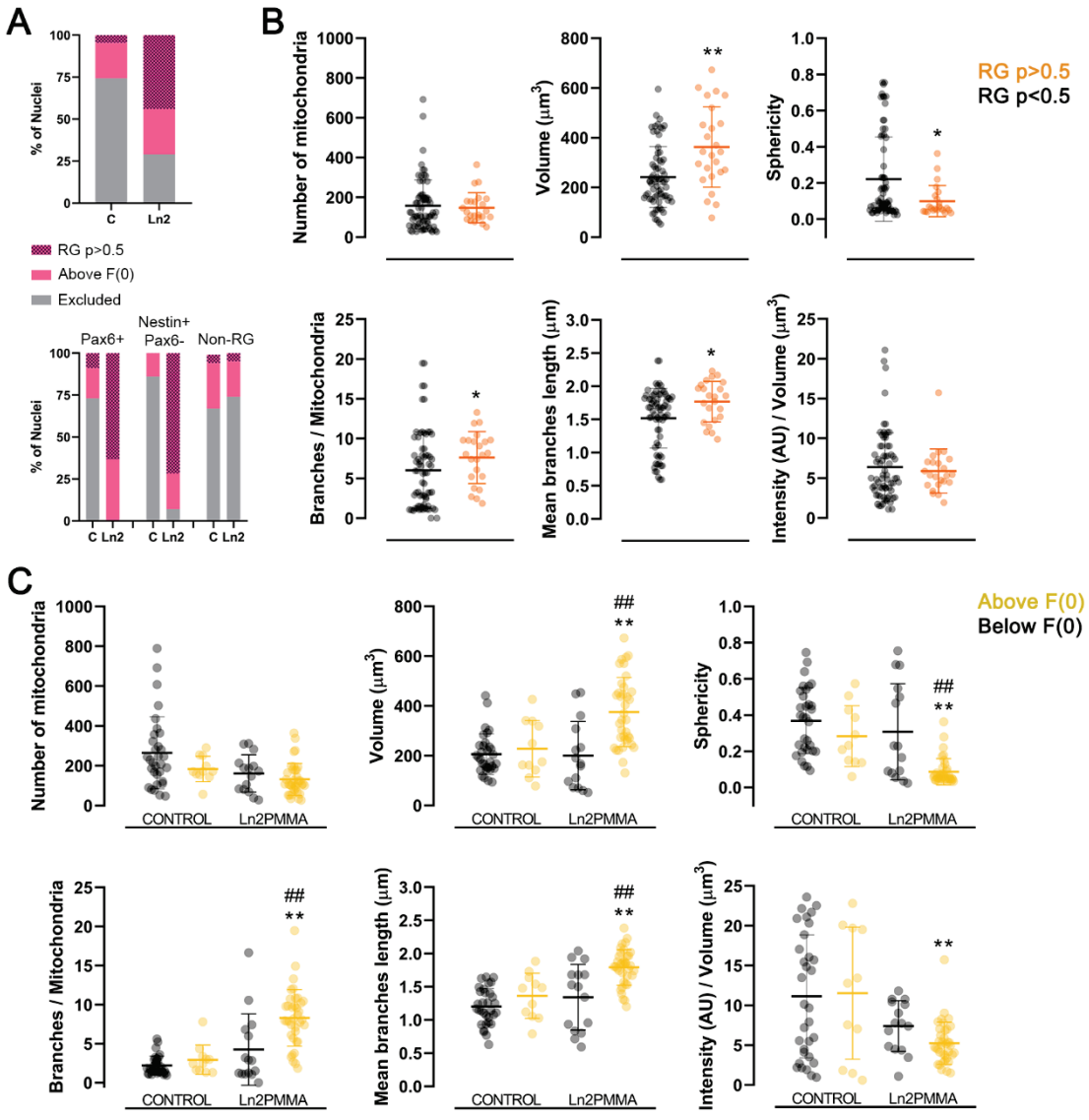


Figure R-4.4- 9 **RG defined by RGM model matched with specific mitochondrial morphologies and network organization defined by the expression of RG markers**. (A) (upper) Bar plot representing

percentages of predicted nuclei with RG p>0.5, nuclei above F(0) from the *LogOdds ratio* function and excluded nuclei. (bottom A) Bar plot representing percentages segregated by cell-type. (B,C) Individual plots showing mean and SD of different mitochondrial morphology parameters from (B) RG p>0.5 (Ln2PMMA=23), RG (p<0.5) (Ln2PMMA=29); (C) nuclei above F(0) (Control=11, Ln2PMMA=37), nuclei below F(0) (Control=32, Ln2PMMA=15). Each individual point represents data per cell. Kruskal Wallis with multiple comparison test, Benjamini and Yekultieli correction. Differences between substrates and same classification: **p<0.01. Differences within substrates, different classification, ##p<0.01. Data from figure R-4.2-4.

As with the previous datasets, nuclei with RG probability p>0.5 by the RGM model belong to different cell-type marker category, but all were within the F(0) category in both substrates, although not all nuclei within the F(0) category were selected by the model as RG p>0.5 (Fig. R-4.4-9 A). Due to the almost lack of RG p>0.5 selected nuclei in control substrate (n=2), we only show data from ln2PMMA substrate (Fig. R-4.4-9B). Cells with RG p>0.5 had significantly more mitochondrial volume, exhibited more elongated mitochondria with longer branches and higher interconnectivity (p<0.01, Fig. R-4.4-9B). On the contrary, the number of mitochondria and ΔΨm were not significantly different between cells with RG p>0.5 or p<0.5 (Fig. R-4.4-9B). When comparing data from nuclei above and below F(0), no significant differences were observed in the control substrate grup, according to the lack of nuclei with RG (p>0.5). However, in ln2PMMA, nuclei above F(0) had significantly higher mitochondrial volume, with significantly more elongated and interconnected mitochondria and lower ΔΨm (Fig. R-4.4-9C).

In summary, our RGM model segregate RG cells with specific mitochondrial morphology and network organization associated with RG nuclear constraints, with similar efficiency than when cells were segregated by RG molecular markers. Differences that were more sharply defined when cells were segregated by their location above and below F(0), suggesting that mitochondrial changes were principally correlated with nuclear entering into the RG region, above F(0), and before acquiring all the characteristics of functional RG.

4.5. Conservation of RG nuclear morphology constraints across species

In collaboration with Ortega's Lab, we gained access to images of human samples and aimed to investigate the consistency of a specific RG nuclear morphology across species. To address this question, we applied our model to different human neural cells preparations in 2D and 3D cultures, and in histological sections of human fetal neuroepithelia (Fig. R-4.5-1A). hRG *in vivo* data was obtained from fetal brains as described in the methods section 3.1, and encompassed two images courtesy of Dr. Alberto Ortega, and the other were obtained from (Hansen et al., 2010). To extract nuclear morphologies, we used ImageJ freehand tool to delimitate distinguishable and non-overlapped nuclei. We automatically measured the nuclear area, and major and minor axis (to calculate eccentricity). Scale from Hansen et al., 2010 data was established as described in the paper figures (Fig. R-4.5-2). RGM model predictions were not addressed due to the lack of microscope settings information. Human induced pluripotent stem cells (hiPSc), neural progenitor cells (NPC) derived from hiPSc, hRG and hNeurons require culturing at very high confluency, well beyond the working confluency range in the RGM model.

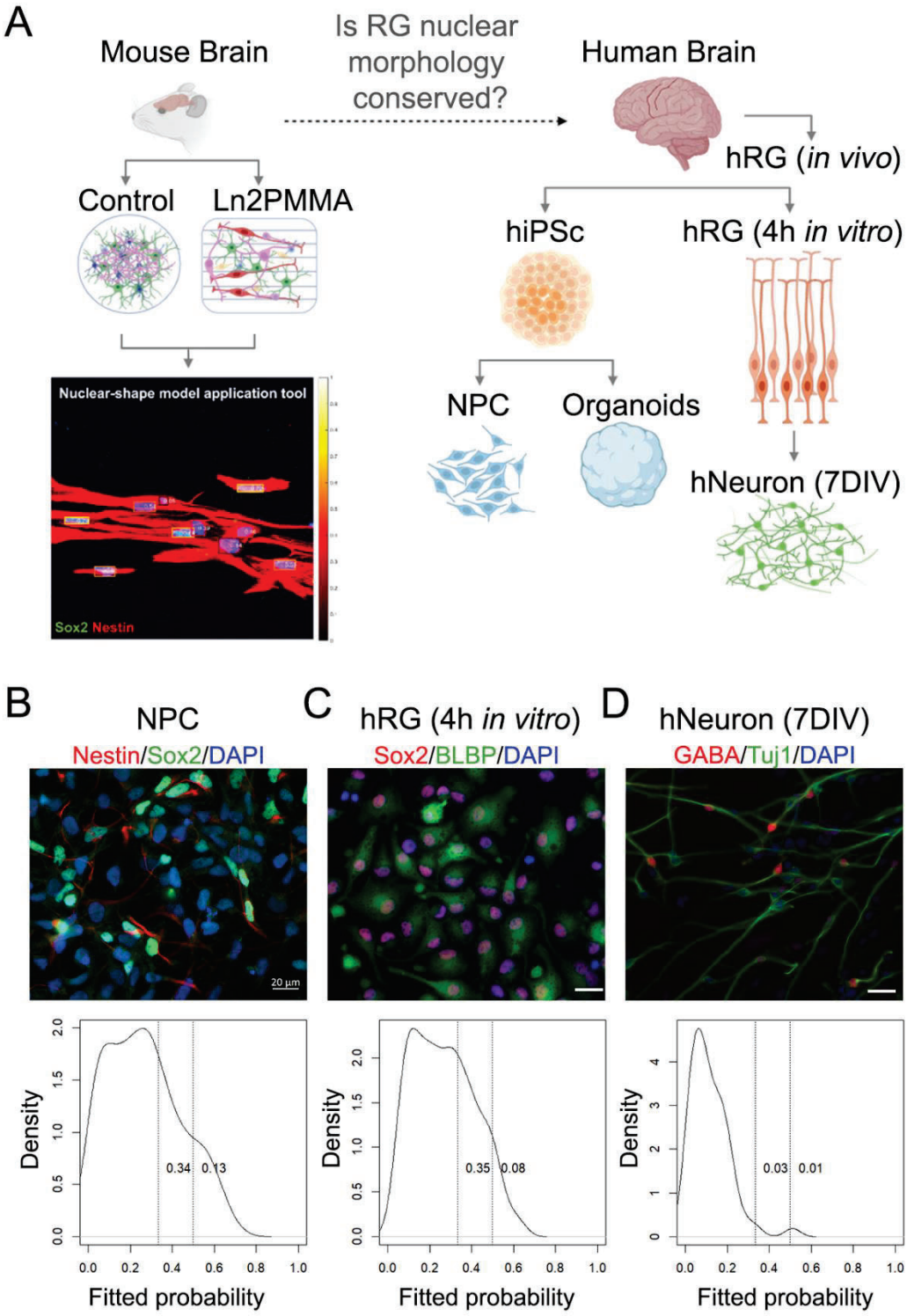


Figure R-4.5- 1 **RG nuclear morphology conservation across species**. (A) Hypothesis testing workflow. RG regression model based on mouse brain cells applied to human brain cells. hiPSc differentiated to NPC (2D) and brain organoids (3D). hRG primary cultures grown in vitro for 4h and differentiated into neurons after 7DIV (described in Ortega et al., 2017). (B-D) Density plots with model fitted probabilities; density (y-axis), fitted probability (x-axis). Dashed line delimitates thresholds at 33% and 50% of probability. The numbers correspond to the AUC from each threshold. (B) NPC's immunstained with nestin/Sox2, N=384/635, 61% extrapolation. (C) hRG immunostained with Sox2/BLBP, N=495/585, 15% extrapolation. (D) hNeuron immunostained with GABA/Tuj1, N=57/1014, 95% extrapolation. DAPI was used to label nuclei.

In the case of brain organoid images, their spatial organization required the use of 3D analysis programs to accurately extract nuclear parameters without bias. We encountered several technical challenges, particularly regarding cell density (hiPSc, 100% extrapolation) and 3D organization, which will be addressed in the following section. Consequently, we used exclusively data that aligns with the established RGM model and excluded extrapolated data (Fig. R-4.5-1B-D). Once selected the non-extrapolated data, we applied the RGM model to identify nuclei with RG p>0.5 and RG p>0.33. As the RGM model was based on mouse data, the calculated probability was mouse RG probability (i.e., mRG p>0.5). The RGM model predicted that 34% of NPC cells drop into mRG p>0.33 with 13% above RG p>0.5 (Fig. R-4.5-1B). In the case of hRG cultures, our RGM model predicted that nearly 35% of nuclei had mRG p>0.33 and 8% mRG p>0.5 (Fig. R-4.5-1C). Conversely, in hNeurons cultures only 2% of cells fall into mRG p>0.33 (Fig. R-4.5-1D). In summary, all human cells were grown on control substrate (without topographic signals), and NPC and hRG predictions aligned with previously described mouse Pax6+ cells grown on control substrate used for fitting and validate the model (Fig. R-4.3-13, -7). Moreover, hNeuron predictions exhibited similar predicted values as for mouse neurons used as negative control for model validation (Fig. R-4.3-9).

Next, we investigated whether we could extract the nuclear morphology of *in vivo* hRG in vivo from sections of human fetal brain, where the anisotropic mechanical RG constraints that In2PMMA mimic were preserved (Fig. R-4.5-2). Fetal human brain images shown in figure R-4.5.2-A corresponded to gestation week 10 (GW10) (1) and GW15 (2). We could segment several nuclei near the ventricular zones, where RG nuclei resided in Fig. R-4.5-2, and in the from Hensen et al., (2010) several Pax6+ RG nuclei were selected (Fig. R-5.2-B). We then calculated the proportion of nuclei above F(0) from the *LogOdds ratio* function for *in vivo* and *in vitro* data. Despite growing on control substrates, 39% of nuclei from Sox2+/nestin+ NPCs were above mRG F(0) region (Fig. R-4.5-3A), and 67,7% of *in vivo* hRG nuclei were above F(0) region (Fig. R-4.5-3B), data reinforcing the idea that functional RG have specific nuclear constraints evolutionary conserved. However, hRG obtained from the embryonic brains shown in R-4.5- 2A and cultured for 4h in a flat control substrate mostly shifted out of the mRG nuclear region, showing only 18% of their nuclei above F(0) limit (Fig. R-4.5-3C). As expected, only 3.6% of hNeuron nuclei were above F(0) limit (Fig. R-4.5-3D). Finally, although F(0) from LogOdds ratio function is determined by specific ranges that theoretically also determine nuclei exclusion criteria, the results from the whole dataset, including those extrapolated,

agreed with the expectations based on predicted percentages from non-extrapolated data.

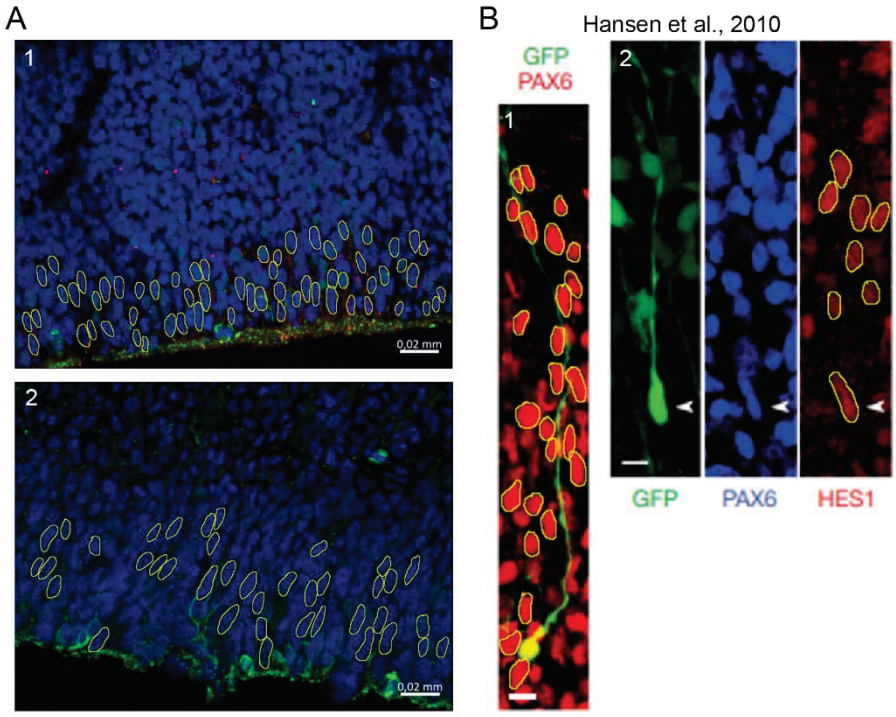


Figure R-4.5- 2 **Human RG nuclear segmentation.** (A) Fetal brains at gestation week 10 (GW10) (1), and GW15 (2). DAPI was used to label nuclei. (B) Fetal brains at GW14 labeled with Pax6 and GFP (1) and at GW15.5 labeled with Pax6, Hes1 and GFP (2). Only Pax6+ nuclei (1) and double stained Pax6+/Hes1+ nuclei (B) were used. Scale bars in (2) 15 µm. Fetal brain obtention is described in the methods section.

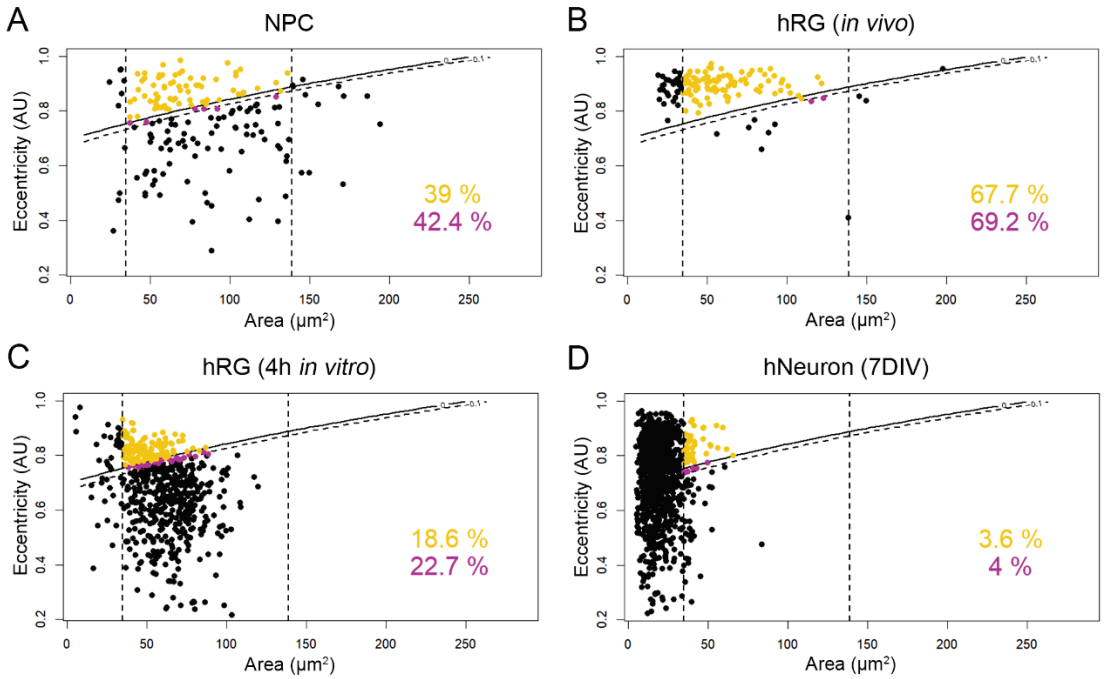


Figure R-4.5- 3 Percentages of nuclei above F(0) form hRG and hNeuron nuclei. Surface plots in function of area (x-axis) and eccentricity (y-axis) representing the *LogOdds ratio* function at F(0) = mouse

RG threshold (straight line) and F(-0.1) (dashed line). Vertical dashed lines delimitate the range of mouse Pax6+ nuclear areas (A_{min}=34.75µm^2 /A_{max}=139µm^2). Percentages correspond to associated colors. Yellow dots are included in purple percentages. (A) Sox2+/nestin+ NPC, N=172; (B) In vivo hRG, N=133; (C) hRG, N=585; and (D) hNeurons, N=1014.

In summary, these results suggest that functional RG can be identified, at least to some extent, by specific nuclear constraints that are evolutionary conserved across species. The loose of mechanical signals from the microenvironment (e.g. apical basal RG anchorage and radially aligned organization in vivo, which are mimicked by ln2PMMA substrate) during culture process on flat substrates disrupt RG structural anisotropy, and significantly affect their nuclear morphology and functionality.

Moreover, employing the RGM model with *in vivo* data transcends the model's limitation tied to established cell density. Nevertheless, *in vivo* conditions do not share the same physical implications and limitations regarding cell density as observed in 2D cultures. In this instance, the RGM model serves as an extra tool for investigating nuclei under entirely distinct physiological conditions then those found in the 2D cultures used to build the model.

4.6. RGM model limitations for 3D and in vivo applications

During RGM model construction, validation, and application, we have encountered many roadblocks that difficulted data integration and process automatization. Without entering into details of statistical model construction, which will be discussed later, data acquisition, image segmentation and model application deserve further attention.

During model construction, we fed the model with nuclear data from 2D images obtained from P0 glial *in vitro* cultures, where the variable cell density resulted critical for model improvement. One hallmark of 2D *in vitro* cultures is that cells grow in a monolayer until cell-contact inhibition is activated by confluence. At confluent zones, cell-contact inhibition induced glial cell exit from cycling, reducing proliferation and potentiating astroglia differentiation process. On this basis, we constructed our model using areas of different cell densities but avoiding extremely crowded areas. This established limits in terms of cell density. Hence, when we tried to apply the model to experimental conditions where cultures were highly confluent, we found high rates of extrapolation. One example is shown in the figure below (Fig. R-4.6-1A), where human induced pluripotent stem cells (hiPSc) cultures required high cell density.

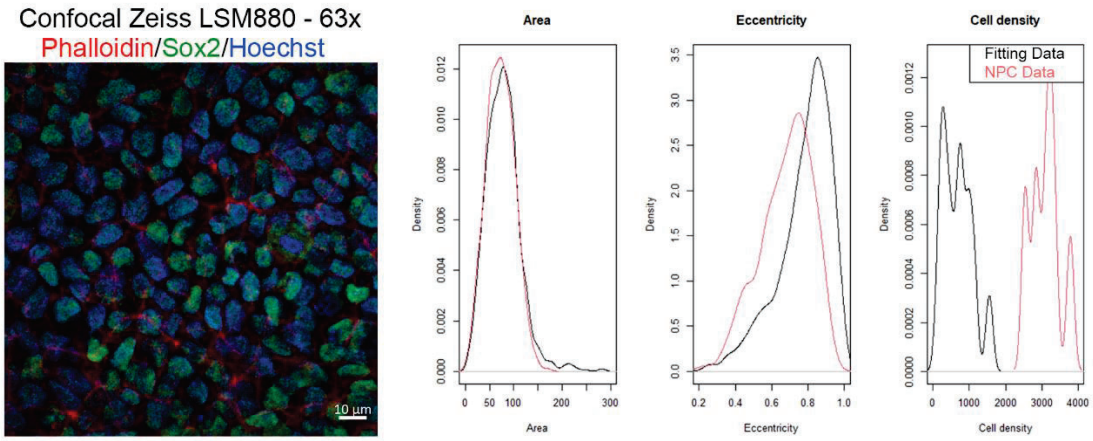


Figure R-4.6- 1 **hiPSC cultures exceeds cell density RGM model limits**. Left: hiPSc stained with phalloidin (red), Sox2 (green) and nuclei counterstained with Hoechst (blue). Right: density line plots in function of area, eccentricity, and cell density. In black, data used for fitting the model, and NPC's data in red.

Another technical challenge was to obtain nuclear morphologies from 3D cultures and brain structures. Nowadays, the study of biology is moving forward to improve 3D cell cultures and obtaining highly complex organoids structures. Beyond that 3D cultures replicate better the physiological conditions than 2D cultures, and that also implies high cell density rates, our image segmentation algorithm was not suitable to obtain nuclear

morphologies from 3D cell cultures. Therefore, in collaboration with Dr. Carlos Borau, we used different approaches to segment 3D organoid images to obtain nuclear area and major and minor axis measurements. However, the lower resolution in Z-plane compared to X and Y hinders a proper reconstruction of the volumes. Furthermore, the extremely high confluence of brain organoids and brain ventricular zones make it difficult to properly segment the entities, requiring time-consuming procedures and higher computational demands. In the future, we plan to obtain better images especially tailored to this objective. In the figure below we show an example of the original image and its render after unsuccessful segmentation (Fig. R-4.6-2 and Fig. S9).

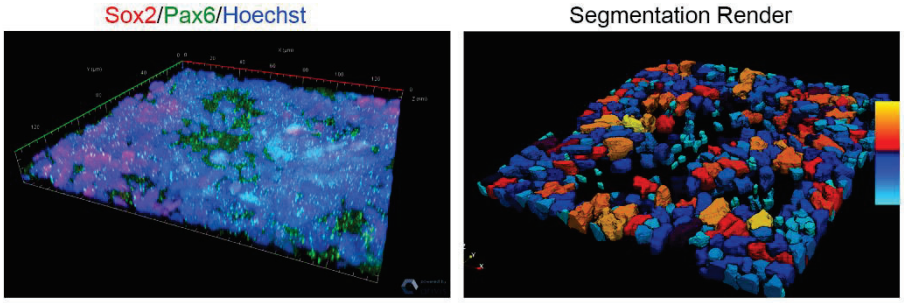


Figure R-4.6- 2 **3D brain organoids confocal image and segmentation render**.

5. DISCUSSION

The RG lineage differentiation is associated to changes in shape, metabolism, and gene expression, and relies on a combination of cell intrinsic mechanisms and non-cell autonomous factors present in their microenvironment (Ferent et al., 2020b; A. R. Kriegstein et al., 2020). Ln2PMMA is a biomimetic material that mimics RG surface properties and scaffolding structure and induces cultured astrocytes to adopt functional RG phenotypes (Mattotti et al., 2012). By taking advantage of RG ln2PMMA we have elucidated some of the mechanotransduction mechanisms that underly biomechanical induction of RG. From the biomechanical point of view, we have found that mechanical signals from the substrate were translated to the glial cell nucleus, changing its shape and size before evident changes in gene expression. Mechanoelectrical changes include a shift in the expression of mechanosensitive ion channels (MSC) and calcium signaling, mediated in part by CaMKII activity. Changes that are associated to a shift in mitochondrial dynamics and metabolism, leading to mostly fused mitochondria with prevalent glycolytic metabolism, characteristics of NSC/RG to promote pluripotency and prevent differentiation. To unravel the intricate interplay between mechanical cues, nuclear characteristics, and broader cellular dynamics within the context of RG lineage differentiation we develop a multivariate logistic regression model (RGM model) to assign RG probabilities based on nuclear morphology. Notably, our mathematical modeling identifies the existence of specific nuclear constraints intrinsic to the RG nucleus and established a mathematical threshold for the permitted RG nuclear shapes. The efficiency of the RGM model to identify RG was similar to the use of known molecular RG markers (e.g. Pax6) and revealed a highly molecular heterogeneity in potential RG. The application of the RGM model to different experimental datasets revealed that RG identified in base of their nuclear morphology share intracellular calcium levels and dynamics, mitochondrial morphology, and network, and increased nuclear β-catenin, independent of their specific combination of RG lineage molecular markers. In the following discussion, we will integrate our observations to establish empirical relationships, and provide suggestions to set the path for future investigations.

Methodological considerations related to glial cell type identification

Phenotypic diversity within cell populations can arise due to variations in their sex, age, local microenvironment, and to intercellular differences in cellular state and responses, which can affect cell fate and differentiation over time. Along these processes, cells activate or repress different genes that dynamically provide the cell with a transcriptional continuum between fates and states (Escartin et al., 2021; Yuste et al., 2020) (Mattiazzi Usaj et al., 2021b). Our primary glial cultures include cells from male and female newborn mice and are highly heterogenous in terms of the glial cell types we depart, even after

astrocyte enrichment. Moreover, individual astrocytes, or RG, can be in different cell state, referring to its metabolic status, position in the cell cycle, and state of quiescence or growth (Mattiazzi Usaj et al., 2021b). In our *in vitro* model, we use borosilicate glass as control 2D model, and micropatterned ln2PMMA, a micro3D substrate that mimic some physical characteristics and topographical organization of RG, as a mechanical model of embryonic RG niche (Mattotti et al., 2012). Both substrates allow similar nutrient availability, and differences in glial cell differentiation and cell state only relay on the different mechanical signals from the substrate.

Thus, the first problem we approached was the correct identification of the cell populations of interest, mature astrocytes, and RG. Traditional cell-type classifiers relay on cell shape (e.g. the presence of radial morphologies or not) and the expression of a reduced set of molecular markers, at protein or RNA level, by using different types of histological techniques. The immunodetection by fluorescence microscopy (IF) approach used in this thesis is commonly used for cell-type identification but has several drawbacks and is extremely hard to replicate quantitively. IF efficiency and background level depend on how fresh the sample is, the staining protocol, the antibody specificity, the type of microscope, the day of the researcher, etc. (Buchwalow et al., 2011; Saper, 2009). Moreover, characterization of RG-astrocyte differentiation process is highly complex, due to the lack of cell-type specific universal markers and the presence of transitional forms. For instance, nestin, a widely used NSC/RG marker, is also expressed in reactive astrocytes and activated microglia/macrophages after injury and has a long-lasting expression in primary cortical astroglial cultures. While GFAP, a widely used mature astrocyte marker, is transiently co-expressed with nestin in NSC/RG (Escartin et al., 2021; Krishnasamy et al., 2017; Sergent-Tanguy et al., 2006; Yuste et al., 2020). On these bases, differences between experimental approaches in combination with the molecular markers used to identify the targeted cell populations can lead to scientific discrepancies. To avoid that, different groups of researchers have claim for a unified nomenclature and definition for proper cell-type identification, which incorporate data from different approaches (omics data, cell signaling, proliferation, cell functions, morphology…), developmental stages, and species, serving as a foundation for aggregating information about their function (Escartin et al., 2021; Mattiazzi Usaj et al., 2021b; Yuste et al., 2020). Therefore, to identify RG in this thesis, we use the combinatorial expression of Sox2, Pax6 and nestin (Kriegstein et al., 2020), together with cellular and nuclear morphological parameters.

Methodological considerations related to image analysis tools

A second important decision was the selection of image analysis tools. Despite all sorts of available open-source software (Smith et al., 2018), we opt to develop a custom-made software specifically adapted to our necessities. Our custom image analysis algorithm allows us to obtain morphological data (including area, eccentricity, bounding box, and orientation), nuclear and cytoplasmic fluorescence intensity (as described in (Elosegui-Artola et al., 2017a), label segmented objects, the total counts, and their position in the picture. We additionally included color enhancers to visualize channels, with labeling to guide during the process of label assignment and avoid, as far as possible, bad assignments. Then, two subroutines were developed, the first one, associated to data acquisition from picture, identify images and objects within each image, calculate the total number of objects/nuclei per picture, which is used for cell density estimation. The second subroutine permits us to create an excel file to proceed with data analysis. We also include distinct microscope resolutions and the conversion factors (pixel/µm), to allow the use of old images. The segmentation procedures, as well as segmentation-microscope correlations were established during my master thesis and further developed by Dr. Carlos Borau. All image acquisition and analysis followed the scientific standards (Mattiazzi Usaj et al., 2021b; Smith et al., 2018). With this software, we are able to correlate multimodal data, such as calcium imaging or mitochondrial morphology data obtained and processed with different programs and integrated with nuclear morphology data. The unification of all morphological data by using the same software increases post-analysis robustness, reduces type I error, and improves data integrity.

Our image analysis process is a semi-automatized pipeline. There is the possibility to segmentate in bulk as many pictures as desired, but object labeling requires user interaction in order to create an expertly labeled dataset. Quality and completeness of data requires researcher expertise to confirm and corroborate that cells are “well” identified, one of the most important steps in a phenotypic screen (Smith et al., 2018).

Nevertheless, we encountered several limitations. The first is that marker expression assignment is bimodal (yes/no) relaying in researcher expert decision, instead in a graded response that more accurately represents real cell behavior. The second limitation affects the perinuclear cytoplasmic area assignment in highly elongated cells. Due to the extremely bipolar morphology of RG cells in ln2PMMA, in a significant number of cells the delineation of a perinuclear cytoplasmic area equaling nuclear area extends beyond the cell boundary. This circumstance has the potential to introduce inaccuracies in fluorescence intensity detection and impact the interpretation of our results.

Another limitation of our methodology is related to segmentation failure in high confluent 2D cultures, as required for maintenance of iPSC (including hiPSC) and their differentiation into different neural cell types, or in 3D culture conditions and tissues. 2D cell culture relies on adherence to a flat surface that provides mechanical support for the cells and allow similar access to nutrients. Although substrate stiffness uses to be significantly different that native tissue, do not provide control of cell shape and can result in a significant alteration of molecular markers expression and unexpected observations. The shift from 2D to 3D *in vitro* models have the advantage that better mimic *in vivo* physiological environment and the drawback of heterogeneous nutrient availability through the culture (Duval et al., 2017). Brain organoids grown from hiPSC self-assemble into 3D cytoarchitectures that reproduce early phases of the developing human brain and had been used to model different human neuropathologies at the cellular scale. Their 3D scale, high cellular heterogeneity, density and complex cytoarchitectural organization require high resolution images and better image analysis and segmentation software (Albanese et al., 2020; Mattiazzi Usaj et al., 2021b). Our application requires an extensive refinement process to adapt to 3D segmentation. Even in 2D cultures the cells are tridimensional. For instance, nuclear lamins A-C and B form integral parts of the nuclear lamina, anchored to the inner nuclear envelope (NE). Changes in nuclear shape and volume are accompanied by switches between smooth and highly wrinkled states of the NE, reflecting different nuclear stiffness (Tang et al., 2023). NE wrinkles are detected in a 2D context as lines of increased lamin intensity within the nucleus, although topographical "roughness" only becomes apparent in 3D environments. A step forward in our image analysis tools will focus on incorporating z-resolution into our program. This enhancement aims to improve cell identification, thereby obtaining new potential descriptors, such as nucleus invaginations and roughness, chromatin and heterochromatin distribution and more precise subcellular and regional distribution of specific markers.

Methodological considerations related to the RGM model construction

The mechanoresponsive capacity of the nucleus relay on its capacity to deform in response to tension, altering their nuclear envelope composition and chromatin organization (Dupont & Wickström, 2022; Kalukula et al., 2022). Recently, nuclear morphology was used to describe changes in neurons across time (Das & Ramanan, 2023), and used as a deep learning biomarker of cellular senescence (Heckenbach et al., 2022b). Here we found that mechanical signals from the In2PMMA substrate were translated to the glial cell nucleus, changing its shape and size as an essential component of biomechanical RG induction. Therefore, the pivotal question arises: what

are the morphological parameters that best characterize RG cell's nucleus? To address this query, we advocate the use of mathematical models over automated random algorithms, such as machine learning approaches. While machine learning methods excel in identifying correlations and wield considerable power, they often yield intricate relations with limited biological significance (Alber et al., 2019; Smith et al., 2018). In contrast, mathematical modeling offers a more insightful exploration of the study's setup and possesses the capacity to predict behaviors (Mattiazzi Usaj et al., 2021c; Smith et al., 2018).

Hence, by employing the mathematical approach, we constructed a multivariate logistic regression model to assign RG probabilities based in identified nuclear morphological traits, and a binary response determined by the presence or absence of neural cell type molecular markers. We constructed the model iteratively, and based on maximum likelihood estimation, to provide associated probabilities to be RG. By including cell density as a covariable, we also consider the "community effect", a biologically relevant concept during cell differentiation and tissue patterning (Gurdon, 1988). The selected model yielded a score of AUC=0.73, and two separate equations for RG probability, one associated with control substrate and another for ln2PMMA substrate, with different accuracy (0.66 and 0.77 respectively). One strength of the model was the inclusion of non-linear interactions, such as quadratic and cubic variable coefficients, which, biological interpretation is still assumable and its substrate-dependent nature enhances the importance between topography, cell density, and nuclear shapes. However, we were concerned by substrate equation dichotomy, as for cells with the same expression patterns and nuclear morphology, a relevant model will raise the same substrate-independent RG probability. During model verification steps (Erdemir et al., 2020), ln2PMMA equation RG probability predictions, at an astringent 50% probability threshold (RG>50%), aligned significantly better with the percentages of RG experimentally observed than control equation, independently of the substrate used. Therefore, as ln2PMMA mimics the architecture of RG niche in the embryonic brain (Mattotti et al., 2012), we renamed the model exclusively based in ln2PMMA equation as Radial Glia Mimetic (RGM) model. The power of our RGM model is that validation was performed with real data instead of using cross-correlation or simulated data, increasing model robustness and consistency (Stone, 1978). RGM model validation with different independent datasets confirmed that Pax6+ transcription factor expression and Nestin+/Sox2+ combination are bona fide RG markers in our glial culture system, and that only cells expressing nestin/GFAP intermediate filaments have the capacity to move

along astrocytic-RG lineage in response to the mechanical stimulus. And accurately defines what is not a potential RG.

Moreover, the RGM model revealed that the acquisition of the RG phenotype was associated with nuclear deformation and the adoption of an RG-specific nuclear shape. To inquire about the mechanical factors limiting the range of possible nuclear shapes in functional RG cells, we calculated the *LogOdds ratio* function from ln2PMMA over control equation. The *LogOdds ratio* function equal 0 (F(0)) delineated the boundary at which the ln2PMMA equation consistently elevated the probability of a nucleus being classified as RG, with no differences between the probabilities associated with control and ln2PMMA substrates. In essence, F(0) line might outline an inherent mechanical factor within the cells, establishing a theoretical threshold for RG nuclei region based solely on nuclear morphology parameters area and eccentricity, but with no associated RG probability. The *LogOdds ratio* function above F(0), allowed us to apply the model in contexts where cell density was not achievable, or was out of the model range, but only provides qualitative and quasi-quantitative information. A more accurate definition of permitted RG nuclear zone was obtained by delimiting the *LogOdds ratio* function above F(0) by the experimental maximum-minimum area range Pax6+ positive RG nuclei in our cultures. The proportion of nuclei fitting into the region above *LogOdds ratio* F(0) and F(-0.1) delimited by the experimental of RG nuclear area interval, roughly matched with model RG predictions at 33% probability. And the effect of ln2PMMA mechanical constraints on the glial cell population with developmental potential to be RG is to force the nuclear transit through F(0) threshold, accumulating them into the defined RG nuclear zone. In summary, by calculating the *LogOdds ratio* function, our model mathematically identified an RG cell-intrinsic mechanical factor that sets limits for the possible nuclear morphologies present in functional RG.

Cell proliferation and division involve nuclear remodeling, the loss of nuclear envelope during mitosis and the total reshape of daughter cells nuclei. This leads us to explore whether nuclear changes during cell cycle progression were confounding effects for RG identification by the RGM model. Mitotic cells identified by PH3 expression (Hans & Dimitrov, 2001), and cycling cells expressing Ki67 (Urruticoechea et al., 2005) were around 13-17% of the total cell population, mainly located in the range of 10-20% RG probability, with a negligible percentage of nuclei above RG>0.5. A future RGM model improvement will include the identification and removal of cycling cells from the analysis.

Another RGM model improvement will be to increase the cell density range of the data used for training the model. Increasing RGM model applicability to high-density cultures during iPSC differentiation across neural cells lineages.

Our RGM model construction followed the standards described by the Committee on Credible Practiced of Modeling and Simulation on Healthcare described in (Erdemir et al., 2020). However, the rules related to third-party supervision, code broadly dissemination, and the use version control (repositories like GitHub) will only be archived after final publication in scientific journal. If possible, we will replicate the model using alternative programming languages or exploring analogous approaches with distinct statistical methods, such as Bayesian.

Finally, we have developed a graphical user interface (GUI) to implement the RGM model directly to files containing image segmentation data. While this app is currently in its early stages, it serves as a preview of forthcoming significant enhancements. Our ultimate goal is to merge image segmentation processes with a semi-automated modeling approach. Unlike conventional pre-defined models, our approach aims to derive mathematical relationships directly from image data and its variables. The envisioned system will show off a user-friendly interface allowing users to effortlessly select or deselect model variables. This will facilitate the identification of potentially significant relationships, making the entire process more accessible, efficient, and user-friendly (Harline et al., 2021). Additionally, the application will feature image quality checkpoints to guide users in assessing the consistency between images and experimental data. This multifaceted approach is set to significantly reduce data processing time, enhance data robustness and reliability, and improve the traceability of model construction.

Temporal sequence of glial response to ln2PMMA biomechanical signals

To start unraveling the precise mechanisms underlying glial response to Ln2PMMA RG-mimetic mechanical signals, we analyzed the temporal sequence of physical and biochemical changes from 1 to 14 DIV cultures on control and ln2PMMA substrate. Astrocytic maturation in primary cultures progress along time in culture and involve morphological and gene expression changes that recapitulate in part, the RG to astrocyte lineage progression (Lange et al., 2012; Lattke et al., 2021).

Our data indicated that mechanical signals from RG-mimetic ln2PMMA were early sensed by glial cells, promoting cellular and nuclear orientation along grooved topography, and producing cell type-specific nuclear conformational changes along the RG-astrocyte lineage from 1DIV. These morphological changes were associated with the reduced lamin A-C/B1nuclear ratio over time in culture. However, significant changes in ln2PMMA mediated RG induction, identified by the expression of molecular markers (Pax6+), were only evident after 3DIV. The observed temporal sequence reflects the initial response to the mechanical properties of the substrate (1DIV), the phase of maximal RG induction in response to ln2PMMA mechanical signals (3-7DIV), and the

astrocyte maturation phase, when increasing confluence and cell-cell signaling overcome mechanical signals from the substrate (14DIV). Data confirming our previous results showing that ln2PMMA biomechanically induced astrocyte to RG transformation is bidirectional (Álvarez, Sena, et al., 2014; Mattotti et al., 2012), as earlier demonstrated in response to diffusible factors (Hunter & Hatren, 1995).

RGM model application revealed some relevant information about the temporal activation of astrocytic mechanotransduction components, demonstrating that reduction in nuclear lamin A-C/B1 ratio and nuclear deformation precede expression changes specific cell-type determinants. This delay in fate decision changes aligned with recent findings related to the dynamics of mechanosensitive NSC differentiation, which highlight that permanent NSC fate changes required sustained mechanical inputs during 12h to 36h (Rammensee et al., 2017). Nuclear mechanical properties are strictly dependent on proportion of lamins type A or type B IF in the nuclear lamina (Lammerding et al., 2006; Swift et al., 2013; Swift & Discher, 2014; Wintner et al., 2020). As lamin A-C increases nuclear lamina stiffness (Swift et al., 2013), the reduction in nuclear lamin A-C/B1 ratio observed in ln2PMMA might reflect more compliant and deformable nuclei. Despite nuclear lamin A-C/B1 ratio reduction was a general trend in glial cells grown in ln2PMMA, only cells expressing nestin/GFAP IF have the capacity to deform their nucleus until acquire the RG-specific nuclear shape defined by our RGM model. Nestin and GFAP can form heteropolymeric filaments, which network dynamics, compliance to small deformations and resistance to mechanical stress mostly depend on GFAP isoforms composition (Potokar et al., 2020). As already described, nestin, GFAP and nuclear lamins have a tightly regulated developmental expression along RG to astrocyte lineage progression. Trough cytoskeletal crosstalk, IF are primary determinants of cell architecture and plasticity, acting as central hubs in mechanosensing and mechanotransduction from the cell membrane to the nucleus (Ndiaye et al., 2022). Therefore, the described changes in IF composition might reflect differences in the mechanosensitive phenotype along RG lineage differentiation. In this sense, lowering lamin B1 expression is associated with concomitant loss of the neurogenesis capacity in the adult brain, and progressive lamin-B1 loose during aging is associated to defective nuclear morphologies and astrocyte aging (bin Imtiaz et al., 2021b; Matias et al., 2022; Pathak et al., 2021; Schlachetzki et al., 2020).

Mechanical regulation of gene expression involves changes in the activity and subcellular localization of transcriptional coregulators, such as YAP/TAZ and β-catenin, which switch between cytoplasmic and nuclear localization in response to multiple signals, including mechanical forces (Elosegui-Artola et al., 2017a; Heng et al., 2020;

Uzer et al., 2018a). During brain development, β-catenin and YAP/TAZ activity are directly involved in different aspects of RG organization and neural progenitor expansion (Gan et al., 2014; Lavado et al., 2021; Rammensee et al., 2017). Therefore, we explored whether YAP/TAZ and β-catenin were implicated in temporal glial response to Ln2PMMA. We found that glial cells grown in ln2PMMA have sustained nuclear β-catenin during the phase of maximal RG induction in response to ln2PMMA mechanical signals (3-7DIV), with no significant changes in YAP/TAZ. Although no particular β-catenin Nuc/Cyto ratio was correlated with RG nuclear morphology, Pax6 is a direct transcriptional target of β-catenin/TCF complex, and genetic ablation of β-catenin inhibits Pax6 expression and RG development (Gan et al., 2014). Pointing to sustained β-catenin nuclear import as part of the mechanotransduction cascade that favors Pax6 expression in competent cells during ln2PMMA mechanical-driving RG induction. Moreover, YAP/TAZ are integral components of the β-catenin destruction complex (Azzolin et al., 2014). Therefore, even though we found no significant YAP/TAZ Nuc/Cyto changes, we cannot rule out a coordinated involvement of YAP/TAZ/β-catenin signaling in the ln2PMMA mechanotransduction cascade that drives functional RG induction. This notion is consistent with the nuclear translocation independent YAP/β-catenin protein interaction described during mechanosensitive neural stem cell differentiation in response to changes in ECM stiffness (Rammensee et al., 2017). Finally, β-catenin and YAP/TAZ, respond specifically to different types of physical forces and have different nuclear entry mechanisms that depend on their association with cytoskeletal and nucleoskeletal components including IF (Redmond & Coulombe, 2021; Sen et al., 2022; Sjöqvist et al., 2021; Uzer et al., 2018b), providing a framework for biomechanical regulation of cell differentiation.

Altogether, our multivariate logistic regression based RGM model supports the existence of cell intrinsic nuclear mechanical constraints within functional RG cells. And that revealed that only those cells with the adequate developmental potential and IF composition can transit across a defined nuclear shape RG threshold, to become functional RG in response to permissive or favorable physical signals. By using a Bayesian linear regression modeling approach, a recent work used collective morphological measurements of chromatin, actin, and focal adhesions within single cells for relating topography structure with gene expression (Cutiongco et al., 2020). The resulted model feasibly predicted gene expression based on morphological data, and together with our findings, strongly support the idea that gene expression is tightly associated with morphological changes associated to microenvironment topography.

Mechanoelectrical transduction components of glial response to ln2PMMA biomechanical signals

Our metanalysis from Di Bella's work (Di Bella et al., 2021) indicated that the mechanoelectrical machinery is expressed in RG-astrocyte lineage cells though development, and that lineage progression involves an increase in genes related to Ca^{2+} signaling and homeostasis, including CaMKII, those associated to mitochondrial Ca^{2+} regulation, and channels responsible for background potassium conductance that keep the hyperpolarized resting membrane potential characteristic of astrocytes. We found that MSC proteins ASIC1, TRPC1, TRESK, Kv7.4 and to less extent TREK1 were upregulated, while TRPA1 and TREK-2 were downregulated in glial cells grown on ln2PMMA with respect to control substrate. While ASIC1, TRPC1, and TRPA1 are excitatory non-selective cation MSCs, Kv7.4, TRESK/TREK are K^+ selective channels that contribute to setting the resting membrane potential, adjusting membrane excitability to counteract the action of excitatory MSCs. These data suggest that the mechano-driven astrocyte-RG dedifferentiation requires a fine-tuned balance between the expression of excitatory and inhibitory MSCs. However, these changes do not inform us about the MSC combination expressed in each glial cell type or whether the different MSCs are in open or close conformation.

Correlation of live Ca^{2+} imagen analysis with RG markers expression revealed that ln2PMMA-mechanical signals significantly reduced intracellular Ca^{2+} concentration and the frequency of spontaneous Ca^{2+} transients in all glial cell types, but to a much lesser extent in RG, identified either by Pax6+ expression or by the application of our RGM model. This reduced Ca^{2+} dynamics correlated well with the lower TRPA1 and higher TRPC1 expression in glial cells grown in ln2PMMA. As TRPA1 pharmacological inhibition in astrocytes block spontaneous Ca^{2+} signals and significantly decrease their intracellular basal Ca^{2+} concentration (Shigetomi et al., 2012), while TRPC1 reduce TRPC3-induced Ca^{2+} entry in cortical astrocytes (Belkacemi et al., 2017). Moreover, TRPC1 expression decreases in fate-restricted cells (Dietrich et al., 2014), therefore, TRPC1 upregulation in ln2PMMA is consistent with RG enrichment and a less differentiated glial culture. Kv7.4, TRESK and TREK/TRAAK K^+ channels sense the asymmetry in the phospholipid bilayer and are differentially gated by monolayer tension setting the resting membrane potential and adjusting membrane excitability. Mechano-gated background channels reduced excitability by hyperpolarizing the resting membrane potential and reducing membrane resistance.

To inquire about the functional state of MSCs and Ca^{2+} signaling requirements for functional RG induction we performed a pharmacological inhibition approach. GsMTx4

is an amphipathic peptide from spider venom that associates with the superficial monolayer in a relaxed phospholipid bilayer membrane and penetrate deeper as tension increases. Under mechanical loading or membrane bending, due to the coupling between both lipid monolayers, GsMTx4 relief of tension in one monolayer increases the tension in the opposite monolayer. Thus, GsMTx4 has simultaneous antagonistic effects, inhibiting excitatory MSC while potentiating inhibitory K^+ selective MSCs (Gnanasambandam et al., 2017; Suchyna, 2017). GsMTx4 administration during 3h abrogate substrate-dependent differences in glial cell-type composition trough a dual effect, blocking RG induction in ln2PMMA while reducing astrocyte phenotypes in control substrate. Demonstrating the involvement of MSCs in the mechanical induction of RG and suggesting that cell type-specific MSCs composition and activation state depend, at least in part, on their membrane mechanical loading in the different substrates.

Instead, KN93 is a molecule that binds Ca^{2+}/CaM binding sites preventing Ca^{2+}/CaM-dependent activities including CaMKII activation (Wong et al., 2019). Inhibition of intracellular Ca^{2+} signaling trough KN93 administration also abrogates substrate-dependent differences in glial cell-type composition, by partially reverting the astrocyte to RG switch induced by ln2PMMA. Suggesting that Ca^{2+}/CaMKII activity is required for functional RG phenotypes, and that mechanoelectrical transduction involves a thigh control of intracellular Ca^{2+} signaling. Additionally, Ca^{2+}/CaM regulates Kv7.4 channels in a calcium-dependent manner (Chang et al., 2018; Zhuang & Yan, 2021), which are upregulated in ln2PMMA.

Nuclear lamins are generalized nuclear mechanosensors that regulate chromatin organization and gene expression to adapt cell fate and behavior to their physical microenvironment (Niethammer, 2021). Nuclear Lamin composition was significantly affected by both pharmacological treatments, KN93 and GsMTx4, which lowered lamins A-C/B1 ratio in glial cells. The observed KN93-iduced reduction in lamins A-C/B1 ratio in glial agree with previous data in cancer cells, which reduced lamin A-C expression after treatment with Ca^{2+}/CaMKII inhibitors (Kim et al., 2022). Unexpectedly, the reduction in lamins A-C/B1 ratio was more pronounced in GsMTx4 treated glial cultures, probably also reflecting a decrease in Ca^{2+}/CaM signaling. Therefore, the lower lamins A-C/B1 ratio observed in ln2PMMA might reflect the lower intracellular Ca^{2+} concentration and a mechanically-induced decrease in Ca^{2+}/CaM signaling. Suggesting a potential regulatory role of the Ca^{2+}/CaMKII pathway in shaping lamin expression dynamics during RG lineage cells development.

As already described, KN93 treatment significantly lowered lamins A-C/B1 ratio in control substrate and increased the proportion of GFAP+ astrocytes in ln2PMMA. RGM model application revealed that pharmacological inhibition of Ca^{2+}/CaM signaling in glial cells grown on ln2PMMA favor the differentiation of GFAP+ astrocytes, and the exit of their nuclei away from the RG region. Conversely, similar Ca^{2+}/CaM inhibition in control substrate partially mimic ln2PMMA biomechanical signals, favoring glial nuclei entering into the RG region and astrocyte dedifferentiation to RG, probably associated to the direct regulation of nuclear lamins composition. Our results agree with recent research describing that stretch-activated intracellular calcium alterations are linked to changes in the nuclear envelope and ER (Lomakin et al., 2020), highlight the role of calcium signaling in mechano-driven astrocyte dedifferentiation. CaMKII exhibit dynamic behavior in cortical astrocytes and can rapidly translocate in and out to the nucleus regulating gene transcription (Zhao & Diaz Brinton, 2003). Opening an intriguing avenue for exploring how mechanical-driven regulation or calcium dynamics and nuclear morphology collectively influence gene transcription and RG lineage progression.

In summary, our data indicate that intracellular calcium dynamics is crucial in the biomechanical induction of astrocyte to RG dedifferentiation. Glial cells adaptation to ln2PMMA substrates implies a reduction in the intracellular calcium concentration and calcium oscillations. Probably associated with a shift in excitatory and inhibitory MSCs expression and conformational state, affecting resting membrane potential and Ca^{2+}/CaM signaling. The pharmacological interference of this calcium-associated mechanoelectrical signal is sufficient to abrogate substrate-induced changes in cell type-specific molecular markers, remodeling nuclear lamins composition, and inducing nuclear morphological changes that favor or prevent the acquisition of RG nuclear constraints in function of the substrate. The identification of different intracellular calcium dynamics between RG and non-RG cells identified by our RGM model highlighted the role of calcium in the acquisition of RG nuclear constraints. Nonetheless, whether these changes were directly associated with the expression of particular MSCs in different cell types, or their relationship with CaMKII activity required further investigation.

Metabolic rewiring and mitochondrial network adaptation during glial response to ln2PMMA biomechanical signals

Metabolic rewiring, often characterized by transitions between glycolytic and oxidative phosphorylation (OXPHOS) and alterations in oxidative state, is commonly linked to cellular differentiation (Chui et al., 2020). Particularly, metabolic rewiring is a major player in RG biology and brain development (Andrews & Pearson, 2023; Angelopoulos et al., 2022b; Iwata & Vanderhaeghen, 2021). Additionally, the intricate interplay between

mechanotransduction and metabolism plays a pivotal role in cellular mechanics and adaptation to mechanical signals (J. S. Park et al., 2020; Phuyal et al., 2023; Romani et al., 2021b). Our data suggest that the biomechanical adaptation of glial cells to ln2PMMA and the resulting astrocyte-RG dedifferentiation involve distinct metabolic adaptations, including a rise in PFKFB3-dependent aerobic glycolysis, PCK2-dependent anabolism, and a profound rewiring of mitochondrial dynamics, to fulfill the metabolic requirements of more proliferative RG.

Fructose-2,6-bisphosphate is an allosteric activator of phosphofructokinase (PFK) enzyme in the second rate-limiting reaction of glycolysis. The PFK-2/FBP-ase-2 (PFKFB) enzyme family has dual kinase and bisphosphatase activities and regulates the levels of fructose-2,6-bisphosphate in the cells, hence glycolytic flux. In this enzyme system, kinase and bisphosphatase activities are modulated mainly through the preferential expression of isoforms with specific kinetic characteristics. For example, the PFKFB3 isoform strongly promotes glycolysis because of increased kinase activity. This isoform then plays a key role in cell proliferation and cell cycle (Yalcin et al., 2009). Pyruvate generated from glycolysis can be converted to lactate or, under aerobic conditions, translocate to mitochondria, where it is irreversibly oxidized into acetyl-CoA through the multienzyme pyruvate dehydrogenase complex (PDC), connecting glycolysis to the TCA cycle and OXPHOS. Allosteric regulation by ATP or acetyl-CoA, together with phosphorylation of the enzyme (pPDH) strongly reduces PDC activity, reducing pyruvate utilization in the mitochondria, OXPHOS and, therefore oxygen consumption (Miyazawa & Aulehla, 2018). Finally, mitochondrial phosphoenolpyruvate carboxykinase 2 (PCK2) catalyzes the conversion of oxaloacetate (OAA) to phosphoenolpyruvate (PEP). PCK2-mediated synthesis of PEP allows cells to convert TCA cycle intermediates into glycolytic intermediates, to fuel multiple biosynthetic processes, such as amino acid, lipids, and nucleotide synthesis (Hyroššová et al., 2021; Leithner et al., 2015). High PFKFB3 levels, as we found here, are associated to self-renewing RG, as PFKFB3 knockdown increases neuron production at the expenses of RG and reduces lactate release and proliferation in reactive astrocytes (Andrews & Pearson, 2023; Dong et al., 2022; Lv et al., 2015b). Similar mechanosensitivity was described for PFK, which degradation is regulated by tissue/ECM stiffness and adhesion conditions, in turn regulating glycolytic rates (J. S. Park et al., 2020; Romani et al., 2021b).

All in all, these data are supportive of the canonical view, however, several data in our model were conflicting with increased glycolysis, including the fact that lactate production was not significantly increased in ln2PMMA, and the reduction in pPDH observed, indicative of enhanced PDC activity. However, the reduction in GPX expression indicates

low ROS production probably through decreased OXPHOS. Hence, we cannot exclude that pPDH in our data is not functionally directive towards increased OXPHOS. Together with data on enhanced PCK2 expression in subsets of nestin+ and nestin- cells we envisage the metabolic profile of glial cells grown on ln2PMMA as mainly driven by aerobic glycolysis and predominantly anabolic . This result is consistent with metabolic analysis showing that neural stem/progenitor cells are predominantly glycolytic, but also required TCA cycle function and PCK2 for self-renewal and neurogenesis (Iwata & Vanderhaeghen, 2021; Zheng et al., 2016). This goes in lane with previous work in our lab showing that lactate-releasing biomimetic materials increase RG and neural progenitor pools in vitro and in vivo trough increasing PCK2-dependent anabolism (Álvarez, Castaño, et al., 2014; Álvarez et al., 2013, 2016).

Mitochondria are highly dynamic bi-layered organelles that, through their interaction with cytoskeletal structures, can change their spatial distribution and remodel their structure, to adapt bioenergetic efficiency depending on cell energy requirements (Baum & Gama, 2021; Iovine et al., 2021). This dynamism relays in a set of specific GTPases mediating cycles of mitochondrial fusion and fission IMM and OMM, adapting mitochondrial morphology and mitochondrial network to cell's metabolic demands (Chakrabarti et al., 2018; De Brito & Scorrano, 2008). In addition, recent studies demonstrated that mitochondria are mechanosensitive and mechanoresponsive organelles, which morphology is modulated by mechanical signals of cell microenvironment to promote adaptative reprograming of mitochondrial function and oxidative stress reliance (J. S. Park et al., 2020; Phuyal et al., 2023; Tharp et al., 2021). Here we found that glial cells grown in ln2PMMA upregulate MFN2, indicating the presence of larger mitochondria with fused OMM; and downregulate OPA1, indicative of less complex inner membrane cristae. Mitochondrial morphology analysis thus revealed that biomechanically induced RG had elongated and highly interconnected mitochondria and more mitochondrial volume per cell, in agreement according with fused mitochondria described in RG (Andrews & Pearson, 2023; Angelopoulos et al., 2022b; Gkini & Namba, 2023a; Iwata & Vanderhaeghen, 2021). Unexpectedly, mitochondrial differences were more sharply defined when cells were segregated by their location above F(0), within RG permissive nuclear region. In addition to higher mitochondrial volume, with more tubular mitochondria and highly ramified and interconnected mitochondrial network, we also found lower ΔΨm. The lower ΔΨm can be related with the observed reduction in OPA1 expression, less complex cristae organization and less efficient OXPHOS. Moreover, the strong association of mitochondrial dynamics rewiring with RG nuclear constraints suggesting that changes in mitochondrial dynamics, were principally correlated with

nuclear entering into the permissive RG region above F(0), and before acquiring all the characteristics of functional RG. Indeed, highly fused, and interconnected mitochondria in RG are associated to a predominant glycolytic metabolism, self-renewing and RG proliferation, instead of differentiation (Iwata et al., 2020b; Khacho et al., 2016; Romero-Morales et al., 2022).

Taken together, our results indicate that mechanical-driven astrocyte to RG dedifferentiation in ln2PMMA involves a complex metabolic reprogramming involving mitochondrial dynamics rewiring. The observed bias towards increased aerobic glycolysis and anabolic metabolism will allow the provision of carbon intermediates from TCA for biosynthetic purposes, essential to fulfil the metabolic demands to sustain stemness and proliferation. However, further study is required to mechanistically support this hypothesis, as lack of homogeneity did not allow directly associate most changes in metabolic enzymes with particular cell types in ln2PMMA or perform functional metabolic studies such as respirometry. Considering cell heterogeneity in our cultures and the strict dependence of substrate attachment of our in vitro system, metabolic analysis in cell suspension like Oxygraphy-2k or Seahorse™ assays, where ln2PMMA substrate cannot fit into their culture wells, challenge those studies. Moreover, the high glucose content (25mM) in our culture media can interfere with ln2PMMA mechanical signals obscuring the identification of relevant metabolic adaptations (Tharp et al., 2021).

Evolutive conservation of RG nuclear allometry

Previous studies of our lab had demonstrated that cultured mouse astrocytes grown on an RG biomimetic micro3D scaffold adopt a functional RG phenotype (Álvarez, Sena, et al., 2014; Mattotti et al., 2012). In this thesis, by using this *in vitro* model we have unraveled that nuclear morphology changes precede the expression of RG-specific genes, during biomechanical induction of RG. Moreover, we found the existence of intrinsic mechanical constraints that limit the type of possible shapes adopting by a functional RG nucleus. Allowing the development of the RGM mathematical model for RG probability calculation based on nuclear parameters.

The role of RG remains consistent across species, suggesting that certain features can be evolutionary conserved. The access to human RG primary cultures, hiPSC and its derivates, hNPC and brain organoids, led us to explore whether these RG nuclear constraints were conserver trough evolution, and the capacity of the RGM model to properly identify hRG. However, our model application is limited by the culture cell density used for training, and these human cell cultures require very high confluency, well beyond the RGM model trained interval. This limits direct RGM model applicability to non-extrapolated data to obtain associated RG probabilities. Nevertheless, the

LogOdds ratio function represents the expected shape for each value of nuclear size at different levels, with level 0 (F(0)) corresponding to the abrogation of the substrate factor defined by the RGM model. *LogOdds ratio* function F(0) establish a threshold that defines a territory of possible nuclear shapes for functional RG phenotypes without associated RG probability, which allow a broader application. Similarly, in developmental evolution studies, this correlates with allometry, which is broadly used in geometric morphometrics and defines the dependence of changes in shape on size during organism's development (Klingenberg, 2010).

Unexpectedly, segmented hRG nuclei from *in vivo* images nicely drop in the RG region above F(0), confirming the evolutive conservation of the RG nuclear constraints. However, RGM model and *LogOdds ratio* function F(0) application to primary hRG cultures sharing the same origin that hRG in fetal brain sections and gave much lower fitting. Indicating that the absence of mechanical signals from the microenvironment during culture on flat substrates disrupts RG structural anisotropy, affecting nuclear morphology and functionality. The loss of mechanical cues such as apical-basal RG anchorage and radially aligned during the culture process on flat substrates may contribute to these effects. As ln2PMMA, a substrate that mimic RG structural anisotropy in the embryonic brain, induced RG phenotypes in mouse glial cultures, it will be worth to evaluate whether the use of this or similar RG mimetic substrates will improve hRG and hNPC maintenance and functionality in culture.

We have also found that during biomechanical induction of RG, nuclear deformation precedes gene expression changes. One way in which mechanical signals can affect gene expression is by altering chromatin structure, the organized and packaged structure of genetic material together with histones and associated proteins. Chromatin is linked to different NE components, such as lamins, trough lamin associated domains (LADs). Changes in lamins composition affect LADs distribution, chromatin organization and gene expression (Goelzer et al., 2021). LADs are evolutionary conserved across species with different extents, for example, between human and macaque, ~85-91%, and between human and mouse, ~70% (Aboelnour & Bonev, 2022; Ahanger et al., 2021). Thus, one plausible explanation for the evolutive conservation of RG nuclear constraints is that nuclear allometry could be associated to specific LADs and chromatin organization. Interestingly, LADs conservation in NPCs was lower when comparing developing mouse brain *in vivo* with *in vitro* NPC cultures, than between NPCs from different species. This aligns with our hypothesis, highlighting that the loss of physiological mechanical signals together with cell adaptation to stiff flat substrates dramatically influences nuclear morphology and consequently gene expression, fate,

and functionality. In this sense, it has been recently described that extrinsic signals orchestrate chromatin remodeling and transcriptional changes leading to astrocyte maturation (Lattke et al., 2021). Therefore, the evolutive conservation of RG nuclear allometry and their relationship with chromatin structure and gene expression requires further extensive investigation.

The success of identifying hRG both *in vivo* and *in vitro* using the RGM model expands its utility, enabling RG investigations under various physiological conditions. For instance, the remarkable progress in brain organoid development since Lancaster et al. established the first whole brain organoid protocol in 2013 (Lancaster & Knoblich, 2014), owes greatly to the dedicated efforts of laboratories worldwide (Mulder et al., 2023). However, a recent systematic review highlighted a widespread lack of standardization in reporting cell types, mostly due to the absence of specific molecular markers (Mulder et al., 2023). The complexity of brain organoid architectures together with the fact that our model is trained with 2D data obstacle its application. So further work will be done to improve nuclear segmentation programs and the RGM model, allowing their application to high density 3D cultures to evaluate if RG in brain organoids also conserve these nuclear constraints. The implementation of volumetric parameters associated to roughness measures, as the obtained from nuclear lamins, or epigenetic marks associated to active transcription in euchromatin ($H3K4me^{1,3}$) and transcriptional repression in heterochromatin ($H3K9me^{2,3}$, $H3K27me^{3}$) distribution, will help to explore chromatin organization. Improvement that will boost RGM model applicability and relevance.

Integrated hypothesis of the mechano-electrical -metabolic and -nuclear components during biomechanical dedifferentiation of astrocytes into RG

Increasing evidence highlight the relevance of mechanical signals from the niche microenvironment in regulating the stemness, proliferation and differentiation of NSC/RG during brain development, adult neurogenesis, and after lesion. The principal findings of this Thesis (summarized in Figure D-1) define the mechano-electrical -metabolic and -nuclear components of astrocyte to RG dedifferentiation in response to substrate biomechanical cues. We propose that the process of astrocyte to RG dedifferentiation is orchestrated by the interplay of intracellular and extracellular factors, including nuclear mechanical constraints, calcium dynamics, and metabolic rewiring involving mitochondrial network reorganization, all of which collectively contribute to the acquisition and maintenance of the RG phenotype in response to mechanical signals provided by the RG biomimetic ln2PMMA substrate.

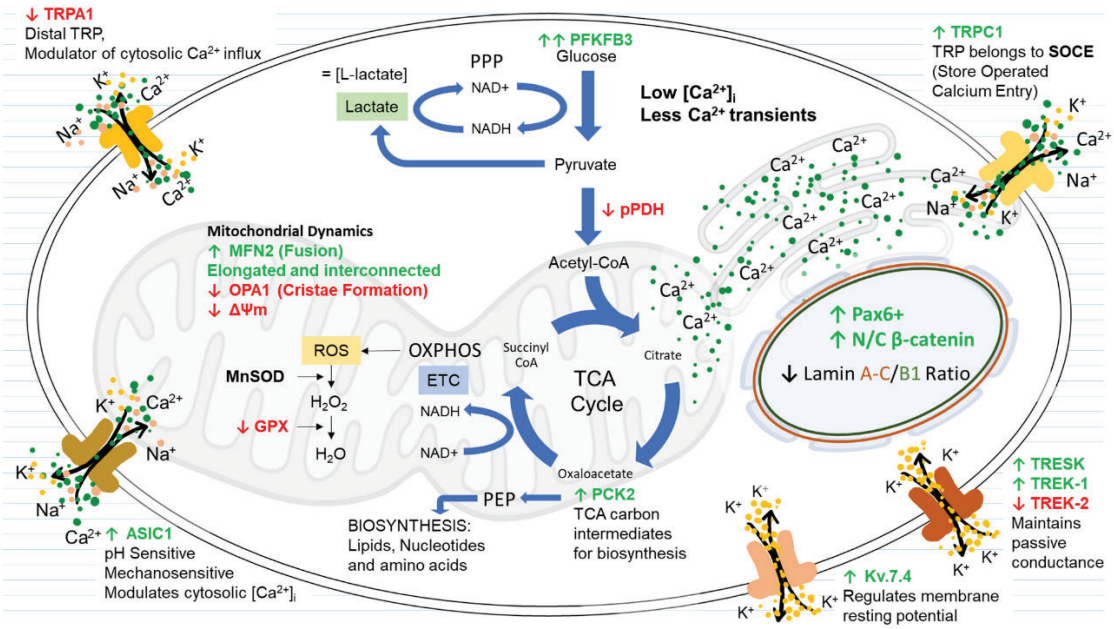


Figure D- 1 **Summary of the principal findings associated to In2PMMA biomechanical induction of astrocyte to RG dedifferentiation.**

Based on our data, only cells expressing nestin and/or GFAP intermediate filaments are capable of astrocyte-RG phenotypic transitions in response to permissive or favorable physical signals. We propose a temporal sequence in which the forces generated by the anisotropic characteristics of In2PMMA substrate are rapidly translated from cell adhesion structures in the plasma membrane to the glial cell's nucleus through the cytoskeleton. Simultaneously, these membrane/cytoskeletal tensions change the open/close state of MSCs at the plasma membrane, generating mechanoelectrical signals that alters CAMKII activity and intracellular calcium dynamics. Reducing intracellular calcium concentration and calcium transients. Together those signals lead to a nuclear deformation, a reduction in lamins A-C/B1 ratio, and higher β-catenin nuclear import that, when sustained in time, produce transcriptional and translational changes in MSCs involved in setting resting membrane potential and calcium dynamics, key metabolic and mitochondrial dynamics enzymes lading to a metabolic reprogramming, and the expression of NSC/RG markers as Pax6 and Sox2. The effective transition from astrocyte to functional RG is limited by RG cell-intrinsic nuclear mechanical constraints, which can be mathematically defined by the RGM model we developed. Cells with nuclei within the region delimited by RG nuclear constraints can be identified by their specific pattern of intracellular calcium dynamic and metabolism. Characterized by elongated and interconnected mitochondria, with a significant reduction ΔΨm and a bias towards increased aerobic glycolysis and anabolic metabolism. This metabolic switch can

facilitate the provision of carbon intermediates from the TCA cycle for biosynthetic purposes, crucial for sustaining stemness and proliferation of NSC/RG cells.

Recent research has unveiled that distinct astrocyte subpopulations are capable of neural stem cell (NSC) functions, indicating a potential for endogenous brain regeneration. Astrocytic regenerative capacity is triggered by Inflammatory signals after lesion, one of them is the suppression of Ca^{2+}/CaMKII pathway (Magnusson et al., 2020; Yang et al., 2023; Zamboni et al., 2020)(Zhang et al., 2024). Therefore, mechanical, and inflammatory signals might share in part molecular mechanisms. This made our *in vitro* model a useful platform to identify key molecular mechanisms to boost astrocytic regenerative potential. Opening new potential therapeutic avenues to enhance endogenous brain repair and recovery post-injury.

Finally, our findings unveiled an evolutionary conservation of specific RG nuclear constraints, which is supported by recent research indicating LADs conservation across species (Aboelnour & Bonev, 2022; Ahanger et al., 2021). RG nuclear constraints conservation across species made our RGM model, and their future improved versions, an invaluable tool with unsuspected possibilities, and aligns with recent standards proposed to improve cell identification beyond the use of cell-type-specific molecular markers (Escartin et al., 2021; Mattiazzi Usaj et al., 2021b; Yuste et al., 2020).

6. CONCLUSIONS

1. Mechanoelectrical machinery components are expressed in RG-astrocyte lineage cells though development. Astrocyte maturation upregulates genes related to Ca^{2+} signaling and homeostasis, K^{+} channels that hyperpolarize resting membrane potential, and increases the ratio lmna/lmnb1.

2. RG-mimetic mechanical signals from ln2PMMA induce changes in nuclear morphology and reduce nuclear lamins A-C/B1 ratio, days before changes in lineage-specific genes.

3. ln2PMMA-induced mechanotransduction probably involve the activation of YAP/TAZ/β-catenin signaling pathways and produce a complex shift in the expression of excitatory and inhibitory MSC in glial cells, upregulating ASIC1, TRPC1, TRESK and Kv7.4 and downregulating TRPA1 and TREK-2.

4. Ln2PMMA mechanoelectrical signaling reduced intracellular Ca^{2+} concentration and spontaneous Ca^{2+} transients in glial cells, in part through inhibition of Ca^{2+}/Calmodulin Kinase II (CaMKII) dependent activity.

5. Ln2PMMA biomechanical induction of RG involved metabolic reprogramming and changes in mitochondrial dynamics. Characterized by increased PFKFB3 expression, large tubular and interconnected mitochondria with reduced membrane potential, and a bias towards aerobic glycolysis and PCK2-dependent anabolism.

6. We have developed a logistic regression model, called Radial Glia Mimetic (RGM) model, for fitting RG probability based in nuclear morphology parameters. The model unraveled the existence of RG-specific nuclear constraints that are evaluatively conserved across species, allowing RG identification independent of the use of molecular markers.

7. RGM model application demonstrated that only glial cells expressing nestin/GFAP intermediate filaments respond to RG-mimetic mechanical signals dedifferentiating into an RG phenotype in ln2PMMA.

8. RGM identified RG are heterogeneous but share Ca^{2+} dynamics and mitochondrial signature. Pharmacological interventions altering Ca^{2+} dynamics force the nucleus exit from the RG region, and the decline of RG molecular markers.

9. The loss of mechanical signals from the niche, e.g. apicobasal attachment and polarity, that occurs in 2D culturing on flat and stiff substrates, markedly reduced RG structural integrity and functionality. The use of RG-mimetic micro 3D materials, like ln2PMMA, that reproduce the structural anisotropy of the embryonic brain might significantly improve the in vitro modeling of early neural development.

10. The evolutionary conservation of functional RG nuclear constraints between species made the RGM model an unvaluable tool for improved RG identification and characterization, by integrating multimodal data with RG nuclear morphology.

7. CONTRIBUTIONS

Dr. Carlos Borau, post-doctoral researcher in biological and mechanical engineering at Multiscale in Mechanical and Biological Engineering group (m2be, University of Zaragoza)

- He developed all MATLAB algorithms and its guided user interferences (GUI) used in this Doctoral Thesis.

Dr. Jesús Asín, associate professor at department of statistical methods, University of Zaragoza, Faculty of Engineering and Architecture.

- He developed the RGM model and performed all previous versions.
- He trained and taught me how to do it, and how to apply the RGM model and become a self-sufficient R programmer to some extent.
- This contribution has involved different periods of time spent in his department.

Dr. Leonardo Garma, post-doctoral researcher at Centro Nacional de Investigaciones Oncológicas (CNIO).

- He performed the single-cell RNA metanalyses.

Dr. Rosalba Sortino, post-doctoral researcher at Nanoprobes and Nanoswitches group at Institute for Bioengineering of Catalonia (IBEC).

- She supervised and performed calcium recordings.

Dr. Juan Alberto Ortega, Ramón y Cajal Investigator at Department of Pathology and Experimental Therapeutics, School of Medicine, University of Barcelona.

- He provides me with iPSC and NPC cultures and brain organoids.
- He provides me images from iPSC, NPC, and brain organoids.
- He provides me images from human RG cultures and derived human neuronal cultures.
- He provides me images from human fetal cortex slices.

8. BIBLIOGRAPHY

A. Stoykova, M. G. P. G. and J. P. (n.d.). *Pax6-dependent regulation of adhesive patterning, R-cadherin expression and boundary formation in developing forebrain*.

Aaku-Saraste, E., Oback, B., Hellwig, A., & Huttner, W. B. (1997). *Neuroepithelial cells downregulate their plasma membrane polarity prior to neural tube closure and neurogenesis*.

Aboelnour, E., & Bonev, B. (2022). Evolutionary conservation and cell type specificity of nuclear compartments in the brain. In *Trends in Neurosciences* (Vol. 45, Issue 1, pp. 3–5). Elsevier Ltd. https://doi.org/10.1016/j.tins.2021.10.007

Abuwarda, H., & Pathak, M. M. (2020a). Mechanobiology of neural development. In *Current Opinion in Cell Biology* (Vol. 66, pp. 104–111). Elsevier Ltd. https://doi.org/10.1016/j.ceb.2020.05.012

Abuwarda, H., & Pathak, M. M. (2020b). Mechanobiology of neural development. In *Current Opinion in Cell Biology* (Vol. 66, pp. 104–111). Elsevier Ltd. https://doi.org/10.1016/j.ceb.2020.05.012

Ahanger, S. H., Delgado, R. N., Gil, E., Cole, M. A., Zhao, J., Hong, S. J., Kriegstein, A. R., Nowakowski, T. J., Pollen, A. A., & Lim, D. A. (2021). Distinct nuclear compartment-associated genome architecture in the developing mammalian brain. *Nature Neuroscience*, *24*(9), 1235–1242. https://doi.org/10.1038/s41593-021-00879-5

Alan, L., & Scorrano, L. (2022). Shaping fuel utilization by mitochondria. In *Current Biology* (Vol. 32, Issue 12, pp. R618–R623). Cell Press. https://doi.org/10.1016/j.cub.2022.05.006

Albanese, A., Swaney, J. M., Yun, D. H., Evans, N. B., Antonucci, J. M., Velasco, S., Sohn, C. H., Arlotta, P., Gehrke, L., & Chung, K. (2020). Multiscale 3D phenotyping of human cerebral organoids. *Scientific Reports*, *10*(1). https://doi.org/10.1038/s41598-020-78130-7

Alber, M., Buganza Tepole, A., Cannon, W. R., De, S., Dura-Bernal, S., Garikipati, K., Karniadakis, G., Lytton, W. W., Perdikaris, P., Petzold, L., & Kuhl, E. (2019). Integrating machine learning and multiscale modeling—perspectives, challenges, and opportunities in the biological, biomedical, and behavioral sciences. In *npj Digital Medicine* (Vol. 2, Issue 1). Nature Research. https://doi.org/10.1038/s41746-019-0193-y

Alexej Verkhratsky, A. B. (2023). *Neuroglia: Function and Pathology* (Academic Press, Ed.; 1st Edition).

Almudevar, A., Oakes, D., & Hall, J. (2020). Statistical Modeling for Biological Systems: In Memory of Andrei Yakovlev. In *Statistical Modeling for Biological Systems: In Memory of Andrei Yakovlev*. Springer International Publishing. https://doi.org/10.1007/978-3-030-34675-1

Álvarez, Z., Castaño, O., Castells, A. A., Mateos-Timoneda, M. A., Planell, J. A., Engel, E., & Alcántara, S. (2014). Neurogenesis and vascularization of the damaged brain using a lactate-releasing biomimetic scaffold. *Biomaterials*, *35*(17), 4769–4781. https://doi.org/10.1016/j.biomaterials.2014.02.051

Álvarez, Z., Hyrossova, P., Perales, J. C., & Alcantara, S. (2016). Neuronal Progenitor Maintenance Requires Lactate Metabolism and PEPCK-M-Directed Cataplerosis. *Cerebral Cortex*, *26*(3), 1046–1058. https://doi.org/10.1093/cercor/bhu281

Álvarez, Z., Mateos-Timoneda, M. A., Hyroššová, P., Castaño, O., Planell, J. A., Perales, J. C., Engel, E., & Alcántara, S. (2013). The effect of the composition of PLA films and lactate release on glial and

neuronal maturation and the maintenance of the neuronal progenitor niche. *Biomaterials*, *34*(9), 2221–2233. https://doi.org/10.1016/j.biomaterials.2012.12.001

Álvarez, Z., Sena, E., Mattotti, M., Engel, E., & Alcántara, S. (2014). An efficient and reproducible method to culture Bergmann and cortical radial glia using textured PMMA. *Journal of Neuroscience Methods*, *232*, 93–101. https://doi.org/10.1016/j.jneumeth.2014.05.011

Andrews, M. G., & Pearson, C. A. (2023). Toward an understanding of glucose metabolism in radial glial biology and brain development. In *Life science alliance* (Vol. 7, Issue 1). https://doi.org/10.26508/lsa.202302193

Andrews, M. G., & Pearson, C. A. (2024). Toward an understanding of glucose metabolism in radial glial biology and brain development. In *Life science alliance* (Vol. 7, Issue 1). https://doi.org/10.26508/lsa.202302193

Andrews, M. G., Subramanian, L., Salma, J., & Kriegstein, A. R. (2022). How mechanisms of stem cell polarity shape the human cerebral cortex. In *Nature Reviews Neuroscience* (Vol. 23, Issue 12, pp. 711–724). Springer Nature. https://doi.org/10.1038/s41583-022-00631-3

Angelopoulos, I., Gakis, G., Birmpas, K., Kyrousi, C., Habeos, E. E., Kaplani, K., Lygerou, Z., Habeos, I., & Taraviras, S. (2022a). Metabolic regulation of the neural stem cell fate: Unraveling new connections, establishing new concepts. In *Frontiers in Neuroscience* (Vol. 16). Frontiers Media S.A. https://doi.org/10.3389/fnins.2022.1009125

Angelopoulos, I., Gakis, G., Birmpas, K., Kyrousi, C., Habeos, E. E., Kaplani, K., Lygerou, Z., Habeos, I., & Taraviras, S. (2022b). Metabolic regulation of the neural stem cell fate: Unraveling new connections, establishing new concepts. In *Frontiers in Neuroscience* (Vol. 16). Frontiers Media S.A. https://doi.org/10.3389/fnins.2022.1009125

Arnold Kriegstein, S. N. and V. M.-C. (2006). *Patterns of neural stem and progenitor cell division may underlie evolutionary cortical expansion*. www.nature.com/reviews/neuro

Arturo Alvarez-Buylla, José Manuel García-Verdugo, & Anthony D. Tramontin. (2001). *A unified hypothesis on the lineage of neural stem cells*.

Austin, S. H. L., Gabarró-Solanas, R., Rigo, P., Paun, O., Harris, L., Guillemot, F., & Urbán, N. (2021). Wnt/β-catenin signalling is dispensable for adult neural stem cell homeostasis and activation. *Development (Cambridge, England)*, *148*(20). https://doi.org/10.1242/dev.199629

Azevedo, F. A. C., Carvalho, L. R. B., Grinberg, L. T., Farfel, J. M., Ferretti, R. E. L., Leite, R. E. P., Filho, W. J., Lent, R., & Herculano-Houzel, S. (2009). Equal numbers of neuronal and nonneuronal cells make the human brain an isometrically scaled-up primate brain. *Journal of Comparative Neurology*, *513*(5), 532–541. https://doi.org/10.1002/cne.21974

Azzolin, L., Panciera, T., Soligo, S., Enzo, E., Bicciato, S., Dupont, S., Bresolin, S., Frasson, C., Basso, G., Guzzardo, V., Fassina, A., Cordenonsi, M., & Piccolo, S. (2014). YAP/TAZ incorporation in the β-catenin destruction complex orchestrates the Wnt response. *Cell*, *158*(1), 157–170. https://doi.org/10.1016/j.cell.2014.06.013

Bading, H. (2013). Nuclear calcium signalling in the regulation of brain function. In *Nature Reviews Neuroscience* (Vol. 14, Issue 9, pp. 593–608). https://doi.org/10.1038/nrn3531

Balakrishnan, S., Raju, S. R., Barua, A., Pradeep, R. P., & Ananthasuresh, G. K. (2021). Two nondimensional parameters for characterizing the nuclear morphology. *Biophysical Journal*, *120*(21), 4698–4709. https://doi.org/10.1016/j.bpj.2021.09.035

Barnes, J. M., Przybyla, L., & Weaver, V. M. (2017). Tissue mechanics regulate brain development, homeostasis and disease. In *Journal of Cell Science* (Vol. 130, Issue 1, pp. 71–82). Company of Biologists Ltd. https://doi.org/10.1242/jcs.191742

Barry, D., & McDermott, H. (2005). Differentiation of radial glia from radial precursor cells and transformation into astrocytes in the developing rat spinal cord. *GLIA*, *50*(3), 187–197. https://doi.org/10.1002/glia.20166

Baum, T., & Gama, V. (2021). Dynamic properties of mitochondria during human corticogenesis. In *Development (Cambridge)* (Vol. 148, Issue 4). Company of Biologists Ltd. https://doi.org/10.1242/dev.194183

Baur, K., Abdullah, Y., Mandl, C., Hölzl-Wenig, G., Shi, Y., Edelkraut, U., Khatri, P., Hagenston, A. M., Irmler, M., Beckers, J., & Ciccolini, F. (2022). A novel stem cell type at the basal side of the subventricular zone maintains adult neurogenesis. *EMBO Reports*, *23*(9). https://doi.org/10.15252/embr.202154078

Beasley, T. M., & Schumacker, R. E. (1995). Multiple Regression Approach to Analyzing Contingency Tables: Post Hoc and Planned. In *Source: The Journal of Experimental Education* (Vol. 64, Issue 1). http://www.jstor.orgURL:http://www.jstor.org/stable/20152474

Beattie, R., & Hippenmeyer, S. (2017). Mechanisms of radial glia progenitor cell lineage progression. In *FEBS Letters* (Vol. 591, Issue 24, pp. 3993–4008). Wiley Blackwell. https://doi.org/10.1002/1873-3468.12906

Bedrosian, T. A., Houtman, J., Eguiguren, J. S., Ghassemzadeh, S., Rund, N., Novaresi, N. M., Hu, L., Parylak, S. L., Denli, A. M., Randolph-Moore, L., Namba, T., Gage, F. H., & Toda, T. (2021). Lamin B1 decline underlies age-related loss of adult hippocampal neurogenesis. *The EMBO Journal*, *40*(3). https://doi.org/10.15252/embj.2020105819

Belkacemi, T., Niermann, A., Hofmann, L., Wissenbach, U., Birnbaumer, L., Leidinger, P., Backes, C., Meese, E., Keller, A., Bai, X., Scheller, A., Kirchhoff, F., Philipp, S. E., Weissgerber, P., Flockerzi, V., & Beck, A. (2017). TRPC1- and TRPC3-dependent Ca2+ signaling in mouse cortical astrocytes affects injury-evoked astrogliosis in vivo. *GLIA*, *65*(9), 1535–1549. https://doi.org/10.1002/glia.23180

Bem, J., Brożko, N., Chakraborty, C., Lipiec, M. A., Koziński, K., Nagalski, A., Szewczyk, Ł. M., & Wiśniewska, M. B. (2019). Wnt/β-catenin signaling in brain development and mental disorders: keeping TCF7L2 in mind. In *FEBS Letters* (Vol. 593, Issue 13, pp. 1654–1674). Wiley Blackwell. https://doi.org/10.1002/1873-3468.13502

Bernal, A., & Arranz, L. (2018). Nestin-expressing progenitor cells: function, identity and therapeutic implications. In *Cellular and Molecular Life Sciences* (Vol. 75, Issue 12, pp. 2177–2195). Birkhauser Verlag AG. https://doi.org/10.1007/s00018-018-2794-z

Bianchi, L. (2021). *DEG/ENaC Ion Channels in the Function of the Nervous System: From Worm to Man* (pp. 165–192). https://doi.org/10.1007/978-981-16-4254-8_9

bin Imtiaz, M. K., Jaeger, B. N., Bottes, S., Machado, R. A. C., Vidmar, M., Moore, D. L., & Jessberger, S. (2021a). Declining lamin B1 expression mediates age-dependent decreases of hippocampal stem cell activity. *Cell Stem Cell*, *28*(5), 967-977.e8. https://doi.org/10.1016/j.stem.2021.01.015

bin Imtiaz, M. K., Jaeger, B. N., Bottes, S., Machado, R. A. C., Vidmar, M., Moore, D. L., & Jessberger, S. (2021b). Declining lamin B1 expression mediates age-dependent decreases of hippocampal stem cell activity. *Cell Stem Cell*, *28*(5), 967-977.e8. https://doi.org/10.1016/j.stem.2021.01.015

Bjornsson, C. S., Apostolopoulou, M., Tian, Y., & Temple, S. (2015). It takes a village: Constructing the neurogenic niche. *Developmental Cell*, *32*(4), 435–446. https://doi.org/10.1016/j.devcel.2015.01.010

Block, J., Schroeder, V., Pawelzyk, P., Willenbacher, N., & Köster, S. (2015). Physical properties of cytoplasmic intermediate filaments. In *Biochimica et Biophysica Acta - Molecular Cell Research* (Vol. 1853, Issue 11, pp. 3053–3064). Elsevier. https://doi.org/10.1016/j.bbamcr.2015.05.009

Bojarskaite, L., Bjørnstad, D. M., Pettersen, K. H., Cunen, C., Hermansen, G. H., Åbjørsbråten, K. S., Chambers, A. R., Sprengel, R., Vervaeke, K., Tang, W., Enger, R., & Nagelhus, E. A. (2020). Astrocytic Ca2+ signaling is reduced during sleep and is involved in the regulation of slow wave sleep. *Nature Communications*, *11*(1). https://doi.org/10.1038/s41467-020-17062-2

Bonaguidi, M. A., McGuire, T., Hu, M., Kan, L., Samantha, J., & Kessler, J. A. (2005). LIF and BMP signaling generate separate and discrete types of GFAP-expressing cells. *Development*, *132*(24), 5503–5514. https://doi.org/10.1242/dev.02166

Bonni, A., Sun, Y., Nadal-Vicens, M., Bhatt, A., Frank, D. A., Rozovsky, I., Stahl, N., Yancopoulos, G. D., & Greenberg, M. E. (n.d.). *Regulation of Gliogenesis in the Central Nervous System by the JAK-STAT Signaling Pathway*. https://www.science.org

Bouron, A. (2020). Transcriptomic Profiling of Ca2+ Transport Systems During the Formation of the Cerebral Cortex in Mice. *Cells*, *9*(8). https://doi.org/10.3390/cells9081800

Boutorine, A. S., Novopashina, D. S., Krasheninina, O. A., Nozeret, K., & Venyaminova, A. G. (2013). Fluorescent probes for nucleic acid visualization in fixed and live cells. In *Molecules* (Vol. 18, Issue 12, pp. 15357–15397). https://doi.org/10.3390/molecules181215357

Buchwalow, I., Samoilova, V., Boecker, W., & Tiemann, M. (2011). Non-specific binding of antibodies in immunohistochemistry: Fallacies and facts. *Scientific Reports*, *1*. https://doi.org/10.1038/srep00028

Budday, S., Sommer, G., Birkl, C., Langkammer, C., Haybaeck, J., Kohnert, J., Bauer, M., Paulsen, F., Steinmann, P., Kuhl, E., & Holzapfel, G. A. (2017). Mechanical characterization of human brain tissue. *Acta Biomaterialia*, *48*, 319–340. https://doi.org/10.1016/j.actbio.2016.10.036

Carvalho, E. D., Morais, M. R. G., Ferreira, H. P., Silva, M. M. C., Guimarães, S. C., & Pêgo, A. P. (2022). A paradigm shift: Bioengineering meets mechanobiology towards overcoming remyelination failure. In *Biomaterials* (Vol. 283). Elsevier Ltd. https://doi.org/10.1016/j.biomaterials.2022.121427

Castellanos, A. (2020). TRESK background K+ channel deletion selectively uncovers enhanced mechanical and cold sensitivity. *Journal of Physiology*, *598*(5), 1017–1038. https://doi.org/10.1113/JP279548

Chakrabarti, R., Ji, W. K., Stan, R. V., Sanz, J. de J., Ryan, T. A., & Higgs, H. N. (2018). INF2-mediated actin polymerization at the ER stimulates mitochondrial calcium uptake, inner membrane constriction, and division. *Journal of Cell Biology*, *217*(1), 251–268. https://doi.org/10.1083/jcb.201709111

Chang, A., Abderemane-Ali, F., Hura, G. L., Rossen, N. D., Gate, R. E., & Minor, D. L. (2018). A Calmodulin C-Lobe Ca2+-Dependent Switch Governs Kv7 Channel Function. *Neuron*, *97*(4), 836-852.e6. https://doi.org/10.1016/j.neuron.2018.01.035

Chaudhry, A., Shi, R., & Luciani, D. S. (2020). INNOVATIVE METHODOLOGY A pipeline for multidimensional confocal analysis of mitochondrial morphology, function, and dynamics in pancreatic-cells Chaudhry A, Shi R, Luciani DS. A pipeline for multidimensional confocal analysis of mitochondrial morphology, function, and dynam-ics in pancreatic-cells. *Am J Physiol Endocrinol Metab*, *318*, 87–101. https://doi.org/10.1152/ajpendo.00457.2019.-Live-cell

Chavali, M., Klingener, M., Kokkosis, A. G., Garkun, Y., Felong, S., Maffei, A., & Aguirre, A. (2018). Non-canonical Wnt signaling regulates neural stem cell quiescence during homeostasis and after demyelination. *Nature Communications*, *9*(1). https://doi.org/10.1038/s41467-017-02440-0

Chen, W., Zhao, H., & Li, Y. (2023). Mitochondrial dynamics in health and disease: mechanisms and potential targets. In *Signal Transduction and Targeted Therapy* (Vol. 8, Issue 1). Springer Nature. https://doi.org/10.1038/s41392-023-01547-9

Chighizola, M., Dini, T., Lenardi, C., Milani, P., Podestà, A., & Schulte, C. (2019). Mechanotransduction in neuronal cell development and functioning. In *Biophysical Reviews* (Vol. 11, Issue 5, pp. 701–720). Springer Verlag. https://doi.org/10.1007/s12551-019-00587-2

Cho, S., Irianto, J., & Discher, D. E. (2017). Mechanosensing by the nucleus: From pathways to scaling relationships. *Journal of Cell Biology*, *216*(2), 305–315. https://doi.org/10.1083/jcb.201610042

Chui, A., Zhang, Q., Dai, Q., & Shi, S. H. (2020). Oxidative stress regulates progenitor behavior and cortical neurogenesis. *Development (Cambridge)*, *147*(5). https://doi.org/10.1242/dev.184150

Collins, M. N., Zamboni, F., Serafin, A., Escobar, A., Stepanian, R., Culebras, M., Reis, R. L., & Oliveira, J. M. (2022). Emerging scaffold- and cellular-based strategies for brain tissue regeneration and imaging. *In Vitro Models*, *1*(2), 129–150. https://doi.org/10.1007/s44164-022-00013-0

Cox, C. D., Bavi, N., & Martinac, B. (2019). Biophysical Principles of Ion-Channel-Mediated Mechanosensory Transduction. In *Cell Reports* (Vol. 29, Issue 1, pp. 1–12). Elsevier B.V. https://doi.org/10.1016/j.celrep.2019.08.075

Cutiongco, M. F. A., Jensen, B. S., Reynolds, P. M., & Gadegaard, N. (2020). Predicting gene expression using morphological cell responses to nanotopography. *Nature Communications*, *11*(1). https://doi.org/10.1038/s41467-020-15114-1

Das, S., & Ramanan, N. (2023). Region-specific heterogeneity in neuronal nuclear morphology in young, aged and in Alzheimer's disease mouse brains. *Frontiers in Cell and Developmental Biology*, *11*. https://doi.org/10.3389/fcell.2023.1032504

De Belly, H., Paluch, E. K., & Chalut, K. J. (2022). Interplay between mechanics and signalling in regulating cell fate. In *Nature Reviews Molecular Cell Biology* (Vol. 23, Issue 7, pp. 465–480). Nature Research. https://doi.org/10.1038/s41580-022-00472-z

De Brito, O. M., & Scorrano, L. (2008). Mitofusin 2 tethers endoplasmic reticulum to mitochondria. *Nature*, *456*(7222), 605–610. https://doi.org/10.1038/nature07534

De Juan Romero, C., & Borrell, V. (2015). Coevolution of radial glial cells and the cerebral cortex. *GLIA*, *63*(8), 1303–1319. https://doi.org/10.1002/glia.22827

De Pascalis, C., Pérez-González, C., Seetharaman, S., Boëda, B., Vianay, B., Burute, M., Leduc, C., Borghi, N., Trepat, X., & Etienne-Manneville, S. (2018). Intermediate filaments control collective migration by restricting traction forces and sustaining cell-cell contacts. *Journal of Cell Biology*, *217*(9), 3031–3044. https://doi.org/10.1083/jcb.201801162

Dean, T., Ghaemmaghami, J., Corso, J., & Gallo, V. (2023). The cortical NG2-glia response to traumatic brain injury. In *GLIA* (Vol. 71, Issue 5, pp. 1164–1175). John Wiley and Sons Inc. https://doi.org/10.1002/glia.24342

Deval, E., & Lingueglia, E. (2015). Acid-Sensing Ion Channels and nociception in the peripheral and central nervous systems. In *Neuropharmacology* (Vol. 94, pp. 49–57). Elsevier Ltd. https://doi.org/10.1016/j.neuropharm.2015.02.009

Di Bella, D. J., Habibi, E., Stickels, R. R., Scalia, G., Brown, J., Yadollahpour, P., Yang, S. M., Abbate, C., Biancalani, T., Macosko, E. Z., Chen, F., Regev, A., & Arlotta, P. (2021). Molecular logic of cellular diversification in the mouse cerebral cortex. *Nature*, *595*(7868), 554–559. https://doi.org/10.1038/s41586-021-03670-5

Dietrich, A., Fahlbusch, M., & Gudermann, T. (2014). Classical transient receptor potential 1 (TRPC1): Channel or channel regulator? In *Cells* (Vol. 3, Issue 4, pp. 939–962). MDPI. https://doi.org/10.3390/cells3040939

Dityatev, A., Seidenbecher, C. I., & Schachner, M. (2010). Compartmentalization from the outside: The extracellular matrix and functional microdomains in the brain. In *Trends in Neurosciences* (Vol. 33, Issue 11, pp. 503–512). Elsevier Ltd. https://doi.org/10.1016/j.tins.2010.08.003

Dong, X., Zhang, Q., Yu, X., Wang, D., Ma, J., Ma, J., & Shi, S. H. (2022). Metabolic lactate production coordinates vasculature development and progenitor behavior in the developing mouse neocortex. *Nature Neuroscience*, *25*(7), 865–875. https://doi.org/10.1038/s41593-022-01093-7

Douguet, D., & Honoré, E. (2019). Mammalian Mechanoelectrical Transduction: Structure and Function of Force-Gated Ion Channels. In *Cell* (Vol. 179, Issue 2, pp. 340–354). Cell Press. https://doi.org/10.1016/j.cell.2019.08.049

Duncan, A. L., Song, W., & Sansom, M. S. P. (2019). Lipid-Dependent Regulation of Ion Channels and G Protein-Coupled Receptors: Insights from Structures and Simulations. *Annual Review of Pharmacology and Toxicology Annu. Rev. Pharmacol. Toxicol. 2020*, *60*, 31–50. https://doi.org/10.1146/annurev-pharmtox-010919

Dupin, I., & Etienne-Manneville, S. (2011). Nuclear positioning: Mechanisms and functions. In *International Journal of Biochemistry and Cell Biology* (Vol. 43, Issue 12, pp. 1698–1707). https://doi.org/10.1016/j.biocel.2011.09.004

Dupont, S., & Wickström, S. A. (2022). Mechanical regulation of chromatin and transcription. In *Nature Reviews Genetics* (Vol. 23, Issue 10, pp. 624–643). Nature Research. https://doi.org/10.1038/s41576-022-00493-6

Duval, K., Grover, H., Han, L. H., Mou, Y., Pegoraro, A. F., Fredberg, J., & Chen, Z. (2017). Modeling physiological events in 2D vs. 3D cell culture. In *Physiology* (Vol. 32, Issue 4, pp. 266–277). American Physiological Society. https://doi.org/10.1152/physiol.00036.2016

Eliasson, C., Sahlgren, C., Berthold, C.-H., Stakeberg, J., Celis, J. E., Betsholtz, C., Eriksson, J. E., & Pekny, M. (1999). *Intermediate Filament Protein Partnership in Astrocytes**. http://www.jbc.org

Elosegui-Artola, A. (2021). The extracellular matrix viscoelasticity as a regulator of cell and tissue dynamics. In *Current Opinion in Cell Biology* (Vol. 72, pp. 10–18). Elsevier Ltd. https://doi.org/10.1016/j.ceb.2021.04.002

Elosegui-Artola, A., Andreu, I., Beedle, A. E. M., Lezamiz, A., Uroz, M., Kosmalska, A. J., Oria, R., Kechagia, J. Z., Rico-Lastres, P., Le Roux, A. L., Shanahan, C. M., Trepat, X., Navajas, D., Garcia-Manyes, S., & Roca-Cusachs, P. (2017a). Force Triggers YAP Nuclear Entry by Regulating Transport across Nuclear Pores. *Cell*, *171*(6), 1397-1410.e14. https://doi.org/10.1016/j.cell.2017.10.008

Elosegui-Artola, A., Andreu, I., Beedle, A. E. M., Lezamiz, A., Uroz, M., Kosmalska, A. J., Oria, R., Kechagia, J. Z., Rico-Lastres, P., Le Roux, A. L., Shanahan, C. M., Trepat, X., Navajas, D., Garcia-Manyes, S., & Roca-Cusachs, P. (2017b). Force Triggers YAP Nuclear Entry by Regulating Transport across Nuclear Pores. *Cell*, *171*(6), 1397-1410.e14. https://doi.org/10.1016/j.cell.2017.10.008

Enari, M., Sakahira, H., Yokoyama, H., Okawa, K., Iwamatsu, A., & Nagata, S. (1997). Acaspase-activatedDNase that degradesDNA during apoptosis, and its inhibitor ICAD. In *Mol. Endocrinol* (Vol. 393). http://www.nature.com

Englund, C. (2005). Pax6, Tbr2, and Tbr1 Are Expressed Sequentially by Radial Glia, Intermediate Progenitor Cells, and Postmitotic Neurons in Developing Neocortex. *Journal of Neuroscience*, *25*(1), 247–251. https://doi.org/10.1523/JNEUROSCI.2899-04.2005

Erdemir, A., Mulugeta, L., Ku, J. P., Drach, A., Horner, M., Morrison, T. M., Peng, G. C. Y., Vadigepalli, R., Lytton, W. W., & Myers, J. G. (2020). Credible practice of modeling and simulation in healthcare: Ten rules from a multidisciplinary perspective. In *Journal of Translational Medicine* (Vol. 18, Issue 1). BioMed Central Ltd. https://doi.org/10.1186/s12967-020-02540-4

Escartin, C., Galea, E., Lakatos, A., O'Callaghan, J. P., Petzold, G. C., Serrano-Pozo, A., Steinhäuser, C., Volterra, A., Carmignoto, G., Agarwal, A., Allen, N. J., Araque, A., Barbeito, L., Barzilai, A., Bergles, D. E., Bonvento, G., Butt, A. M., Chen, W. T., Cohen-Salmon, M., … Verkhratsky, A. (2021). Reactive astrocyte nomenclature, definitions, and future directions. In *Nature Neuroscience* (Vol. 24, Issue 3, pp. 312–325). Nature Research. https://doi.org/10.1038/s41593-020-00783-4

Evangelisti, C., Rusciano, I., Mongiorgi, S., Ramazzotti, G., Lattanzi, G., Manzoli, L., Cocco, L., & Ratti, S. (2022). The wide and growing range of lamin B-related diseases: from laminopathies to cancer. In *Cellular and Molecular Life Sciences* (Vol. 79, Issue 2). Springer Science and Business Media Deutschland GmbH. https://doi.org/10.1007/s00018-021-04084-2

Eze, U. C., Bhaduri, A., Haeussler, M., Nowakowski, T. J., & Kriegstein, A. R. (2021). Single-cell atlas of early human brain development highlights heterogeneity of human neuroepithelial cells and early radial glia. *Nature Neuroscience*, *24*(4), 584–594. https://doi.org/10.1038/s41593-020-00794-1

Faissner, A., & Reinhard, J. (2015). The extracellular matrix compartment of neural stem and glial progenitor cells. In *GLIA* (Vol. 63, Issue 8, pp. 1330–1349). John Wiley and Sons Inc. https://doi.org/10.1002/glia.22839

Fame, R. M., & Lehtinen, M. K. (2021). Mitochondria in Early Forebrain Development: From Neurulation to Mid-Corticogenesis. In *Frontiers in Cell and Developmental Biology* (Vol. 9). Frontiers Media S.A. https://doi.org/10.3389/fcell.2021.780207

Fan, W., Jurado-Arjona, J., Alanis-Lobato, G., Péron, S., Berger, C., Andrade-Navarro, M. A., Falk, S., & Berninger, B. (2023). The transcriptional co-activator Yap1 promotes adult hippocampal neural stem cell activation. *The EMBO Journal*, *42*(11). https://doi.org/10.15252/embj.2021110384

Ferent, J., Zaidi, D., & Francis, F. (2020a). Extracellular Control of Radial Glia Proliferation and Scaffolding During Cortical Development and Pathology. In *Frontiers in Cell and Developmental Biology* (Vol. 8). Frontiers Media S.A. https://doi.org/10.3389/fcell.2020.578341

Ferent, J., Zaidi, D., & Francis, F. (2020b). Extracellular Control of Radial Glia Proliferation and Scaffolding During Cortical Development and Pathology. In *Frontiers in Cell and Developmental Biology* (Vol. 8). Frontiers Media S.A. https://doi.org/10.3389/fcell.2020.578341

Foster, V. S., Rash, L. D., King, G. F., & Rank, M. M. (2021). Acid-Sensing Ion Channels: Expression and Function in Resident and Infiltrating Immune Cells in the Central Nervous System. In *Frontiers in Cellular Neuroscience* (Vol. 15). Frontiers Media S.A. https://doi.org/10.3389/fncel.2021.738043

Franze, K., Janmey, P. A., & Guck, J. (2013). Mechanics in neuronal development and repair. *Annual Review of Biomedical Engineering*, *15*, 227–251. https://doi.org/10.1146/annurev-bioeng-071811-150045

Fuentealba, L. C., Rompani, S. B., Parraguez, J. I., Obernier, K., Romero, R., Cepko, C. L., & Alvarez-Buylla, A. (2015). Embryonic Origin of Postnatal Neural Stem Cells. *Cell*, *161*(7), 1644–1655. https://doi.org/10.1016/j.cell.2015.05.041

Fujita, I., Shitamukai, A., Kusumoto, F., Mase, S., Suetsugu, T., Omori, A., Kato, K., Abe, T., Shioi, G., Konno, D., & Matsuzaki, F. (2020). Endfoot regeneration restricts radial glial state and prevents translocation into the outer subventricular zone in early mammalian brain development. *Nature Cell Biology*, *22*(1), 26–37. https://doi.org/10.1038/s41556-019-0436-9

Gan, Q., Lee, A., Suzuki, R., Yamagami, T., Stokes, A., Nguyen, B. C., Pleasure, D., Wang, J., Chen, H. W., & Zhou, C. J. (2014). Pax6 mediates β-catenin signaling for self-renewal and neurogenesis by neocortical radial glial stem cells. *Stem Cells*, *32*(1), 45–58. https://doi.org/10.1002/stem.1561

Gao, J., Liao, Y., Qiu, M., & Shen, W. (2021a). Wnt/β-Catenin Signaling in Neural Stem Cell Homeostasis and Neurological Diseases. In *Neuroscientist* (Vol. 27, Issue 1, pp. 58–72). SAGE Publications Inc. https://doi.org/10.1177/1073858420914509

Gao, J., Liao, Y., Qiu, M., & Shen, W. (2021b). Wnt/β-Catenin Signaling in Neural Stem Cell Homeostasis and Neurological Diseases. In *Neuroscientist* (Vol. 27, Issue 1, pp. 58–72). SAGE Publications Inc. https://doi.org/10.1177/1073858420914509

Gao, S., & Hu, J. (2021). Mitochondrial Fusion: The Machineries In and Out. In *Trends in Cell Biology* (Vol. 31, Issue 1, pp. 62–74). Elsevier Ltd. https://doi.org/10.1016/j.tcb.2020.09.008

Garcia, K. E., Kroenke, C. D., & Bayly, P. V. (2018). Mechanics of cortical folding: Stress, growth and stability. In *Philosophical Transactions of the Royal Society B: Biological Sciences* (Vol. 373, Issue 1759). Royal Society Publishing. https://doi.org/10.1098/rstb.2017.0321

Ge, W. P., Miyawaki, A., Gage, F. H., Jan, Y. N., & Jan, L. Y. (2012). Local generation of glia is a major astrocyte source in postnatal cortex. *Nature*, *484*(7394), 376–380. https://doi.org/10.1038/nature10959

Gkini, V., & Namba, T. (2023a). Glutaminolysis and the Control of Neural Progenitors in Neocortical Development and Evolution. In *Neuroscientist* (Vol. 29, Issue 2, pp. 177–189). SAGE Publications Inc. https://doi.org/10.1177/10738584211069060

Gkini, V., & Namba, T. (2023b). Glutaminolysis and the Control of Neural Progenitors in Neocortical Development and Evolution. In *Neuroscientist* (Vol. 29, Issue 2, pp. 177–189). SAGE Publications Inc. https://doi.org/10.1177/10738584211069060

Gnanasambandam, R., Ghatak, C., Yasmann, A., Nishizawa, K., Sachs, F., Ladokhin, A. S., Sukharev, S. I., & Suchyna, T. M. (2017). GsMTx4: Mechanism of Inhibiting Mechanosensitive Ion Channels. *Biophysical Journal*, *112*(1), 31–45. https://doi.org/10.1016/j.bpj.2016.11.013

Goelzer, M., Goelzer, J., Ferguson, M. L., Neu, C. P., & Uzer, G. (2021). Nuclear envelope mechanobiology: linking the nuclear structure and function. In *Nucleus* (Vol. 12, Issue 1, pp. 90–114). Taylor and Francis Ltd. https://doi.org/10.1080/19491034.2021.1962610

Goenaga, J., Araque, A., Kofuji, P., & Herrera Moro Chao, D. (2023). Calcium signaling in astrocytes and gliotransmitter release. In *Frontiers in Synaptic Neuroscience* (Vol. 15). Frontiers Media S.A. https://doi.org/10.3389/fnsyn.2023.1138577

Gurdon, J. A. (1988). A community effect in animal development. *Nature*, *336*, 772–774. https://www.nature.com/articles/336772a0

Halfter, W., Dong, S., Yip, Y.-P., Willem, M., & Mayer, U. (2002). *A Critical Function of the Pial Basement Membrane in Cortical Histogenesis*.

Halim, N. D., Mcfate, T., Mohyeldin, A., Okagaki, P., Korotchkina, L. G., Patel, M. S., Jeoung, N. H., Harris, R. A., Schell, M. J., & Verma, A. (2010). Phosphorylation status of pyruvate dehydrogenase distinguishes metabolic phenotypes of cultured rat brain astrocytes and neurons. *GLIA*, *58*(10), 1168–1176. https://doi.org/10.1002/glia.20996

Hans, F., & Dimitrov, S. (2001). Histone H3 phosphorylation and cell division. In *Oncogene* (Vol. 20). www.nature.com/onc

Hansen, D. V., Lui, J. H., Parker, P. R. L., & Kriegstein, A. R. (2010). Neurogenic radial glia in the outer subventricular zone of human neocortex. *Nature*, *464*(7288), 554–561. https://doi.org/10.1038/nature08845

Haolong, C., Du, N., Hongchao, T., Yang, Y., Wei, Z., Hua, Z., Wenliang, Z., Lei, S., & Po, T. (2013). Enterovirus 71 VP1 Activates Calmodulin-Dependent Protein Kinase II and Results in the

Rearrangement of Vimentin in Human Astrocyte Cells. *PLoS ONE*, *8*(9). https://doi.org/10.1371/journal.pone.0073900

Harline, K., Martínez-Gómez, J., Specht, C. D., & Roeder, A. H. K. (2021). A Life Cycle for Modeling Biology at Different Scales. In *Frontiers in Plant Science* (Vol. 12). Frontiers Media S.A. https://doi.org/10.3389/fpls.2021.710590

Haubensak, W., Attardo, A., Denk, W., Huttner, W. B., & Simons, K. (2004). Neurons arise in the basal neuroepithelium of the early mammalian telencephalon: A major site of neurogenesis. In *PNAS March* (Vol. 2, Issue 9). www.pnas.orgcgidoi10.1073pnas.0308600100

He, F., Ge, W., Martinowich, K., Becker-Catania, S., Coskun, V., Zhu, W., Wu, H., Castro, D., Guillemot, F., Fan, G., De Vellis, J., & Sun, Y. E. (2005). A positive autoregulatory loop of Jak-STAT signaling controls the onset of astrogliogenesis. *Nature Neuroscience*, *8*(5), 616–625. https://doi.org/10.1038/nn1440

Heckenbach, I., Mkrtchyan, G. V., Ezra, M. Ben, Bakula, D., Madsen, J. S., Nielsen, M. H., Oró, D., Osborne, B., Covarrubias, A. J., Idda, M. L., Gorospe, M., Mortensen, L., Verdin, E., Westendorp, R., & Scheibye-Knudsen, M. (2022a). Nuclear morphology is a deep learning biomarker of cellular senescence. *Nature Aging*, *2*(8), 742–755. https://doi.org/10.1038/s43587-022-00263-3

Heckenbach, I., Mkrtchyan, G. V., Ezra, M. Ben, Bakula, D., Madsen, J. S., Nielsen, M. H., Oró, D., Osborne, B., Covarrubias, A. J., Idda, M. L., Gorospe, M., Mortensen, L., Verdin, E., Westendorp, R., & Scheibye-Knudsen, M. (2022b). Nuclear morphology is a deep learning biomarker of cellular senescence. *Nature Aging*, *2*(8), 742–755. https://doi.org/10.1038/s43587-022-00263-3

Heidenreich, M., Lechner, S. G., Vardanyan, V., Wetzel, C., Cremers, C. W., De Leenheer, E. M., Aránguez, G., Moreno-Pelayo, M. Á., Jentsch, T. J., & Lewin, G. R. (2012). KCNQ4 K + channels tune mechanoreceptors for normal touch sensation in mouse and man. *Nature Neuroscience*, *15*(1), 138–145. https://doi.org/10.1038/nn.2985

Heng, B. C., Zhang, X., Aubel, D., Bai, Y., Li, X., Wei, Y., Fussenegger, M., & Deng, X. (2020). Role of YAP/TAZ in Cell Lineage Fate Determination and Related Signaling Pathways. In *Frontiers in Cell and Developmental Biology* (Vol. 8). Frontiers Media S.A. https://doi.org/10.3389/fcell.2020.00735

Heo, S. J., Driscoll, T. P., Thorpe, S. D., Nerurkar, N. L., Baker, B. M., Yang, M. T., Chen, C. S., Lee, D. A., & Mauck, R. L. (2016). Differentiation alters stem cell nuclear architecture, mechanics, and mechano-sensitivity. *eLife*, *5*(NOVEMBER2016), 1–21. https://doi.org/10.7554/eLife.18207

Heppt, J., Wittmann, M., Schäffner, I., Billmann, C., Zhang, J., Vogt-Weisenhorn, D., Prakash, N., Wurst, W., Taketo, M. M., & Lie, D. C. (2020). β-catenin signaling modulates the tempo of dendritic growth of adult-born hippocampal neurons. *The EMBO Journal*, *39*(21). https://doi.org/10.15252/embj.2020104472

Herculano-Houzel, S. (2012). The remarkable, yet not extraordinary, human brain as a scaled-up primate brain and its associated cost. In *Proceedings of the National Academy of Sciences of the United States of America* (Vol. 109, Issue SUPPL.1, pp. 10661–10668). https://doi.org/10.1073/pnas.1201895109

Herrmann, H., Bär, H., Kreplak, L., Strelkov, S. V., & Aebi, U. (2007). Intermediate filaments: From cell architecture to nanomechanics. In *Nature Reviews Molecular Cell Biology* (Vol. 8, Issue 7, pp. 562–573). https://doi.org/10.1038/nrm2197

Herrmann, H., Strelkov, S. V., Burkhard, P., & Aebi, U. (2009). Intermediate filaments: Primary determinants of cell architecture and plasticity. In *Journal of Clinical Investigation* (Vol. 119, Issue 7, pp. 1772–1783). https://doi.org/10.1172/JCI38214

Heuser, K., & Enger, R. (2021). Astrocytic Ca2+ Signaling in Epilepsy. In *Frontiers in Cellular Neuroscience* (Vol. 15). Frontiers Media S.A. https://doi.org/10.3389/fncel.2021.695380

Hinrichsen, J., Reiter, N., Bräuer, L., Paulsen, F., Kaessmair, S., & Budday, S. (2023). Inverse identification of region-specific hyperelastic material parameters for human brain tissue. *Biomechanics and Modeling in Mechanobiology*, *22*(5), 1729–1749. https://doi.org/10.1007/s10237-023-01739-w

Hobson, C. M., & Stephens, A. D. (2020). Modeling of Cell Nuclear Mechanics: Classes, Components, and Applications. In *Cells* (Vol. 9, Issue 7). NLM (Medline). https://doi.org/10.3390/cells9071623

Hockfield, S. (1985). *Identification of Major Cell Classes in the Developing Mammalian Nervous System'* (Vol. 5, Issue 12).

Hol, E. M., & Pekny, M. (2015). Glial fibrillary acidic protein (GFAP) and the astrocyte intermediate filament system in diseases of the central nervous system. In *Current Opinion in Cell Biology* (Vol. 32, pp. 121–130). Elsevier Ltd. https://doi.org/10.1016/j.ceb.2015.02.004

Hookway, C., Ding, L., Davidson, M. W., Rappoport, J. Z., Danuser, G., & Gelfand, V. I. (2015). Microtubule-dependent transport and dynamics of vimentin intermediate filaments. *Molecular Biology of the Cell*, *26*(9), 1675–1686. https://doi.org/10.1091/mbc.E14-09-1398

Hou, Y., Ouyang, X., Wan, R., Cheng, H., Mattson, M. P., & Cheng, A. (2012). Mitochondrial superoxide production negatively regulates neural progenitor proliferation and cerebral cortical development. *Stem Cells*, *30*(11), 2535–2547. https://doi.org/10.1002/stem.1213

Hu, X., li, J., Fu, M., Zhao, X., & Wang, W. (2021). The JAK/STAT signaling pathway: from bench to clinic. In *Signal Transduction and Targeted Therapy* (Vol. 6, Issue 1). Springer Nature. https://doi.org/10.1038/s41392-021-00791-1

Huang, Z., Hu, J., Pan, J., Wang, Y., Hu, G., Zhou, J., Mei, L., & Xiong, W. C. (2016). YAP stabilizes SMAD1 and promotes BMP2-induced neocortical astrocytic differentiation. *Development (Cambridge)*, *143*(13), 2398–2409. https://doi.org/10.1242/dev.130658

Hughes, L. J., Park, R., Lee, M. J., Terry, B. K., Lee, D. J., Kim, H., Cho, S. H., & Kim, S. (2020). Yap/Taz are required for establishing the cerebellar radial glia scaffold and proper foliation. *Developmental Biology*, *457*(1), 150–162. https://doi.org/10.1016/j.ydbio.2019.10.002

Hunter, K. E., & Hatren, M. E. (1995). Radial glial cell transformation to astrocytes is bidirectional: Regulation by a diffusible factor in embryonic forebrain. In *Neurobiology* (Vol. 92). https://www.pnas.org

Hyroššová, P., Aragó, M., Moreno-Felici, J., Fu, X., Mendez-Lucas, A., García-Rovés, P. M., Burgess, S., Figueras, A., Viñals, F., & Perales, J. C. (2021). PEPCK-M recoups tumor cell anabolic potential in a PKC-ζ-dependent manner. *Cancer and Metabolism*, *9*(1). https://doi.org/10.1186/s40170-020-00236-3

Infante, E., & Etienne-Manneville, S. (2022). Intermediate filaments: Integration of cell mechanical properties during migration. In *Frontiers in Cell and Developmental Biology* (Vol. 10). Frontiers Media S.A. https://doi.org/10.3389/fcell.2022.951816

Iovine, J. C., Claypool, S. M., & Alder, N. N. (2021). Mitochondrial compartmentalization: emerging themes in structure and function. In *Trends in Biochemical Sciences* (Vol. 46, Issue 11, pp. 902–917). Elsevier Ltd. https://doi.org/10.1016/j.tibs.2021.06.003

Iozzo, R. V., & Schaefer, L. (2015). Proteoglycan form and function: A comprehensive nomenclature of proteoglycans. In *Matrix Biology* (Vol. 42, pp. 11–55). Elsevier. https://doi.org/10.1016/j.matbio.2015.02.003

Iwata, R., Casimir, P., Erkol, E., Boubakar, L., Planque, M., Gallego López, I. M., Ditkowska, M., Gaspariunaite, V., Beckers, S., Remans, D., Vints, K., Vandekeere, A., Poovathingal, S., Bird, M., Vlaeminck, I., Creemers, E., Wierda, K., Corthout, N., Vermeersch, P., … Vanderhaeghen, P. (2023a). Mitochondria metabolism sets the species-specific tempo of neuronal development. *Science*, *379*(6632). https://doi.org/10.1126/science.abn4705

Iwata, R., Casimir, P., Erkol, E., Boubakar, L., Planque, M., Gallego López, I. M., Ditkowska, M., Gaspariunaite, V., Beckers, S., Remans, D., Vints, K., Vandekeere, A., Poovathingal, S., Bird, M., Vlaeminck, I., Creemers, E., Wierda, K., Corthout, N., Vermeersch, P., … Vanderhaeghen, P. (2023b). Mitochondria metabolism sets the species-specific tempo of neuronal development. *Science*, *379*(6632). https://doi.org/10.1126/science.abn4705

Iwata, R., Casimir, P., & Vanderhaeghen, P. (n.d.). *Mitochondrial dynamics in postmitotic cells regulate neurogenesis*. https://www.science.org

Iwata, R., Casimir, P., & Vanderhaeghen, P. (2020a). Mitochondrial dynamics in postmitotic cells regulate neurogenesis. *Science*, *369*(6505), 858–862. https://doi.org/10.1126/science.aba9760

Iwata, R., Casimir, P., & Vanderhaeghen, P. (2020b). Mitochondrial dynamics in postmitotic cells regulate neurogenesis. *Science*, *369*(6505), 858–862. https://doi.org/10.1126/science.aba9760

Iwata, R., & Vanderhaeghen, P. (2021). Regulatory roles of mitochondria and metabolism in neurogenesis. In *Current Opinion in Neurobiology* (Vol. 69, pp. 231–240). Elsevier Ltd. https://doi.org/10.1016/j.conb.2021.05.003

Jackson, J. G., & Robinson, M. B. (2015). Reciprocal regulation of mitochondrial dynamics and calcium signaling in astrocyte processes. *Journal of Neuroscience*, *35*(45), 15199–15213. https://doi.org/10.1523/JNEUROSCI.2049-15.2015

Jagielska, A., Lowe, A. L., Makhija, E., Wroblewska, L., Guck, J., Franklin, R. J. M., Shivashankar, G. V., & Van Vliet, K. J. (2017). Mechanical Strain Promotes Oligodendrocyte Differentiation by Global Changes of Gene Expression. *Frontiers in Cellular Neuroscience*, *11*(April), 1–16. https://doi.org/10.3389/fncel.2017.00093

Janssen, A. F. J., Breusegem, S. Y., & Larrieu, D. (2022). Current Methods and Pipelines for Image-Based Quantitation of Nuclear Shape and Nuclear Envelope Abnormalities. In *Cells* (Vol. 11, Issue 3). MDPI. https://doi.org/10.3390/cells11030347

Javier-Torrent, M., Zimmer-Bensch, G., & Nguyen, L. (2021). Mechanical Forces Orchestrate Brain Development. In *Trends in Neurosciences* (Vol. 44, Issue 2, pp. 110–121). Elsevier Ltd. https://doi.org/10.1016/j.tins.2020.10.012

Ji, F., Shen, T., Zou, W., & Jiao, J. (2017). UCP2 Regulates Embryonic Neurogenesis via ROS-Mediated Yap Alternation in the Developing Neocortex. *Stem Cells*, *35*(6), 1479–1492. https://doi.org/10.1002/stem.2605

Jin, P., Jan, L. Y., & Jan, Y.-N. (2020). Annual Review of Neuroscience Mechanosensitive Ion Channels: Structural Features Relevant to Mechanotransduction Mechanisms. *Annu. Rev. Neurosci. 2020*, *43*, 207–229. https://doi.org/10.1146/annurev-neuro-070918

José Pablo Soriano Esqué Director Soledad Alcántara Horrillo José Manuel García Aznar, A. (2017). *Final Master Thesis Análisis poblacional y morfológico asociado a la conversión de astrocito a glía radial inducida por el Ln2 PMMA Population and morphological analysis associated to astrocyte to radial glia conversion induced by Ln2 PMMA*.

Kalukula, Y., Stephens, A. D., Lammerding, J., & Gabriele, S. (2022). Mechanics and functional consequences of nuclear deformations. In *Nature Reviews Molecular Cell Biology* (Vol. 23, Issue 9, pp. 583–602). Nature Research. https://doi.org/10.1038/s41580-022-00480-z

Kamakura, S., Oishi, K., Yoshimatsu, T., Nakafuku, M., Masuyama, N., & Gotoh, Y. (2004). Hes binding to STAT3 mediates crosstalk between Notch and JAK-STAT signalling. *Nature Cell Biology*, *6*(6), 547–554. https://doi.org/10.1038/ncb1138

Kanemaru, K., Kubota, J., Sekiya, H., Hirose, K., Okubo, Y., & Iino, M. (2013). Calcium-dependent N-cadherin up-regulation mediates reactive astrogliosis and neuroprotection after brain injury. *Proceedings of the National Academy of Sciences of the United States of America*, *110*(28), 11612–11617. https://doi.org/10.1073/pnas.1300378110

Kang, S. mi, Yoon, M. H., & Park, B. J. (2018). Laminopathies; Mutations on single gene and various human genetic diseases. In *BMB Reports* (Vol. 51, Issue 7, pp. 327–337). The Biochemical Society of the Republic of Korea. https://doi.org/10.5483/BMBRep.2018.51.7.113

Karoutas, A., & Akhtar, A. (2021). Functional mechanisms and abnormalities of the nuclear lamina. In *Nature Cell Biology* (Vol. 23, Issue 2, pp. 116–126). Nature Research. https://doi.org/10.1038/s41556-020-00630-5

Katiyar, A., Tocco, V. J., Li, Y., Aggarwal, V., Tamashunas, A. C., Dickinson, R. B., & Lele, T. P. (2019). Nuclear size changes caused by local motion of cell boundaries unfold the nuclear lamina and dilate chromatin and intranuclear bodies. *Soft Matter*, *15*(45), 9310–9317. https://doi.org/10.1039/c9sm01666j

Kennedy, Z., Newberg, J., Goelzer, M., Judex, S., Fitzpatrick, C. K., & Uzer, G. (2021). Modeling stem cell nucleus mechanics using confocal microscopy. *Biomechanics and Modeling in Mechanobiology*, *20*(6), 2361–2372. https://doi.org/10.1007/s10237-021-01513-w

Khacho, M., Clark, A., Svoboda, D. S., Azzi, J., MacLaurin, J. G., Meghaizel, C., Sesaki, H., Lagace, D. C., Germain, M., Harper, M. E., Park, D. S., & Slack, R. S. (2016). Mitochondrial Dynamics Impacts Stem Cell Identity and Fate Decisions by Regulating a Nuclear Transcriptional Program. *Cell Stem Cell*, *19*(2), 232–247. https://doi.org/10.1016/j.stem.2016.04.015

Khacho, M., Clark, A., Svoboda, D. S., MacLaurin, J. G., Lagace, D. C., Park, D. S., & Slack, R. S. (2017). Mitochondrial dysfunction underlies cognitive defects as a result of neural stem cell depletion and impaired neurogenesis. *Human Molecular Genetics*, *26*(17), 3327–3341. https://doi.org/10.1093/hmg/ddx217

Kierans, S. J., & Taylor, C. T. (2021). Regulation of glycolysis by the hypoxia-inducible factor (HIF): implications for cellular physiology. In *Journal of Physiology* (Vol. 599, Issue 1, pp. 23–37). Blackwell Publishing Ltd. https://doi.org/10.1113/JP280572

Kim, H. J., Lee, P. C. W., & Hong, J. H. (2022). Lamin-A/C Is Modulated by the Involvement of Histamine-Mediated Calcium/Calmodulin-Dependent Kinase II in Lung Cancer Cells. *International Journal of Molecular Sciences*, *23*(16). https://doi.org/10.3390/ijms23169075

Kirby, T. J., & Lammerding, J. (2018). Emerging views of the nucleus as a cellular mechanosensor. In *Nature Cell Biology* (Vol. 20, Issue 4, pp. 373–381). Nature Publishing Group. https://doi.org/10.1038/s41556-018-0038-y

Klingenberg, C. P. (2010). Evolution and development of shape: Integrating quantitative approaches. In *Nature Reviews Genetics* (Vol. 11, Issue 9, pp. 623–635). https://doi.org/10.1038/nrg2829

Komabayashi-Suzuki, M., Yamanishi, E., Watanabe, C., Okamura, M., Tabata, H., Iwai, R., Ajioka, I., Matsushita, J., Kidoya, H., Takakura, N., Okamoto, T., Kinoshita, K., Ichihashi, M., Nagata, K. ichi, Ema, M., & Mizutani, K. ichi. (2019). Spatiotemporally Dependent Vascularization Is Differently Utilized among Neural Progenitor Subtypes during Neocortical Development. *Cell Reports*, *29*(5), 1113-1129.e5. https://doi.org/10.1016/j.celrep.2019.09.048

Koo, B., Lee, K. H., Ming, G. li, Yoon, K. J., & Song, H. (2023). Setting the clock of neural progenitor cells during mammalian corticogenesis. In *Seminars in Cell and Developmental Biology* (Vol. 142, pp. 43–53). Elsevier Ltd. https://doi.org/10.1016/j.semcdb.2022.05.013

Kostic, M., Paridaen, J. T. M. L., Long, K. R., Kalebic, N., Langen, B., Grübling, N., Wimberger, P., Kawasaki, H., Namba, T., & Huttner, W. B. (2019a). YAP Activity Is Necessary and Sufficient for Basal Progenitor Abundance and Proliferation in the Developing Neocortex. *Cell Reports*, *27*(4), 1103-1118.e6. https://doi.org/10.1016/j.celrep.2019.03.091

Kostic, M., Paridaen, J. T. M. L., Long, K. R., Kalebic, N., Langen, B., Grübling, N., Wimberger, P., Kawasaki, H., Namba, T., & Huttner, W. B. (2019b). YAP Activity Is Necessary and Sufficient for Basal Progenitor Abundance and Proliferation in the Developing Neocortex. *Cell Reports*, *27*(4), 1103-1118.e6. https://doi.org/10.1016/j.celrep.2019.03.091

Kraus, F., Roy, K., Pucadyil, T. J., & Ryan, M. T. (2021). Function and regulation of the divisome for mitochondrial fission. In *Nature* (Vol. 590, Issue 7844, pp. 57–66). Nature Research. https://doi.org/10.1038/s41586-021-03214-x

Kriegstein, A., & Alvarez-Buylla, A. (2009). The glial nature of embryonic and adult neural stem cells. In *Annual Review of Neuroscience* (Vol. 32, pp. 149–184). https://doi.org/10.1146/annurev.neuro.051508.135600

Kriegstein, A. R., & Götz, M. (2003). Radial glia diversity: A matter of cell fate. *GLIA*, *43*(1), 37–43. https://doi.org/10.1002/glia.10250

Kriegstein, A. R., & Noctor, S. C. (2004). Patterns of neuronal migration in the embryonic cortex. *Trends in Neurosciences*, *27*(7), 392–399. https://doi.org/10.1016/j.tins.2004.05.001

Kriegstein, A. R., Subramanian, L., Obernier, K., & Alvarez-Buylla, A. (2020). Neural stem cells among glia. In *Patterning and Cell Type Specification in the Developing CNS and PNS: Comprehensive Developmental Neuroscience, Second Edition* (pp. 775–806). Elsevier. https://doi.org/10.1016/B978-0-12-814405-3.00031-X

Krishnasamy, S., Weng, Y. C., Thammisetty, S. S., Phaneuf, D., Lalancette-Hebert, M., & Kriz, J. (2017). Molecular imaging of nestin in neuroinflammatory conditions reveals marked signal induction in activated microglia. *Journal of Neuroinflammation*, *14*(1). https://doi.org/10.1186/s12974-017-0816-7

La Manno, G., Siletti, K., Furlan, A., Gyllborg, D., Vinsland, E., Mossi Albiach, A., Mattsson Langseth, C., Khven, I., Lederer, A. R., Dratva, L. M., Johnsson, A., Nilsson, M., Lönnerberg, P., & Linnarsson, S. (2021). Molecular architecture of the developing mouse brain. *Nature*, *596*(7870), 92–96. https://doi.org/10.1038/s41586-021-03775-x

Lambris, J. D. (n.d.). *Advances in Experimental Medicine and Biology*. http://www.springer.com/series/5584

Lammerding, J., Fong, L. G., Ji, J. Y., Reue, K., Stewart, C. L., Young, S. G., & Lee, R. T. (2006). Lamins a and C but not lamin B1 regulate nuclear mechanics. *Journal of Biological Chemistry*, *281*(35), 25768–25780. https://doi.org/10.1074/jbc.M513511200

Lancaster, M. A., & Knoblich, J. A. (2014). Generation of cerebral organoids from human pluripotent stem cells. *Nature Protocols*, *9*(10), 2329–2340. https://doi.org/10.1038/nprot.2014.158

Lange, S. C., Bak, L. K., Waagepetersen, H. S., Schousboe, A., & Norenberg, M. D. (2012). Primary cultures of astrocytes: Their value in understanding astrocytes in health and disease. In *Neurochemical Research* (Vol. 37, Issue 11, pp. 2569–2588). https://doi.org/10.1007/s11064-012-0868-0

Larsson, J. E., Frampton, D. J. A., & Liin, S. I. (2020). Polyunsaturated Fatty Acids as Modulators of KV7 Channels. In *Frontiers in Physiology* (Vol. 11). Frontiers Media S.A. https://doi.org/10.3389/fphys.2020.00641

Lattke, M., Goldstone, R., Ellis, J. K., Boeing, S., Jurado-Arjona, J., Marichal, N., MacRae, J. I., Berninger, B., & Guillemot, F. (2021). Extensive transcriptional and chromatin changes underlie astrocyte maturation in vivo and in culture. *Nature Communications*, *12*(1). https://doi.org/10.1038/s41467-021-24624-5

Lautrup, S., Sinclair, D. A., Mattson, M. P., & Fang, E. F. (2019). NAD+ in Brain Aging and Neurodegenerative Disorders. In *Cell Metabolism* (Vol. 30, Issue 4, pp. 630–655). Cell Press. https://doi.org/10.1016/j.cmet.2019.09.001

Lavado, A., Gangwar, R., Paré, J., Wan, S., Fan, Y., & Cao, X. (2021). YAP/TAZ maintain the proliferative capacity and structural organization of radial glial cells during brain development. *Developmental Biology*, *480*, 39–49. https://doi.org/10.1016/j.ydbio.2021.08.010

Leithner, K., Hrzenjak, A., Trötzmüller, M., Moustafa, T., Köfeler, H. C., Wohlkoenig, C., Stacher, E., Lindenmann, J., Harris, A. L., Olschewski, A., & Olschewski, H. (2015). PCK2 activation mediates an adaptive response to glucose depletion in lung cancer. *Oncogene*, *34*(8), 1044–1050. https://doi.org/10.1038/onc.2014.47

Lengyel, M., Enyedi, P., & Czirják, G. (2021). Negative influence by the force: mechanically induced hyperpolarization via k2p background potassium channels. *International Journal of Molecular Sciences*, *22*(16). https://doi.org/10.3390/ijms22169062

Levine, J. H., Simonds, E. F., Bendall, S. C., Davis, K. L., Amir, E. A. D., Tadmor, M. D., Litvin, O., Fienberg, H. G., Jager, A., Zunder, E. R., Finck, R., Gedman, A. L., Radtke, I., Downing, J. R., Pe'er, D., & Nolan, G. P. (2015). Data-Driven Phenotypic Dissection of AML Reveals Progenitor-like Cells that Correlate with Prognosis. *Cell*, *162*(1), 184–197. https://doi.org/10.1016/j.cell.2015.05.047

Liesa, M., & Shirihai, O. S. (2013). Mitochondrial dynamics in the regulation of nutrient utilization and energy expenditure. In *Cell Metabolism* (Vol. 17, Issue 4, pp. 491–506). https://doi.org/10.1016/j.cmet.2013.03.002

Lim, D., Semyanov, A., Genazzani, A., & Verkhratsky, A. (2021). Calcium signaling in neuroglia. In *International Review of Cell and Molecular Biology* (Vol. 362, pp. 1–53). Elsevier Inc. https://doi.org/10.1016/bs.ircmb.2021.01.003

Lim, D., Tapella, L., Dematteis, G., Talmon, M., & Genazzani, A. A. (2023). Calcineurin Signalling in Astrocytes: From Pathology to Physiology and Control of Neuronal Functions. In *Neurochemical Research* (Vol. 48, Issue 4, pp. 1077–1090). Springer. https://doi.org/10.1007/s11064-022-03744-4

Linka, K., Reiter, N., Würges, J., Schicht, M., Bräuer, L., Cyron, C. J., Paulsen, F., & Budday, S. (2021). Unraveling the Local Relation Between Tissue Composition and Human Brain Mechanics Through Machine Learning. *Frontiers in Bioengineering and Biotechnology*, *9*. https://doi.org/10.3389/fbioe.2021.704738

Liu, J., Xiao, Q., Xiao, J., Niu, C., Li, Y., Zhang, X., Zhou, Z., Shu, G., & Yin, G. (2022). Wnt/β-catenin signalling: function, biological mechanisms, and therapeutic opportunities. In *Signal Transduction and Targeted Therapy* (Vol. 7, Issue 1). Springer Nature. https://doi.org/10.1038/s41392-021-00762-6

Liu, S. Y., & Ikegami, K. (2020). Nuclear lamin phosphorylation: an emerging role in gene regulation and pathogenesis of laminopathies. In *Nucleus* (Vol. 11, Issue 1, pp. 299–314). Bellwether Publishing, Ltd. https://doi.org/10.1080/19491034.2020.1832734

Liu, X., Hashimoto-Torii, K., Torii, M., Ding, C., & Rakic, P. (2010). Gap junctions/hemichannels modulate interkinetic nuclear migration in the forebrain precursors. *Journal of Neuroscience*, *30*(12), 4197–4209. https://doi.org/10.1523/JNEUROSCI.4187-09.2010

Liu, X., Hashimoto-Torii, K., Torii, M., Haydar, T. F., & Rakic, P. (2008). *The role of ATP signaling in the migration of intermediate neuronal progenitors to the neocortical subventricular zone*. www.pnas.orgcgidoi10.1073pnas.0805180105

Llorens-Bobadilla, E., Zhao, S., Baser, A., Saiz-Castro, G., Zwadlo, K., & Martin-Villalba, A. (2015). Single-Cell Transcriptomics Reveals a Population of Dormant Neural Stem Cells that Become Activated upon Brain Injury. *Cell Stem Cell*, *17*(3), 329–340. https://doi.org/10.1016/j.stem.2015.07.002

Lomakin, A. J., Cattin, C. J., Cuvelier, D., Alraies, Z., Molina, M., Nader, G. P. F., Srivastava, N., Saez, P. J., Garcia-Arcos, J. M., Zhitnyak, I. Y., Bhargava, A., Driscoll, M. K., Welf, E. S., Fiolka, R., Petrie, R. J., de Silva, N. S., González-Granado, J. M., Manel, N., Lennon-Duménil, A. M., … Piel, M. (2020). The

nucleus acts as a ruler tailoring cell responses to spatial constraints. *Science*, *370*(6514). https://doi.org/10.1126/science.aba2894

Loo, L., Simon, J. M., Xing, L., McCoy, E. S., Niehaus, J. K., Guo, J., Anton, E. S., & Zylka, M. J. (2019a). Single-cell transcriptomic analysis of mouse neocortical development. *Nature Communications*, *10*(1). https://doi.org/10.1038/s41467-018-08079-9

Loo, L., Simon, J. M., Xing, L., McCoy, E. S., Niehaus, J. K., Guo, J., Anton, E. S., & Zylka, M. J. (2019b). Single-cell transcriptomic analysis of mouse neocortical development. *Nature Communications*, *10*(1). https://doi.org/10.1038/s41467-018-08079-9

López-Juárez, A., Howard, J., Ullom, K., Howard, L., Grande, A., Pardo, A., Waclaw, R., Sun, Y. Y., Yang, D., Kuan, C. Y., Campbell, K., & Nakafuku, M. (2013). Gsx2 controls region-specific activation of neural stem cells and injury-induced neurogenesis in the adult subventricular zone. *Genes and Development*, *27*(11), 1272–1287. https://doi.org/10.1101/gad.217539.113

LoTurco, J. J., Owens, D. F., Heath, M. J. S., Davis, M. B. E., & Kriegstein, A. R. (1995). GABA and glutamate depolarize cortical progenitor cells and inhibit DNA synthesis. *Neuron*, *15*(6), 1287–1298. https://doi.org/10.1016/0896-6273(95)90008-X

Louhivuori, L. M., Jansson, L., Turunen, P. M., Jäntti, M. H., Nordström, T., Louhivuori, V., & Åkerman, K. E. (2015). Transient receptor potential channels and their role in modulating radial glial-neuronal interaction: A signaling pathway involving mGluR5. *Stem Cells and Development*, *24*(6), 701–713. https://doi.org/10.1089/scd.2014.0209

Lourenço, T., & Grãos, M. (2016). Modulation of oligodendrocyte differentiation by mechanotransduction. In *Frontiers in Cellular Neuroscience* (Vol. 10, Issue NOV2016). Frontiers Media S.A. https://doi.org/10.3389/fncel.2016.00277

Luo, J., & Li, P. (2022). Context-dependent transcriptional regulations of YAP/TAZ in stem cell and differentiation. In *Stem Cell Research and Therapy* (Vol. 13, Issue 1). BioMed Central Ltd. https://doi.org/10.1186/s13287-021-02686-y

Luo, Y., Huang, L., Liao, P., & Jiang, R. (2021). Contribution of Neuronal and Glial Two-Pore-Domain Potassium Channels in Health and Neurological Disorders. *Neural Plasticity*, *2021*. https://doi.org/10.1155/2021/8643129

Lv, Y., Zhang, B., Zhai, C., Qiu, J., Zhang, Y., Yao, W., & Zhang, C. (2015a). PFKFB3-mediated glycolysis is involved in reactive astrocyte proliferation after oxygen-glucose deprivation/reperfusion and is regulated by Cdh1. *Neurochemistry International*, *91*, 26–33. https://doi.org/10.1016/j.neuint.2015.10.006

Lv, Y., Zhang, B., Zhai, C., Qiu, J., Zhang, Y., Yao, W., & Zhang, C. (2015b). PFKFB3-mediated glycolysis is involved in reactive astrocyte proliferation after oxygen-glucose deprivation/reperfusion and is regulated by Cdh1. *Neurochemistry International*, *91*, 26–33. https://doi.org/10.1016/j.neuint.2015.10.006

MacDonald, B. T., Tamai, K., & He, X. (2009). Wnt/β-Catenin Signaling: Components, Mechanisms, and Diseases. In *Developmental Cell* (Vol. 17, Issue 1, pp. 9–26). https://doi.org/10.1016/j.devcel.2009.06.016

Machon, O., Backman, M., Machonova, O., Kozmik, Z., Vacik, T., Andersen, L., & Krauss, S. (2007). A dynamic gradient of Wnt signaling controls initiation of neurogenesis in the mammalian cortex and cellular specification in the hippocampus. *Developmental Biology*, *311*(1), 223–237. https://doi.org/10.1016/j.ydbio.2007.08.038

Magnusson, J. P., Zamboni, M., Santopolo, G., Mold, J. E., Barrientos-Somarribas, M., Talavera-Lopez, C., Andersson, B., & Frisén, J. (2020). Activation of a neural stem cell transcriptional program in parenchymal astrocytes. *eLife*, *9*, 1–25. https://doi.org/10.7554/ELIFE.59733

Mahajani, S., Giacomini, C., Marinaro, F., De Pietri Tonelli, D., Contestabile, A., & Gasparini, L. (2017). Lamin B1 levels modulate differentiation into neurons during embryonic corticogenesis. *Scientific Reports*, *7*(1). https://doi.org/10.1038/s41598-017-05078-6

Makhija, E., Jagielska, A., Zhu, L., Bost, A. C., Ong, W., Chew, S. Y., Shivashankar, G. V., & Van Vliet, K. J. (2018). Mechanical strain alters cellular and nuclear dynamics at early stages of oligodendrocyte differentiation. *Frontiers in Cellular Neuroscience*, *12*. https://doi.org/10.3389/fncel.2018.00059

Malatesta, P., Hartfuss, E., & Götz, M. (2000a). Isolation of radial glial cells by fluorescent-activated cell sorting reveals a neural lineage. *Development*, *127*(24), 5253–5263. https://doi.org/10.1242/dev.127.24.5253

Malatesta, P., Hartfuss, E., & Götz, M. (2000b). Isolation of radial glial cells by fluorescent-activated cell sorting reveals a neuronal lineage. *Development*, *127*(24), 5253–5263. http://www.ncbi.nlm.nih.gov/pubmed/11076748

Mandel, G., Zheng, X., Boyer, L., Jin, M., Mertens, J., Kim, Y., Ma, L., Hamm, M., Gage, F. H., & Hunter, T. (2016). *Metabolic reprogramming during neuronal differentiation from aerobic glycolysis to neuronal oxidative phosphorylation*. https://doi.org/10.7554/eLife.13374.001

Manzari-Tavakoli, A., Babajani, A., Farjoo, M. H., Hajinasrollah, M., Bahrami, S., & Niknejad, H. (2022). The Cross-Talks Among Bone Morphogenetic Protein (BMP) Signaling and Other Prominent Pathways Involved in Neural Differentiation. In *Frontiers in Molecular Neuroscience* (Vol. 15). Frontiers Media S.A. https://doi.org/10.3389/fnmol.2022.827275

Marinval, N., & Chew, S. Y. (2021). Mechanotransduction assays for neural regeneration strategies: A focus on glial cells. In *APL Bioengineering* (Vol. 5, Issue 2). American Institute of Physics Inc. https://doi.org/10.1063/5.0037814

Markey, K. M., Saunders, J. C., Smuts, J., von Reyn, C. R., & Garcia, A. D. R. (2023). Astrocyte development—More questions than answers. In *Frontiers in Cell and Developmental Biology* (Vol. 11). Frontiers Media S.A. https://doi.org/10.3389/fcell.2023.1063843

Márquez-Zacarías, P., Pineau, R. M., Gomez, M., Veliz-Cuba, A., Murrugarra, D., Ratcliff, W. C., & Niklas, K. J. (2021). Evolution of Cellular Differentiation: From Hypotheses to Models. In *Trends in Ecology and Evolution* (Vol. 36, Issue 1, pp. 49–60). Elsevier Ltd. https://doi.org/10.1016/j.tree.2020.07.013

Matias, I., Diniz, L. P., Damico, I. V., Araujo, A. P. B., Neves, L. da S., Vargas, G., Leite, R. E. P., Suemoto, C. K., Nitrini, R., Jacob-Filho, W., Grinberg, L. T., Hol, E. M., Middeldorp, J., & Gomes, F. C. A. (2022). Loss of lamin-B1 and defective nuclear morphology are hallmarks of astrocyte senescence in vitro and in the aging human hippocampus. *Aging Cell*, *21*(1). https://doi.org/10.1111/acel.13521

Mattiazzi Usaj, M., Yeung, C. H. L., Friesen, H., Boone, C., & Andrews, B. J. (2021a). Single-cell image analysis to explore cell-to-cell heterogeneity in isogenic populations. In *Cell Systems* (Vol. 12, Issue 6, pp. 608–621). Cell Press. https://doi.org/10.1016/j.cels.2021.05.010

Mattiazzi Usaj, M., Yeung, C. H. L., Friesen, H., Boone, C., & Andrews, B. J. (2021b). Single-cell image analysis to explore cell-to-cell heterogeneity in isogenic populations. In *Cell Systems* (Vol. 12, Issue 6, pp. 608–621). Cell Press. https://doi.org/10.1016/j.cels.2021.05.010

Mattiazzi Usaj, M., Yeung, C. H. L., Friesen, H., Boone, C., & Andrews, B. J. (2021c). Single-cell image analysis to explore cell-to-cell heterogeneity in isogenic populations. In *Cell Systems* (Vol. 12, Issue 6, pp. 608–621). Cell Press. https://doi.org/10.1016/j.cels.2021.05.010

Mattotti, M., Alvarez, Z., Delgado, L., Mateos-Timoneda, M. A., Aparicio, C., Planell, J. A., Alcántara, S., & Engel, E. (2017). Differential neuronal and glial behavior on flat and micro patterned chitosan films. *Colloids and Surfaces B: Biointerfaces*, *158*, 569–577. https://doi.org/10.1016/j.colsurfb.2017.07.045

Mattotti, M., Alvarez, Z., Ortega, J. A., Planell, J. A., Engel, E., & Alcántara, S. (2012). Inducing functional radial glia-like progenitors from cortical astrocyte cultures using micropatterned PMMA. *Biomaterials*, *33*(6), 1759–1770. https://doi.org/10.1016/j.biomaterials.2011.10.086

Maurer, M., & Lammerding, J. (2019a). *The Driving Force: Nuclear Mechanotransduction in Cellular Function, Fate, and Disease*. https://doi.org/10.1146/annurev-bioeng-060418

Maurer, M., & Lammerding, J. (2019b). *The Driving Force: Nuclear Mechanotransduction in Cellular Function, Fate, and Disease*. https://doi.org/10.1146/annurev-bioeng-060418

McKinney, A. A., Petrova, R., & Panagiotakos, G. (2022). Calcium and activity-dependent signaling in the developing cerebral cortex. In *Development (Cambridge)* (Vol. 149, Issue 17). Company of Biologists Ltd. https://doi.org/10.1242/dev.198853

Merkle, F. T., Fuentealba, L. C., Sanders, T. A., Magno, L., Kessaris, N., & Alvarez-Buylla, A. (2014). Adult neural stem cells in distinct microdomains generate previously unknown interneuron types. *Nature Neuroscience*, *17*(2), 207–214. https://doi.org/10.1038/nn.3610

Mestres, I., Houtman, J., Calegari, F., & Toda, T. (2022a). A Nuclear Belt Fastens on Neural Cell Fate. In *Cells* (Vol. 11, Issue 11). MDPI. https://doi.org/10.3390/cells11111761

Mestres, I., Houtman, J., Calegari, F., & Toda, T. (2022b). A Nuclear Belt Fastens on Neural Cell Fate. In *Cells* (Vol. 11, Issue 11). MDPI. https://doi.org/10.3390/cells11111761

Middeldorp, J., & Hol, E. M. (2011). GFAP in health and disease. In *Progress in Neurobiology* (Vol. 93, Issue 3, pp. 421–443). https://doi.org/10.1016/j.pneurobio.2011.01.005

Miller, F. D., & Gauthier, A. S. (2007). Timing Is Everything: Making Neurons versus Glia in the Developing Cortex. In *Neuron* (Vol. 54, Issue 3, pp. 357–369). https://doi.org/10.1016/j.neuron.2007.04.019

Miyamoto, Y., Sakane, F., & Hashimoto, K. (2015). N-cadherin-based adherens junction regulates the maintenance, proliferation, And differentiation of neural progenitor cells during development. In *Cell Adhesion and Migration* (Vol. 9, Issue 3, pp. 183–192). Taylor and Francis Inc. https://doi.org/10.1080/19336918.2015.1005466

Miyazawa, H., & Aulehla, A. (2018). Revisiting the role of metabolism during development. *Development (Cambridge)*, *145*(19). https://doi.org/10.1242/dev.131110

Momin, A., Bahrampour, S., Min, H. K., Chen, X., Wang, X., Sun, Y., & Huang, X. (2021). Channeling Force in the Brain: Mechanosensitive Ion Channels Choreograph Mechanics and Malignancies. In *Trends in Pharmacological Sciences* (Vol. 42, Issue 5, pp. 367–384). Elsevier Ltd. https://doi.org/10.1016/j.tips.2021.02.006

Moore, K. A., & Lemischka, I. R. (2006). *Stem Cells and Their Niches*. https://www.science.org

Möpert, K., Hajek, P., Frank, S., Chen, C., Kaufmann, J., & Santel, A. (2009). Loss of Drp1 function alters OPA1 processing and changes mitochondrial membrane organization. *Experimental Cell Research*, *315*(13), 2165–2180. https://doi.org/10.1016/j.yexcr.2009.04.016

Moshayedi, P., Da F Costa, L., Christ, A., Lacour, S. P., Fawcett, J., Guck, J., & Franze, K. (2010). Mechanosensitivity of astrocytes on optimized polyacrylamide gels analyzed by quantitative morphometry. *Journal of Physics Condensed Matter*, *22*(19). https://doi.org/10.1088/0953-8984/22/19/194114

Mota, B., & Herculano-Houzel, S. (2014). All brains are made of this: A fundamental building block of brain matter with matching neuronal and glial masses. *Frontiers in Neuroanatomy*, *8*(November). https://doi.org/10.3389/fnana.2014.00127

Movilla, N., Borau, C., Valero, C., & García-Aznar, J. M. (2018). Degradation of extracellular matrix regulates osteoblast migration: A microfluidic-based study. *Bone*, *107*, 10–17. https://doi.org/10.1016/j.bone.2017.10.025

Mukhtar, T., Breda, J., Grison, A., Karimaddini, Z., Grobecker, P., Iber, D., Beisel, C., van Nimwegen, E., & Taylor, V. (2020). Tead transcription factors differentially regulate cortical development. *Scientific Reports*, *10*(1). https://doi.org/10.1038/s41598-020-61490-5

Mulder, L. A., Depla, J. A., Sridhar, A., Wolthers, K., Pajkrt, D., & Vieira de Sá, R. (2023). A beginner's guide on the use of brain organoids for neuroscientists: a systematic review. *Stem Cell Research and Therapy*, *14*(1). https://doi.org/10.1186/s13287-023-03302-x

Murao, N., Noguchi, H., & Nakashima, K. (2016). Epigenetic regulation of neural stem cell property from embryo to adult. In *Neuroepigenetics* (Vol. 5, pp. 1–10). Elsevier Inc. https://doi.org/10.1016/j.nepig.2016.01.001

Najas, S., Pijuan, I., Esteve-Codina, A., Usieto, S., Martinez, J. D., Zwijsen, A., Arbonés, M. L., Martı, E., & Le Dréau, G. (2020). A SMAD1/5-YAP signalling module drives radial glia self-amplification and growth of the developing cerebral cortex. *Development (Cambridge)*, *147*(13). https://doi.org/10.1242/dev.187005

Namihira, M., Kohyama, J., Semi, K., Sanosaka, T., Deneen, B., Taga, T., & Nakashima, K. (2009). Committed Neuronal Precursors Confer Astrocytic Potential on Residual Neural Precursor Cells. *Developmental Cell*, *16*(2), 245–255. https://doi.org/10.1016/j.devcel.2008.12.014

Nandi, A., Chartrand, T., Van Geit, W., Buchin, A., Yao, Z., Lee, S. Y., Wei, Y., Kalmbach, B., Lee, B., Lein, E., Berg, J., Sümbül, U., Koch, C., Tasic, B., & Anastassiou, C. A. (2022). Single-neuron models linking

electrophysiology, morphology, and transcriptomics across cortical cell types. *Cell Reports*, *40*(6). https://doi.org/10.1016/j.celrep.2022.111176

Nardone, G., Oliver-De La Cruz, J., Vrbsky, J., Martini, C., Pribyl, J., Skládal, P., Pešl, M., Caluori, G., Pagliari, S., Martino, F., Maceckova, Z., Hajduch, M., Sanz-Garcia, A., Pugno, N. M., Stokin, G. B., & Forte, G. (2017). YAP regulates cell mechanics by controlling focal adhesion assembly. *Nature Communications*, *8*. https://doi.org/10.1038/ncomms15321

Nava, M. M., Miroshnikova, Y. A., Biggs, L. C., Whitefield, D. B., Metge, F., Boucas, J., Vihinen, H., Jokitalo, E., Li, X., García Arcos, J. M., Hoffmann, B., Merkel, R., Niessen, C. M., Dahl, K. N., & Wickström, S. A. (2020). Heterochromatin-Driven Nuclear Softening Protects the Genome against Mechanical Stress-Induced Damage. *Cell*, *181*(4), 800-817.e22. https://doi.org/10.1016/j.cell.2020.03.052

Ndiaye, A. B., Koenderink, G. H., & Shemesh, M. (2022). Intermediate Filaments in Cellular Mechanoresponsiveness: Mediating Cytoskeletal Crosstalk From Membrane to Nucleus and Back. In *Frontiers in Cell and Developmental Biology* (Vol. 10). Frontiers Media S.A. https://doi.org/10.3389/fcell.2022.882037

Neal, J., Takahashi, M., Silva, M., Tiao, G., Walsh, C. A., & Sheen, V. L. (2007). Insights into the gyrification of developing ferret brain by magnetic resonance imaging. *Journal of Anatomy*, *210*(1), 66–77. https://doi.org/10.1111/j.1469-7580.2006.00674.x

Niari, S. A., Rahbarghazi, R., Geranmayeh, M. H., & Karimipour, M. (2022). Biomaterials patterning regulates neural stem cells fate and behavior: The interface of biology and material science. In *Journal of Biomedical Materials Research - Part A* (Vol. 110, Issue 3, pp. 725–737). John Wiley and Sons Inc. https://doi.org/10.1002/jbm.a.37321

Nicole, O., Bell, D. M., Leste-Lasserre, T., Doat, H., Guillemot, F., & Pacary, E. (2018). A novel role for CAMKIIβ in the regulation of cortical neuron migration: implications for neurodevelopmental disorders. *Molecular Psychiatry*, *23*(11), 2209–2226. https://doi.org/10.1038/s41380-018-0046-0

Nicole, O., & Pacary, E. (2020). Camkiiβ in neuronal development and plasticity: An emerging candidate in brain diseases. In *International Journal of Molecular Sciences* (Vol. 21, Issue 19, pp. 1–15). MDPI AG. https://doi.org/10.3390/ijms21197272

Nielsen, J., Gejl, K. D., Hey-Mogensen, M., Holmberg, H. C., Suetta, C., Krustrup, P., Elemans, C. P. H., & Ørtenblad, N. (2017). Plasticity in mitochondrial cristae density allows metabolic capacity modulation in human skeletal muscle. *Journal of Physiology*, *595*(9), 2839–2847. https://doi.org/10.1113/JP273040

Niethammer, P. (2021). *Components and Mechanisms of Nuclear Mechanotransduction*. https://doi.org/10.1146/annurev-cellbio-120319

Nmezi, B., Xu, J., Fu, R., Armiger, T. J., Rodriguez-Bey, G., Powell, J. S., Ma, H., Sullivan, M., Tu, Y., Chen, N. Y., Young, S. G., Stolz, D. B., Dahl, K. N., Liu, Y., & Padiath, Q. S. (2019). Concentric organization of A- and B-type lamins predicts their distinct roles in the spatial organization and stability of the nuclear lamina. *Proceedings of the National Academy of Sciences of the United States of America*, *116*(10), 4307–4315. https://doi.org/10.1073/pnas.1810070116

Noctor, A. C. F. T. A. W. R. S. D. & A. R. K. (2001). *Neuronsderived fromradial glial cells establish radial units in neocortex*.

Noctor, S. C., Martinez-Cerdeño, V., Ivic, L., & Kriegstein, A. R. (2004). Cortical neurons arise in symmetric and asymmetric division zones and migrate through specific phases. *Nature Neuroscience*, *7*(2), 136–144. https://doi.org/10.1038/nn1172

Nolfi-Donegan, D., Braganza, A., & Shiva, S. (2020). Mitochondrial electron transport chain: Oxidative phosphorylation, oxidant production, and methods of measurement. In *Redox Biology* (Vol. 37). Elsevier B.V. https://doi.org/10.1016/j.redox.2020.101674

Nowakowski, T. J., Pollen, A. A., Sandoval-Espinosa, C., & Kriegstein, A. R. (2016a). Transformation of the Radial Glia Scaffold Demarcates Two Stages of Human Cerebral Cortex Development. *Neuron*, *91*(6), 1219–1227. https://doi.org/10.1016/j.neuron.2016.09.005

Nowakowski, T. J., Pollen, A. A., Sandoval-Espinosa, C., & Kriegstein, A. R. (2016b). Transformation of the Radial Glia Scaffold Demarcates Two Stages of Human Cerebral Cortex Development. *Neuron*, *91*(6), 1219–1227. https://doi.org/10.1016/j.neuron.2016.09.005

Obernier, K., & Alvarez-Buylla, A. (2019). Neural stem cells: Origin, heterogeneity and regulation in the adult mammalian brain. In *Development (Cambridge)* (Vol. 146, Issue 4). Company of Biologists Ltd. https://doi.org/10.1242/dev.156059

Ortega, J. A., Radonjić, N. V., & Zecevic, N. (2013). Sonic hedgehog promotes generation and maintenance of human forebrain Olig2 progenitors. *Frontiers in Cellular Neuroscience*, *7*(DEC). https://doi.org/10.3389/fncel.2013.00254

Ortega, J. A., Sirois, C. L., Memi, F., Glidden, N., & Zecevic, N. (2017a). Oxygen Levels Regulate the Development of Human Cortical Radial Glia Cells. *Cerebral Cortex*, *27*(7), 3736–3751. https://doi.org/10.1093/cercor/bhw194

Ortega, J. A., Sirois, C. L., Memi, F., Glidden, N., & Zecevic, N. (2017b). Oxygen Levels Regulate the Development of Human Cortical Radial Glia Cells. *Cerebral Cortex*, *27*(7), 3736–3751. https://doi.org/10.1093/cercor/bhw194

Owens, D. F., & Kriegstein, A. R. (1998). *Patterns of Intracellular Calcium Fluctuation in Precursor Cells of the Neocortical Ventricular Zone*.

Ozgun, A., Lomboni, D., Arnott, H., Staines, W. A., Woulfe, J., & Variola, F. (2022). Biomaterials-based strategies for in vitro neural models. In *Biomaterials Science* (Vol. 10, Issue 5, pp. 1134–1165). Royal Society of Chemistry. https://doi.org/10.1039/d1bm01361k

Parekh, A. B. (2008). Ca2+ microdomains near plasma membrane Ca2+ channels: Impact on cell function. *Journal of Physiology*, *586*(13), 3043–3054. https://doi.org/10.1113/jphysiol.2008.153460

Paridaen, J. T., & Huttner, W. B. (2014). Neurogenesis during development of the vertebrate central nervous system. In *EMBO Reports* (Vol. 15, Issue 4, pp. 351–364). Wiley-VCH Verlag. https://doi.org/10.1002/embr.201438447

Park, J. S., Burckhardt, C. J., Lazcano, R., Solis, L. M., Isogai, T., Li, L., Chen, C. S., Gao, B., Minna, J. D., Bachoo, R., DeBerardinis, R. J., & Danuser, G. (2020). Mechanical regulation of glycolysis via cytoskeleton architecture. *Nature*, *578*(7796), 621–626. https://doi.org/10.1038/s41586-020-1998-1

Park, M. G., Jang, H., Lee, S. H., & Justin Lee, C. (2017). Flow shear stress enhances the proliferative potential of cultured radial glial cells possibly via an activation of mechanosensitive calcium channel. *Experimental Neurobiology*, *26*(2), 71–81. https://doi.org/10.5607/en.2017.26.2.71

Pathak, R. U., Soujanya, M., & Mishra, R. K. (2021). Deterioration of nuclear morphology and architecture: A hallmark of senescence and aging. In *Ageing Research Reviews* (Vol. 67). Elsevier Ireland Ltd. https://doi.org/10.1016/j.arr.2021.101264

Pekny, M., Johansson, C. B., Eliasson, C., Stakeberg, J., Wallén, Å., Perlmann, T., Lendahl, U., Betsholtz, C., Berthold, C.-H., & Frisén, J. (1999). Abnormal Reaction to Central Nervous System Injury in Mice Lacking Glial Fibrillary Acidic Protein and Vimentin. In *The Journal of Cell Biology* (Vol. 145, Issue 3). http://www.jcb.org503

Petridou, N. I., Spiró, Z., & Heisenberg, C.-P. (2017). Multiscale force sensing in development. *Nature Cell Biology*, *19*(6), 581–588. https://doi.org/10.1038/ncb3524

Phuyal, S., Romani, P., Dupont, S., & Farhan, H. (2023). Mechanobiology of organelles: illuminating their roles in mechanosensing and mechanotransduction. In *Trends in Cell Biology*. Elsevier Ltd. https://doi.org/10.1016/j.tcb.2023.05.001

Piccolo, S., Dupont, S., & Cordenonsi, M. (2014). The Biology of YAP/TAZ: Hippo Signaling and Beyond. *Physiological Reviews*, *94*(4), 1287–1312. https://doi.org/10.1152/physrev.00005.2014

Potokar, M., Morita, M., Wiche, G., & Jorgačevski, J. (2020). The Diversity of Intermediate Filaments in Astrocytes. In *Cells* (Vol. 9, Issue 7). NLM (Medline). https://doi.org/10.3390/cells9071604

Procès, A., Luciano, M., Kalukula, Y., Ris, L., & Gabriele, S. (2022). Multiscale Mechanobiology in Brain Physiology and Diseases. In *Frontiers in Cell and Developmental Biology* (Vol. 10). Frontiers Media S.A. https://doi.org/10.3389/fcell.2022.823857

Prozorovski, T., Schulze-Topphoff, U., Glumm, R., Baumgart, J., Schröter, F., Ninnemann, O., Siegert, E., Bendix, I., Brüstle, O., Nitsch, R., Zipp, F., & Aktas, O. (2008). Sirt1 contributes critically to the redox-dependent fate of neural progenitors. *Nature Cell Biology*, *10*(4), 385–394. https://doi.org/10.1038/ncb1700

Quintana-Cabrera, R., & Scorrano, L. (2023). Determinants and outcomes of mitochondrial dynamics. In *Molecular Cell* (Vol. 83, Issue 6, pp. 857–876). Cell Press. https://doi.org/10.1016/j.molcel.2023.02.012

Radonjić, N. V., Memi, F., Ortega, J. A., Glidden, N., Zhan, H., & Zecevic, N. (2016). The Role of Sonic Hedgehog in the Specification of Human Cortical Progenitors in Vitro. *Cerebral Cortex*, *26*(1), 131–143. https://doi.org/10.1093/cercor/bhu183

Rakic, P. (1972). *Mode of Cell Migration to the Superficial Layers of Fetal Monkey Neocortex ’*.

Rakic, P. (1995). *A small step for the cell, a giant leap for mankind: a hypothesis of neocortical expansion during evolution*.

Rakic, P. (2003). Elusive radial glial cells: Historical and evolutionary perspective. *GLIA*, *43*(1), 19–32. https://doi.org/10.1002/glia.10244

Rakic, P. (2009). Evolution of the neocortex: A perspective from developmental biology. In *Nature Reviews Neuroscience* (Vol. 10, Issue 10, pp. 724–735). https://doi.org/10.1038/nrn2719

Rammensee, S., Kang, M. S., Georgiou, K., Kumar, S., & Schaffer, D. V. (2017). Dynamics of Mechanosensitive Neural Stem Cell Differentiation. *Stem Cells*, *35*(2), 497–506. https://doi.org/10.1002/stem.2489

Ranade, S. S., Syeda, R., & Patapoutian, A. (2015). Mechanically Activated Ion Channels. In *Neuron* (Vol. 87, Issue 6, pp. 1162–1179). Cell Press. https://doi.org/10.1016/j.neuron.2015.08.032

Rash, B. G., Ackman, J. B., & Rakic, P. (2016). Bidirectional radial Ca2+ activity regulates neurogenesis and migration during early cortical column formation. *Science Advances*, *2*(2). https://doi.org/10.1126/sciadv.1501733

Rash, B. G., Micali, N., Huttner, A. J., Morozov, Y. M., Horvath, T. L., & Rakic, P. (2018). Metabolic regulation and glucose sensitivity of cortical radial glial cells. *Proceedings of the National Academy of Sciences of the United States of America*, *115*(40), 10142–10147. https://doi.org/10.1073/pnas.1808066115

Rasmussen, R. N., Asiminas, A., Carlsen, E. M. M., Kjaerby, C., & Smith, N. A. (2023). Astrocytes: integrators of arousal state and sensory context. In *Trends in Neurosciences* (Vol. 46, Issue 6, pp. 418–425). Elsevier Ltd. https://doi.org/10.1016/j.tins.2023.03.003

Redmond, C. J., & Coulombe, P. A. (2021). Intermediate filaments as effectors of differentiation. In *Current Opinion in Cell Biology* (Vol. 68, pp. 155–162). Elsevier Ltd. https://doi.org/10.1016/j.ceb.2020.10.009

Reillo, I., De Juan Romero, C., García-Cabezas, M. Á., & Borrell, V. (2011). A Role for intermediate radial glia in the tangential expansion of the mammalian cerebral cortex. *Cerebral Cortex*, *21*(7), 1674–1694. https://doi.org/10.1093/cercor/bhq238

Riera, L., Manzano, A., Navarro-Sabate, A., Perales, J. C., & Bartrons, R. (2002). *Rapid report Insulin induces PFKFB3 gene expression in HT29 human colon adenocarcinoma cells*. www.bba-direct.com

Robert, A., Herrmann, H., Davidson, M. W., & Gelfand, V. I. (2014). Microtubule-dependent transport of vimentin filament precursors is regulated by actin and by the concerted action of Rho- and p21-activated kinases. *FASEB Journal*, *28*(7), 2879–2890. https://doi.org/10.1096/fj.14-250019

Rocha, D. N., Carvalho, E. D., Relvas, J. B., Oliveira, M. J., & Pêgo, A. P. (2022). Mechanotransduction: Exploring New Therapeutic Avenues in Central Nervous System Pathology. In *Frontiers in Neuroscience* (Vol. 16). Frontiers Media S.A. https://doi.org/10.3389/fnins.2022.861613

Rocha, D. N., Ferraz-Nogueira, J. P., Barrias, C. C., Relvas, J. B., & Pêgo, A. P. (2015). Extracellular environment contribution to astrogliosis—lessons learned from a tissue engineered 3D model of the glial scar. *Frontiers in Cellular Neuroscience*, *9*(SEPTEMBER). https://doi.org/10.3389/fncel.2015.00377

Romani, P., Valcarcel-Jimenez, L., Frezza, C., & Dupont, S. (2021a). Crosstalk between mechanotransduction and metabolism. *Nature Reviews Molecular Cell Biology*, *22*(1), 22–38. https://doi.org/10.1038/s41580-020-00306-w

Romani, P., Valcarcel-Jimenez, L., Frezza, C., & Dupont, S. (2021b). Crosstalk between mechanotransduction and metabolism. In *Nature Reviews Molecular Cell Biology* (Vol. 22, Issue 1, pp. 22–38). Nature Research. https://doi.org/10.1038/s41580-020-00306-w

Romero-Morales, A. I., Robertson, G. L., Rastogi, A., Rasmussen, M. L., Temuri, H., McElroy, G. S., Chakrabarty, R. P., Hsu, L., Almonacid, P. M., Millis, B. A., Chandel, N. S., Cartailler, J. P., & Gama, V. (2022). Human iPSC-derived cerebral organoids model features of Leigh syndrome and reveal abnormal corticogenesis. *Development (Cambridge)*, *149*(20). https://doi.org/10.1242/dev.199914

Rosenbloom, A. B., Tarczy nski, M., Lam, N., Kane, R. S., Bugaj, L. J., & Schaffer, D. V. (2020). *β-Catenin signaling dynamics regulate cell fate in differentiating neural stem cells*. *117*(46), 28828–28837. https://doi.org/10.1073/pnas.2008509117/-/DCSupplemental

Rouleau, N., Murugan, N. J., & Kaplan, D. L. (2023). Functional bioengineered models of the central nervous system. *Nature Reviews Bioengineering*, *1*(4), 252–270. https://doi.org/10.1038/s44222-023-00027-7

Royal, P., Andres-Bilbe, A., Ávalos Prado, P., Verkest, C., Wdziekonski, B., Schaub, S., Baron, A., Lesage, F., Gasull, X., Levitz, J., & Sandoz, G. (2019). Migraine-Associated TRESK Mutations Increase Neuronal Excitability through Alternative Translation Initiation and Inhibition of TREK. *Neuron*, *101*(2), 232-245.e6. https://doi.org/10.1016/j.neuron.2018.11.039

Ruan, Z., Osei-Owusu, J., Du, J., Qiu, Z., & Lü, W. (2020). Structures and pH-sensing mechanism of the proton-activated chloride channel. *Nature*, *588*(7837), 350–354. https://doi.org/10.1038/s41586-020-2875-7

Saha, K., Keung, A. J., Irwin, E. F., Li, Y., Little, L., Schaffer, D. V., & Healy, K. E. (2008). Substrate modulus directs neural stem cell behavior. *Biophysical Journal*, *95*(9), 4426–4438. https://doi.org/10.1529/biophysj.108.132217

Saka, Y., Lhoussaine, C., Kuttler, C., Ullner, E., & Thiel, M. (2011). Theoretical basis of the community effect in development. *BMC Systems Biology*, *5*. https://doi.org/10.1186/1752-0509-5-54

Sanghvi-Shah, R., & Weber, G. F. (2017). Intermediate filaments at the junction of mechanotransduction, migration, and development. In *Frontiers in Cell and Developmental Biology* (Vol. 5, Issue SEP). Frontiers Media S.A. https://doi.org/10.3389/fcell.2017.00081

Saper, C. B. (2009). A guide to the perplexed on the specificity of antibodies. In *Journal of Histochemistry and Cytochemistry* (Vol. 57, Issue 1, pp. 1–5). https://doi.org/10.1369/jhc.2008.952770

Saunders, N. R., Habgood, M. D., Møllgård, K., & Dziegielewska, K. M. (2016). The biological significance of brain barrier mechanisms: Help or hindrance in drug delivery to the central nervous system? In *F1000Research* (Vol. 5). Faculty of 1000 Ltd. https://doi.org/10.12688/f1000research.7378.1

Savic Azoulay, I., Liu, F., Hu, Q., Rozenfeld, M., Ben Kasus Nissim, T., Zhu, M. X., Sekler, I., & Xu, T. Le. (2020). ASIC1a channels regulate mitochondrial ion signaling and energy homeostasis in neurons. *Journal of Neurochemistry*, *153*(2), 203–215. https://doi.org/10.1111/jnc.14971

Sawamura et al. (2017). *Neurobiology of TRP Channels* (T. L. R. Emir, Ed.). CRC Press. https://doi.org/10.4324/9781315152837

Schildge, S., Bohrer, C., Beck, K., & Schachtrup, C. (2013). Isolation and Culture of Mouse Cortical Astrocytes. *Journal of Visualized Experiments*, *71*, 1–7. https://doi.org/10.3791/50079

Schlachetzki, J. C. M., Toda, T., & Mertens, J. (2020). When function follows form: Nuclear compartment structure and the epigenetic landscape of the aging neuron. In *Experimental Gerontology* (Vol. 133). Elsevier Inc. https://doi.org/10.1016/j.exger.2020.110876

Segel, M., Neumann, B., Hill, M. F. E., Weber, I. P., Viscomi, C., Zhao, C., Young, A., Agley, C. C., Thompson, A. J., Gonzalez, G. A., Sharma, A., Holmqvist, S., Rowitch, D. H., Franze, K., Franklin, R. J. M., & Chalut, K. J. (2019). Niche stiffness underlies the ageing of central nervous system progenitor cells. *Nature*, *573*(7772), 130–134. https://doi.org/10.1038/s41586-019-1484-9

Seidman, R. A., Khattab, H., Polanco, J. J., Broome, J. E., & Sim, F. J. (2022). Oscillatory calcium release and sustained store-operated oscillatory calcium signaling prevents differentiation of human oligodendrocyte progenitor cells. *Scientific Reports*, *12*(1). https://doi.org/10.1038/s41598-022-10095-1

Sen, B., Xie, Z., Howard, S., Styner, M., van Wijnen, A. J., Uzer, G., & Rubin, J. (2022). Mechanically Induced Nuclear Shuttling of β-Catenin Requires Co-transfer of Actin. *Stem Cells*, *40*(4), 332–345. https://doi.org/10.1093/stmcls/sxac006

Sergent-Tanguy, S., Michel, D. C., Neveu, I., & Naveilhan, P. (2006). Long-lasting coexpression of nestin and glial fibrillary acidic protein in primary cultures of astroglial cells with a major participation of nestin +/GFAP- cells in cell proliferation. *Journal of Neuroscience Research*, *83*(8), 1515–1524. https://doi.org/10.1002/jnr.20846

Sero, J. E., & Bakal, C. (2017). Multiparametric Analysis of Cell Shape Demonstrates that β-PIX Directly Couples YAP Activation to Extracellular Matrix Adhesion. *Cell Systems*, *4*(1), 84-96.e6. https://doi.org/10.1016/j.cels.2016.11.015

Sessa, A., Mao, C. an, Hadjantonakis, A. K., Klein, W. H., & Broccoli, V. (2008). Tbr2 Directs Conversion of Radial Glia into Basal Precursors and Guides Neuronal Amplification by Indirect Neurogenesis in the Developing Neocortex. *Neuron*, *60*(1), 56–69. https://doi.org/10.1016/j.neuron.2008.09.028

Sharma, G., Shin, E. J., Sharma, N., Nah, S. Y., Mai, H. N., Nguyen, B. T., Jeong, J. H., Lei, X. G., & Kim, H. C. (2021). Glutathione peroxidase-1 and neuromodulation: Novel potentials of an old enzyme. In *Food and Chemical Toxicology* (Vol. 148). Elsevier Ltd. https://doi.org/10.1016/j.fct.2020.111945

Sheshadri, P., & Kumar, A. (2016). Managing odds in stem cells: Insights into the role of mitochondrial antioxidant enzyme MnSOD. In *Free Radical Research* (Vol. 50, Issue 5, pp. 570–584). Taylor and Francis Ltd. https://doi.org/10.3109/10715762.2016.1155708

Shigetomi, E., Tong, X., Kwan, K. Y., Corey, D. P., & Khakh, B. S. (2012). TRPA1 channels regulate astrocyte resting calcium and inhibitory synapse efficacy through GAT-3. *Nature Neuroscience*, *15*(1), 70–80. https://doi.org/10.1038/nn.3000

Shimazaki, T., & Okano, H. (2016). Heterochronic micrornas in temporal specification of neural stem cells: Application toward rejuvenation. *Npj Aging and Mechanisms of Disease*, *2*(1). https://doi.org/10.1038/npjamd.2015.14

Sjöqvist, M., Antfolk, D., Suarez-Rodriguez, F., & Sahlgren, C. (2021). From structural resilience to cell specification — Intermediate filaments as regulators of cell fate. In *FASEB Journal* (Vol. 35, Issue 1). John Wiley and Sons Inc. https://doi.org/10.1096/fj.202001627R

Skinner, B. M., & Johnson, E. E. P. (2017). Nuclear morphologies: their diversity and functional relevance. *Chromosoma*, *126*(2), 195–212. https://doi.org/10.1007/s00412-016-0614-5

Smart, I., Dehay, C., Giroud, P., Berland, M., & Kennedy, H. (2002). *Unique Morphological Features of theProliferative Zones and PostmitoticCompartments of the Neural EpitheliumGiving Rise to Striate and ExtrastriateCortex in the Monkey*.

Smith, K., Piccinini, F., Balassa, T., Koos, K., Danka, T., Azizpour, H., & Horvath, P. (2018). Phenotypic Image Analysis Software Tools for Exploring and Understanding Big Image Data from Cell-Based Assays. In *Cell Systems* (Vol. 6, Issue 6, pp. 636–653). Cell Press. https://doi.org/10.1016/j.cels.2018.06.001

Soles, A., Selimovic, A., Sbrocco, K., Ghannoum, F., Hamel, K., Moncada, E. L., Gilliat, S., & Cvetanovic, M. (2023). Extracellular Matrix Regulation in Physiology and in Brain Disease. In *International Journal of Molecular Sciences* (Vol. 24, Issue 8). Multidisciplinary Digital Publishing Institute (MDPI). https://doi.org/10.3390/ijms24087049

Startek, J. B., Boonen, B., Talavera, K., & Meseguer, V. (2019). TRP channels as sensors of chemically-induced changes in cell membrane mechanical properties. In *International Journal of Molecular Sciences* (Vol. 20, Issue 2). MDPI AG. https://doi.org/10.3390/ijms20020371

Steinert, P. M., Chou, Y. H., Prahlad, V., Parry, D. A. D., Marekov, L. N., Wu, K. C., Jang, S. I., & Goldman, R. D. (1999). A high molecular weight intermediate filament-associated protein in BHK- 21 cells is nestin, a type VI intermediate filament protein: Limited co- assembly in vitro to form heteropolymers with type III vimentin and type IV α-internexin. *Journal of Biological Chemistry*, *274*(14), 9881–9890. https://doi.org/10.1074/jbc.274.14.9881

Stiles, J., & Jernigan, T. L. (2010). The basics of brain development. In *Neuropsychology Review* (Vol. 20, Issue 4, pp. 327–348). https://doi.org/10.1007/s11065-010-9148-4

Stone, M. (1978). Cross-validation:a review. *Series Statistics*, *9*(1), 127–139. https://doi.org/10.1080/02331887808801414

Stukel, J. M., & Willits, R. K. (2016). Mechanotransduction of neural cells through cell-substrate interactions. In *Tissue Engineering - Part B: Reviews* (Vol. 22, Issue 3, pp. 173–182). Mary Ann Liebert Inc. https://doi.org/10.1089/ten.teb.2015.0380

Suchyna, T. M. (2017). Piezo channels and GsMTx4: Two milestones in our understanding of excitatory mechanosensitive channels and their role in pathology. In *Progress in Biophysics and Molecular Biology* (Vol. 130, pp. 244–253). Elsevier Ltd. https://doi.org/10.1016/j.pbiomolbio.2017.07.011

Sun, X., Zhao, D., Li, Y. L., Sun, Y., Lei, X. H., Zhang, J. N., Wu, M. M., Li, R. Y., Zhao, Z. F., Zhang, Z. R., & Jiang, C. L. (2013). Regulation of ASIC1 by Ca2+/calmodulin-dependent protein kinase II in human glioblastoma multiforme. *Oncology Reports*, *30*(6), 2852–2858. https://doi.org/10.3892/or.2013.2777

Sun, Y., Nadal-Vicens, M., Misono, S., Lin, M. Z., Zubiaga, A., Hua, X., Fan, G., & Greenberg, M. E. (2001). Neurogenin Promotes Neurogenesis and Inhibits Glial Differentiation by Independent Mechanisms embryonic stages behave in a manner that mimics the normal process of development (Burrows et

al., 1997; Qian et al., 2000). Progenitors from rat embryonic day 14 (E14) mains of CBP/p300 (Nakashima et al. In *Cell* (Vol. 104).

Swift, J., & Discher, D. E. (2014). The nuclear lamina is mechano-responsive to ECM elasticity in mature tissue. *Journal of Cell Science*, *127*(14), 3005–3015. https://doi.org/10.1242/jcs.149203

Swift, J., Ivanovska, I. L., Buxboim, A., Harada, T., Dingal, P. C. D. P., Pinter, J., Pajerowski, J. D., Spinler, K. R., Shin, J.-W., Tewari, M., Rehfeldt, F., Speicher, D. W., & Discher, D. E. (2013). Nuclear Lamin-A Scales with Tissue Stiffness and Enhances Matrix-Directed Differentiation. *Science*, *341*(6149), 1240104–1240104. https://doi.org/10.1126/science.1240104

Tabata, H., & Nakajima, K. (2003). *Brief Communication Multipolar Migration: The Third Mode of Radial Neuronal Migration in the Developing Cerebral Cortex*. www.jneurosci.org

Takamori, Y., Hirahara, Y., Wakabayashi, T., Mori, T., Koike, T., Kataoka, Y., Tamura, Y., Kurebayashi, S., Kurokawa, K., & Yamada, H. (2018). Differential expression of nuclear lamin subtypes in the neural cells of the adult rat cerebral cortex. *IBRO Reports*, *5*, 99–109. https://doi.org/10.1016/j.ibror.2018.11.001

Takeuchi, Y., Yamamoto, H., Fukunaga, K., Miyakawa, T., & Miyamoto, E. (2000). Identification of the isoforms of Ca2+/calmodulin-dependent protein kinase II in rat astrocytes and their subcellulur localization. *Journal of Neurochemistry*, *74*(6), 2557–2567. https://doi.org/10.1046/j.1471-4159.2000.0742557.x

Tang, W., Chen, X., Wang, X., Zhu, M., Shan, G., Wang, T., Dou, W., Wang, J., Law, J., Gong, Z., Hopyan, S., Huang, X., & Sun, Y. (2023). Indentation induces instantaneous nuclear stiffening and unfolding of nuclear envelop wrinkles. *Proceedings of the National Academy of Sciences of the United States of America*, *120*(36). https://doi.org/10.1073/pnas.2307356120

Taupin, P. (2006). Adult neural stem cells, neurogenic niches, and cellular therapy. *Stem Cell Rev*, *2*(3), 213–219. https://doi.org/SCR:2:3:213 [pii]\r10.1007/s12015-006-0049-0

Terry, B. K., & Kim, S. (2022a). The role of Hippo-YAP/TAZ signaling in brain development. In *Developmental Dynamics* (Vol. 251, Issue 10, pp. 1644–1665). John Wiley and Sons Inc. https://doi.org/10.1002/dvdy.504

Terry, B. K., & Kim, S. (2022b). The role of Hippo-YAP/TAZ signaling in brain development. In *Developmental Dynamics* (Vol. 251, Issue 10, pp. 1644–1665). John Wiley and Sons Inc. https://doi.org/10.1002/dvdy.504

Tharp, K. M., Higuchi-Sanabria, R., Timblin, G. A., Ford, B., Garzon-Coral, C., Schneider, C., Muncie, J. M., Stashko, C., Daniele, J. R., Moore, A. S., Frankino, P. A., Homentcovschi, S., Manoli, S. S., Shao, H., Richards, A. L., Chen, K. H., Hoeve, J. ten, Ku, G. M., Hellerstein, M., … Weaver, V. M. (2021). Adhesion-mediated mechanosignaling forces mitohormesis. *Cell Metabolism*, *33*(7), 1322-1341.e13. https://doi.org/10.1016/j.cmet.2021.04.017

Topol, A., Tran, N. N., & Brennand, K. J. (2015). A guide to generating and using hiPSC derived NPCs for the study of neurological diseases. *Journal of Visualized Experiments*, *96*. https://doi.org/10.3791/52495

Totaro, A., Panciera, T., & Piccolo, S. (2018). YAP/TAZ upstream signals and downstream responses. *Nature Cell Biology*, *20*(8), 888–899. https://doi.org/10.1038/s41556-018-0142-z

Turovsky, E. A., Braga, A., Yu, Y., Esteras, N., Korsak, A., Theparambil, S. M., Hadjihambi, A., Hosford, P. S., Teschemacher, A. G., Marina, N., Lythgoe, M. F., Haydon, P. G., & Gourine, A. V. (2020). Mechanosensory signaling in astrocytes. *Journal of Neuroscience*, *40*(49), 9364–9371. https://doi.org/10.1523/JNEUROSCI.1249-20.2020

Urayama, S., Semi, K., Sanosaka, T., Hori, Y., Namihira, M., Kohyama, J., Takizawa, T., & Nakashima, K. (2013). Chromatin Accessibility at a STAT3 Target Site Is Altered Prior to Astrocyte Differentiation. In *CELL STRUCTURE AND FUNCTION* (Vol. 38).

Urruticoechea, A., Smith, I. E., & Dowsett, M. (2005). Proliferation marker Ki-67 in early breast cancer. In *Journal of Clinical Oncology* (Vol. 23, Issue 28, pp. 7212–7220). https://doi.org/10.1200/JCO.2005.07.501

Uzer, G., Bas, G., Sen, B., Xie, Z., Birks, S., Olcum, M., McGrath, C., Styner, M., & Rubin, J. (2018a). Sun-mediated mechanical LINC between nucleus and cytoskeleton regulates βcatenin nuclear access. *Journal of Biomechanics*, *74*, 32–40. https://doi.org/10.1016/j.jbiomech.2018.04.013

Uzer, G., Bas, G., Sen, B., Xie, Z., Birks, S., Olcum, M., McGrath, C., Styner, M., & Rubin, J. (2018b). Sun-mediated mechanical LINC between nucleus and cytoskeleton regulates βcatenin nuclear access. *Journal of Biomechanics*, *74*, 32–40. https://doi.org/10.1016/j.jbiomech.2018.04.013

Uzquiano, A., Gladwyn-Ng, I., Nguyen, L., Reiner, O., Götz, M., Matsuzaki, F., & Francis, F. (2018). Cortical progenitor biology: key features mediating proliferation versus differentiation. In *Journal of Neurochemistry* (Vol. 146, Issue 5, pp. 500–525). Blackwell Publishing Ltd. https://doi.org/10.1111/jnc.14338

Vahabikashi, A., Adam, S. A., Medalia, O., & Goldman, R. D. (2022). Nuclear lamins: Structure and function in mechanobiology. In *APL Bioengineering* (Vol. 6, Issue 1). American Institute of Physics Inc. https://doi.org/10.1063/5.0082656

Vahabikashi, A., Sivagurunathan, S., Ann Sadsad Nicdao, F., Long Han, Y., Young Park, C., Kittisopikul, M., Wong, X., Tran, J. R., Gundersen, G. G., Reddy, K. L., Gant Luxton, G. W., Guo, M., Fredberg, J. J., Zheng, Y., Adam, S. A., Goldman, R. D., Yale Goldman, M. E., & Article, R. (2023). *Nuclear lamin isoforms differentially contribute to LINC complex-dependent nucleocytoskeletal coupling and whole-cell mechanics*. https://doi.org/10.1073/pnas

van Asperen, J. V., Robe, P. A. J. T., & Hol, E. M. (2022). GFAP Alternative Splicing and the Relevance for Disease – A Focus on Diffuse Gliomas. In *ASN Neuro* (Vol. 14). SAGE Publications Inc. https://doi.org/10.1177/17590914221102065

van Tienen, F. H. J., Lindsey, P. J., Kamps, M. A. F., Krapels, I. P., Ramaekers, F. C. S., Brunner, H. G., van den Wijngaard, A., & Broers, J. L. V. (2019). Assessment of fibroblast nuclear morphology aids interpretation of LMNA variants. *European Journal of Human Genetics*, *27*(3), 389–399. https://doi.org/10.1038/s41431-018-0294-0

Vergnes, L., Terfy, P., Bergo, M. O., Young, S. G., & Reue, K. (2004). *Lamin B1 is required for mouse development and nuclear integrity*. www.pnas.orgcgidoi10.1073pnas.0401424101

Verkhratsky, A., & Nedergaard, M. (2018). PHYSIOLOGY OF ASTROGLIA. *Physiology of Astroglia. Physiol Rev*, *98*, 239–389. https://doi.org/10.1152/physrev.00042.2016.-Astro

Verkhratsky, A., Reyes, R. C., & Parpura, V. (2014). TRP channels coordinate ion signalling in astroglia. *Reviews of Physiology, Biochemistry and Pharmacology*, *166*. https://doi.org/10.1007/112_2013_15

Vicente-Gutierrez, C., Bonora, N., Bobo-Jimenez, V., Jimenez-Blasco, D., Lopez-Fabuel, I., Fernandez, E., Josephine, C., Bonvento, G., Enriquez, J. A., Almeida, A., & Bolaños, J. P. (2019). Astrocytic mitochondrial ROS modulate brain metabolism and mouse behaviour. In *Nature Metabolism* (Vol. 1, Issue 2, pp. 201–211). Nature Research. https://doi.org/10.1038/s42255-018-0031-6

Wagh, K., Ishikawa, M., Garcia, D. A., Stavreva, D. A., Upadhyaya, A., & Hager, G. L. (2021). Mechanical Regulation of Transcription: Recent Advances. In *Trends in Cell Biology* (Vol. 31, Issue 6, pp. 457–472). Elsevier Ltd. https://doi.org/10.1016/j.tcb.2021.02.008

Wang, L., Xia, J., Li, J., Hagemann, T. L., Jones, J. R., Fraenkel, E., Weitz, D. A., Zhang, S. C., Messing, A., & Feany, M. B. (2018). Tissue and cellular rigidity and mechanosensitive signaling activation in Alexander disease. *Nature Communications*, *9*(1). https://doi.org/10.1038/s41467-018-04269-7

Wang, M., Ivanovska, I., Vashisth, M., & Discher, D. E. (2022). Nuclear mechanoprotection: From tissue atlases as blueprints to distinctive regulation of nuclear lamins. In *APL Bioengineering* (Vol. 6, Issue 2). American Institute of Physics Inc. https://doi.org/10.1063/5.0080392

Weissman, T. A., Riquelme, P. A., Ivic, L., Flint, A. C., & Kriegstein, A. R. (2004a). Calcium waves propagate through radial glial cells and modulate proliferation in the developing neocortex. *Neuron*, *43*(5), 647–661. https://doi.org/10.1016/j.neuron.2004.08.015

Weissman, T. A., Riquelme, P. A., Ivic, L., Flint, A. C., & Kriegstein, A. R. (2004b). Calcium waves propagate through radial glial cells and modulate proliferation in the developing neocortex. *Neuron*, *43*(5), 647–661. https://doi.org/10.1016/j.neuron.2004.08.015

Wen, J., Hu, Q., Li, M., Wang, S., Zhang, L., Chen, Y., & Li, L. (2008). *Pax6 directly modulate Sox2 expression in the neural progenitor cells*. http://journals.lww.com/neuroreport

White, S. M., Avantaggiati, M. L., Nemazanyy, I., Di Poto, C., Yang, Y., Pende, M., Gibney, G. T., Ressom, H. W., Field, J., Atkins, M. B., & Yi, C. (2019). YAP/TAZ Inhibition Induces Metabolic and Signaling Rewiring Resulting in Targetable Vulnerabilities in NF2-Deficient Tumor Cells. *Developmental Cell*, *49*(3), 425-443.e9. https://doi.org/10.1016/j.devcel.2019.04.014

Wichmann, L., & Althaus, M. (2020). Evolution of epithelial sodium channels: Current concepts and hypotheses. In *American Journal of Physiology - Regulatory Integrative and Comparative Physiology* (Vol. 319, Issue 4, pp. R387–R400). American Physiological Society. https://doi.org/10.1152/ajpregu.00144.2020

Wintner, O., Hirsch-Attas, N., Schlossberg, M., Brofman, F., Friedman, R., Kupervaser, M., Kitsberg, D., & Buxboim, A. (2020). A Unified Linear Viscoelastic Model of the Cell Nucleus Defines the Mechanical Contributions of Lamins and Chromatin. *Advanced Science*, *7*(8). https://doi.org/10.1002/advs.201901222

Wolf, F. A., Angerer, P., & Theis, F. J. (2018). SCANPY: Large-scale single-cell gene expression data analysis. *Genome Biology*, *19*(1). https://doi.org/10.1186/s13059-017-1382-0

Wolock, S. L., Lopez, R., & Klein, A. M. (2019). Scrublet: Computational Identification of Cell Doublets in Single-Cell Transcriptomic Data. *Cell Systems*, *8*(4), 281-291.e9. https://doi.org/10.1016/j.cels.2018.11.005

Wong, M. H., Samal, A. B., Lee, M., Vlach, J., Novikov, N., Niedziela-Majka, A., Feng, J. Y., Koltun, D. O., Brendza, K. M., Kwon, H. J., Schultz, B. E., Sakowicz, R., Saad, J. S., & Papalia, G. A. (2019). The KN-93 Molecule Inhibits Calcium/Calmodulin-Dependent Protein Kinase II (CaMKII) Activity by Binding to Ca2+/CaM. *Journal of Molecular Biology*, *431*(7), 1440–1459. https://doi.org/10.1016/j.jmb.2019.02.001

Wrobel, C. N., Mutch, C. A., Swaminathan, S., Taketo, M. M., & Chenn, A. (2007). Persistent expression of stabilized β-catenin delays maturation of radial glial cells into intermediate progenitors. *Developmental Biology*, *309*(2), 285–297. https://doi.org/10.1016/j.ydbio.2007.07.013

Yalcin, A., Telang, S., Clem, B., & Chesney, J. (2009). Regulation of glucose metabolism by 6-phosphofructo-2-kinase/fructose-2,6-bisphosphatases in cancer. In *Experimental and Molecular Pathology* (Vol. 86, Issue 3, pp. 174–179). https://doi.org/10.1016/j.yexmp.2009.01.003

Yang, J. L., Fan, H., Fu, F. F., Guo, B. L., Huang, Y., Sun, L., Wang, W. T., Xing, J. L., Hu, X. T., Ding, Y. Q., Zhang, K., Hu, Y. Z., & Wang, Y. Z. (2023). Transient neurogenesis in ischemic cortex from Sox2 + astrocytes. *Neural Regeneration Research*, *18*(7), 1521–1526. https://doi.org/10.4103/1673-5374.357910

Yano, S., Fukunaga, K., Ushio, Y., & Miyamoto, E. (1994). Activation of Ca2+/calmodulin-dependent protein kinase II and phosphorylation of intermediate filament proteins by stimulation of glutamate receptors in cultured rat cortical astrocytes. *Journal of Biological Chemistry*, *269*(7), 5428–5439. https://doi.org/10.1016/s0021-9258(17)37704-9

Yokota, Y., Eom, T. Y., Stanco, A., Kim, W. Y., Rao, S., Snider, W. D., & Anton, E. S. (2010). Cdc42 and Gsk3 modulate the dynamics of radial glial growth, inter-radial glial interactions and polarity in the developing cerebral cortex. *Development*, *137*(23), 4101–4110. https://doi.org/10.1242/dev.048637

Yuste, R., Hawrylycz, M., Aalling, N., Aguilar-Valles, A., Arendt, D., Arnedillo, R. A., Ascoli, G. A., Bielza, C., Bokharaie, V., Bergmann, T. B., Bystron, I., Capogna, M., Chang, Y., Clemens, A., de Kock, C. P. J., DeFelipe, J., Dos Santos, S. E., Dunville, K., Feldmeyer, D., … Lein, E. (2020). A community-based transcriptomics classification and nomenclature of neocortical cell types. In *Nature Neuroscience* (Vol. 23, Issue 12, pp. 1456–1468). Nature Research. https://doi.org/10.1038/s41593-020-0685-8

Zamboni, M., Llorens-Bobadilla, E., Magnusson, J. P., & Frisén, J. (2020). A Widespread Neurogenic Potential of Neocortical Astrocytes Is Induced by Injury. *Cell Stem Cell*, *27*(4), 605-617.e5. https://doi.org/10.1016/j.stem.2020.07.006

Zhang, M., Liu, Q., Meng, H., Duan, H., Liu, X., Wu, J., Gao, F., Wang, S., Tan, R., & Yuan, J. (2024). Ischemia-reperfusion injury: molecular mechanisms and therapeutic targets. In *Signal Transduction and Targeted Therapy* (Vol. 9, Issue 1). Springer Nature. https://doi.org/10.1038/s41392-023-01688-x

Zhang, Y., Liu, G., Guo, T., Liang, X. G., Du, H., Yang, L., Bhaduri, A., Li, X., Xu, Z., Zhang, Z., Li, Z., He, M., Tsyporin, J., Kriegstein, A. R., Rubenstein, J. L., Yang, Z., & Chen, B. (2020). Cortical Neural Stem Cell Lineage Progression Is Regulated by Extrinsic Signaling Molecule Sonic Hedgehog. *Cell Reports*, *30*(13), 4490-4504.e4. https://doi.org/10.1016/j.celrep.2020.03.027

Zhao, L., & Diaz Brinton, R. (2003). *Vasopressin-Induced Cytoplasmic and Nuclear Calcium Signaling in Embryonic Cortical Astrocytes: Dynamics of Calcium and Calcium-Dependent Kinase Translocation vasopressin receptor; mitogen-activated protein kinase; protein kinase C; Ca 2 /calmodulin-dependent protein kinase II; cAMP response element-binding protein; cortical astrocytes*.

Zheng, X., Boyer, L., Jin, M., Mertens, J., Kim, Y., Ma, L., Hamm, M., Gage, F. H., & Hunter, T. (2016). *Metabolic reprogramming during neuronal differentiation from aerobic glycolysis to neuronal oxidative phosphorylation*. https://doi.org/10.7554/eLife.13374.001

Zhuang, W., & Yan, Z. (2021). The S2–S3 Loop of Kv7.4 Channels Is Essential for Calmodulin Regulation of Channel Activation. *Frontiers in Physiology*, *11*. https://doi.org/10.3389/fphys.2020.604134

Zilles, K., Palomero-Gallagher, N., & Amunts, K. (2013). Development of cortical folding during evolution and ontogeny. In *Trends in Neurosciences* (Vol. 36, Issue 5, pp. 275–284). https://doi.org/10.1016/j.tins.2013.01.006

9. SUPPLEMENTARY FIGURES

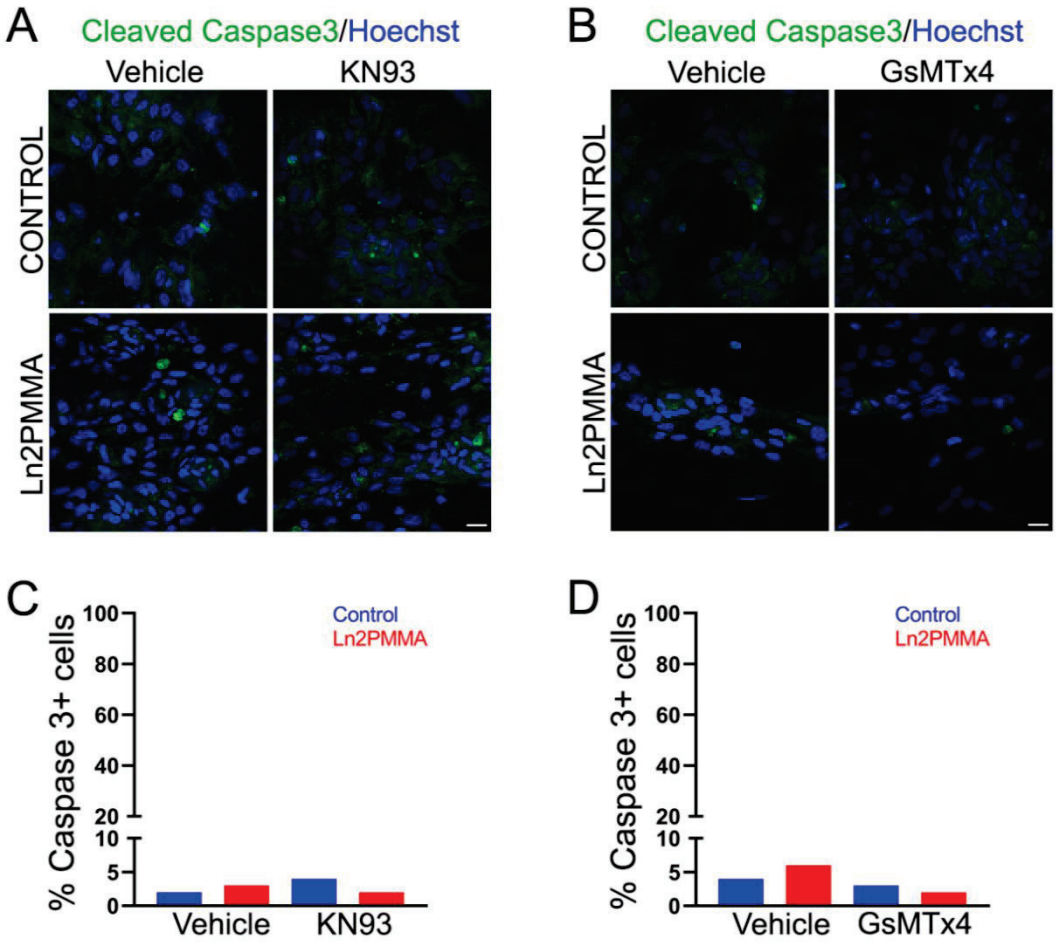


Figure S1 KN93 and GsMTx4 inhibitors did not induce additional cell apoptosis. (A, B) Confocal pictures of glial cells grown in controls and ln2PMMA substrates and immunostained for cleaved caspase 3 marker, and Hoechst 33342 for nuclei (blue); treated with (A) vehicle (DMSO, 5µM) and CaMKII inhibitor KN93 (5µM), or (B) vehicle (PBS 1.22µM) and stretch gating channels inhibitor GsMTx4 (1.22µM). (C, D) Plots showing the percentage of apoptotic cells expressing cleaved caspase3 in control and ln2PMMA substrates treated with (D) vehicle and KN93 (E) vehicle and GsMTx4. Chi-square test to observe significant differences.

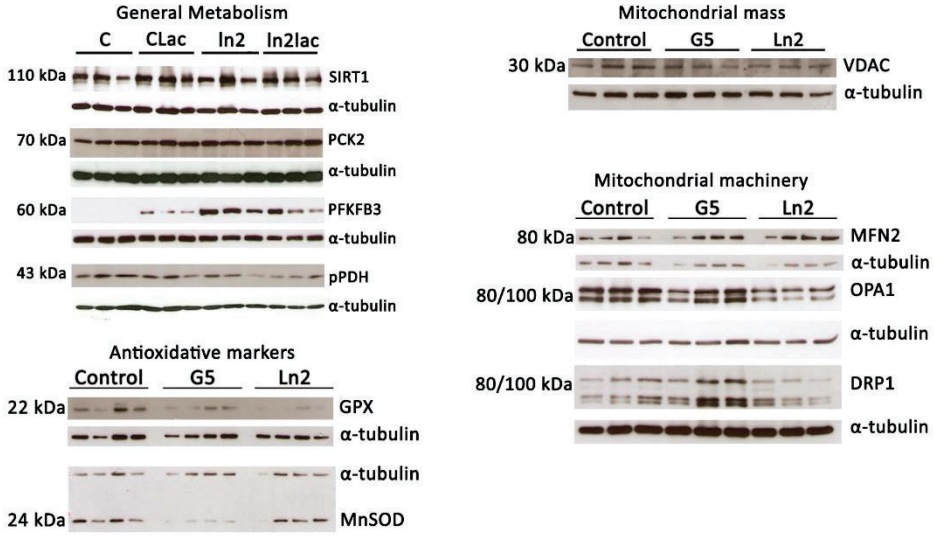


Figure S2 Complete WB membranes presented in section 4.2. We cut membranes to present results of protein expression of glial cells grown on control and ln2PMMA substrates. Lactate condition, which is not discussed in the present work, consisted in glial cultures grown for 3DIV with 4mM of l-lactate acid. G5 condition is neither considered in this thesis, and consisted in glial cells with G5 supplement, which is a cocktail containing EGF, FGF2, vitamins and hormones that chemically induces astrocytes to adopt an immature and proliferative state.

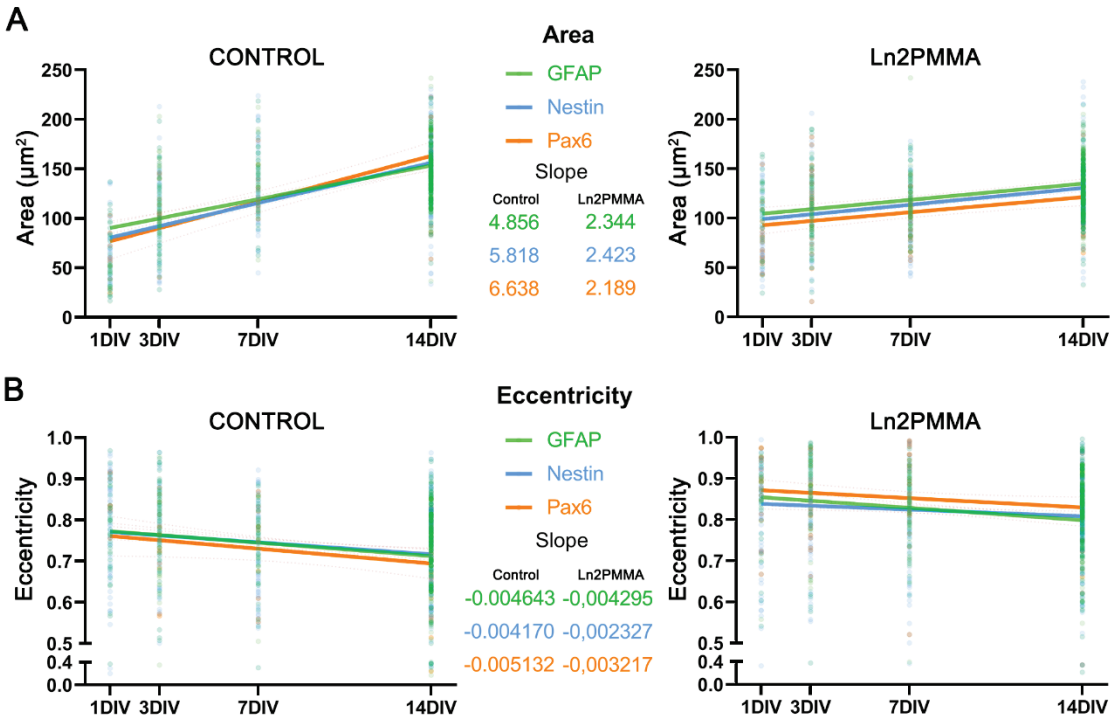


Figure S3 Nuclear area follows cell type-specific dynamics over time in control and ln2PMMA. (A) Graphs showing linear regressions for nuclear area for cells expressing GFAP, nestin and Pax6 at different time points (1-14DIV). Control slopes: p<0.001; ln2PMMA slopes: p=ns, intercepts: p<0.001. Graphs showing linear regressions for eccentricity. Control slopes: p=ns, intercepts: p=ns; ln2PMMA slopes: p=ns, intercepts: p<0.05. ANCOVA test.

Table S1 Area and Eccentricity of glial cells in control and ln2PMMA. Paired t-test between substrates for the same cell type. ** p<0.001.

	Marker	N	C (+)	Ln2 (+)
AREA	Sox2	898	83 ± 39,4	86 ± 31,8
	Pax6	1050	88 ± 30,8	88 ± 25,4
	Gsx2	236	62 ± 17,3	56 ± 16,7
	GFAP	851	95 ± 34,9	73 ± 25,2 **
	Nestin	1777	105 ± 44,9	88 ± 29,6 **
	NG2	603	59 ± 23,8	48 ± 28,1
ECCENTRICITY	Sox2	898	0,75 ± 0,13	0,84 ± 0,12 **
	Pax6	1050	0,78 ± 0,12	0,88 ± 0,10 **
	Gsx2	236	0,65 ± 0,16	0,59 ± 0,15
	GFAP	851	0,76 ± 0,12	0,85 ± 0,12 **
	Nestin	1777	0,76 ± 0,13	0,86 ± 0,10 **
	NG2	603	0,76 ± 0,14	0,82 ± 0,11

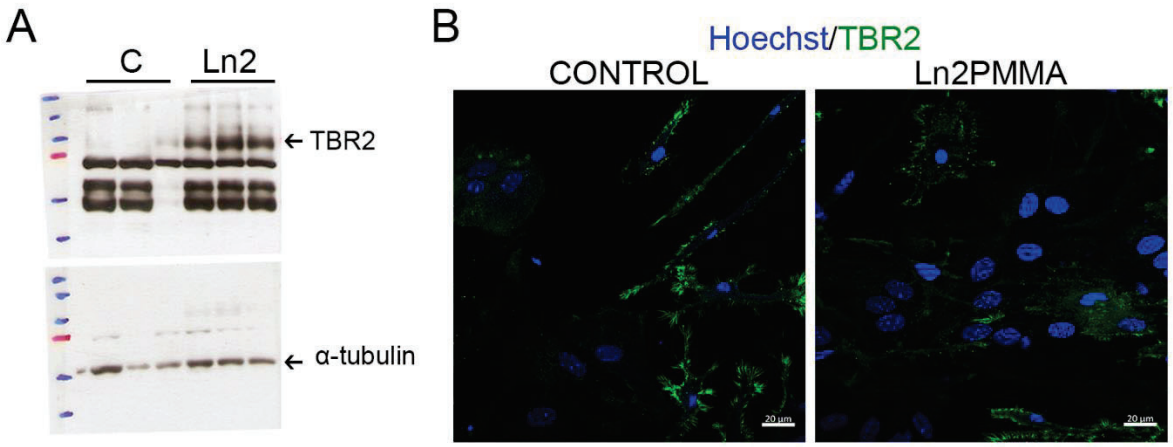


Figure S 4 **TBR2 antibody is not suitable for ICC**. Glial cells grown on control and ln2PMMA substrates for 3DIV. Nuclei counterstained with Hoechst 33342. (A) Unexpected bands in WB and (B) unspecific binding in immunocytochemistry assays.

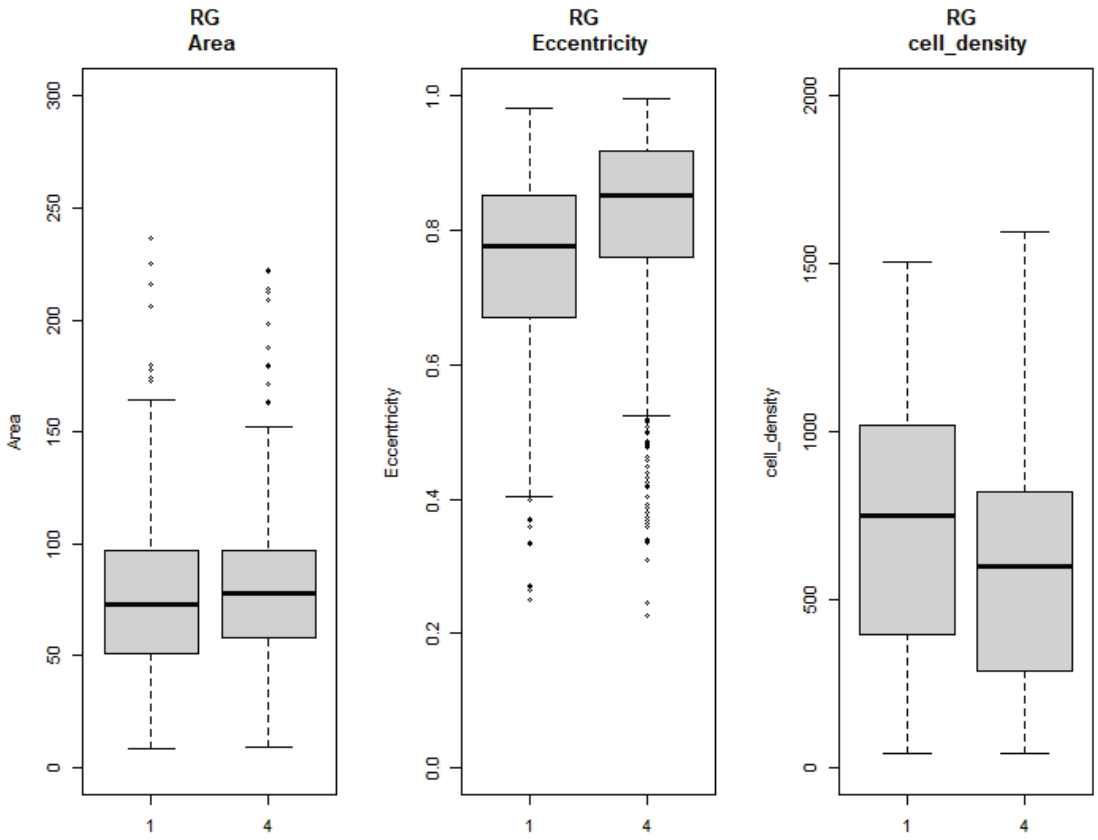


Figure S5 Descriptive of data used for fitting. Box plots of area, eccentricity, and cell density of control (1) and ln2PMMA (4). **Figure S1** area and eccentricity was determined by quantiles: min-q25, q25-q50, q50-q75, and q75-max . Cell density of **Fig. R-4.1-5** was based on quantiles ranges: min-q25, q-25-q75 and q75-max

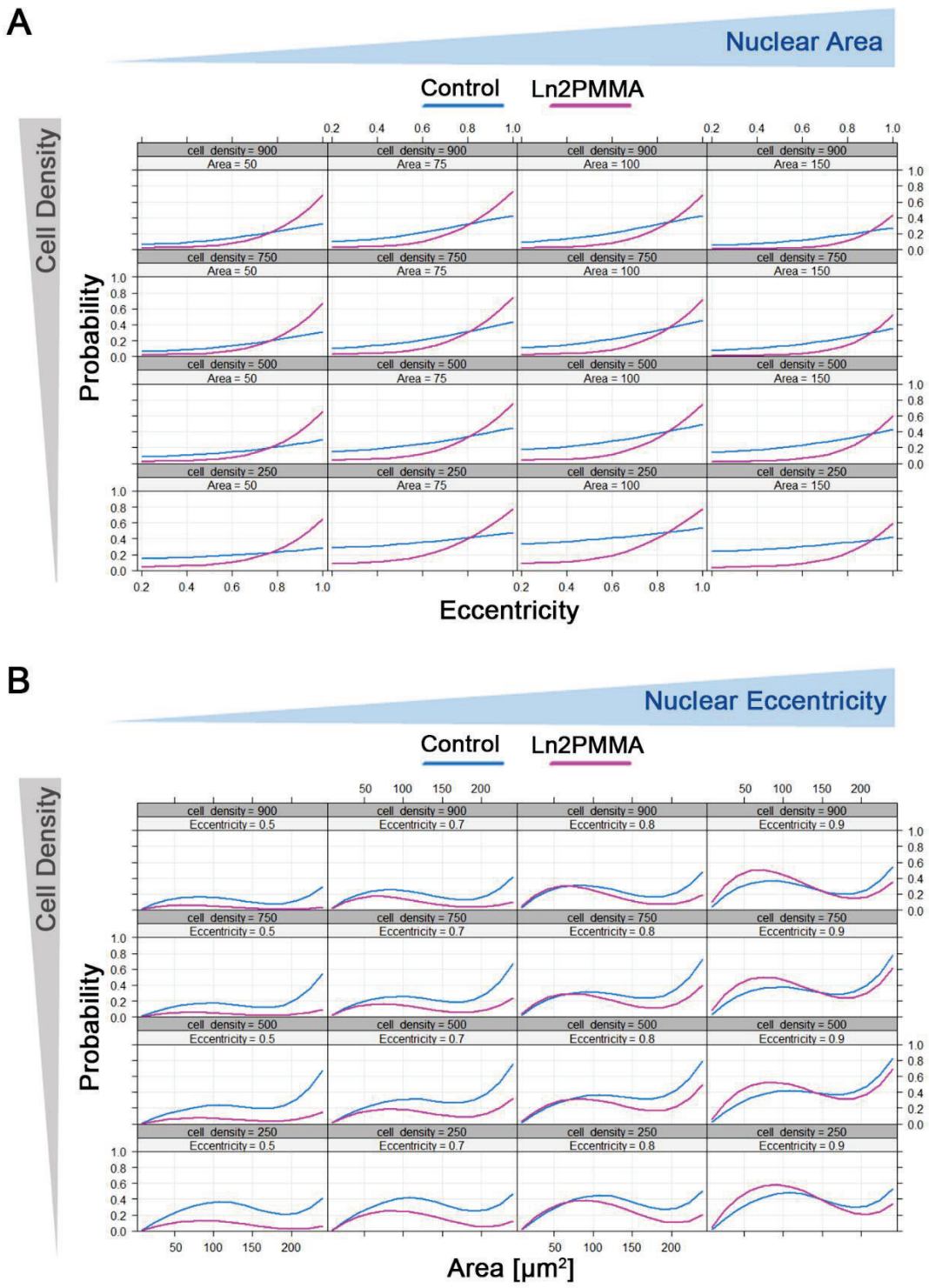


Figure S6 Model terms behavior in control and ln2PMMA substrates at different cell density scenarios. In A and B multi-panels, cell density decreased from up to down, points at 900, 750, 500 and 250 cells/mm^2. (A) Linear plots showing RG probability in function of eccentricity. From left to right, individual plots for nuclei with areas of 50, 75, 100 and 150μm^2 (B) Linear plots showing RG probability in function of area. From left to right, individual plots for nuclei with eccentricities of 0.5, 0.7, 0.8 and 0.9. Control substrate in blue and ln2PMMA substrate in magenta. Cell density ranges were established based on quantiles, trying to match control and ln2PMMA data (min-q25, q25-q50, q50-q75, and q75-max).

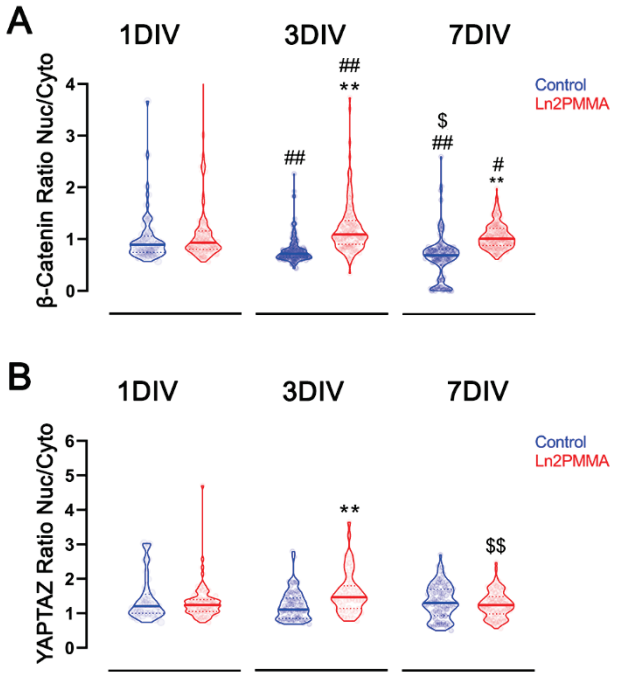


Figure S7 Different dynamisms of Nuclei and Cytoplasm β-catenin but not YAP/TAZ ratio of astrocytes dedifferentiation over time. Glial cells cultured in control and ln2PMMA for 1DIV (N=487), 3DIV (N=553), and 7DIV (N=532). Two different biological samples. (A) Violin plots of β-catenin ratio at 1, 3, and 7DIV. Data points correspond to individual cells. (B) Violin plots of YAPTAZ ratio at 1, 3, and 7DIV. Data points correspond to individual cells. Mann Whitney to explore differences between control and ln2PMMA at each time point. ** p<0.01. Kruskal Wallis to determine differences between time points within the same substrate, respect to 1DIV ## p<0.01; respect to 3DIV $ p<0.05, $$ p>0.01.

Multiple comparison of AREA

Phys	(I) Inhibitor	(J) Inhibitor	Diferencia de medias (I-J)	Error estándar	Sig.[b]	95% de intervalo de confianza para diferencia[b] Límite inferior	Límite superior
C_	DMSO	GsMTx-4_5	,578	2,209	1,000	-5,254	6,410
		KN93	8,056*	2,192	,001	2,268	13,843
		PBS	5,154	2,542	,256	-1,558	11,866
	GsMTx-4_5	DMSO	-,578	2,209	1,000	-6,410	5,254
		KN93	7,478*	2,218	,005	1,623	13,333
		PBS	4,576	2,564	,447	-2,194	11,346
	KN93	DMSO	-8,056*	2,192	,001	-13,843	-2,268
		GsMTx-4_5	-7,478*	2,218	,005	-13,333	-1,623
		PBS	-2,902	2,550	1,000	-9,634	3,830
	PBS	DMSO	-5,154	2,542	,256	-11,866	1,558
		GsMTx-4_5	-4,576	2,564	,447	-11,346	2,194
		KN93	2,902	2,550	1,000	-3,830	9,634
Ln2_	DMSO	GsMTx-4_5	-6,574*	1,604	,000	-10,810	-2,338
		KN93	10,442*	1,515	,000	6,441	14,443
		PBS	3,738	1,772	,210	-,941	8,417
	GsMTx-4_5	DMSO	6,574*	1,604	,000	2,338	10,810
		KN93	17,016*	1,571	,000	12,868	21,164
		PBS	10,312*	1,820	,000	5,506	15,117
	KN93	DMSO	-10,442*	1,515	,000	-14,443	-6,441
		GsMTx-4_5	-17,016*	1,571	,000	-21,164	-12,868
		PBS	-6,704*	1,742	,001	-11,304	-2,104
	PBS	DMSO	-3,738	1,772	,210	-8,417	,941
		GsMTx-4_5	-10,312*	1,820	,000	-15,117	-5,506
		KN93	6,704*	1,742	,001	2,104	11,304

Se basa en medias marginales estimadas

*. La diferencia de medias es significativa en el nivel ,05.

b. Ajuste para varias comparaciones: Bonferroni.

Multiple comparison of ECCENTRICITY

Phys	(I) Inhibitor	(J) Inhibitor	Diferencia de medias (I-J)	Error estándar	Sig.[a]	95% de intervalo de confianza para diferencia[a] Límite inferior	Límite superior
C_	DMSO	GsMTx-4_5	-,009	,007	1,000	-,029	,010
		KN93	-,015	,007	,245	-,034	,004
		PBS	,002	,008	1,000	-,020	,025
	GsMTx-4_5	DMSO	,009	,007	1,000	-,010	,029
		KN93	-,005	,007	1,000	-,025	,014
		PBS	,012	,008	,951	-,010	,034
	KN93	DMSO	,015	,007	,245	-,004	,034
		GsMTx-4_5	,005	,007	1,000	-,014	,025
		PBS	,017	,008	,240	-,005	,040
	PBS	DMSO	-,002	,008	1,000	-,025	,020
		GsMTx-4_5	-,012	,008	,951	-,034	,010
		KN93	-,017	,008	,240	-,040	,005
Ln2_	DMSO	GsMTx-4_5	-,016	,007	,182	-,035	,003
		KN93	,008	,007	1,000	-,011	,026
		PBS	-,008	,008	1,000	-,029	,014
	GsMTx-4_5	DMSO	,016	,007	,182	-,003	,035
		KN93	,024*	,007	,006	,005	,043
		PBS	,008	,008	1,000	-,014	,030
	KN93	DMSO	-,008	,007	1,000	-,026	,011
		GsMTx-4_5	-,024*	,007	,006	-,043	-,005
		PBS	-,015	,008	,316	-,037	,006
	PBS	DMSO	,008	,008	1,000	-,014	,029
		GsMTx-4_5	-,008	,008	1,000	-,030	,014
		KN93	,015	,008	,316	-,006	,037

Se basa en medias marginales estimadas

*. La diferencia de medias es significativa en el nivel ,05.

a. Ajuste para varias comparaciones: Bonferroni.

Figure S8 Multiple comparison results of AREA and ECCENTRICITY of nuclei treated with GsMTx4 and KN93 inhibitors. Green squares highlight vehicles comparisons in control or ln2PMMA substrates. Blue squares highlight comparisons between vehicles and treatments within each substrate.

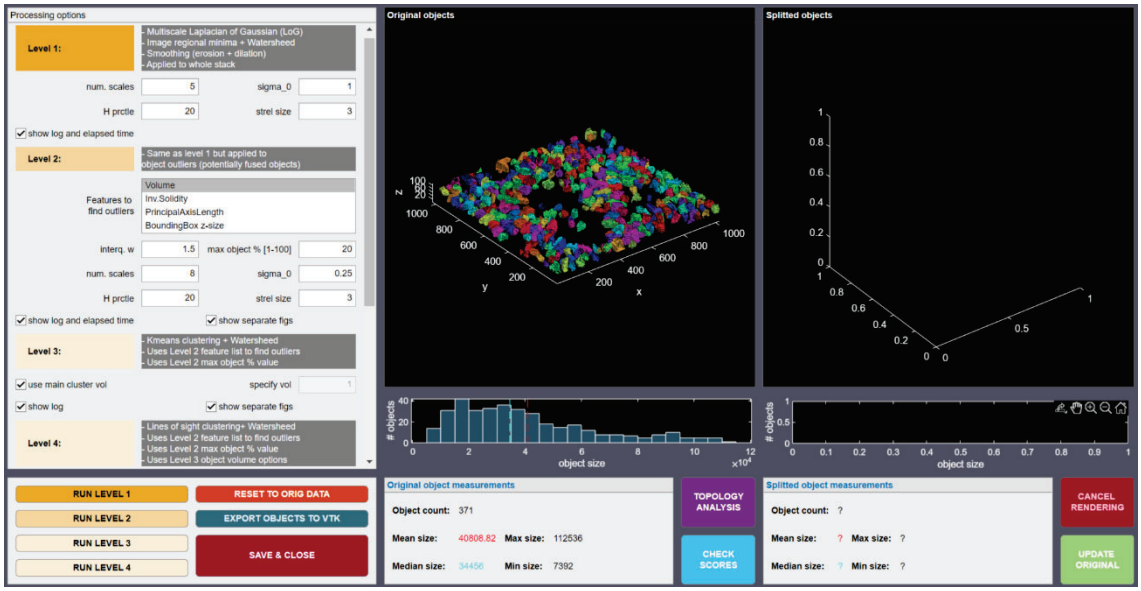


Figure S 9 Advanced 3D segmentation procedure.

10. ANNEX

Ion channels	Gene	Gene Symbol	Present	E13	E14	E15	E16	E17	E18	P1	P4	Mean expression	Var	Difference E13-E14_P1-P4
ASIC1 (Acid Sensing Ion Channel Subunit 1)	ASIC1	Asic1	YES	1,37E-03	1,35E-02	4,80E-03	4,79E-03	0,00E+00	1,62E-02	1,29E-02	1,07E-02	8,03E-03	3,68E-05	8,67E-03
ASIC2 (Acid Sensing Ion Channel Subunit 2)	ASIC2	Asic2	YES	6,36E-03	1,79E-03	2,03E-03	1,56E-03	0,00E+00	1,00E-02	1,09E-02	1,15E-02	5,52E-03	2,25E-05	1,42E-02
ASIC3 (Acid Sensing Ion Channel Subunit 3)	ASIC3	Asic3	YES	0,00E+00	0,00E+00	0,00E+00	0,00E+00	0,00E+00	0,00E+00	0,00E+00	0,00E+00	0,00E+00	0,00E+00	0,00E+00
ASIC4	ASIC4	Asic4	YES	0,00E+00	0,00E+00	0,00E+00	1,09E-03	0,00E+00	2,72E-03	1,24E-03	0,00E+00	6,31E-04	9,90E-07	1,24E-03
ASIC5	ASIC5	Asic5	YES	0,00E+00	0,00E+00	0,00E+00	0,00E+00	0,00E+00	0,00E+00	0,00E+00	0,00E+00	0,00E+00	0,00E+00	0,00E+00
ASIC6	ASIC6	Asic6	NO											
SERCA1	ATP2A1	Atp2a1	YES	3,87E-04	1,98E-03	0,00E+00	0,00E+00	0,00E+00	0,00E+00	0,00E+00	0,00E+00	2,95E-04	4,80E-07	-2,36E-03
ATP2A2 (ATPase Sarcoplasmic/Endoplasmic Reticulum Ca2+ Transporting 2) SERCA2	ATP2A2	Atp2a2	YES	2,13E-01	3,50E-01	2,17E-01	3,25E-01	1,84E-01	3,21E-01	5,10E-01	3,07E-01	3,03E-01	1,08E-02	2,53E-01
SERCA3	ATP2A3	Atp2a3	YES	0,00E+00	0,00E+00	0,00E+00	1,67E-03	0,00E+00	0,00E+00	0,00E+00	0,00E+00	2,08E-04	3,47E-07	0,00E+00
ATP2B1 (ATPase Plasma Membrane Ca2+ Transporting 1) PMCA1	ATP2B1	Atp2b1	YES	2,92E-01	3,36E-01	2,73E-01	3,60E-01	2,47E-01	3,75E-01	3,06E-01	1,73E-01	2,95E-01	4,31E-03	-1,49E-01
ATP2B2 (ATPase Plasma Membrane Ca2+ Transporting 2) PMCA2	ATP2B2	Atp2b2	YES	2,93E-03	4,35E-03	4,20E-03	1,41E-02	2,53E-02	5,48E-02	1,71E-02	1,39E-02	1,71E-02	2,91E-04	2,37E-02
PMCA3	ATP2B3	Atp2b3	YES	0,00E+00	0,00E+00	0,00E+00	1,66E-03	0,00E+00	0,00E+00	0,00E+00	0,00E+00	2,08E-04	3,46E-07	0,00E+00
ATP2B4 (ATPase Plasma Membrane Ca2+ Transporting 4) PMCA4	ATP2B4	Atp2b4	YES	3,40E-03	8,35E-03	7,99E-03	3,06E-02	3,80E-02	8,86E-02	8,29E-02	9,18E-02	4,40E-02	1,46E-03	1,63E-01
ATP2C1 (ATPase Secretory Pathway Ca2+ Transporting 1) SPCA1	ATP2C1	Atp2c1	YES	1,37E-01	1,45E-01	1,42E-01	2,12E-01	1,02E-01	1,49E-01	2,78E-01	1,88E-01	1,69E-01	3,06E-03	1,84E-01
CACNA1A (Calcium Voltage-Gated Channel Subunit Alpha1 A) Cav2.1	CACNA1A	Cacna1a	YES	7,96E-02	1,03E-01	1,20E-01	2,83E-02	1,18E-02	3,27E-02	2,14E-02	2,12E-02	5,22E-02	1,77E-03	-1,40E-01

CACNA1B (Calcium Voltage-Gated Channel Subunit Alpha1 B) Cav2.2	CACNA1B	Cacna1b	YES	1,21E-03	6,55E-03	1,91E-03	4,77E-03	6,76E-03	2,24E-02	2,88E-03	6,55E-03	6,63E-03	4,55E-05	1,68E-03
Cav1.2	CACNA1C	Cacna1c	YES	2,84E-03	3,47E-03	3,93E-03	7,34E-03	0,00E+00	3,79E-03	8,36E-03	1,34E-02	5,39E-03	1,72E-05	1,54E-02
CACNA1D (Calcium Voltage-Gated Channel Subunit Alpha1 D) Cav1.3	CACNA1D	Cacna1d	YES	1,26E-03	7,57E-03	5,30E-04	1,76E-03	1,23E-02	4,29E-03	1,27E-02	1,85E-02	7,37E-03	4,32E-05	2,24E-02
CACNA1E (Calcium Voltage-Gated Channel Subunit Alpha1 E) Cav2.3	CACNA1E	Cacna1e	YES	9,35E-04	6,96E-03	2,87E-03	9,03E-03	5,21E-03	2,93E-02	1,28E-02	2,49E-02	1,15E-02	1,07E-04	2,97E-02
Cav1.4	CACNA1F	Cacna1f	YES	0,00E+00	0,00E+00	0,00E+00	0,00E+00	0,00E+00	0,00E+00	0,00E+00	0,00E+00	0,00E+00	0,00E+00	0,00E+00
Cav3.1	CACNA1G	Cacna1g	YES	4,03E-03	3,91E-03	3,55E-03	1,07E-03	5,20E-03	9,42E-03	4,38E-03	6,14E-03	4,71E-03	5,76E-06	2,58E-03
Cav3.2	CACNA1H	Cacna1h	YES	3,64E-03	9,12E-03	7,68E-03	5,67E-03	1,54E-02	1,91E-02	1,46E-02	2,60E-02	1,27E-02	5,70E-05	2,78E-02
Cav3.3	CACNA1I	Cacna1i	YES	0,00E+00	0,00E+00	6,36E-04	0,00E+00	0,00E+00	2,27E-03	0,00E+00	2,11E-02	3,01E-03	5,43E-05	2,11E-02
Cav1.1	CACNA1S	Cacna1s	YES	0,00E+00	0,00E+00	0,00E+00	0,00E+00	0,00E+00	0,00E+00	1,92E-03	6,89E-03	1,10E-03	5,92E-06	8,81E-03
CASR	CASR	Casr	YES	0,00E+00	0,00E+00	0,00E+00	0,00E+00	0,00E+00	0,00E+00	0,00E+00	0,00E+00	0,00E+00	0,00E+00	0,00E+00
nAChR Ï±3	CHRNA3	Chrna3	YES	1,20E-03	0,00E+00	3,38E-04	1,34E-03	0,00E+00	2,01E-03	1,22E-02	0,00E+00	2,14E-03	1,71E-05	1,10E-02
nAChR Ï±4	CHRNA4	Chrna4	YES	0,00E+00	0,00E+00	0,00E+00	0,00E+00	3,46E-03	3,85E-03	3,26E-03	0,00E+00	1,32E-03	3,35E-06	3,26E-03
nAChR Î²2	CHRNB2	Chrnb2	NO											
FAIM2 (Fas Apoptotic Inhibitory Molecule 2). TMBIM1 paralog	Faim2	Faim2	YES	7,16E-04	1,83E-03	1,55E-03	3,21E-03	2,12E-02	3,49E-02	9,22E-02	9,22E-02	3,10E-02	1,57E-03	1,82E-01
GHITM (Growth Hormone Inducible Transmembrane Protein). TMBIM6 paralog	Ghitm	Ghitm	YES	4,70E-01	3,22E-01	3,74E-01	3,78E-01	3,06E-01	4,12E-01	5,71E-01	9,68E-01	4,75E-01	4,68E-02	7,47E-01
GJA1 (Gap Junction Protein Alpha 1) CX43	GJA1	Gja1	YES	1,98E-01	1,20E-01	1,09E-01	1,55E-01	6,66E-02	1,64E-01	3,65E-01	8,25E-01	2,51E-01	6,18E-02	8,71E-01
CX37	GJA4	Gja4	YES	2,42E-04	0,00E+00	4,42E-04	0,00E+00	0,00E+00	0,00E+00	3,57E-03	0,00E+00	5,31E-04	1,53E-06	3,32E-03

GJC1 (Gap Junction Protein Gamma 1) CX45	GJC1	Gjc1	YES	2,88E-01	3,90E-01	2,85E-01	1,92E-01	1,26E-01	1,79E-01	8,81E-02	5,15E-02	2,00E-01	1,31E-02	-5,39E-01
CX36	GJD2	Gjd2	YES	8,14E-04	0,00E+00	0,00E+00	2,54E-03	4,48E-03	0,00E+00	0,00E+00	0,00E+00	9,80E-04	2,79E-06	-8,14E-04
GRIA2 (Glutamate Ionotropic Receptor AMPA Type Subunit 2) GluA2	GRIA2	Gria2	YES	2,38E-01	4,77E-01	3,01E-01	5,37E-01	3,65E-01	4,83E-01	5,12E-01	3,46E-01	4,07E-01	1,20E-02	1,43E-01
GRIK5 (Glutamate Ionotropic Receptor Kainate Type Subunit 5) GluK5	GRIK5	Grik5	YES	5,42E-02	1,15E-01	8,49E-02	1,22E-01	3,37E-02	1,43E-01	2,11E-01	1,40E-01	1,13E-01	3,13E-03	1,82E-01
GluN1	GRIN1	Grin1	YES	0,00E+00	0,00E+00	1,82E-03	4,66E-03	8,83E-03	2,14E-02	1,62E-02	3,84E-02	1,14E-02	1,79E-04	5,46E-02
GRIN2B (Glutamate Ionotropic Receptor NMDA Type Subunit 2B) GluN2B	GRIN2B	Grin2b	YES	1,90E-03	2,86E-02	5,29E-02	2,33E-01	2,30E-01	1,83E-01	1,64E-01	9,30E-02	1,23E-01	8,29E-03	2,26E-01
GRINA (Glutamate Ionotropic Receptor NMDA Type Subunit Associated Protein 1Ã)	Grina	Grina	YES	5,90E-02	9,78E-02	1,04E-01	1,19E-01	1,76E-01	2,65E-01	3,63E-01	4,57E-01	2,05E-01	2,05E-02	6,63E-01
5-HT1A	HTR1A	Htr1a	YES	3,18E-04	1,50E-03	0,00E+00	9,43E-04	0,00E+00	3,05E-03	1,23E-03	0,00E+00	8,81E-04	1,13E-06	-5,83E-04
5-HT1B	HTR1B	Htr1b	YES	0,00E+00	0,00E+00	0,00E+00	0,00E+00	5,22E-03	0,00E+00	0,00E+00	1,87E-03	8,87E-04	3,50E-06	1,87E-03
HTR3A (5-Hydroxytryptamine Receptor 3A) 5-HT3R	HTR3A	Htr3a	YES	1,28E-02	5,08E-03	3,22E-03	0,00E+00	9,53E-03	8,64E-03	2,95E-03	0,00E+00	5,27E-03	2,15E-05	-1,49E-02
5-HT5A	HTR5A	Htr5a	YES	0,00E+00	0,00E+00	0,00E+00	0,00E+00	0,00E+00	0,00E+00	0,00E+00	0,00E+00	0,00E+00	0,00E+00	0,00E+00
ITPR1 (Inositol 1, 4, 5-Trisphosphate Receptor Type 1)	ITPR1	Itpr1	YES	1,66E-02	2,96E-02	2,16E-02	3,15E-02	2,70E-02	3,40E-02	3,17E-02	4,53E-02	2,97E-02	7,33E-05	3,07E-02
ITPR2 (Inositol 1, 4, 5-Trisphosphate Receptor Type 2)	ITPR2	Itpr2	YES	1,57E-03	3,91E-03	4,04E-03	8,85E-03	1,46E-02	2,39E-02	2,98E-02	3,95E-02	1,58E-02	1,94E-04	6,38E-02
IP3R3	ITPR3	Itpr3	YES	0,00E+00	0,00E+00	0,00E+00	0,00E+00	0,00E+00	2,51E-03	0,00E+00	0,00E+00	3,14E-04	7,90E-07	0,00E+00
ROMK	KCNJ1	Kcnj1	YES	0,00E+00	0,00E+00	0,00E+00	0,00E+00	0,00E+00	0,00E+00	0,00E+00	0,00E+00	0,00E+00	0,00E+00	0,00E+00
KCNK1 (Potassium Two Pore Domain Channel	KCNK1	Kcnk1	YES	7,40E-03	1,14E-02	1,71E-02	3,69E-02	5,28E-02	1,94E-01	3,38E-01	3,70E-01	1,28E-01	2,31E-02	6,89E-01

Subfamily K Member 1) TWIK1														
KCNK10 (Potassium Two Pore Domain Channel Subfamily K Member 10) TREK2	KCNK10	Kcnk10	YES	4,26E-02	8,62E-02	1,31E-01	1,19E-01	8,55E-02	1,60E-01	1,82E-01	7,21E-02	1,10E-01	2,20E-03	1,25E-01
THIK2	KCNK12	Kcnk12	YES	2,87E-03	3,65E-03	3,49E-03	5,92E-03	3,12E-03	6,87E-03	3,15E-03	5,28E-03	4,29E-03	2,29E-06	1,91E-03
THIK1	KCNK13	Kcnk13	YES	3,22E-04	0,00E+00	0,00E+00	0,00E+00	0,00E+00	0,00E+00	0,00E+00	0,00E+00	4,03E-05	1,30E-08	-3,22E-04
TASK5	KCNK15	Kcnk15	YES	0,00E+00	1,76E-03	0,00E+00	0,00E+00	0,00E+00	0,00E+00	0,00E+00	0,00E+00	2,20E-04	3,86E-07	-1,76E-03
TALK1	KCNK16	Kcnk16	YES	0,00E+00	0,00E+00	0,00E+00	0,00E+00	0,00E+00	0,00E+00	0,00E+00	0,00E+00	0,00E+00	0,00E+00	0,00E+00
TALK2	KCNK17	Kcnk17	NO											
KCNK18 (Potassium Two Pore Domain Channel Subfamily K Member 18) TRESK	KCNK18	Kcnk18	YES	0,00E+00	0,00E+00	0,00E+00	0,00E+00	0,00E+00	0,00E+00	0,00E+00	0,00E+00	0,00E+00	0,00E+00	0,00E+00
KCNK2 (Potassium Two Pore Domain Channel Subfamily K Member 2) TREK1	KCNK2	Kcnk2	YES	8,55E-02	2,03E-01	3,15E-01	5,51E-01	6,65E-01	9,21E-01	1,16E+00	1,26E+00	6,46E-01	1,93E-01	2,14E+00
TASK1	KCNK3	Kcnk3	YES	3,76E-04	3,07E-03	1,15E-03	1,03E-03	0,00E+00	5,65E-03	8,72E-04	0,00E+00	1,52E-03	3,75E-06	-2,58E-03
KCNK4 (Potassium Two Pore Domain Channel Subfamily K Member 4) TRAAK	KCNK4	Kcnk4	YES	0,00E+00	0,00E+00	0,00E+00	0,00E+00	0,00E+00	0,00E+00	0,00E+00	0,00E+00	0,00E+00	0,00E+00	0,00E+00
KCNK5 (Potassium Two Pore Domain Channel Subfamily K Member 5) TASK2	KCNK5	Kcnk5	YES	2,58E-02	6,25E-02	3,99E-02	1,79E-02	1,47E-02	1,64E-02	1,48E-02	4,46E-03	2,45E-02	3,40E-04	-6,90E-02
TWIK2	KCNK6	Kcnk6	YES	0,00E+00	0,00E+00	0,00E+00	0,00E+00	0,00E+00	0,00E+00	0,00E+00	0,00E+00	0,00E+00	0,00E+00	0,00E+00
KCNK7	KCNK7	Kcnk7	YES	0,00E+00	0,00E+00	0,00E+00	7,92E-04	0,00E+00	0,00E+00	2,84E-03	0,00E+00	4,55E-04	1,01E-06	2,84E-03
TASK3	KCNK9	Kcnk9	YES	0,00E+00	0,00E+00	0,00E+00	0,00E+00	0,00E+00	0,00E+00	0,00E+00	0,00E+00	0,00E+00	0,00E+00	0,00E+00
KCNK9 (potassium two pore domain channel subfamily K member 9)	KCNK9	Kcnk9	YES	0,00E+00	0,00E+00	0,00E+00	0,00E+00	0,00E+00	0,00E+00	0,00E+00	0,00E+00	0,00E+00	0,00E+00	0,00E+00
BK	KCNMA1	Kcnma1	YES	0,00E+00	1,97E-03	0,00E+00	4,28E-03	0,00E+00	7,67E-03	4,22E-03	6,55E-03	3,09E-03	9,37E-06	8,81E-03

SK1	KCNN1	Kcnn1	YES	3,46E-03	4,41E-03	7,84E-03	6,58E-03	4,86E-03	1,83E-02	1,95E-02	1,50E-02	9,99E-03	4,30E-05	2,66E-02
KCNN2 (Potassium Calcium-Activated Channel Subfamily N Member 2) SK2	KCNN2	Kcnn2	YES	2,70E-02	7,05E-02	4,68E-02	8,49E-02	9,36E-02	2,12E-01	2,38E-01	1,86E-01	1,20E-01	6,46E-03	3,27E-01
KCNN3 (Potassium Calcium-Activated Channel Subfamily N Member 3) SK3	KCNN3	Kcnn3	YES	2,07E-03	4,34E-03	3,65E-03	2,00E-02	1,04E-02	1,76E-02	2,25E-02	5,15E-03	1,07E-02	6,69E-05	2,12E-02
KV7.1 voltage-gated potassium (K+) channel	KCNQ1	Kcnq1	YES	0,00E+00	0,00E+00	0,00E+00	0,00E+00	0,00E+00	0,00E+00	0,00E+00	0,00E+00	0,00E+00	0,00E+00	0,00E+00
KV7.2 voltage-gated potassium (K+) channel	KCNQ2	Kcnq2	YES	1,23E-02	2,85E-02	8,78E-03	1,28E-02	2,01E-02	1,49E-02	2,31E-02	2,41E-02	1,81E-02	4,73E-05	6,41E-03
KV7.3 voltage-gated potassium (K+) channel	KCNQ3	Kcnq3	YES	1,32E-03	9,94E-03	1,48E-02	9,42E-03	8,23E-03	1,64E-02	1,16E-02	4,02E-03	9,46E-03	2,56E-05	4,32E-03
KV7.4 voltage-gated potassium (K+) channel	KCNQ4	Kcnq4	YES	1,36E-03	2,15E-03	2,40E-03	1,96E-03	8,15E-03	4,73E-03	9,06E-03	0,00E+00	3,73E-03	1,08E-05	5,55E-03
KV7.5 voltage-gated potassium (K+) channel	KCNQ5	Kcnq5	YES	4,68E-04	0,00E+00	2,73E-04	4,10E-03	1,41E-03	2,05E-03	0,00E+00	0,00E+00	1,04E-03	2,10E-06	-4,68E-04
LETM1 (Leucine Zipper And EF-Hand Containing Transmembrane Protein 1)	LETM1	Letm1	YES	1,98E-01	2,69E-01	2,50E-01	3,23E-01	2,32E-01	2,82E-01	2,50E-01	2,96E-01	2,62E-01	1,50E-03	7,96E-02
LETM2 (Leucine Zipper And EF-Hand Containing Transmembrane Protein 2)	LETM2	Letm2	YES	8,76E-03	1,79E-02	1,55E-02	1,41E-02	2,05E-02	1,06E-02	3,01E-02	4,22E-02	2,00E-02	1,24E-04	4,56E-02
LRRC8A (Leucine Rich Repeat Containing 8 VRAC Subunit A)	LRRC8A	Lrrc8a	YES	3,19E-01	1,89E-01	2,17E-01	2,64E-01	1,08E-01	2,37E-01	4,47E-01	2,73E-01	2,57E-01	9,86E-03	2,11E-01
LRRC8B (Leucine Rich Repeat Containing 8 VRAC Subunit B)	LRRC8B	Lrrc8b	YES	2,48E-02	4,60E-02	3,09E-02	4,90E-02	2,69E-02	5,90E-02	4,23E-02	1,67E-02	3,69E-02	2,05E-04	-1,18E-02
LRRC8C (Leucine Rich Repeat Containing 8 VRAC Subunit C)Ã	LRRC8C	Lrrc8c	YES	2,55E-02	5,10E-02	5,75E-02	8,06E-02	1,06E-01	1,34E-01	1,08E-01	1,26E-01	8,60E-02	1,49E-03	1,58E-01
LRRC8D (Leucine Rich Repeat Containing 8 VRAC Subunit D)Ã	LRRC8D	Lrrc8d	YES	7,19E-02	9,66E-02	8,65E-02	1,04E-01	4,54E-02	7,68E-02	9,57E-02	2,56E-02	7,53E-02	7,43E-04	-4,73E-02
LRRC8E	LRRC8E	Lrrc8e	YES	0,00E+00	0,00E+00	0,00E+00	2,76E-03	0,00E+00	2,17E-03	0,00E+00	5,28E-03	1,28E-03	3,88E-06	5,28E-03

MCOLN1 (Mucolipin TRP Cation Channel 1) TRPML1	MCOLN1	Mcoln1	YES	2,36E-02	5,43E-02	2,42E-02	6,38E-02	5,02E-02	5,19E-02	4,86E-02	4,17E-02	4,48E-02	2,04E-04	1,24E-02
TRPML2	MCOLN2	Mcoln2	YES	0,00E+00	0,00E+00	0,00E+00	0,00E+00	0,00E+00	0,00E+00	0,00E+00	0,00E+00	0,00E+00	0,00E+00	0,00E+00
TRPML3	MCOLN3	Mcoln3	YES	1,66E-03	4,19E-03	4,30E-04	0,00E+00	0,00E+00	0,00E+00	0,00E+00	0,00E+00	7,85E-04	2,22E-06	-5,85E-03
MCU (Mitochondrial Calcium Uniporter)	MCU	Mcu	YES	2,11E-02	7,49E-02	3,78E-02	1,11E-01	9,12E-02	1,31E-01	1,32E-01	5,55E-02	8,19E-02	1,75E-03	9,19E-02
MCUB (Mitochondrial Calcium Uniporter Dominant Negative Subunit Beta)	MCUB	Mcub	NO											
MCUR1 (Mitochondrial Calcium Uniporter Regulator 1)	MCUR1	Mcur1	YES	8,67E-02	1,26E-01	1,14E-01	1,23E-01	4,00E-02	7,85E-02	2,13E-01	2,27E-01	1,26E-01	4,16E-03	2,27E-01
ORAI1 (ORAI Calcium Release-Activated Calcium Modulator 1)Ã	ORAI1	Orai1	YES	2,08E-02	3,60E-02	8,70E-02	9,23E-02	6,49E-02	1,95E-01	2,73E-01	2,87E-01	1,32E-01	1,11E-02	5,03E-01
ORAI2	ORAI2	Orai2	YES	4,66E-03	2,37E-02	1,73E-02	2,84E-02	1,83E-02	2,99E-02	2,30E-02	2,72E-02	2,16E-02	6,69E-05	2,18E-02
ORAI3 (ORAI Calcium Release-Activated Calcium Modulator 3)Ã	ORAI3	Orai3	YES	8,22E-03	2,81E-02	2,04E-02	2,59E-02	5,11E-02	7,05E-02	8,19E-02	9,10E-02	4,71E-02	9,62E-04	1,37E-01
PANX1 (Pannexin 1)	PANX1	Panx1	YES	8,85E-02	1,22E-01	7,63E-02	8,00E-02	7,30E-02	7,47E-02	5,69E-02	3,58E-02	7,59E-02	6,11E-04	-1,18E-01
PANX2	PANX2	Panx2	YES	6,45E-03	2,19E-02	8,57E-03	2,33E-02	8,02E-03	2,28E-02	2,49E-02	2,07E-02	1,71E-02	6,25E-05	1,72E-02
PANX3	PANX3	Panx3	YES	0,00E+00	0,00E+00	0,00E+00	0,00E+00	0,00E+00	0,00E+00	0,00E+00	0,00E+00	0,00E+00	0,00E+00	0,00E+00
PIEZO1	PIEZO1	Piezo1	YES	6,38E-04	0,00E+00	4,32E-04	8,09E-04	7,21E-03	9,34E-03	5,31E-03	1,50E-02	4,85E-03	2,96E-05	1,97E-02
PIEZO2	PIEZO2	Piezo2	YES	1,21E-03	4,02E-03	3,78E-03	4,09E-03	2,70E-03	4,25E-03	0,00E+00	0,00E+00	2,51E-03	3,39E-06	-5,23E-03
PKD1 (Polycystin 1 Transient Receptor Potential Channel Interacting) TRPP1	PKD1	Pkd1	YES	1,41E-02	4,61E-02	3,09E-02	6,02E-02	4,81E-02	4,63E-02	6,09E-02	3,30E-02	4,25E-02	2,49E-04	3,36E-02
PKD1L1	PKD1L1	Pkd1l1	YES	0,00E+00	0,00E+00	1,27E-03	1,27E-03	0,00E+00	6,26E-03	3,72E-03	5,24E-03	2,22E-03	6,32E-06	8,96E-03
PKD1L2	PKD1L2	Pkd1l2	YES	0,00E+00	0,00E+00	0,00E+00	0,00E+00	0,00E+00	0,00E+00	0,00E+00	0,00E+00	0,00E+00	0,00E+00	0,00E+00
PKD1L3	PKD1L3	Pkd1l3	YES	0,00E+00	0,00E+00	0,00E+00	0,00E+00	0,00E+00	0,00E+00	0,00E+00	0,00E+00	0,00E+00	0,00E+00	0,00E+00

PKD2 (Polycystin 2 Transient Receptor Potential Cation Channel) TRPP2	PKD2	Pkd2	YES	4,88E-02	1,05E-01	6,78E-02	1,29E-01	7,08E-02	1,23E-01	2,03E-01	1,26E-01	1,09E-01	2,36E-03	1,75E-01
PKD2L1	PKD2L1	Pkd2l1	YES	0,00E+00	0,00E+00	0,00E+00	0,00E+00	0,00E+00	0,00E+00	0,00E+00	0,00E+00	0,00E+00	0,00E+00	0,00E+00
PKD2L1	PKD2L1	Pkd2l1	YES	0,00E+00	0,00E+00	0,00E+00	0,00E+00	0,00E+00	0,00E+00	0,00E+00	0,00E+00	0,00E+00	0,00E+00	0,00E+00
RYR1	RYR1	Ryr1	YES	7,40E-03	1,90E-02	1,64E-02	3,01E-02	2,49E-02	3,04E-02	6,82E-02	2,18E-02	2,73E-02	3,31E-04	6,37E-02
RYR2	RYR2	Ryr2	YES	0,00E+00	0,00E+00	1,62E-03	3,48E-03	9,38E-03	1,57E-02	5,52E-03	9,34E-03	5,63E-03	3,04E-05	1,49E-02
SCNN1A (Sodium Channel Epithelial 1 Subunit Alpha) ENaCa	SCNN1A	Scnn1a	YES	1,89E-04	1,87E-03	0,00E+00	1,18E-03	0,00E+00	0,00E+00	5,94E-03	1,03E-02	2,43E-03	1,41E-05	1,42E-02
SCNN1B (Sodium Channel Epithelial 1 Subunit Beta) ENaCb	SCNN1B	Scnn1b	YES	0,00E+00	0,00E+00	0,00E+00	0,00E+00	0,00E+00	0,00E+00	0,00E+00	0,00E+00	0,00E+00	0,00E+00	0,00E+00
SCNN1G (Sodium Channel Epithelial 1 Subunit Gamma) ENaCg	SCNN1G	Scnn1g	YES	0,00E+00	0,00E+00	0,00E+00	0,00E+00	0,00E+00	0,00E+00	0,00E+00	0,00E+00	0,00E+00	0,00E+00	0,00E+00
SEC61A1 (SEC61 Translocon Subunit Alpha 1)	SEC61A1	Sec61a1	YES	9,89E-02	3,53E-01	1,35E-01	2,26E-01	2,36E-01	2,70E-01	2,34E-01	2,24E-01	2,22E-01	6,09E-03	5,78E-03
SEC61A2 (SEC61 Translocon Subunit Alpha 2)	SEC61A2	Sec61a2	YES	1,31E-01	3,80E-01	2,50E-01	3,34E-01	2,52E-01	2,75E-01	2,74E-01	3,12E-01	2,76E-01	5,37E-03	7,45E-02
SEC61B (SEC61 Translocon Subunit Beta)Ã	SEC61B	Sec61b	YES	1,25E+00	1,35E+00	1,49E+00	1,44E+00	1,25E+00	1,32E+00	1,10E+00	1,06E+00	1,28E+00	2,25E-02	-4,32E-01
SEC61G (SEC61 Translocon Subunit Gamma)	SEC61G	Sec61g	YES	2,35E+00	1,93E+00	2,14E+00	2,23E+00	2,25E+00	1,47E+00	1,70E+00	1,38E+00	1,93E+00	1,41E-01	-1,20E+00
NCKX1	SLC24A1	Slc24a1	YES	0,00E+00	0,00E+00	0,00E+00	0,00E+00	0,00E+00	0,00E+00	0,00E+00	0,00E+00	0,00E+00	0,00E+00	0,00E+00
NCKX2	SLC24A2	Slc24a2	YES	1,71E-03	0,00E+00	6,54E-04	8,17E-04	3,10E-03	2,69E-03	0,00E+00	0,00E+00	1,12E-03	1,54E-06	-1,71E-03
SLC24A3 (Solute Carrier Family 24 Member 3) NCKX3	SLC24A3	Slc24a3	YES	3,86E-04	0,00E+00	3,39E-03	3,56E-03	8,93E-03	6,70E-03	1,41E-02	4,98E-03	5,26E-03	2,17E-05	1,87E-02
NCKX4	SLC24A4	Slc24a4	YES	9,37E-04	4,49E-03	3,02E-03	3,68E-03	0,00E+00	5,42E-03	3,79E-03	1,87E-03	2,90E-03	3,37E-06	2,32E-04
SLC24A5 (Solute Carrier Family 24 Member 5) NCKX5	SLC24A5	Slc24a5	YES	4,55E-01	4,17E-01	4,35E-01	7,33E-01	2,81E-01	4,56E-01	5,46E-01	2,18E-01	4,43E-01	2,47E-02	-1,08E-01

NCX1	SLC8A1Ä	Slc8a1	YES	3,46E-04	4,33E-03	7,62E-04	7,41E-03	0,00E+00	3,30E-03	2,36E-03	0,00E+00	2,31E-03	6,86E-06	-2,32E-03
NCX2	SLC8A2	Slc8a2	YES	7,20E-03	2,16E-02	9,23E-03	1,21E-02	7,36E-03	3,00E-02	2,45E-02	1,01E-02	1,53E-02	7,75E-05	5,87E-03
NCX3	SLC8A3Ä	Slc8a3	YES	5,94E-04	5,56E-04	4,06E-04	9,95E-04	0,00E+00	5,18E-03	5,56E-03	0,00E+00	1,66E-03	5,35E-06	4,41E-03
SLC8B1 (Solute Carrier Family 8 Member B1) NCLX6	SLC8B1	Slc8b1	YES	3,21E-03	5,07E-03	9,89E-03	7,36E-03	3,10E-02	4,14E-02	1,11E-01	1,75E-01	4,79E-02	3,89E-03	2,77E-01
SMDT1 (Single-Pass Membrane Protein with Aspartate Rich Tail 1) EMRE	SMDT1	Smdt1	YES	1,27E+00	1,27E+00	1,47E+00	1,50E+00	1,66E+00	1,59E+00	1,59E+00	1,60E+00	1,49E+00	2,30E-02	6,55E-01
TMBIM1 (Transmembrane BAX Inhibitor Motif Containing 1)Ã	TMBIM1	Tmbim1	YES	5,07E-03	1,96E-02	1,93E-02	4,37E-02	2,22E-02	7,53E-02	1,20E-01	1,73E-01	5,98E-02	3,52E-03	2,69E-01
TMBIM2	TMBIM2	Tmbim2	NO											
TMBIM3	TMBIM3	Tmbim3	NO											
TMBIM4 (Transmembrane BAX Inhibitor Motif Containing 4)	TMBIM4	Tmbim4	YES	2,58E-01	1,98E-01	2,57E-01	3,04E-01	2,17E-01	4,03E-01	4,26E-01	4,45E-01	3,14E-01	9,59E-03	4,15E-01
TMBIM5	TMBIM5	Tmbim5	NO											
TMBIM6 (Transmembrane BAX Inhibitor Motif Containing 6)	TMBIM6	Tmbim6	YES	7,72E-01	9,06E-01	9,82E-01	9,89E-01	1,11E+00	1,54E+00	1,84E+00	2,43E+00	1,32E+00	3,27E-01	2,59E+00
TMCO1 (Transmembrane and Coiled-Coil Domains 1)	TMCO1	Tmco1	YES	4,90E-01	5,29E-01	4,83E-01	6,53E-01	7,00E-01	6,22E-01	7,02E-01	6,46E-01	6,03E-01	8,08E-03	3,30E-01
TMCO2	TMCO2	Tmco2	YES	0,00E+00	0,00E+00	3,25E-04	0,00E+00	0,00E+00	0,00E+00	0,00E+00	0,00E+00	4,06E-05	1,32E-08	0,00E+00
TMCO3 (Transmembrane and Coiled-Coil Domains 3)	TMCO3	Tmco3	YES	4,32E-02	7,77E-02	8,54E-02	1,20E-01	8,29E-02	1,63E-01	1,78E-01	2,25E-01	1,22E-01	3,78E-03	2,82E-01
TMCO4	TMCO4	Tmco4	YES	1,39E-03	1,76E-03	1,52E-02	6,42E-03	1,41E-02	1,70E-02	1,83E-02	2,24E-02	1,21E-02	6,21E-05	3,75E-02
TMCO5	TMCO5	Tmco5	YES	0,00E+00	0,00E+00	0,00E+00	0,00E+00	0,00E+00	0,00E+00	0,00E+00	0,00E+00	0,00E+00	0,00E+00	0,00E+00
TMCO6 (Transmembrane and Coiled-Coil Domains 6)	TMCO6	Tmco6	YES	2,95E-02	5,77E-02	2,60E-02	3,62E-02	5,02E-02	4,05E-02	5,82E-02	4,34E-02	4,27E-02	1,46E-04	1,44E-02

TMEM109	TMEM109	Tmem109	YES	5,68E-02	1,44E-01	1,13E-01	1,06E-01	1,20E-01	1,48E-01	1,52E-01	1,33E-01	1,22E-01	9,67E-04	8,46E-02
TACAN	TMEM120A	Tmem120a	YES	9,44E-02	1,27E-01	1,36E-01	1,57E-01	1,79E-01	2,13E-01	2,39E-01	2,61E-01	1,76E-01	3,39E-03	2,79E-01
TMEM 150 A (tentonin 1)	TMEM150A	Tmem150a	YES	4,16E-03	1,72E-02	1,53E-02	2,11E-02	4,05E-02	6,36E-02	8,90E-02	1,03E-01	4,42E-02	1,36E-03	1,71E-01
TMEM 150 B (tentonin 2)	TMEM150B	Tmem150b	YES	9,06E-04	0,00E+00	0,00E+00	1,63E-03	0,00E+00	0,00E+00	0,00E+00	0,00E+00	3,16E-04	3,80E-07	-9,06E-04
TMEM 150 C (tentonin 3)	TMEM150C	Tmem150c	YES	5,95E-03	4,91E-03	1,03E-02	8,59E-03	1,24E-02	2,77E-02	5,30E-02	3,21E-02	1,94E-02	2,86E-04	7,43E-02
TMEM165	TMEM165	Tmem165	YES	6,08E-01	6,66E-01	6,07E-01	6,20E-01	1,25E-01	3,45E-01	7,42E-01	5,18E-01	5,29E-01	4,03E-02	-1,34E-02
TRIC-A	TMEM38A	Tmem38a	YES	3,53E-02	6,19E-02	6,99E-02	8,62E-02	1,33E-01	2,14E-01	2,14E-01	2,15E-01	1,29E-01	5,78E-03	3,32E-01
TRIC-B	TMEM38B	Tmem38b	YES	5,66E-02	6,90E-02	6,57E-02	7,18E-02	2,46E-02	8,71E-02	1,29E-01	9,68E-02	7,50E-02	9,28E-04	9,96E-02
TPCN1 (Two Pore Segment Channel 1)	TPCN1	Tpcn1	YES	2,40E-02	5,85E-02	4,52E-02	1,19E-01	1,60E-01	3,08E-01	3,10E-01	3,40E-01	1,71E-01	1,70E-02	5,67E-01
TPC2	TPCN2	Tpcn2	YES	5,17E-03	1,13E-02	9,04E-03	1,49E-02	8,06E-03	1,46E-02	7,07E-03	2,89E-02	1,24E-02	5,63E-05	1,95E-02
TRPA1 (Transient Receptor Potential Cation Channel Subfamily A Member 1)	TRPA1	Trpa1	YES	0,00E+00	0,00E+00	0,00E+00	0,00E+00	2,88E-03	2,32E-03	0,00E+00	4,38E-03	1,20E-03	3,05E-06	4,38E-03
TRPC1 (Transient Receptor Potential Cation Channel Subfamily C Member 1)	TRPC1	Trpc1	YES	3,98E-02	8,99E-02	7,81E-02	8,96E-02	4,32E-02	7,63E-02	1,56E-01	1,47E-01	9,00E-02	1,80E-03	1,73E-01
TRPC2	TRPC2	Trpc2	YES	0,00E+00	0,00E+00	0,00E+00	0,00E+00	0,00E+00	0,00E+00	0,00E+00	0,00E+00	0,00E+00	0,00E+00	0,00E+00
TRPC3	TRPC3	Trpc3	YES	4,98E-03	9,65E-03	3,73E-03	0,00E+00	1,70E-03	8,15E-03	1,80E-03	4,02E-03	4,25E-03	1,08E-05	-8,81E-03
TRPC4 (Transient Receptor Potential Cation Channel Subfamily C Member 4)	TRPC4	Trpc4	YES	6,85E-04	3,38E-03	6,58E-03	1,28E-02	1,18E-02	2,86E-02	1,40E-02	9,26E-03	1,09E-02	7,30E-05	1,92E-02
TRPC5	TRPC5	Trpc5	YES	0,00E+00	0,00E+00	6,83E-04	7,81E-04	4,78E-03	1,97E-02	2,58E-02	0,00E+00	6,48E-03	1,06E-04	2,58E-02
TRPC6 (Transient Receptor Potential Cation Channel Subfamily C Member 6)	TRPC6	Trpc6	YES	0,00E+00	0,00E+00	0,00E+00	0,00E+00	0,00E+00	0,00E+00	0,00E+00	0,00E+00	0,00E+00	0,00E+00	0,00E+00
TRPC7	TRPC7	Trpc7	YES	3,53E-04	1,62E-03	0,00E+00	0,00E+00	0,00E+00	5,62E-03	1,01E-02	3,10E-02	6,09E-03	1,15E-04	3,91E-02

TRPM1	TRPM1	Trpm1	YES	0,00E+00	0,00E+00	1,84E-03	1,64E-03	2,36E-03	1,88E-03	1,29E-02	1,09E-02	3,94E-03	2,51E-05	2,38E-02
TRPM2	TRPM2	Trpm2	YES	7,86E-05	0,00E+00	3,49E-04	1,18E-03	0,00E+00	0,00E+00	1,47E-03	0,00E+00	3,85E-04	3,58E-07	1,39E-03
TRPM3 (Transient Receptor Potential Cation Channel Subfamily M Member 3)Â	TRPM3	Trpm3	YES	0,00E+00	0,00E+00	6,39E-04	0,00E+00	0,00E+00	9,72E-03	7,02E-03	0,00E+00	2,17E-03	1,52E-05	7,02E-03
TRPM4	TRPM4	Trpm4	YES	3,33E-03	5,89E-03	8,41E-03	3,78E-03	2,06E-03	1,76E-02	1,82E-02	2,14E-02	1,01E-02	6,00E-05	3,04E-02
TRPM5	TRPM5	Trpm5	YES	3,87E-04	0,00E+00	0,00E+00	0,00E+00	0,00E+00	0,00E+00	0,00E+00	0,00E+00	4,84E-05	1,88E-08	-3,87E-04
TRPM6	TRPM6	Trpm6	YES	3,56E-03	1,67E-02	9,75E-03	7,91E-03	1,92E-02	2,59E-02	8,92E-03	3,79E-02	1,62E-02	1,28E-04	2,66E-02
TRPM7 (Transient Receptor Potential Cation Channel Subfamily M Member 7)	TRPM7	Trpm7	YES	8,33E-02	1,79E-01	1,07E-01	1,77E-01	7,95E-02	7,99E-02	1,33E-01	9,93E-02	1,17E-01	1,71E-03	-2,98E-02
TRPM8	TRPM8	Trpm8	YES	0,00E+00	0,00E+00	0,00E+00	0,00E+00	0,00E+00	0,00E+00	0,00E+00	0,00E+00	0,00E+00	0,00E+00	0,00E+00
TRPV1	TRPV1	Trpv1	YES	0,00E+00	0,00E+00	0,00E+00	0,00E+00	0,00E+00	0,00E+00	0,00E+00	0,00E+00	0,00E+00	0,00E+00	0,00E+00
TRPV2	TRPV2	Trpv2	YES	2,72E-03	6,24E-03	1,24E-03	4,64E-03	2,51E-03	4,72E-03	5,24E-03	6,59E-03	4,24E-03	3,60E-06	2,88E-03
TRPV3	TRPV3	Trpv3	YES	0,00E+00	0,00E+00	0,00E+00	0,00E+00	0,00E+00	0,00E+00	0,00E+00	0,00E+00	0,00E+00	0,00E+00	0,00E+00
TRPV4 (Transient Receptor Potential Cation Channel Subfamily V Member 4)	TRPV4	Trpv4	YES	3,10E-03	0,00E+00	3,29E-04	0,00E+00	0,00E+00	0,00E+00	0,00E+00	0,00E+00	4,28E-04	1,18E-06	-3,10E-03
TRPV5	TRPV5	Trpv5	YES	0,00E+00	0,00E+00	0,00E+00	0,00E+00	0,00E+00	0,00E+00	0,00E+00	0,00E+00	0,00E+00	0,00E+00	0,00E+00
TRPV6	TRPV6	Trpv6	YES	0,00E+00	0,00E+00	0,00E+00	0,00E+00	0,00E+00	0,00E+00	0,00E+00	0,00E+00	0,00E+00	0,00E+00	0,00E+00
CAMK2A	CAMK2A	Camk2a	YES	1,39E-02	3,63E-02	2,36E-02	7,02E-02	9,73E-02	4,16E-02	2,26E-02	1,62E-02	4,02E-02	8,61E-04	-1,14E-02
CAMK2B	CAMK2B	Camk2b	YES	8,97E-03	3,11E-02	2,03E-02	1,96E-02	1,68E-02	9,86E-02	4,83E-02	3,65E-02	3,50E-02	8,15E-04	4,47E-02
CAMK2D	CAMK2D	Camk2d	YES	3,80E-02	1,80E-01	1,25E-01	2,82E-01	4,45E-01	5,36E-01	6,87E-01	5,09E-01	3,50E-01	5,20E-02	9,78E-01
CAMK2G	CAMK2G	Camk2g	YES	1,14E-01	2,43E-01	1,66E-01	1,63E-01	1,43E-01	2,59E-01	3,72E-01	5,75E-01	2,55E-01	2,36E-02	5,90E-01